

# Verification of the process reliability and scalability of an airborne measuring system for the heliostat orientation in solar power tower plants

Masterarbeit im Studiengang M.Sc. Mechatronik

Friedrich-Alexander-Universität Erlangen-Nürnberg  
Lehrstuhl für Fertigungsautomatisierung und Produktionssystematik  
Prof. Dr.-Ing. Jörg Franke



Bearbeiter: Michael Fischer, M. Sc., 22067080

Betreuer: Prof. Dr.-Ing. Jörg Franke  
Christian Hofmann (M.Sc.), FAPS  
Wilko Jessen (M.Eng.), German Aerospace Center (DLR)

Abgabetermin: 15.12.2020

Bearbeitungszeit: 6 Monate



# Non-disclosure Notice

This master's thesis contains no confidential data of German Aerospace Center (Deutsches Zentrum für Luft- und Raumfahrt e.V.) (DLR). Since DLR is a state-financed research company, all publications, including this thesis, are accessible to the general public through [elib.dlr.de](http://elib.dlr.de).

Erlangen, December 15, 2020



Michael Fischer



# Statutory Declaration

I hereby confirm that I have prepared the work without the assistance of others and without using sources other than those indicated and that the work has not yet been submitted to any other examination office in the same or similar form and has been accepted by them as part of an examination paper. All statements that have been adopted verbatim or analogously are marked as such.

I hereby declare that the thesis submitted is my own unaided work. All direct or indirect sources used are acknowledged as references. I am aware that the thesis in digital form can be examined for the use of unauthorized aid and in order to determine whether the thesis as a whole or parts incorporated in it may be deemed as plagiarism. For the comparison of my work with existing sources I agree that it shall be entered in a database where it shall also remain after examination, to enable comparison with future theses submitted.

*Ich versichere, dass ich die Arbeit ohne fremde Hilfe und ohne Benutzung anderer als der angegebenen Quellen angefertigt habe und dass die Arbeit in gleicher oder ähnlicher Form noch keiner anderen Prüfungsbehörde vorgelegen hat und von dieser als Teil einer Prüfungsleistung angenommen wurde. Alle Ausführungen, die wörtlich oder sinngemäß übernommen wurden, sind als solche gekennzeichnet.*

*Ich erkläre hiermit ehrenwörtlich, dass ich die vorliegende Arbeit selbständig angefertigt habe. Die aus fremden Quellen direkt und indirekt übernommenen Gedanken sind als solche kenntlich gemacht. Ich weiß, dass die Arbeit in digitalisierter Form daraufhin überprüft werden kann, ob unerlaubte Hilfsmittel verwendet wurden und ob es sich – insgesamt oder in Teilen – um ein Plagiat handelt. Zum Vergleich meiner Arbeit mit existierenden Quellen darf sie in eine Datenbank eingestellt werden und nach der Überprüfung zum Vergleich mit künftig eingehenden Arbeiten dort verbleiben. Weitere Vervielfältigungs- und Verwertungsrechte werden dadurch nicht eingeräumt. Die Arbeit wurde weder einer anderen Prüfungsbehörde vorgelegt noch veröffentlicht.*

Erlangen, December 15, 2020



Michael Fischer



# Abstract

The efficiency of a solar tower power plant (STPP) is noticeably impaired by incorrect orientation of the heliostats. An error in tracking the heliostat orientations causes a partial loss of incident irradiance during reflection. This reduces the yield of an STPP. The conventional flux density measurement (FDM) method, where the heliostat orientations are calibrated by sequentially pointing the heliostats onto a target, is a very slow process. To date, in fact, no commercially available solution for orientation monitoring of STPPs has been established that is both fast and accurate, especially for large STPPs. Therefore, German Aerospace Center (Deutsches Zentrum für Luft- und Raumfahrt e.V.) (DLR) has developed “QFLY”, a measuring system for quality control of utility scale solar fields<sup>1</sup> (QFLY), which utilizes an unmanned aerial vehicle (UAV) to measure Parabolic Trough Power Plants (PTPP) within a few hours. DLR has extended the functionality of QFLY for the application on STPPs, which is still to be fully approved. The goal of this thesis is to verify the measurement accuracy and scalability of QFLY for STPPs. Measurement campaigns including QFLY and the reference measurement FDM took place on the CESA-1<sup>2</sup> (CESA-1) at the Plataforma Solar de Almería<sup>3</sup> (PSA), and at the STPP in Jülich, Germany<sup>4</sup> (Jülich). Based on the measured values, different models for the quality assessment and the performance of QFLY are created and finally compared with the reference data.

The first approach is to analyze an early intermediate result of QFLY, called “QFly ZERO ASSUMPTION”<sup>5</sup> (ZA), which gives a rough estimation of the orientation of the heliostats. If a certain heliostat is visible on an image, in a best-case-scenario an orientation is calculated for this heliostat, judging by its outer corners. On average 69 (CESA-1-2018) or 207 (CESA-1-2020) ZA orientations per heliostat are calculated. For the CESA-1-2020 data-set, the normal vectors are deviating with a standard deviation of 34 mrad around the respective heliostat’s mean normal vector, which is quite a lot. In this thesis a novel parameter-based optimization process was developed, which filters the calculated alignments, independently from the reference result. In the context of the data basis, parameters like the distance of the heliostat to the camera or

---

<sup>1</sup>QFLY is a trademark name of a process developed by *DLR* for the supply of airborne imaging and related software to obtain information on the geometric, optical and thermal properties of a measured CSP or PV plant.

<sup>2</sup>CESA-1 is a STPP featured on the PSA. Technical specifications: 300 heliostats with 40 m<sup>2</sup> each, 7 MWth, tower height 83 m. [1]

<sup>3</sup>The PSA is a research facility on CSP technology, located in Tabernas, southeastern Spain, owned by CIEMAT.

<sup>4</sup>STPP-JÜLICH is a research facility covering the world’s first commercial STPP erected in the city of Juelich, Germany, starting operation in 2008. [2]

<sup>5</sup>The so-called ZERO ASSUMPTION is a preliminary assumption of orientation of heliostats as part of the QFly code structure.

the angle, which is calculated from the heliostat mirror normal vector and the connecting line between camera and heliostat center ( $\alpha_{\text{cam2Helio3D}}$ ), which can also be viewed in a differentiated way when projected onto the XY plane, play a decisive role for the optimization. It was shown in the case of CESA-1-2020, that for  $\alpha_{\text{cam2Helio3D}} = [58^\circ, 70^\circ]$  an improvement of 38.2% of the deviation from the reference measurement is achieved based on an unfiltered data set. The mean deviation between FDM and ZA for all available FDM heliostats is 8.9 mrad (standard deviance of 7.0 mrad), and therefore lies within the required error spectrum of 10 mrad compared to the reference measurement. The ZA results are thus as accurate as the PG result, which has a mean deviation in normal vector of 8.9 mrad for the same FDM heliostats.

The process scalability of QFLY can be tremendously improved by aiming at the photogrammetric calculation at the end of the QFLY process in “AICON 3D STUDIO”<sup>6</sup> (AICON). In fact over 70% of the QFLY processing duration is spent with the QFly photogrammetry in AICON (PG) in AICON. The currently forbidding long processing duration could be improved by reducing the number of images given into AICON as an input. To this end, a program has been written to transfer only high-quality images and detection data to the photogrammetric software, while maintaining the information content and interconnectivity of the images. This is done by eliminating redundant images and detections of features. Redundancy in images is present, the more similar the camera position, camera viewing direction and the detected features are. In addition, image-specific parameters are developed, such as the fill level and coverage of detections per image. Another important aspect is the filtering of detections based on expected weak results – this can be defined by a ZA calculation with all detected features instead of the outer corners. Further improvement is done by reducing the quantity of detections per feature to a certain fixed value, while deciding to keep those detections, for which the camera positions are most distinct to each other. It could be approved, that filtering images having similar EOR ( $<0.5\text{m}$ ), similar viewing direction ( $<0.5^\circ$ ) and similar detections ( $>90\%$ ) calculate 8% faster than filtering out the same quantity of images randomly. The accuracy of the measurement regarding the heliostat orientation was not scope of the investigations.

---

<sup>6</sup>AICON 3D STUDIO is a photogrammetry software developed by AICON 3D SYSTEMS GMBH in 2002. The company got meanwhile acquired by HEXAGON MANUFACTURING INTELLIGENCE.





# Kurzzusammenfassung

Die Effizienz eines STPP wird durch eine falsche Ausrichtung der Heliostaten merklich beeinträchtigt. Ein Fehler bei der Nachführung der Heliostatenausrichtungen bewirkt einen teilweisen Verlust der einfallenden Bestrahlungsstärke bei der Reflexion. Dies reduziert die Ausbeute eines STPP. Die herkömmliche FDM-Methode, bei der die Heliostatenausrichtungen durch sequentielles Ausrichten der Heliostaten auf ein Ziel kalibriert werden, ist ein sehr langsamer Prozess. Bis heute gibt es keine kommerziell erhältliche Lösung für die Orientierungsüberwachung von STPPs, die sowohl schnell als auch genau ist, insbesondere für große STPPs. Daher hat DLR QFLY entwickelt, das eine UAV bereits serienmäßig verwendet, um STPP innerhalb weniger Stunden zu messen. Das DLR will die Funktionalität von QFLY für die Anwendung auf STPPs erweitern. Das Ziel dieser Arbeit ist es, die Messgenauigkeit und Skalierbarkeit von QFLY für STPPs zu verifizieren. Messkampagnen mit QFLY und der Referenzmessung FDM fanden an der PSA im Kraftwerk CESA-1 und in Jülich statt. Basierend auf den Messwerten werden verschiedene Modelle für die Qualitätsbewertung und die Leistung von QFLY erstellt und schließlich mit den Referenzdaten verglichen.

Der erste Ansatz besteht darin, ein frühes Zwischenergebnis von QFLY, genannt ZA, zu analysieren, das eine grobe Abschätzung der Ausrichtung der Heliostaten liefert. Wenn ein bestimmter Heliostat auf einem Bild sichtbar ist, wird unter entsprechenden Umständen eine Orientierung für diesen Heliostaten anhand seiner äußeren Ecken berechnet. Im Durchschnitt werden 69 (CESA-1-2018) bzw. 207 (CESA-1-2020) ZA-Orientierungen pro Heliostat berechnet. Für den CESA-1-2020-Datensatz weichen die Normalvektoren mit einer Standardabweichung von 34 mrad um den mittleren Normalvektor des jeweiligen Heliostaten ab. In dieser Arbeit wurde ein neuartiges parameterbasiertes Optimierungsverfahren entwickelt, das die ZA-Ergebnisse unabhängig vom Referenzergebnis filtert. Parameter wie der Abstand des Heliostaten zur Kamera oder der Winkel, der sich aus dem Heliostatenspiegelnormalvektor und der Verbindungslinie zwischen Kamera und Heliostatenmittelpunkt ( $\alpha_{\text{cam2Helio3D}}$ ) errechnet, der auch bei Projektion auf die XY-Ebene differenziert betrachtet werden kann, eine entscheidende Rolle für die Optimierung. Im Fall von CESA-1-2020 wurde gezeigt, dass für  $\alpha_{\text{cam2Helio3D}} = [58^\circ, 70^\circ]$  eine Verbesserung von 38,2% der Abweichung von der Referenzmessung auf Basis eines ungefilterten Datensatzes erreicht wird. Die mittlere Abweichung zwischen FDM und ZA für alle verfügbaren FDM-Heliostaten beträgt 8,9 mrad (Standardabweichung von 7,0 mrad) und liegt damit innerhalb des geforderten Fehlerspektrums von 10 mrad gegenüber der Referenzmessung. Die ZA-Ergebnisse sind damit ebenso genau wie das PG-Ergebnis, das für die gleichen FDM-Heliostaten

eine mittlere Abweichung im Normalvektor von ebenfalls 8,9 mrad aufweist.

Die Prozessskalierbarkeit von QFLY kann enorm verbessert werden, indem man die photogrammetrische Berechnung am Ende des QFLY-Prozesses in AICON fokussiert. In der Tat werden über 70% der QFLY-Verarbeitungsdauer mit der PG in AICON verbracht. Die derzeit unzulässig lange Verarbeitungsdauer könnte verbessert werden, indem die Anzahl der in AICON als Eingabe gegebenen Bilder reduziert wird. Zu diesem Zweck wurde ein Programm geschrieben, das nur qualitativ hochwertige Bilder und Featuredetektionen an die Photogrammetriesoftware übergibt, wobei der Informationsgehalt und die Zusammenhänge der Bilder erhalten bleiben. Dies geschieht durch die Eliminierung redundanter Bilder und Detektionen von Features. Redundanz in Bildern ist umso mehr vorhanden, je ähnlicher die Kameraposition, die Kamerablickrichtung und die detektierten Features sind. Darüber hinaus werden bildspezifische Parameter entwickelt, wie z. B. der Füllgrad und die Abdeckung der Detektionen pro Bild. Ein weiterer wichtiger Aspekt ist die Filterung der Detektionen auf Basis zu erwartender ungenauer Detektionen – dies kann durch eine Berechnung mit allen erkannten Merkmalen anstelle der äußeren Ecken definiert werden. Eine weitere Verbesserung wird erreicht, indem die Anzahl der Detektionen pro Merkmal auf einen bestimmten festen Wert reduziert wird, wobei die Detektionen behalten werden, deren Kamerapositionen am deutlichsten voneinander abweichen. Es konnte bestätigt werden, dass ein Datensatz, der durch Filtern von Bildern mit ähnlicher EOR ( $<0.5\text{m}$ ), ähnlicher Blickrichtung ( $<0.5^\circ$ ) und ähnlichen Detektionen ( $>90\%$ ) erzeugt wird, 8% schneller berechnet wird als ein Datensatz, bei dem dieselbe Menga an Bildern zufällig herausgefiltert wurde. Die Genauigkeit der Messung bezüglich der Heliostatenausrichtung war nicht Gegenstand der Untersuchungen.





# Acknowledgements

First of all I would like to thank my supervisor Wilko Jessen, German Aerospace Center (Deutsches Zentrum für Luft- und Raumfahrt e.V.) (DLR), for his helpfulness and politeness. His support was crucial to put this thesis together. Almost the entire time was spent in the home office, and the process of preparing this work required a deep understanding of “QFLY”, a measuring system for quality control of utility scale solar fields<sup>7</sup> (QFLY) and its associated software code. In this respect, I was glad about the daily arranged meetings and the support I received by Wilko. Wilko is currently conducting his Ph.D. at RWTH Aachen, and the majority of results of this thesis will gather in his research.

I would also like to thank my supervisor from my university, Mr. Christian Hofmann, Chair of Manufacturing Automation and Production Systematics (Lehrstuhl für Fertigungsautomatisierung und Produktionssystematik) (FAPS), whose constructive suggestions have contributed significantly to the success of this thesis. His confidence over the whole eight months was simply unique, and due to the extraordinary situation we had this year not a matter of course.

I would also like to thank all my colleagues at DLR in Almería for the pleasant working atmosphere and the support they provided. Special thanks go to Christoph Prah, Marc Röger, and Vladimir Harwardt. Christoph Prah is significantly responsible for the development of the QFLY project and was therefore the foundation of my work as well as a universal source for answering questions. Marc Röger was able to provide a decisive feedback loop on the quality of the results of this work through decades of excellence in solar research. Vladimir Harwardt was always able to assist with programming questions. In addition, I was always able to find inspiration for new solutions through his universal view of things.

Many thanks also to all those who have contributed in any way to the current state of QFLY – especially Christoph Prah, Marc Röger and Wilko Jessen.

I also want to pay tribute to CIEMAT, the Spanish Center for Energy, Environmental and Technological Research (Centro de Investigaciones Energéticas, Medioambientales y Tecnológicas)<sup>8</sup> (CIEMAT) for providing access to their facilities at the Plataforma Solar de Almería<sup>9</sup> (PSA) and assisting in operation of the heliostats. Special thanks go to Blas Díaz Sánchez, CIEMAT, who was responsible for the control of the heliostats in the command center, and David Mu-

---

<sup>7</sup>QFLY is a trademark name of a process developed by *DLR* for the supply of airborne imaging and related software to obtain information on the geometric, optical and thermal properties of a measured CSP or PV plant.

<sup>8</sup>CIEMAT is under the direct political supervision of the Spanish Ministry of Research and Development.

<sup>9</sup>The PSA is a research facility on CSP technology, located in Tabernas, southeastern Spain, owned by CIEMAT.

ruve Tejada, DLR, responsible for workshop activities and assistance during measurements. At the same time, sincere thanks to Benjamin Brix of CSP SERVICES GMBH<sup>10</sup> (CSP SERVICES), who was responsible for the hand photogrammetry and tachymeter measurements during the measurement campaigns.

I'm also expressing deep gratitude to the German Federal Ministry for Economic Affairs and Energy (BMWi) for their financial support for the project HELIOPPOINT<sup>11</sup> (HELIOPPOINT) – the project this thesis is associated with (sponsorship ID: 0324201).

After three weeks of office, by mid-March, all DLR employees were sent to the home office because of the Corona crisis, and this did not change until the end of my employment. I am all the more thankful that the present work could be completed within the planned time frame. From this point of view, special thanks are due to my roommates Yann Fabel, Johannes Hirth, Lorenz Friedlein, and again Vladimir Harwardt, all of them also conducting research at DLR, and who pushed me during these pandemic times through their commitment and determination.

Special thanks are due to my parents Ruth and Klaus Fischer, who have supported me in the best possible way during my career to date. My twin brother Martin Fischer always had a word of encouragement, even in times of deepest winter. Special thanks also go to the Christian congregations Iglesia Cristiana Evangélica la Puerta and Iglesia Evangélica FIEIDE de Almería, where I was always able to recharge my batteries on a spiritual level. The bottom line is that a simple prayer always helps to stay motivated and focused by His mere presence.

To all of you a hearty thank you!

Almería, 12th September 2020

*Michael Fischer*

---

<sup>10</sup>CSP SERVICES develops innovative tools and methods to analyze, qualify, test, and improve components and systems for CSP technology.

<sup>11</sup>HELIOPPOINT is a joint project for automated and UAV-based measurement of CSP power plants.





# Preface

*This thesis aims to leverage QFLY as a standard application for heliostat tracking worldwide, thus giving concentrated solar power (CSP) plants the chance to make a significant contribution to tomorrow's energy production. Therefore, it deals with theory behind the orientation calculation of heliostats and the methodology, application and results to validate the process accuracy and scalability of QFLY. The thesis was written during my work as a master's degree candidate from February 2020 to November 2020 at DLR in the QFLY-SF department, and will be submitted to FAPS, a chair at the Friedrich-Alexander-Universität Erlangen-Nürnberg (FAU). The results in this thesis are mainly related to the research facilities the DLR operates in Tabernas, southeastern Spain, and Jülich, Germany.*

The DLR employs about 9,800 people (as of November 2020) and has 40 different institutes and numerous other test and operating facilities at a total of 30 locations in Germany. The main location in Cologne employs about 1500 people. [3]

The desert of Tabernas, located in southern Spain, provides with about 3000 hours of direct sun exposure each year an excellent environment for investigation in solar energy. Because it is the place with the highest solar irradiation in Europe, it has been elected for the deployment of the PSA, in 1981. The research facility is hosted by CIEMAT with its headquarters in Madrid. It is a demonstration platform that was and is used to show the functioning and the feasibility of CSP technologies. It does not generate electrical power but concentrates on development in conventional and new energy resources in general and in solar thermal energy in particular. Components of solar thermal power are tested under real exposure conditions on an area of over 100 hectares. The PSA is the largest research, development and test center for concentrated solar technology in Europe. The DLR, and in particular the DLR Institute of Solar Research, played a major role in the construction of the PSA in the early 80s and has been making use of the facility ever since. A permanent delegation of currently 25 scientists and engineers and several students conduct solar technology testing and development work for the DLR in Almería. CIEMAT, which owns and operates the PSA today, is represented by a scientific staff of approximately 100 employees. [4]

The correct alignment of the heliostats in a solar tower power plant (STPP) – also called solar power tower technology or central receiver system (CRS) – is an important prerequisite for concentrating the direct radiation of the sun on the receiver. Due to the large distances, even slight errors in the heliostat orientation can cause the reflected radiation to miss the receiver. The currently established method for checking the alignment is based on flux density measure-



**Figure 1:** QFLY in application at the PSA: A quadcopter is equipped with a camera to take pictures of the heliostat field (blurred in the background). Afterwards the calculation of the heliostat orientations is done on the computer.

ment (FDM) and uses a white surface attached to the tower to check one to four heliostats simultaneously. Especially after the construction of a new STPP it can take several months to calibrate the orientation control of all heliostats. The airborne measurement system presented here is able to capture the entire heliostat field by means of an unmanned aerial vehicle (UAV) in overflight, see fig. 1. This makes it possible to calibrate the field control even before the tower is completed, thus significantly accelerating the commissioning of the power plant. In addition, the heliostat field can be recalibrated if necessary with little time expenditure.

The measuring procedure is divided into two stages [5]. The first part is the measurement with *photogrammetric* methods. The goal is to achieve a measurement accuracy of the heliostat alignment of less than 10 mrad. In the second step the so-called “QFly DEFLECTOMETRY”<sup>12</sup> (deflectometry) is used for fine measurement with the goal of a measurement accuracy less than 0.3 mrad – theoretical studies on this have been carried out by LEWIN HAJER [7]. In the thesis presented here however, only the photogrammetric approach plays a role, which is divided into the following five steps:

---

<sup>12</sup>The DEFLECTOMETRY is a measuring method intended to determine the shape of the mirror surface as well as the canting (orientation in space) of heliostats. For this purpose it is necessary that the normal vectors are determined at as many points of the heliostat surface as possible. Shape and orientation can then be derived or calculated. The primary goal is therefore the determination of these vectors with an accuracy of 0.3 mrad. [6]

- Step 1:** Circular flight for photogrammetric images
- Step 2:** Image registration and alignment to obtain the interior orientation<sup>13</sup> (IOR) and exterior orientation<sup>14</sup> (EOR) of the camera
- Step 3:** Recognition and assignment of mirror corners in the two dimensional (2D) image
- Step 4:** Photogrammetry to determine the three dimensional (3D) coordinates
- Step 5:** Calculation of heliostat normal vectors from the photogrammetry result

The first validation measurement was carried out at the PSA in 2018. The reference orientation for three heliostats was determined by FDM. The validation goal of a measurement error below 10 mrad was met for these three heliostats.

---

<sup>13</sup>IOR is a set of parameters describing the internal geometry and lens distortion of the camera. [8]

<sup>14</sup>EOR are the camera positions obtained by photogrammetric evaluation. [8]



# Contents

List of Figures . . . . .	v
List of Tables . . . . .	ix
Abbreviations . . . . .	xi
Nomenclature . . . . .	xv
<b>1 Introduction. . . . .</b>	<b>3</b>
1.1 Problem definition and scope of this thesis: Industrializability of QFly . . . . .	5
1.2 Thesis at a glance . . . . .	6
<b>2 State of the Art on heliostat orientation . . . . .</b>	<b>9</b>
2.1 CSP . . . . .	9
2.1.1 CSP types . . . . .	11
2.1.2 Heliostat . . . . .	12
2.1.3 Research centers of DLR . . . . .	16
2.2 Photogrammetry . . . . .	18
2.3 Established methods for orientation measurement of heliostats . . . . .	19
2.3.1 Flux density measurement . . . . .	20
2.3.2 Camera in heliostat center, pointing in NVec direction to observe sun. . . . .	22
2.3.3 Camera in heliostat center, several points are observed besides sun. . . . .	22
2.3.4 Stripe Pattern projected on target, reflection on heliostat mirrors analyzed in pictures . . . . .	23
2.3.5 Cameras on tower, image recognition of heliostat edges (SAPHIR) . . . . .	23
2.3.6 Several cameras mounted elevated around field. . . . .	23
2.3.7 Drawbacks of the mentioned methods . . . . .	24
2.3.8 Deflectometry with tower . . . . .	24
2.3.9 RTK and PTK . . . . .	25
2.4 QFly. . . . .	26
2.4.1 QFly process for STPPs: Two-step process for heliostat characterization. . . . .	26
2.4.2 QFly program flow . . . . .	27
2.4.3 Obtaining the heliostat orientation with the FDM approach . . . . .	31
2.5 Capture reference data as part of a measurement campaign . . . . .	32
<b>3 Evaluation of tests, data provision and analysis. . . . .</b>	<b>35</b>

3.1	Acquired datasets. . . . .	35
3.2	Reference measurement: FDM. . . . .	37
3.3	Agisoft . . . . .	38
3.4	ZA results. . . . .	39
3.5	PG results . . . . .	42
3.6	Tachymeter results: Z-differences between tachymeter measurement 2018 and 2020 .	43
3.7	Interpretation and correlation of final and intermediate results and reference measurements . . . . .	43
<b>4</b>	<b>Zero Assumption Optimization . . . . .</b>	<b>47</b>
4.1	Analyzing the datasets. . . . .	48
4.2	Methodology for the ZA optimization. . . . .	50
4.3	Testing and Results . . . . .	52
<b>5</b>	<b>Improving Performance of PG in AICON . . . . .</b>	<b>55</b>
5.1	Methodology. . . . .	55
5.1.1	Image reduction . . . . .	56
5.1.2	Image quality . . . . .	57
5.1.3	Keeping most distinct detections for each feature . . . . .	58
5.2	Experimental setup and testing . . . . .	64
5.2.1	Defining a base model . . . . .	64
5.2.2	Running .phc-files in AICON. . . . .	65
5.3	Results . . . . .	67
5.4	Discussion. . . . .	77
<b>6</b>	<b>Conclusion and Outlook . . . . .</b>	<b>83</b>
	<b>Glossary . . . . .</b>	<b>89</b>
	<b>Bibliography . . . . .</b>	<b>95</b>
	<b>Appendices . . . . .</b>	<b>103</b>
A	Appendix Original task description (Aufgabenstellung) . . . . .	105
B	Appendix Data . . . . .	107
B.1	Technical infrastructure . . . . .	107
B.2	Agisoft testing data . . . . .	107
C	Appendix Plots . . . . .	109
C.1	Measurement results . . . . .	109

C.2	General overview of data sets . . . . .	109
C.3	Plots for AICON Testing . . . . .	109
C.3.1	Reduction of image and detections quantity through “ <i>Farthest Neighbors</i> ” algorithm . . . . .	109
C.3.2	Residuals of each test AICON result compared to the base model . . . . .	109
C.3.3	Reducing images for AICONRED_stepped . . . . .	109
C.4	Plots for FDM . . . . .	109
C.4.1	Plots showing final results for each series . . . . .	109
C.4.2	Flux Spot movement of different series . . . . .	109
C.4.3	Photos of FDM measurement. . . . .	109
D	Appendix Flowcharts . . . . .	137
E	Appendix Further Images . . . . .	139
F	Appendix Data sheets . . . . .	143
F.1	Tachymeter: Trimble S8 . . . . .	143
F.2	UAV: Microdrones mdMapper1000+ . . . . .	146
G	Appendix Data stored on flash disk . . . . .	151
H	Appendix Curriculum Vitae . . . . .	153



# List of Figures

1	UAV with camera flying. . . . .	t
2.1	Solar resource map. . . . .	10
2.2	Concentrator types with different kinds of tracking. . . . .	11
2.3	Scheme of a Central Tower CSP Plant. . . . .	12
2.4	Azimuth and elevation. . . . .	13
2.5	Heliostat Field Hydrosol. . . . .	15
2.6	Measurement set-up used for heliostat measurements in the field. . . . .	16
2.7	CESA 1 Heliostat - Corners, gaps and crosses nomenclature. . . . .	17
2.8	STPPs that are currently used as test facilities of DLR. . . . .	17
2.10	Currently available calibration system classes. . . . .	20
2.13	Reflex-based process. . . . .	27
2.14	Flowchart of QFLY process, with usual calculation durations.. . . .	28
2.15	Twist and distortion of the ideal heliostat model. . . . .	29
2.16	Feature detection explained. . . . .	30
3.1	Measured 3D model and concentrator normal vectors in the first experimental setup .	37
3.2	Off-target in FDM flux spot tracking. . . . .	38
3.3	Filtering for outliers in FDM. . . . .	39
3.4	EOR-calculation results taken from the “AGISOFT METASHAPE” <sup>15</sup> (AGISOFT) report for CESA-1-2020. . . . .	40
4.1	QFly process: FD and PG take up 70% of the processing time. . . . .	48
4.3	CESA-1-2020, heliostat 108, unfiltered ZA results. . . . .	50
4.4	Parameters for quality analysis of ZA-result. . . . .	51
5.2	Overview over the different quality parameters. . . . .	59
5.5	Results after applying the “ <i>Farthest Neighbors</i> ”-algorithm.. . . .	62
5.6	Delete feautres and all their detections. . . . .	63
5.7	Features eventually staying in dataset. . . . .	63
5.9	AICON: dataset reduced. . . . .	67
5.10	Covered are of feature detections on image. . . . .	68

---

<sup>15</sup>AGISOFT METASHAPE is a stand-alone software product that performs photogrammetric processing of digital images and generates 3D spatial data to be used in GIS applications, cultural heritage documentation, and visual effects production as well as for indirect measurements of objects of various scales, developed by AGISOFT LLC.

---

5.11	Distribution of feature detections on image. . . . .	69
5.13	State before reduction process sets in. . . . .	71
5.14	Feature equivalence compared for two images. . . . .	72
5.15	Reduction of images. . . . .	73
5.16	Viewing directions depending on feature location. . . . .	74
5.17	Comparing input data with AICON results. . . . .	75
5.19	Results from AICON - residuals plottet compared to base model. . . . .	77
5.20	Barplot showing different data-sets as given to AICON. . . . .	78
5.22	AICON results. . . . .	80
C.1	Comparison ZA, FDM and PG – ZA-measurement close to PG and FDM. . . . .	.111
C.2	Comparison ZA, FDM and PG – ZA-measurement hight deviation to PG and FDM. . . . .	.112
C.5	Feature detection reduction: Maximum 15 detections per feature. . . . .	.115
C.6	Feature detection reduction: Maximum 20 detections per feature. . . . .	.116
C.7	Feature detection reduction: Maximum 40 detections per feature. . . . .	.117
C.8	comparison of EOR and detections in .phc file creation, 441 images remaining. . . . .	.118
C.9	comparison of EOR and detections in .phc file creation, 570 images remaining. . . . .	.118
C.10	comparison of EOR and detections in .phc file creation, 524 images remaining. . . . .	.119
D.1	Program structure QFLY. . . . .	.138
E.1	Measurement 2020 - impressions. . . . .	.139
E.2	Ivanpah Solar Electric Generating System . . . . .	.140
E.3	Selecting the outer corners of the target . . . . .	.141
E.4	Difference in Tachy measurements heights. . . . .	.142
E.5	Working mechanism of the image recognition. . . . .	.142
G.1	Data on flash disk. . . . .	.152





# List of Tables

- 3.1 Characteristics values of datasets. . . . . 36
- 3.2 Cross comparison PG, FDM and ZA. . . . . 44
  
- 5.1 Test specifications of individual data-sets for AICON testing. . . . . 66
  
- B.1 Computers used for calculations. . . . . .107



# Abbreviations

**Agisoft** “AGISOFT METASHAPE”<sup>16</sup>.

**Aicon** “AICON 3D STUDIO”<sup>17</sup>.

**CSP Services** CSP SERVICES GMBH<sup>18</sup>.

**HelioPoint** HELIOPOINT<sup>19</sup>.

**Matlab** “MATLAB”<sup>20</sup>.

**QDec** deflectometric measurement system, initiated by DLR and further developed by CSP Services, called “QDEC”.

**QFly** “QFLY”, a measuring system for quality control of utility scale solar fields<sup>21</sup>.

**SAPHIR** SAPHIR (a project of DLR)<sup>22</sup>.

**2D** two dimensional.

**3D** three dimensional.

**BMWi** German Federal Ministry for Economic Affairs and Energy.

**CESA-1** CESA-1<sup>23</sup>.

---

<sup>16</sup>AGISOFT METASHAPE is a stand-alone software product that performs photogrammetric processing of digital images and generates 3D spatial data to be used in GIS applications, cultural heritage documentation, and visual effects production as well as for indirect measurements of objects of various scales, developed by AGISOFT LLC.

<sup>17</sup>AICON 3D STUDIO is a photogrammetry software developed by AICON 3D SYSTEMS GMBH in 2002. The company got meanwhile acquired by HEXAGON MANUFACTURING INTELLIGENCE.

<sup>18</sup>CSP SERVICES develops innovative tools and methods to analyze, qualify, test, and improve components and systems for CSP technology.

<sup>19</sup>HELIOPOINT is a joint project for automated and UAV-based measurement of CSP power plants.

<sup>20</sup>MATLAB is a proprietary multi-paradigm programming language and numerical computing environment developed by MATHWORKS.

<sup>21</sup>QFLY is a trademark name of a process developed by *DLR* for the supply of airborne imaging and related software to obtain information on the geometric, optical and thermal properties of a measured CSP or PV plant.

<sup>22</sup>The goal of SAPHIR was to develop optical measurement systems to support the heliostat prototype development, the facet and heliostat assembly and the final inspection of heliostat fields for STPPs, Funding code 16UM0068.

<sup>23</sup>CESA-1 is a STPP featured on the PSA. Technical specifications: 300 heliostats with 40 m<sup>2</sup> each, 7 MWth, tower height 83 m. [1]

**CIEMAT** CIEMAT, the Spanish Center for Energy, Environmental and Technological Research (Centro de Investigaciones Energéticas, Medioambientales y Tecnológicas)<sup>24</sup>.

**CORS** Cross-origin resource sharing.

**CRS** central receiver system.

**CSP** concentrated solar power.

**deflectometry** “QFly DEFLECTOMETRY”<sup>25</sup>.

**DLR** German Aerospace Center (Deutsches Zentrum für Luft- und Raumfahrt e.V.).

**DNI** direct normal irradiance.

**EOR** exterior orientation<sup>26</sup>.

**FAPS** Chair of Manufacturing Automation and Production Systematics (Lehrstuhl für Fertigungsautomatisierung und Produktionssystematik).

**FAU** Friedrich-Alexander-Universität Erlangen-Nürnberg.

**FD** “QFly FEATURE DETECTION”<sup>27</sup>.

**FDM** flux density measurement.

**GHG** greenhouse gas emissions.

**GNSS** Global Navigation Satellite System<sup>28</sup>.

**GPS** Global Positioning System.

**IOR** interior orientation<sup>29</sup>.

**Jülich** STPP in Jülich, Germany<sup>30</sup>.

---

<sup>24</sup>CIEMAT is under the direct political supervision of the Spanish Ministry of Research and Development.

<sup>25</sup>The DEFLECTOMETRY is a measuring method intended to determine the shape of the mirror surface as well as the canting (orientation in space) of heliostats. For this purpose it is necessary that the normal vectors are determined at as many points of the heliostat surface as possible. Shape and orientation can then be derived or calculated. The primary goal is therefore the determination of these vectors with an accuracy of 0.3 mrad. [6]

<sup>26</sup>EOR are the camera positions obtained by photogrammetric evaluation. [8]

<sup>27</sup>The FEATURE DETECTION is an edge-based image recognition process that detects as many features per heliostat as possible, be searching for the edges of facets and their crossing points.

<sup>28</sup>A Global Navigation Satellite System (GNSS) is a constellation of satellites providing signals from space that transmit positioning and timing data to the GNSS receiver (PPK module). Each satellite constantly sends its position and the time to the receiver. The receiver then uses this data, correlated from multiple satellites, to precisely determine its location.

<sup>29</sup>IOR is a set of parameters describing the internal geometry and lens distortion of the camera. [8]

<sup>30</sup>STPP-JÜLICH is a research facility covering the world’s first commercial STPP erected in the city of Juelich, Germany, starting operation in 2008. [2]

**mrad** milliradians.

**Nadir** Nadir<sup>31</sup>.

**NREL** National Renewable Energy Laboratory.

**PG** QFly photogrammetry in AICON.

**PPK** Post-Processed Kinematic.

**PSA** Plataforma Solar de Almería<sup>33</sup>.

**PTPP** Parabolic Trough Power Plants.

**PV** photovoltaic.

**RTK** Real Time Kinematic.

**SDGs** Sustainable Development Goals.

**STPP** solar tower power plant.

**UAV** unmanned aerial vehicle.

**VRS** Virtual Reference Station.

**ZA** “QFly ZERO ASSUMPTION”<sup>34</sup>.

---

<sup>31</sup>The nadir is the direction pointing directly below a particular location. A nadir image is a satellite image or aerial photo of the Earth taken vertically [9]. For CESA-1<sup>32</sup> (CESA-1)-2020, both two different image datasets (nadiral and oblique (45°)) have been generated. The nadir flight acquired images from an height of 80m / 120m.

<sup>33</sup>The PSA is a research facility on CSP technology, located in Tabernas, southeastern Spain, owned by CIEMAT.

<sup>34</sup>The so-called ZERO ASSUMPTION is a preliminary assumption of orientation of heliostats as part of the QFly code structure.



# Nomenclature

## Calculation Operators

Abbr.	Description	Definition
$d$	Distance of two points in space	$d(P_1, P_2) = \sqrt{(x_2 - x_1)^2 + (y_2 - y_1)^2 + (z_2 - z_1)^2}$
$\eta$	median	$\begin{cases} \frac{x_{\frac{n+1}{2}} & n \text{ odd} \\ \frac{1}{2}(x_{\frac{n}{2}} + x_{\frac{n}{2}+1}) & n \text{ even} \end{cases}$
$\mu$	mean	$\mu = \frac{1}{n} \sum_{i=1}^n a_i = \frac{a_1 + a_2 + \dots + a_n}{n}$
$\mathbf{R}$	rotation $\mathbf{R}$ about any arbitrary axis can be written in terms of successive rotations about the Z, Y, and finally X axes using matrix multiplication	$\mathbf{R} = \mathbf{R}_z \mathbf{R}_y \mathbf{R}_x$
$\mathbf{R}_x(\gamma)$	<i>roll</i> : counterclockwise rotation of $\gamma$ about the $x$ -axis	$\begin{pmatrix} 1 & 0 & 0 \\ 0 & \cos \gamma & -\sin \gamma \\ 0 & \sin \gamma & \cos \gamma \end{pmatrix}$
$\mathbf{R}_y(\beta)$	<i>pitch</i> : counterclockwise rotation of $\beta$ about the $y$ -axis	$\begin{pmatrix} \cos \beta & 0 & \sin \beta \\ 0 & 1 & 0 \\ -\sin \beta & 0 & \cos \beta \end{pmatrix}$

$\mathbf{R}_z(\alpha)$	<i>yaw</i> : counterclockwise rotation of $\alpha$ about the $z$ -axis	$\begin{pmatrix} \cos \alpha & -\sin \alpha & 0 \\ \sin \alpha & \cos \alpha & 0 \\ 0 & 0 & 1 \end{pmatrix}$
$RMS$	Root mean square	$\sqrt{\frac{1}{n} \sum_i x_i^2}$
$RMSE$	Root mean square error / deviation	$\sqrt{\frac{1}{n} \sum_{i=1}^n \left( \frac{d_i - f_i}{\sigma_i} \right)^2}$
$\sigma$	standard deviation	$\sqrt{\frac{\sum (x_i - \mu)^2}{N}}$
$\theta$	angle between two vectors	$\cos \theta = \frac{\vec{u} \cdot \vec{v}}{ \vec{u}   \vec{v} }$
$S^2$	variance	$S^2 = \frac{\sum (x_i - \Psi)^2}{n-1}$

### Greek Symbols

Symbol	Description	Dimensions	Units
$\alpha, \beta$	Angle of view	–	°
$\theta$	Angle between two vectors	–	°

### Further Abbreviations

Symbol	Description	Dimensions	Units
<i>Azim</i>	Azimuth	–	°, rad
<i>Elev</i>	Elevation	–	°, rad
<i>NVec</i>	Normal vector	–	°, rad





# 1 Introduction

*“Energy is central to nearly every major challenge and opportunity the world faces today, including poverty eradication, gender equality, adaptation to climate change, food security, health, education, sustainable cities, jobs and transport” — 193 member states of the United Nations agreed on this at the end of 2015 when they signed the Sustainable Development Goals (SDGs), where it says that one goal is to “ensure access to affordable, reliable, sustainable and modern energy for all by 2030”. [10]*

*The growing world population and increasing industrialization mean that the global demand for energy is constantly increasing. This causes the concentration of greenhouse gases in the atmosphere to rise, and, at the same time, a warming of the earth’s surface temperature [11]. Energy production and use reflect about two thirds of the worldwide greenhouse gas emissions (GHG), while modern renewable energy sources (wind/solar/biomass/geothermal/ocean) currently supply 11.0% of the total global final energy consumption. On the contrary, 79.9% is still covered by fossil fuels such as coal and oil [12]. The harmful influences on environment and climate, as well as the knowledge of their finite availability, which are associated with the production of energy from these fuels, have the consequence that research is increasingly being done on so-called renewable energies, which are far less harmful to climate and environment and characterized by sheer abundance. [13, 14, 15, 16, 17]*

*“I’m passionate of renewable energy. But the real renewable energy. The stuff that falls from the sky. Solar Power.” — Danny Kennedy, venture capitalist for renewable energy start-ups from California.*

*A particularly promising means of generating renewable energy and reducing greenhouse gas emissions is the concentration of solar energy due to the large occurrence of this resource and the good potential for coupling it with storage. Investment costs for photovoltaic (PV) and concentrated solar power (CSP) are decreasing year after year, and green electricity generated today is in many places cheaper than coal-fired or nuclear power. Especially new power plants are correlated with large storage facilities to achieve record prices. [18, 19, 20]*

In a solar tower power plant (STPP), energy is generated using concentrated sunlight. The bundling of the sunlight is achieved by parabolic-shaped sun mirrors, so-called heliostats, which are positioned on the ground in front or around the tower. Incident sunlight is reflected by the heliostats in the direction of a receiver on the tower to heat a transfer medium which drives a turbine to generate electricity.

For the most efficient operation of the STPP it is necessary that the heliostats are aligned at all times so that the sunlight is reflected directly onto the receiver. Exact knowledge about the orientation of the heliostats is therefore especially important.

After the construction phase, the initial setup of the heliostat field controls and the elimination of offsets in the alignment of the light beam can take several months before the system can operate at full capacity. A rapid ramp-up to nominal production levels is an important factor in achieving low electricity costs.

The classic approach to heliostat calibration is to focus a limited number of heliostats<sup>1</sup> on a white target for different angles of the sun one after the other to measure the deviation between the target and the nominal point. Since this procedure depends on the position of the sun and the availability of a target without a focal point, this sequential procedure takes too long for industrial-scale systems.

For this reason, “QFLY”, a measuring system for quality control of utility scale solar fields<sup>3</sup> (QFLY) was developed. By means of an unmanned aerial vehicle (UAV) and a camera attached to it the heliostat field is overflown – following a pre-defined flight curve, mostly consisting of concentric circles and Nadir<sup>4</sup> (Nadir) flights – and captured in photographs. Using image recognition and photogrammetric methods the orientation of the heliostats can be determined. For such a measurement the heliostat field has to be taken out of operation for only a few hours, as the heliostat’s orientation is not supposed to change during the measurement.

The segments of the solar field can be calibrated as soon as their control system is put into operation. This can result in power plants reaching their maximum output months earlier than it would be the case with conventional calibration methods. Several research groups and the industry have addressed the issue of heliostat calibration. In 2017, DLR started the HELIOPoint<sup>5</sup> (HELIOPoint) project, which follows a two-step calibration method, with a photogrammetric approach as first step and a deflectometric approach as second step. [5]

However, especially for large data sets, the calculations involved require a considerable amount of time of several weeks (depending on the quantity of images taken and further aspects, as shown later in section 3). Therefore, from the point of view of process reliability, possibilities to improve the performance of QFLY were considered and analyzed in this thesis.

---

<sup>1</sup>a maximum number of four heliostats can be analyzed simultaneously in the case of CESA-1<sup>2</sup> (CESA-1)

<sup>3</sup>QFLY is a trademark name of a process developed by *DLR* for the supply of airborne imaging and related software to obtain information on the geometric, optical and thermal properties of a measured CSP or PV plant.

<sup>4</sup>The nadir is the direction pointing directly below a particular location. A nadir image is a satellite image or aerial photo of the Earth taken vertically [9]. For CESA-1-2020, both two different image datasets (nadir and oblique (45°)) have been generated. The nadir flight acquired images from an height of 80m / 120m.

<sup>5</sup>HELIOPoint is a joint project for automated and UAV-based measurement of CSP power plants.

## 1.1 Problem definition and scope of this thesis:

### Industrializability of QFly

The goal of this thesis is to evaluate the scalability and accuracy of sub-steps of the QFLY process. The efficiency, robustness and duration of the evaluation are relevant for the scalability. Scalability is also related to the number of images used for the final photogrammetry, since the effort for single sub-steps of the procedure increases exponentially with the number of images. A possible approach is the investigation of the scalability with reference to the selection of the used images under photogrammetric aspects. For the evaluation of the accuracy of the procedure the new approaches have to be checked against reference methods. In the course of this, suitable parameters are defined to systematically optimize the QFLY results and the scalability. The work includes the following main topics:

- Step 1:** Literature research on solar thermal energy and measurement of heliostat alignment
- Step 2:** Analysis of the data-sets describing the pre-alignment of the heliostat
- Step 3:** Optimization of the evaluation of the QFly measurements by suitable adjustment of the parameters of the image data processing
- Step 4:** Reduction of the required number of images while maintaining good results
- Step 5:** Comparison of the results of partial steps of the QFly system with reference data
- Step 6:** Evaluation of the scalability and accuracy of the QFly measurement

Of the over 200 individual “QFly ZERO ASSUMPTION”<sup>6</sup> (ZA)-measurements per heliostat<sup>7</sup>, there are about 8%<sup>8</sup> of the measurements that lay in  $\pm 1$ rad deviation range to the reference measurement. Therefore, in this thesis a process shall be developed, which allows to use the ZA orientations in general, in order to give a reliable statement about the actual heliostat orientation. Thus, the time needed for QFly can be reduced by at least 70%, as fig. 4.1 shows.

The overall goal of this thesis is to verify the individual process steps of QFLY. The drawbacks for the orientations calculated from “AICON 3D STUDIO”<sup>9</sup> (AICON) are obvious: Not for all heliostats an alignment can be calculated. In the CESA-1-2018 measurement it was only 142 of 300 heliostats, including 3 out of 4 flux density measurement (FDM) heliostats; in CESA-1-2020 only 146 out of 300 heliostats, including 28 of the 31 FDM heliostats. For CESA-1-2020 it’s remarkable that not all FDM heliostats are calculated, as the south-eastern part of the field was mainly captured on photographs, since the FDM heliostats are located in this area. Several heliostats are without PG-result, even though features have been detected 50-100 times on average. On the contrary – and therefore talking about the benefits of ZA – all heliostats are

---

<sup>6</sup>The so-called ZERO ASSUMPTION is a preliminary assumption of orientation of heliostats as part of the QFly code structure.

<sup>7</sup>valid for CESA-1-2020 measurement

<sup>8</sup>deviation in azimuth angle

<sup>9</sup>AICON 3D STUDIO is a photogrammetry software developed by AICON 3D SYSTEMS GMBH in 2002. The company got meanwhile acquired by HEXAGON MANUFACTURING INTELLIGENCE.

recognized in the ZA. Even for CESA-1-2020, where the Northern part of the field was mostly neglected on photographs, 283 of 300 heliostats were recognized.

As for the accuracy however, without any applied optimization for ZA, the deviations between ZA and FDM are significantly higher compared to QFly photogrammetry in AICON (PG) and FDM.

## 1.2 Thesis at a glance

The thesis is divided into four parts:

First, the **state of the art** is described, cf. section 2. The measurement method QFly and the functionality of STPPs play a decisive role. In addition, an overview of established as well as novel measurement principles for orientation determination is given, and the basic principles of the FDM, which is applied in this thesis, is discussed. Furthermore, it is explained how the QFly and reference measurement data acquisition is structured. Moreover, the essential parts of the QFly program, which is completely written in “MATLAB”<sup>10</sup> (MATLAB), are explained and corresponding flow charts are shown. Thus the overall context of the novel program sections developed as part of this thesis becomes clearly visible. Additionally, the general process of reference data acquisition within the scope of a measurement campaign is explained.

The second part of the thesis deals with the **evaluation, comparison and discussion of the measurement results**, cf. section 3. The measurements include the QFly photogrammetry results, the intermediate results of ZA and “QFly FEATURE DETECTION”<sup>11</sup> (FD), tachymeter measurements, and the reference measurement FDM. Special attention is given to the FDM, since considerable changes were made to the existing code in the course of this thesis. In addition, methodical investigations are included, such as overwriting the original EOR data with the PG-EOR for ZA, or recalculating the ZA using the detected features from the FD.

The third chapter of this thesis deals with the **Optimization of ZA results**, cf. section 4. Correlations are made between different parameters like the distance of the UAV to the heliostat to determine the accuracy of the measured value. The optimizations are subject to a test execution, mainly based on the available measurement CESA-1-2020.

In the last chapter the **performance of QFly** is analyzed, cf. section 5. The decisive time factor is the photogrammetric calculation in AICON, which can take several weeks to complete, depending on the number of prominent points and images. Under photogrammetric aspects different input data sets are created. It is examined to what extent the assumptions made for the image information reduction can actually reduce the computing time as well as improve the

---

<sup>10</sup>MATLAB is a proprietary multi-paradigm programming language and numerical computing environment developed by MATHWORKS.

<sup>11</sup>The FEATURE DETECTION is an edge-based image recognition process that detects as many features per heliostat as possible, by searching for the edges of facets and their crossing points.

accuracy of the measurement results in AICON. The experiments are carried out using specifically reduced data sets, based on the CESA-1-2020 measurement, in order to save processing time.

In the end, the results are **summarized and an outlook is given**, cf. section 6.



## 2 State of the art on solar tower power plants and heliostat orientation measurement and accuracy

*CSP continues to spread to new markets such as France, Israel and Kuwait. In 2019, 600 MW of capacity have gone online, adding up another 11% to the 6.2 GW installed worldwide. For the first time, as much tower capacity as parabolic trough capacity was completed during 2019. [12]. R&D activities focus on further improving CSP economics through increasing operating efficiency. Implementing rapid heliostat calibration systems such as QFLY help monitoring the field, as misalignment of mirrors can severely dent output [21].*

*Apart from soiling (contamination), reflectivity (degradation) or availability (break), incorrectly adjusted mirrors (geometry deviation) reduce the energy output [13]. To explain the whole topic around the accuracy analysis of heliostat mirror orientation using the QFLY process, some basics are necessary. These are explained in this chapter.*

*A critical component of a central receiver system (CRS) is the heliostat field which focuses the incident solar irradiation onto the central receiver. Each heliostat is required to track the movement of the sun with high accuracy throughout the day in order to maintain focus of the reflected beam at the desired location [22]. Improper tracking causes less solar irradiation to be reflected onto the receiver, leading to losses in power output and profit. [23]*

In section 2.1 the state of the art of an STPP is described. It is explained explicitly how such a plant works, what a heliostat is and how the orientation of the heliostat is changed to ensure maximum energy yield. In addition, the research facilities of the German Aerospace Center (Deutsches Zentrum für Luft- und Raumfahrt e.V.) (DLR) are highlighted. Subsequently, basics in the field of **photogrammetry** are explained. The state of the art of **methods for orientation determination** both on industrial and research level is analyzed in section 2.3 before the **QFly process** developed by DLR is explained in section 2.4. Finally, the common process of **measuring campaigns** for the orientation determination of heliostats at DLR is described (cf. section 2.5), emphasizing the measuring campaigns performed in the context of this thesis.

### 2.1 CSP

The sun provides renewable energy in incomparable abundance, and its energy can be obtained in various ways. The first distinction for solar energy generation is made between PV<sup>1</sup> and CSP.

---

<sup>1</sup>Technology in which solar cells convert energy in a photon directly into electrical energy via the photoelectric effect. This technology can be used on any scale. Since the price of standard crystalline photovoltaic modules has

Compared to PV, CSP is characterized by the fact that the solar energy is storable in the form of heat, thus the electricity, which is generated via steam turbines, becomes dispatchable also during nighttime. [25]

CSP can only process direct normal irradiance (DNI) due to its light concentration via reflectors. Diffuse irradiance remains unused. For this reason, CSP sites require a predominantly clear sky without clouds and a low concentration of aerosols [26]. Thus, CSP technology is most effectively used at locations in the so-called “Earth’s sunbelt”, which mainly captures Mediterranean regions, Northern Africa, South Africa, China and India, Latin America, and Australia [27]. The recent global map of satellite-based annual DNI is shown in fig. 2.1.

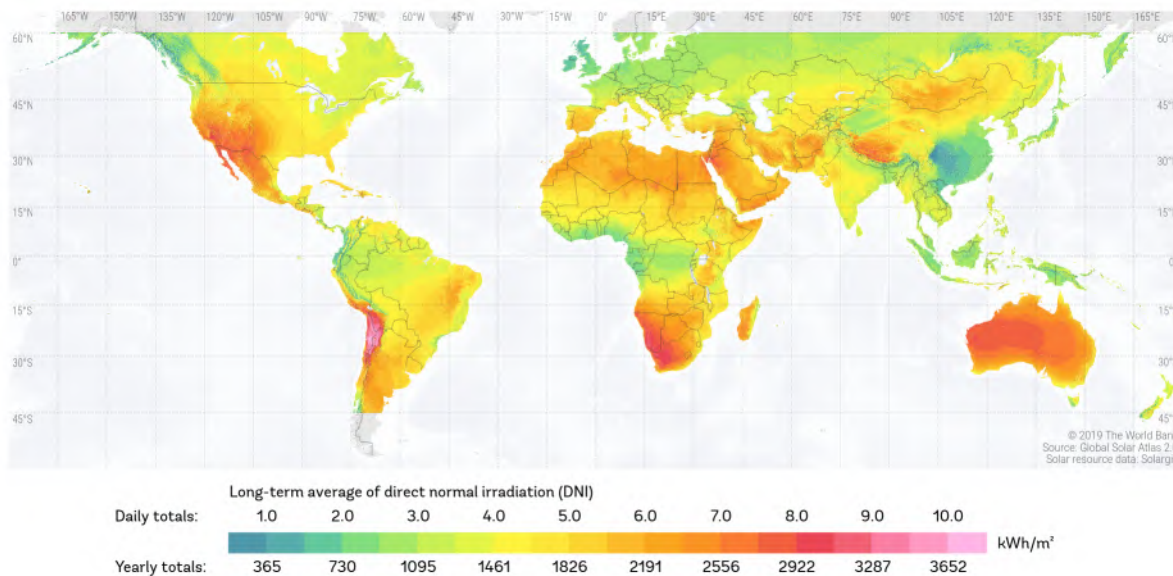


**Figure 2.1:** Global Map of DNI, measured at the Earth’s surface at a given location with a surface element perpendicular to the Sun [28]. It excludes diffuse solar radiation (radiation that is scattered or reflected by atmospheric components). Image source: [29]

The price for electricity from CSP will potentially fall into the range of USD 0.06 to USD 0.10/kWh. Due to its ability to store heat and the improved cloud and weather forecasting, the share of CSP will increase in areas with good direct solar resources [30]. CSP is forecast to grow by 3.4 GW during 2019-24 [31]. Many countries set themselves big goals and commission huge CSPs: Saudi Arabia targets to install 2.7GW CSP by 2030 [32], while Spain’s government announced a target of 5 GW capacity by 2030 [33].

Large-scale STPPs usually feature tens of thousands of heliostats with maximum distances between heliostat and tower ranging between 1 and 1.77 km. Heliostat mirror areas range from small (1-15 m<sup>2</sup>), to medium sized (30-50 m<sup>2</sup>) – as the one on CESA-1 – and large (100-200 m<sup>2</sup>). [34]

One of the largest plants in terms of size and installed capacity currently operating worldwide fallen dramatically in recent years, the PV approach is currently the most important competitor of STPP. [24]

are Ivanpah (377 MWe, USA, 2014), cf. fig. E.2, Noor Ouarzazate III (150 MWe, Morocco, 2018) and Huanghe Qinghai Delingha (135 MWe, China, 2017), among others. [35]

### 2.1.1 CSP types

Four CSP systems are currently seen on the market, cf. fig. 2.2. They all have in common, that parallel sunlight is reflected by a mirror in such a way that it is concentrated either on a line in parabolic trough systems or on a single point in dish or STPP system. A liquid medium with a high heat capacity is used in this receiver, usually special thermal oils or molten salt. Steam is produced in a heat exchanger, which drives a steam turbine connected to an electrical generator. [36]

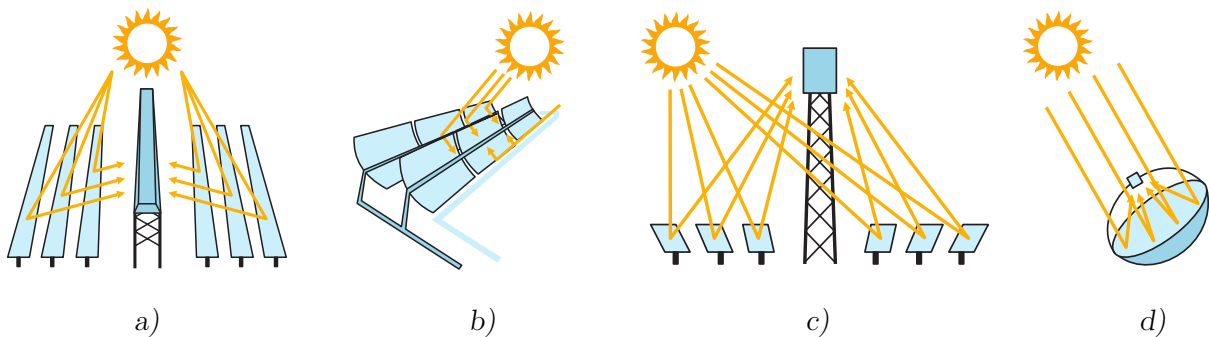


**Figure 2.2:** Concentrator types with uniaxial tracking in (a) linear Fresnel and (b) parabolic trough and biaxial tracking in (c) central receiver and (d) parabolic dish. Parabolic trough is by far most popular in terms of installed capacity worldwide (82% of CSP), followed by STPPs with 13%, linear fresnel with 4% and parabolic dish <1% [37]. (adapted from [38])

#### 2.1.1.1 Parabolic trough

In parabolic trough systems, a curved mirror forms a parabola that runs along a horizontal receiver tube. Solar tracking is only required in one dimension (horizontal axis). A long receiver pipe means more heat loss and the system temperature is lower than with a STPP. The thermal energy is converted into electricity in the same way as in a solar tower, typically with steam turbines. A more recent variant of parabolic trough technology is the *linear Fresnel<sup>2</sup> technology*, in which the curved mirror is divided into flat mirror element strips, which can reduce investment costs. The facets concentrate the radiation in a focal line in which the tubular receiver is located. [35]

<sup>2</sup>named after Augustin-Jean Fresnel, a French civil engineer and physicist

### 2.1.1.2 Solar Dish

Solar Dish is the concept with the highest theoretical efficiency. A paraboloid-shaped mirror is tracked in 2 directions and a receiver is located in the focal point. Among the technical solutions demonstrated are mini-sterling motors, which are located at the focal point of the mirror and convert the thermal energy into electrical energy. The Solar Dish technology is more maintenance and cost intensive than the other solutions, and therefore less common. [39]

### 2.1.1.3 Solar tower power plants

In STPPs, many individual mirrors are bundling solar radiation to a point at the top of the tower, called *receiver*, cf. fig. 2.3. There the radiation heats a circulating heat storage medium to operating temperatures ranging from 560°C in case of molten salt circuits, 680°C for air systems, and up to 900°C in case of particle systems. The heat generates steam which drives a turbine that transfers its rotational energy to a generator to produce electricity [40]. Further utilization concepts are, for example, to provide process heat for the manufacturing industry, such as steam for an aluminum production process [41], or to produce hydrogen for mobility applications. [42]

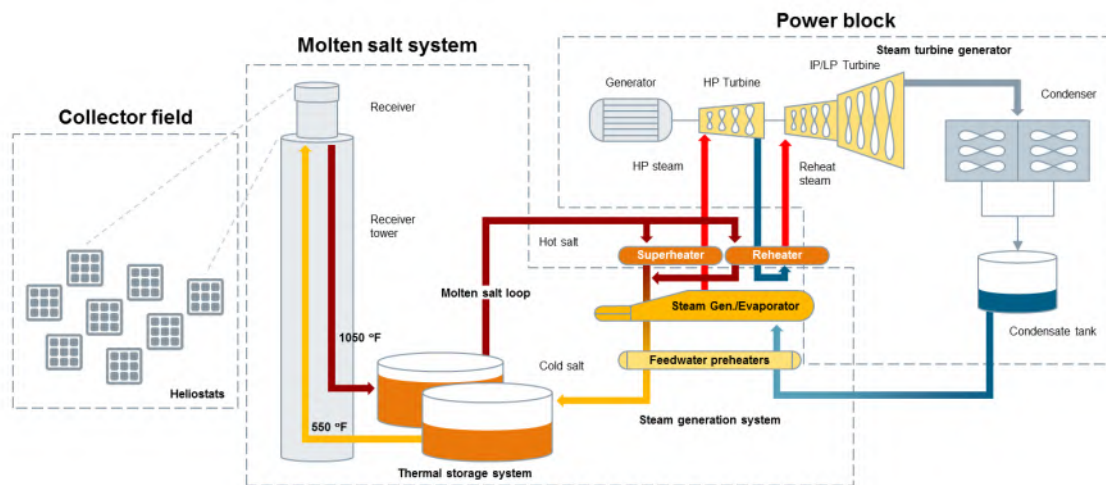


Figure 2.3: Scheme of a Central Tower CSP Plant. [43]

## 2.1.2 Heliostat

Derived from manufacturing and maintenance reasons, a heliostat usually consists of several mirrors with a parabolic shape. Therefore, the reflecting rays of parallel incident sunlight intersect on a small receiver surface. During operation, it turns so as to keep reflecting sunlight toward a predetermined target, compensating for the sun's apparent motions in the sky. To do this, the reflective surface of the mirror is kept perpendicular to the bisector of the angle between the directions of the sun and the target as seen from the mirror. [44]

### 2.1.2.1 Azimuth and elevation

The change in orientation of heliostats is done by two computer-controlled drives, that are adjusting *azimuth* and *elevation* of the heliostat, cf. fig. 2.4 [34]. A correctly aligned heliostat is characterized by the fact that it always reflects sunlight to the same point on the solar tower regardless of the position of the sun in the sky. Since the position of the sun is constantly changing not only on a daily, but also a yearly basis, its orientation must always be adjusted. Therefore, the heliostat mirrors are mounted on two motorized axes (azimuth and elevation axis), cf. fig. 2.4. By specifying the azimuth and elevation angle the mirror surface can be oriented accordingly. The azimuth angle is the angular displacement from North of the projection of beam radiation on the horizontal plane; displacements east of North are positive and west of north are negative, cf. fig. 2.4 a). [45]



a) Solar vector and geometry as viewed from observer on earth surface (adapted from [46]). b) Heliostat back with heliostat axes: Azimuth (blue), elevation (red). [7]

**Figure 2.4:** For an azimuth–elevation tracking heliostat, the primary axis is the azimuth axis which is fixed to the ground plane pointing towards the zenith. The secondary axis is the elevation axis which is rotating together with the mirror surface around the azimuth axis. [47]

The deviation of actual and desired heliostat orientation – also called tracking error – is usually extremely small, and can be illustrated by the following example: A heliostat at a distance of 1 km north from the tower had a tracking error of 1 mrad. This results in an offset of around 2m between the heliostat’s desired aim point and the actual position of the solar focus on the target. The tolerance of the misalignment of a heliostat is therefore predominantly based on the dimensions of a STPP. [34]

### 2.1.2.2 Quality parameters of heliostats

The heliostat’s performance is affected by errors in both the mirror surface and tracking [48]. Errors in tracking result in the mirror surface of the heliostat not being ideally aligned, which causes the incident sunlight to be reflected towards an incorrect position. The mirror surface can be affected by several errors: Waviness, non-standard curvature, tilt, and roughness affect

the quality of the reflecting light beam. In order to compensate for the above mentioned error influences, they must be measured first.

The methods used to qualify the heliostat tracking are explained within section 2.3, while the deflectometric measurement system, initiated by DLR and further developed by CSP Services, called “QDEC” (QDEC) is explained hereafter.

### 2.1.2.3 Facets and Shape

According to [49], large heliostats have a surface area of up to 180m<sup>2</sup>. However, the mirror size is limited due to manufacturing and assembly, which is why larger mirrors are composed of individual mirror facets. These must be aligned in such a way that reflected light beams are bundled at the receiver. This alignment process is called “*canting*”. The facets are adjusted by means of threaded screws that are attached to them at various points through an adhesive bond. Nevertheless, only the fine adjustment can be carried out with this process, since the mirror only reacts in a break-resistant manner up to a certain degree of deformation. It is therefore common practice to manufacture facets with a parabolic basic shape in the first place. Depending on the focal length<sup>3</sup> the facet must be curved accordingly to achieve high concentrations. This calculation needs to be done for every facet in the field, however, to minimize costs, if the heliostats are located concentric around the central tower, only one calculation needs to be done for every row. Especially for larger systems the heliostats are even grouped according to the distance to the receiver. The mirror facets of heliostats of one group are manufactured with the same focal lengths. On the Hydrosol pilot plant, the heliostat field is divided into twelve rows (59m, 67m, 77m, 89m 97m 104m 113m 122m, 133m, 143m, 156m and 169m) with five different focal lengths (67m, 95m, 115m, 136m and 162m), cf. fig. 2.5. Rows 1 to 3 were cantered with a focal length of 67m, rows 4 to 6 with a focal length of 95m. [14, 36, 50]

Studies have shown, that even though canting has been done individually for every facet of the heliostat, a change of the heliostat’s orientation (azimuth and/or elevation) can lead again to a misalignment of focal points of the individual features. The reasons for facets no longer converging uniformly in one point, for example are wear in the mechanical drives, gravitational influences on the support structure or the control of the motors. [36]

The shape of the mirror facets can be measured with *QDEC*, cf. fig. 2.6. *QDEC* is performed through the night, where a stripe pattern is projected onto the target. The stripe patterns reflecting on the mirror facets, and are recorded with a digital camera. Digital image processing is used to match the reflection with its origin on the projection surface. The positions of camera, screen and reflecting surface must be known in order to determine the local normal vectors of the reflecting surface based on the vector geometry. [51]

In the case of CESA-1-2020, the last fine *QDEC* measurement was conducted in 2012<sup>4</sup>. A high

---

<sup>3</sup>distance of facet to receiver

<sup>4</sup>Wilko Jessen, personal communication

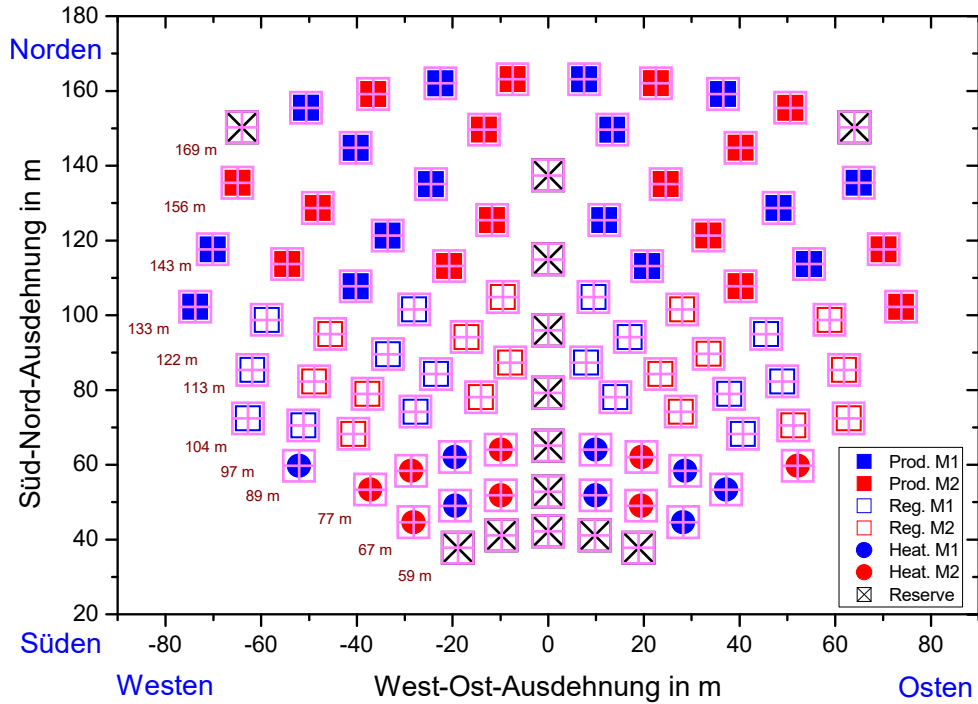


**Figure 2.5:** Heliostat Field Hydrosol, pilot plant in Southern Spain. The different focal length groups are shown. [14]

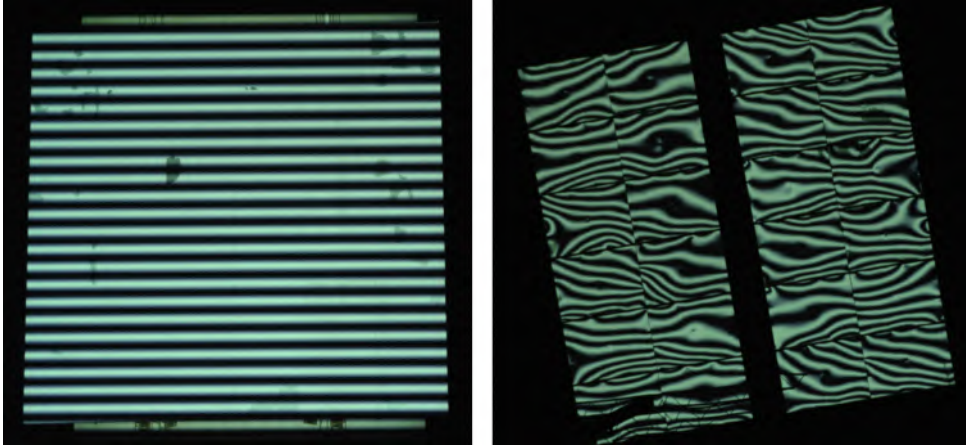
degree of deformation of the facets has occurred over the years, as the FDM images show, cf. fig. C.40.

At regular intervals, the facets are checked for defects, e.g. breakage or detachment of the mirror surface (transparent). In this case such a heliostat is noted. For the FDM measurement within the scope of the CESA-1-2020 measurement campaign, only heliostats with intact facets are selected.

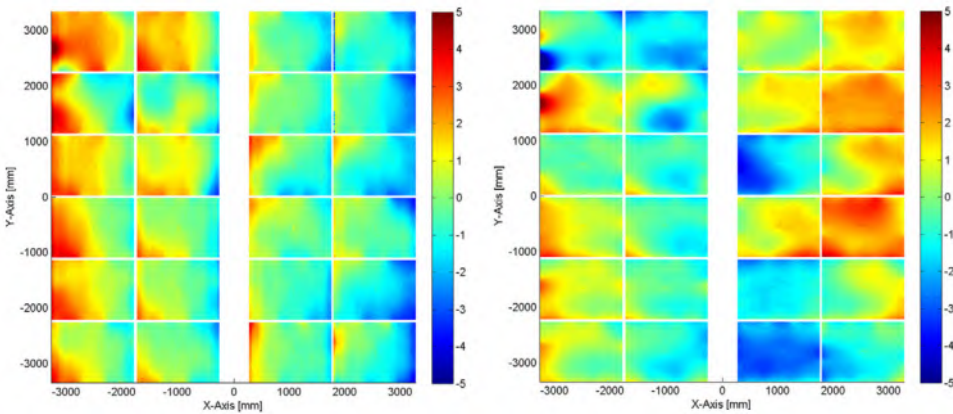
#### 2.1.2.4 Features and their nomenclature

A heliostat consists of several *mirror facets*. Mirror facets are mounted with a gap to each other, usually between 1-2cm. At CESA-1, heliostats are embedded in a steel frame. In any case, this design means that individual mirror facets can be clearly separated. In image recognition, these lines or edges between the heliostat facets can be traced. This is also the reason why these points are relevant for QFLY. With the help of these intersection points, a large number of points in the image can be searched for photogrammetry, thus ensuring a highly accurate orientation.

These intersection points are called *features*. Depending on the mirror type, a different number of features can be defined, see fig. 2.7. On CESA-1 there are two different heliostat types, each with 38 or 25 features respectively.



a) Example of a regular horizontal stripe pattern – projected on target (*left*), reflection on heliostat mirror (*right*).



b) Measurement result showing slope deviations from ideal surface in azimuth (*left*) and elevation (*right*) in milliradians (mrad).

**Figure 2.6:** Measurement set-up of QDEC used for heliostat surface measurements. [52]

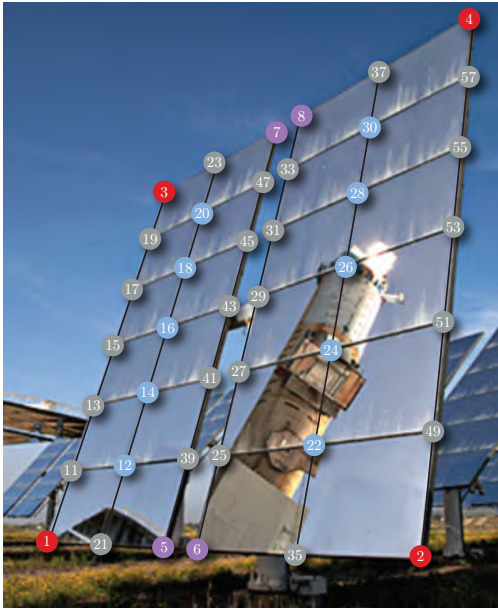
### 2.1.3 Research centers of DLR

In the context of this work, datasets from two test centers of DLR are provided - CESA-1 on the Plataforma Solar de Almería<sup>5</sup> (PSA) and the STPP in Jülich, cf. fig. 2.8

#### 2.1.3.1 PSA in Almería, Spain

The CESA-1 project, cf. fig. 2.8 a), was promoted by the Spanish Ministry of Industry and Energy and inaugurated in May 1983 to demonstrate the feasibility of central receiver solar plants and enable the development of the necessary technology. At present, the CESA-1 does not produce electricity, but is a very flexible facility operated for testing subsystems and components such as heliostats, solar receivers, thermal storage, solarized gas turbines, control systems and concentrated high flux solar radiation measurement instrumentation. It is also used for other

<sup>5</sup>The PSA is a research facility on CSP technology, located in Tabernas, southeastern Spain, owned by CIEMAT.



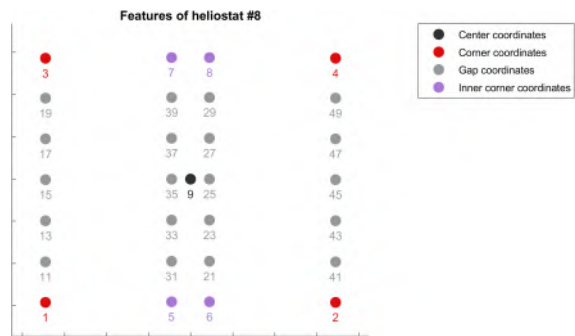
a) Heliostat with separated facets on each heliostat mirror side (newer heliostat models).



b) Heliostat with single facets on each heliostat mirror side (original heliostat models).



c) 39 features / 24 facets layout, derived from data structure saved in MATLAB for heliostat 1.



d) 25 features / 12 facets layout, derived from data structure saved in MATLAB for heliostat 8.

**Figure 2.7:** CESA 1 Heliostat - Corners, gaps and crosses nomenclature. Initially, heliostats with 12 facets have been installed. Due to several reasons, if mirror facets need to be exchanged, the 24 facets layout is chosen.



a) STPP in Jülich, Germany. [40]



b) Top view of CESA-1 on PSA in Almería. The picture shows the two towers with their corresponding heliostat field, several line focusing parabolic trough collectors and Stirling dish collectors on the lower left side. [4]

**Figure 2.8:** STPPs that are currently used by the DLR to perform tests and measurements for new technologies.

applications that require high photon concentrations on relatively large surfaces, such as in chemical or high-temperature processes, surface treatment of materials or astrophysics experiments. [53]

Direct solar radiation is collected by the facility's 330 x 250-m south-facing field of 300 39.6-m<sup>2</sup> heliostats distributed in 16 rows. The heliostats have a nominal mean 90% reflectivity, the solar tracking error on each axis is 1.2 mrad and the reflected beam image quality is 3 mrad. In spite of its over 37 years of age, the heliostat field is in good working condition due to a strategic program of continual mirror-facet replacement and drive mechanism maintenance and replacement. The maximum thermal power delivered by the field onto the receiver aperture is 7 MW at a typical design irradiance of 950 W/m<sup>2</sup>, achieving a peak flux of 3.3 MW/m<sup>2</sup>. 99% of the power is focused on a 4m-diameter circle and 90% in a 2.8m circle. [53]

### 2.1.3.2 STPP in Jülich, Germany

The STPP in Jülich, Germany, features a 60-metre high tower and is Germany's sole plant using this type of solar power technology, cf. fig. 2.8 b). Over 2,000 dual-axis sun-tracking mirrors heat air to 700°C, which is used to generate steam which flows through a turbine to generate electricity. Insulated steel tanks allow storage of heat for 1.5 hours in the event of clouds passing over. The total electric output of the plant is 1.5 MW. [40, 54]

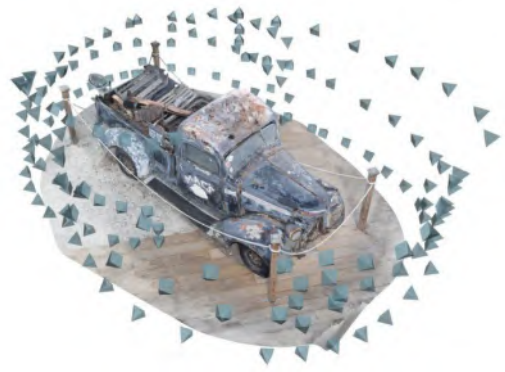
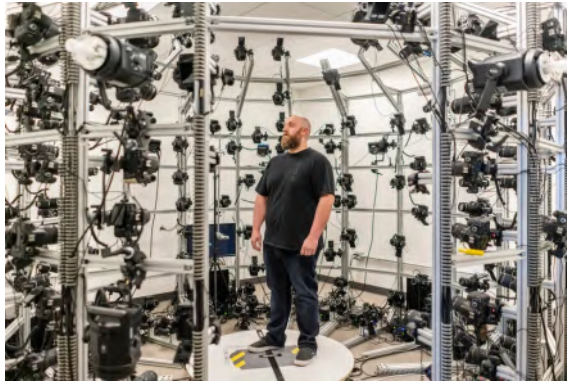
For this thesis, the data is not analyzed in detail. During the measurement campaign in 2018 no FDM was been conducted. In general, comparability is difficult, as quantity of heliostats, size and quantity of features are different.

## 2.2 Photogrammetry

Photogrammetry is a three-dimensional measurement technique based on central-perspective imaging as a mathematical model, cf. fig. 2.9. To photograph an object for photogrammetric reconstruction, a series of overlapping photographs of this object from different angles have to be taken. Photogrammetry software detects features on the object and the surroundings, finding common points in overlapping pairs of photos which can be used to find the camera's placement in relation to the object for each photo. By solving for all of the common points simultaneously, the software builds a 3D representation of the object made up of individual points on the surface. This model is called point cloud.

The following basic rules have established in order to improve calculation speed:

- Rule 1:** Quality of image – for rectangular objects such as heliostat surfaces oblique images providing a viewing direction of camera to heliostat normal vector of 45° work best.
- Rule 2:** Camera calibration and initial orientations.
- Rule 3:** Avoid blurring in the photographs.



a) Photogrammetry room designed by Bernardo Antoniazzi used for the development of Modern Warfare. [55]      b) A car being shot from different angles, picture taken from a photogrammetric software. [56]

**Figure 2.9:** Photogrammetric approaches

**Rule 4:** High-contrast patterns on the surfaces.

**Rule 5:** No movements of the object during photography.

**Rule 6:** High quantity of images.

**Rule 7:** High resolution of images.

**Rule 8:** Each point in the scene surface should be clearly visible in at least two high quality images.

**Rule 9:** Photos of object from all directions in a circular way.

**Rule 10:** Nadir images.

**Rule 11:** Images covering of the whole object.

**Rule 12:** Images focusing on details.

**Rule 13:** Images with little information or indistinctive observations increase computation time.

## 2.3 Established methods for orientation measurement of heliostats

For an efficiently operating STPP it is necessary that the heliostats are continuously and automatically tracked during the operating time so that the sunlight is reflected on the receiver at any time. For each heliostat, a motion model is available from which the heliostat orientation in the form of rotation around the two heliostat axes is determined based on input parameters (position of the sun, position of the receiver, etc.). The error influences (cf. subsection 2.1.2.2) cause that the assumed motion model may change over time, and the reflecting light does not reach the receiver. The errors must therefore be determined and the motion model must be adapted accordingly.

### 2.3.1 Flux density measurement

In the course of time, various methods have been developed to determine the optimal heliostat alignment. A large part of them can be summarized to the group of the so-called flux density based methods. These methods check in different ways whether the sunlight reflected by the heliostat hits the receiver or how much the actual point of incidence deviates from the receiver in order to make appropriate corrections to the motion model. Various established procedures are introduced hereafter, cf. fig. 2.10.

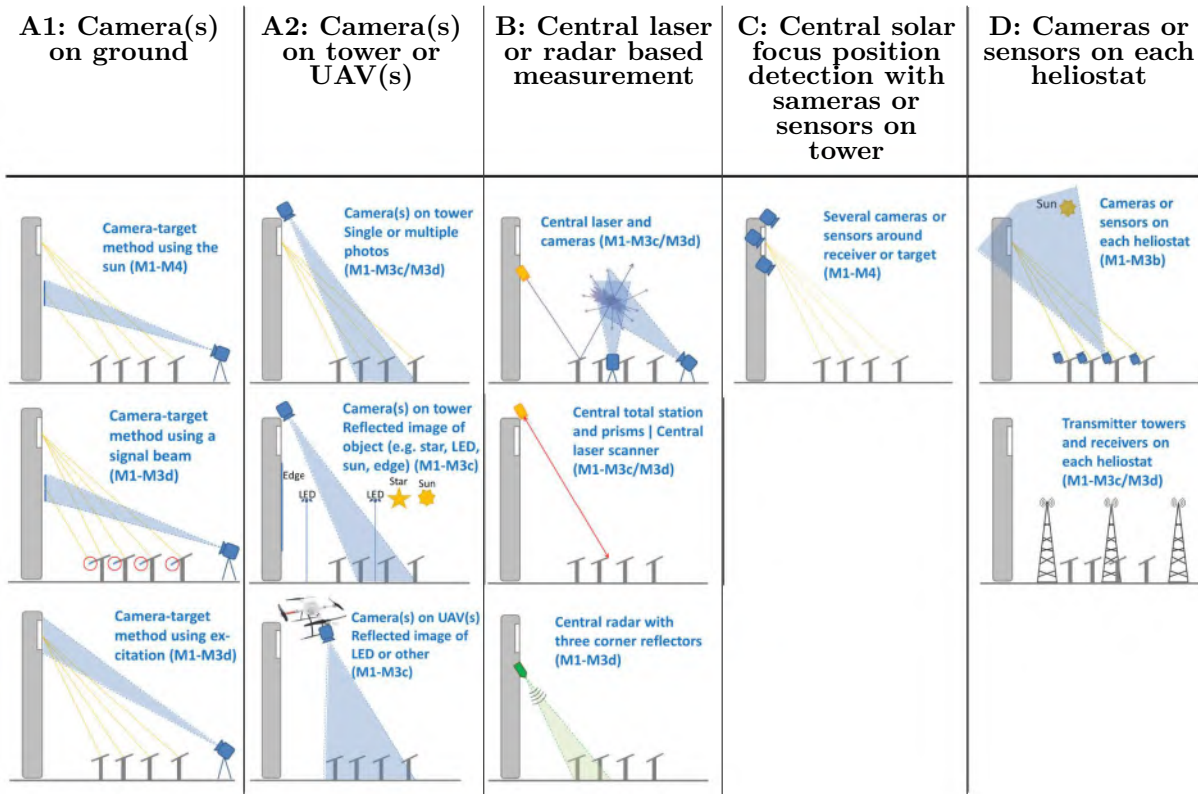


**Figure 2.10:** Visualisation of currently available calibration system classes according to the classification criterion location, type and number of measuring devices or sensors. [34]

**FDM with camera and target.** A method to check a heliostat’s misorientation is to determine the distance between a target point and the center of the solar troid projected by the heliostat [57], cf. fig. 2.11. On the tower of a STPP a white-coated target with Lambertian properties is used<sup>6</sup> (target), is mounted. A camera captures the target from a central position in front of the tower. The target is automatically detected in the image and its center is calculated in the image. The target center is set as the target point for a heliostat, which then aligns itself based on the underlying motion model. On the target the reflected sunlight can now be seen in form of a centroid, if the heliostat is not grossly misaligned. The centroid in the image is automatically

<sup>6</sup>the intensity of the radiation emitted by an area element  $dA$  is the same in every direction of space.

detected by thresholding and its center is also determined. If the heliostat is perfectly aligned, the centers of the target and the sunlight centroid coincide. The horizontal and vertical deviation between the two centers of the image is calculated. To determine the correction parameters, the deviations in pixels must first be converted into meters and finally into encoder steps to adjust azimuth and elevation. This form of FDM is used as reference measurement system for this thesis. The orientation can be determined as the bisecting line of the angle between the position of the sun and the vector between the heliostat and the focal point.[17, 14, 15]

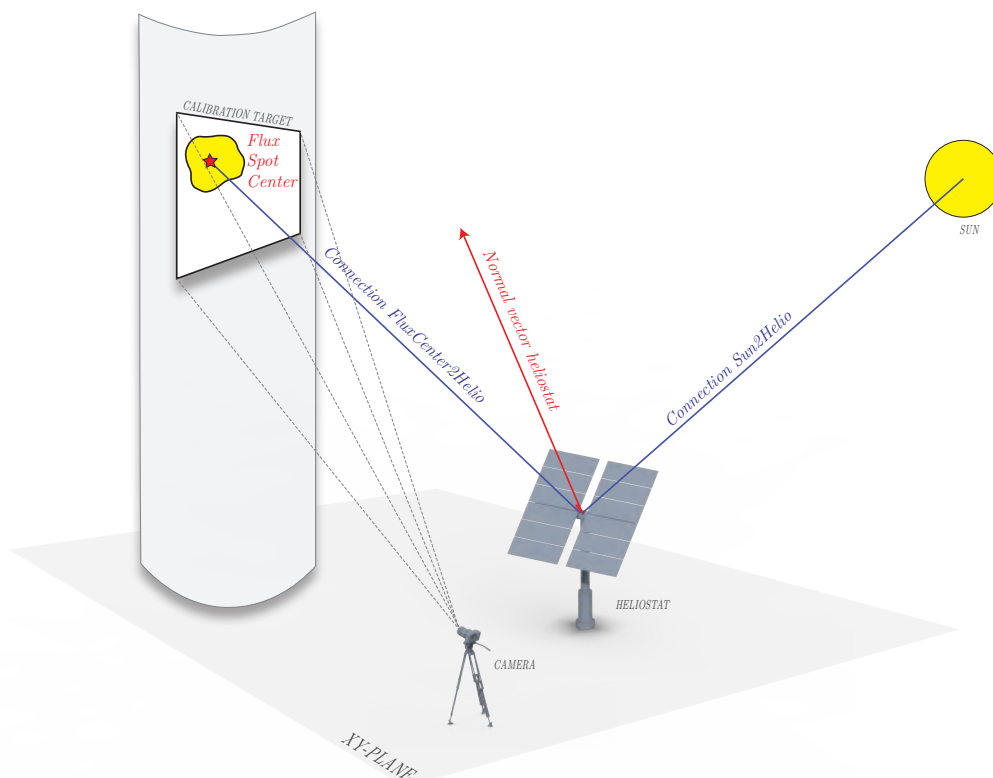


**Figure 2.11:** Illustration of the camera-target invented by [58]. A camera is used to take photos of the flux spot reflection on a target. Reflection of solar rays at heliostat spans a triangle whose bisector corresponds to the normal vector of the heliostat mirror surface.

**FDM with four cameras placed around receiver** In another method, instead of a target, a camera is placed left, right, above and below the receiver [59]. These are aligned so that each camera captures the entire heliostat field. Each heliostat is uniquely identified in one shot per camera so that the approximate position of each heliostat in the image is known. The cameras capture the field in short time intervals. If possible, i.e. at low contrast, each heliostat mirror area in the image is detected by a pattern recognition algorithm. Otherwise, the image area of the mirror surface is estimated by an analytical model. Then the average brightness of each area is calculated. The average brightness values of a heliostat from one image each of two opposite cameras are compared. If the values differ, the heliostat is not optimally aligned and

its orientation must be corrected. Based on the product of the difference in brightness and an empirically determined scaling factor, a correction parameter is generated for the corresponding heliostat axis (cameras above and below the receiver for elevation axis; cameras left and right for azimuth axis). This parameter is forwarded to the control unit for immediate correction of the heliostat's orientation.

**FDM with photodiodes around receiver and vibration.** In another flux density method, no cameras but photodiodes are positioned around the receiver, which collect reflected sunlight from one or more misaligned heliostats [60]. To distinguish the heliostats, they are vibrated by piezo actuators (electrical signals are converted into mechanical motion) with different frequencies. The reflecting beam of rays vibrates at the same frequency. By Fourier analysis and detection of the maxima of the outgoing signal of a photodiode, the reflecting heliostat of a beam can be clearly assigned. The correction parameters for azimuth and elevation axis are also derived from the signal.

### **2.3.2 Camera in heliostat center, pointing in NVec direction to observe sun.**

A camera is positioned in the center of the heliostat mirror surface and aligned in such a way that its optical axis coincides with that of the heliostat. Through that, the sun is observed for drawing conclusions about the heliostat orientation from the sun's position [61]. The motion pattern of the heliostat is similar to that of a solar tracker during calibration, i.e. the heliostat is always oriented towards the sun. The camera regularly takes images in which the sun is detected and its center is determined. The change in position of the sun center in the images provides information about the tracking accuracy of the heliostat (drift in azimuth and elevation direction).

### **2.3.3 Camera in heliostat center, several points are observed besides sun**

In a similar procedure, a large number of other points with known positions are observed besides the sun [62]. These are automatically detected in the camera images by image processing methods and must be clearly identifiable (e.g. lights, prominent parts of buildings, sun, moon). Based on the positions of the points in the images the motion model of a heliostat shall be adapted in an iterative process. To observe such a point, the heliostat and the camera are moved around its azimuth and elevation axis until it is detected in the camera image. For each image the point ID and the rotation angle of both axes are stored, which are recorded by so-called encoders. The motion model uses the encoder values to calculate the heliostat orientation and the position of the corresponding point in the image. This is done in the same way for all other points. The deviation between calculated and actual point positions in the images is then used to adjust the heliostat motion model. This process is repeated iteratively until the motion model cannot be significantly improved any more.

### 2.3.4 Stripe Pattern projected on target, reflection on heliostat mirrors analyzed in pictures

One method to analyze not only the orientation but also the mirror surface is the so-called fringe projection [61]. Here, a stripe pattern is projected by means of a projector onto the target on the power plant tower. The heliostat to be measured is aligned so that it reflects the pattern from the target into a camera also mounted on the tower. The reflected stripes are distorted due to incorrect orientation and defects in the mirror facets. In order to obtain information about the causes of the errors, four striped patterns (each phase-shifted by  $\frac{\pi}{2}$ ) are projected onto the target one after the other. The mirror surface is then mapped by means of phase-unwrapping, making any errors in the geometry visible.

### 2.3.5 Cameras on tower, image recognition of heliostat edges (SAPHIR)

Another possibility to determine the heliostat orientation is the use of edge detection methods, which was developed by DLR under the project SAPHIR (a project of DLR)<sup>7</sup> (SAPHIR). Here, the entire heliostat field is captured by a camera from the receiver tower [63]. The individual heliostats in the acquired images are detected by a threshold value method. A further, more complex thresholding method is applied to each detected heliostat to separate the individual heliostat panels from each other. Their edges are extracted. The device equations are determined by Hough transformation. The intersection points of the lines form the four corner points of a heliostat panel. From the aspect ratio and the size of the four interior angles within a heliostat panel in the image, its orientation relative to the camera is calculated (assuming the position of the heliostat and the camera is known).

### 2.3.6 Several cameras mounted elevated around field

Over a heliostat field several towers are built, each with a camera on top. Several heliostats were to be oriented in such a way that they reflect the sunlight in the direction of one of the cameras. In order to derive the geometric information required for the calibration, similar to other flux density methods [64]. To be independent of daylight, colored LEDs were mounted on the towers [65]. A heliostat is aligned to reflect the LED of one tower into the camera of the same or another tower. When the light reaches the camera, the intensity of the light beam is evaluated. Based on the results of this evaluation the Heliostat is automatically reoriented. This happens in real time and several times in a row, as well as for several camera-LED pairs. The parameters of the kinematic model of the heliostat are improved from the observed rotation angle of the heliostat axes when the LED reflections are detected by the camera, as well as the known positions of cameras, LEDs and the heliostat. The cameras used are wide-angle cameras, which allows the

---

<sup>7</sup>The goal of SAPHIR was to develop optical measurement systems to support the heliostat prototype development, the facet and heliostat assembly and the final inspection of heliostat fields for STPPs, Funding code 16UM0068.

detection of a wide range of the heliostat field. A LED reflected in a heliostat only makes up a very small part of the camera image. Reflected light from different heliostats can therefore be clearly separated from each other in the image if they are located at a certain distance from each other. This makes it possible to calibrate several heliostats per camera at the same time.

### 2.3.7 Drawbacks of the mentioned methods

- The FDM methods only work for one (four, depending on the size of target) heliostat at a time, so the time of execution is a limiting factor especially for large plants. Furthermore, measurements can only be made when there is sufficient solar radiation and thus only within the time frame in which the tower power plant is in operation.
- The change of the heliostat orientation for FDM (sunlight is reflected on a target and no longer on the receiver) necessary for the measurement reduces the power of the power plant to a small extent.
- The methods mentioned in section 2.3.2 and section 2.3.3 require temporary installation of cameras on the heliostats, which leads to a high workload and time expenditure. Depending on how many heliostats are to be calibrated at the same time, more hardware (costs) or more time has to be planned. In addition, the first method depends on the sun and therefore has the same disadvantages as the flux density methods.
- The deflectometric method with pattern projection also requires a high expenditure of time, because only one heliostat can be measured at the same time. Furthermore, this method can only be realized at night.
- Also the procedure with cameras and artificial light sources mounted on additional towers can only be carried out at night. In addition, the costs for the camera towers are high.
- A general disadvantage of most procedures is the accuracy with which deviations in the heliostat orientation are determined.

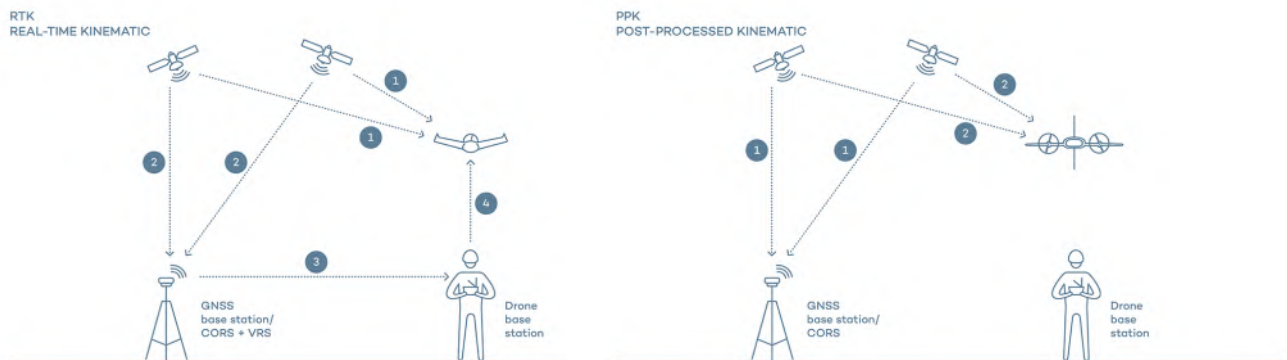
Due to these limitations, research is being conducted on alternative methods for heliostat characterization to make them more efficient.

### 2.3.8 Deflectometry with tower

The National Renewable Energy Laboratory (NREL) has developed another form of deflectometry measurement in which at least as many images are taken per heliostat as there are facets in the direction of the width, either at different times or from different positions. The camera position has to be chosen so that the tower is reflected in the heliostat. For heliostats in the first row, images can be taken from the ground. For heliostats in the field, a UAV can be used to take images from the air. In the images the heliostat and its facets are first detected by image recognition, and then the edge of the tower is localized. Based on the shape of the tower, the heliostats orientation and shape can be obtained. [66]

### 2.3.9 RTK and PTK

**RTK.** Real Time Kinematic (RTK) positioning, cf. fig. 2.12 a) is a satellite navigation technique used to enhance the precision of position data derived from a Global Navigation Satellite System<sup>8</sup> (GNSS), which allows to further improve the exterior orientation<sup>9</sup> (EOR) by real-time based EOR acquisition [67]. RTK relies also on a stable radio link between a base station on the ground and a Global Positioning System (GPS) antenna on board the UAV. Due to these requirements, RTK positioning can have its downsides, with radio link outages and GNSS signal blocks. Due to the long distances between the UAV and the base station, signals can be obstructed resulting in loss of correction data and a lower percentage of accurate camera positions in the flight. [68]



a) RTK requires four constant communication lines to correct satellite location data: 1. the line between satellites and drone, 2. the line between satellites and GNSS base station or CORS (supporting Virtual Reference Station (VRS) via mobile) network, 3. the line between the GNSS base station or Cross-origin resource sharing (CORS)/VRS and the drone base station, and 4. the line between drone base station and drone. [69]

b) Post-Processed Kinematic (PPK) requires two constant communication lines to correct satellite location data: 1. The line between satellites and GNSS base station or CORS network, and 2. the line between satellites and drone. [69]

**Figure 2.12:** Difference between RTK and PPK. [69]

**PPK.** PPK, on the other hand, processes the positioning information after the flight, not during. Data is logged in the UAV and combined with data from the base station when the flight is completed. As a result, there is no risk of data or initialization loss due to radio link disruptions. PPK drones therefore offer more flexibility in terms of how and where the drone is deployed.

<sup>8</sup>A Global Navigation Satellite System (GNSS) is a constellation of satellites providing signals from space that transmit positioning and timing data to the GNSS receiver (PPK module). Each satellite constantly sends its position and the time to the receiver. The receiver then uses this data, correlated from multiple satellites, to precisely determine its location.

<sup>9</sup>EOR are the camera positions obtained by photogrammetric evaluation. [8]

## 2.4 QFly

The following part includes mainly existing work from the DLR working group SF-QLF<sup>a</sup>, which is currently not yet published. Large parts of this thesis are based on these developments, such as the QFLY program structure in MATLAB, which is furthermore being improved and extended on a daily basis.

<sup>a</sup>Solarforschung Qualifizierung

In the following the measuring principle of QFly and important correlations in the program structure in MATLAB are explained.

### 2.4.1 QFly process for STPPs: Two-step process for heliostat characterization

QFLY is a two-step process consisting of a *photogrammetry* to create a three-dimensional model of the mirror facet corners to estimate the heliostat alignment, and the “QFly DEFLECTOMETRY”<sup>10</sup> (deflectometry), in which the highly accurate heliostat orientation is derived from the deflectometric measurement of the mirror form, cf. fig. 2.13. [5]

Due to the strong contrast between background and sky reflection on the mirror surface, the facet edges can be detected. These individual features are used as photogrammetric reference points. Thus, the most important necessity is to identify each feature in images from as different viewing angles as possible and to recognize its exact pixel position within the images. The overall QFly process consists of the following five steps:

- QFly Step 1:** Route planning and image acquisition for photogrammetry
- QFly Step 2:** Photogrammetric evaluation with coarse orientation result: Once the images are obtained, the camera position can be determined to detect and correctly identify all heliostats and features within an image (ZA and FD).
- QFly Step 3:** Once the visible features in each image are located and identified, the exact 3D setup can be determined using commercially available photogrammetric software (PG). As a final step, the heliostat normal vector is determined by fitting the ideal heliostat geometry to the measured 3D model.
- QFly Step 4:** Route planning and image acquisition for deflectometry, based on previous photogrammetric result.
- QFly Step 5:** Deflectometric evaluation with fine orientation.

Further in this thesis, deflectometry is not discussed any longer. For the sake of simplicity, when

<sup>10</sup>The DEFLECTOMETRY is a measuring method intended to determine the shape of the mirror surface as well as the canting (orientation in space) of heliostats. For this purpose it is necessary that the normal vectors are determined at as many points of the heliostat surface as possible. Shape and orientation can then be derived or calculated. The primary goal is therefore the determination of these vectors with an accuracy of 0.3 mrad. [6]

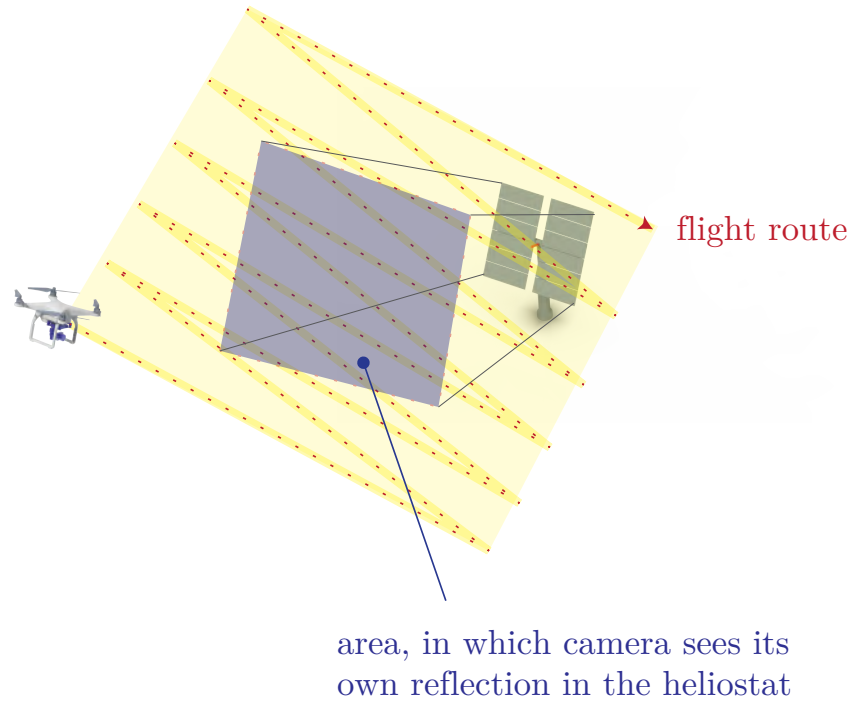


**Figure 2.13:** Reflex-based process *deflectometry*. The considered heliostat is overflow meander-like. A meander flight route consists of a certain number of two straight sections, which are attached to each other in alternating order. If the UAV is on or near the optical axis of a heliostat and at the same time oriented towards it, both the heliostat itself and the UAV reflected in it will be visible in the acquired image. Afterwards the images on which the target is visible are used to determine the exact orientation. [70]

mentioning the term “QFLY” hereafter, the first part of QFLY – the photogrammetric part – is meant.

### 2.4.2 QFly program flow

QFLY is a collection of several thousand functions written in MATLAB and is used in many ways in the field of solar research. In addition to heliostat orientations, parabolic trough CSP, infrared measurements, PV soiling, and much more can be analyzed. The individually required function is started from a personalized calling function, in which the path to the configuration file is specified. The entire QFLY process can be roughly divided into pre-processing and post-processing, cf. fig. 2.14.

The processing durations mentioned hereafter adhere to datasets such as those acquired on the PSA, and would increase for utility scale plants. In detail, QFly for STPPs works according to the following steps, cf. fig. 2.14. The whole QFly-Code Flowchart is displayed in fig. D.1.

**Route planning and image acquisition for photogrammetry.** The flight routes were chosen in a circle around different points of interest in order to achieve a relatively even coverage of the area and at the same time ensure a wide range of viewing angles. Additionally for the

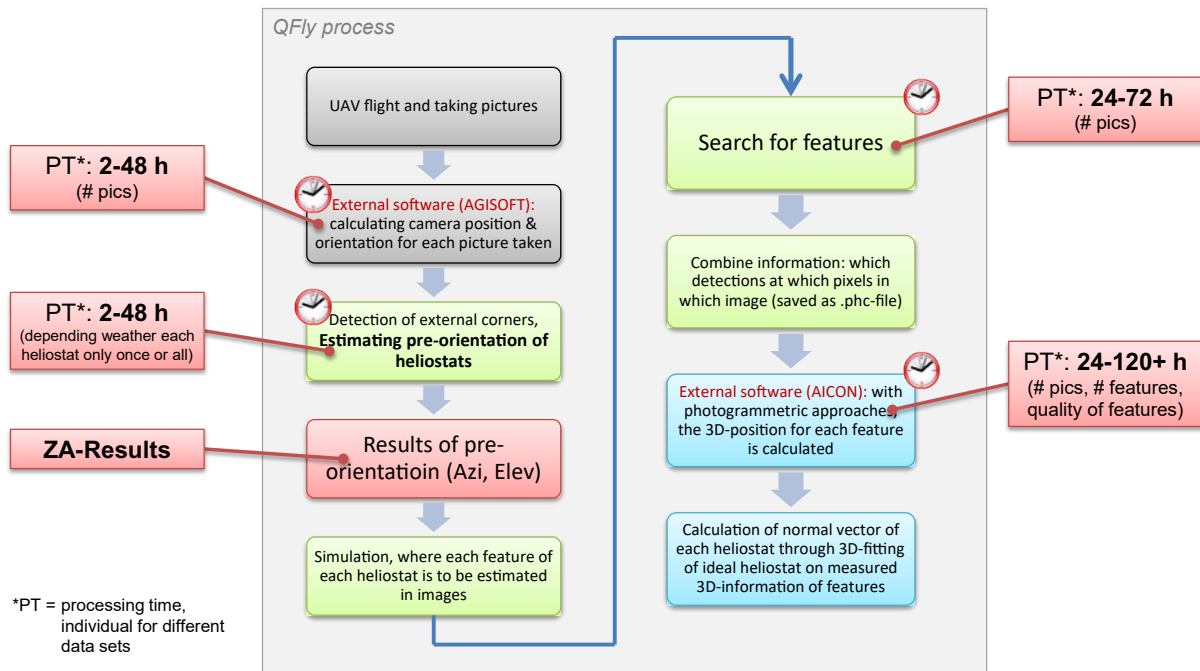


Figure 2.14: Flowchart of QFLY process, with usual calculation durations.

CESA-1-2020 measurement, nadir images were taken. Photographs of the plant are taken using a MICRODRONES MDMAPPER1000+, cf. section F.2.

**EOR recognition.** The images are given to “AGISOFT METASHAPE”<sup>11</sup> (AGISOFT), which is a photogrammetric software, to determine the EOR for each image. Additionally, at least 4 reference points have to be set with their actual coordinates. For CESA-1-2020, seven reference points were selected, cf. fig. 3.4. This allows AGISOFT to scale the point cloud to the correct size. The calculated camera positions are passed back to MATLAB. The processing time is massively influenced by the number of images and takes between several hours to several days.

**Pre-orientation (ZA).** The ZA is an image recognition that detects the four outer corners of the heliostat mirrors. To obtain the **pre-orientation**, the ideal heliostat geometry is fitted (stretched, rotated, distorted) onto the 2D detected outer corners. With the transformation matrix, the orientation is calculated with a certain deviation (residuals) to the original 3D heliostat, cf. fig. 2.15. The process takes between several hours to several days, depending whether a heliostat only has to be detected once (one ZA result per heliostat overall) or as often as possible.

In the ideal Matlab 3D model, all heliostats point upwards (azimuth = 0°, elevation = 0°). This

<sup>11</sup> AGISOFT METASHAPE is a stand-alone software product that performs photogrammetric processing of digital images and generates 3D spatial data to be used in GIS applications, cultural heritage documentation, and visual effects production as well as for indirect measurements of objects of various scales, developed by AGISOFT LLC.

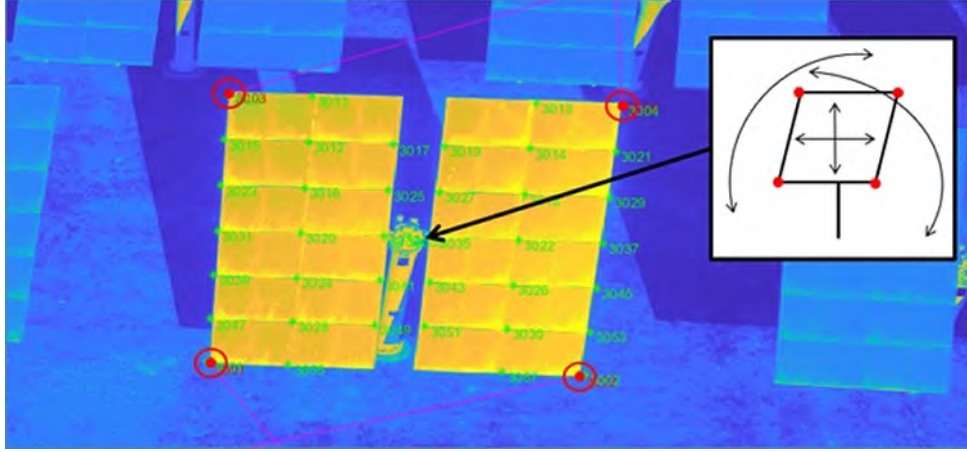


**Figure 2.15:** The ideal heliostat (white background) is shifted and distorted to cover the detected outer corners in the image as accurately as possible. Using the transformation matrix thus generated, the orientation of the heliostat can be calculated (Roll, Pitch, Yaw).

3D-field gets projected into the camera coordinate system using the rotation matrix

$$\mathbf{R} = \mathbf{R}_z \mathbf{R}_y \mathbf{R}_x. \quad (2.1)$$

Through that, the position of heliostats on the image can be predicted. This list of existing heliostats in the image is then processed in sequence. A heliostat is to be located at a certain distance from the camera. The distance between heliostat center  $P_1$  and camera position  $P_2$  must not exceed 250m for CESA-1-2020:

$$d(P_1, P_2) \leq \sqrt{(x_2 - x_1)^2 + (y_2 - y_1)^2 + (z_2 - z_1)^2} \quad (2.2)$$

$$d(P_1, P_2) \leq 250\text{m}$$

A search area, 50 mm larger than the estimated extension of the outer corners, is defined around the heliostat. Some checks are made, e.g. if the heliostat is covered by another heliostat or even overlaps a heliostat behind it. If this is the case, the corner detection would produce errors and is therefore aborted at this point.

The ZA plays a major role in this thesis, and is therefore explained more in detail hereafter. Through the obtained EOR (camera position and viewing direction), it can be assumed which heliostats with all their four outer corners are captured on a given image. For all these heliostats, their outer corners are localized exactly through image recognition. Checks and filters are set to minimize error tolerance. It consists of the following image recognition steps:

**ZA Step 1:** An orthoimage is created from the image section, resulting in a rectangular image section.

- ZA Step 2:** The image is converted to a grayscale image, and then to a binary image. Helio-  
stat mirrors are now white (1), the background is black (0).
- ZA Step 3:** Objects touching the edge of the image section (e.g. neighboring heliostats) are  
eliminated.
- ZA Step 4:** Holes are filled.
- ZA Step 5:** The now existing objects in the image are counted.
- ZA Step 6:** Get a rough position of corners.
- ZA Step 7:** Get an exact position of corners.

The ideal heliostat (azimuth =  $0^\circ$ , elevation =  $0^\circ$ ) is rotated and distorted until its outer corners match the detected ones. Thus, a preliminary orientation (ZA-results) is obtained, and coordinates can be estimated for all other features.

**Feature Detection.** Provided that all 4 outer corners have been found, an exact search area can be defined for each feature of this heliostat. The FD works *edge-based*, therefore the facet edges are searched and crossing points discovered. Per image several hundred detections can be made, as shown in fig. 2.16. The image number, the feature numbers on this image, and the respective x and y pixel coordinates are then passed to AICON in a phc-file. The FD takes one to three days.

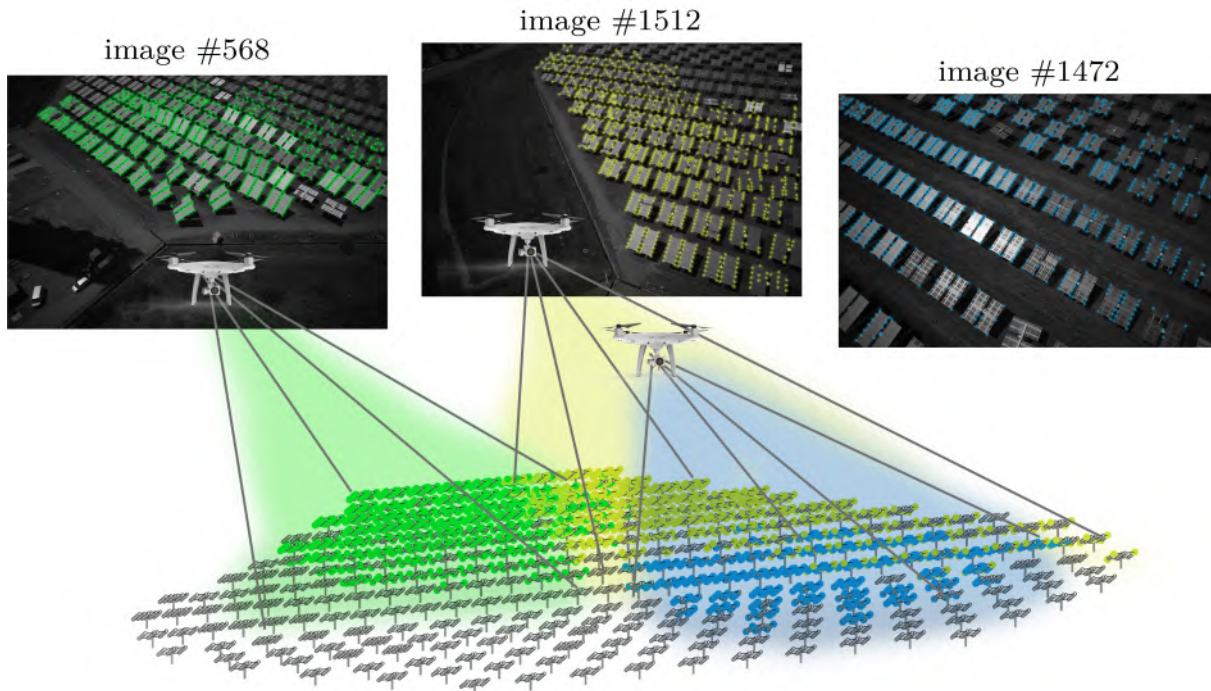


**Figure 2.16:** Feature detection shown on CESA-1-2020 images #1472 (54 detected heliostats, 873 detected features), #568 (84 detected heliostats, 1252 detected features), and #1512 (89 detected heliostats, 1038 features). With two images already a good part of the field is covered.

**Photogrammetry and final orientations.** AICON uses photogrammetric approaches to align all the detections. Camera positions are obtained automatically. The calculated feature coordinates are still in a random coordinate system and have to be fitted on the ideal heliostat field. Leveraging the feature 3D coordinates, the normal vectors are calculated for each heliostat. The PG in AICON was experienced to be the most time consuming step. It's chiefly depending on the quantity of feature detections given as input into AICON (quite different numbers for CESA-1-2020 and CESA-1-2018, as shown in section 3.1).

### 2.4.3 Obtaining the heliostat orientation with the FDM approach

The FDM orientation software can be seen as an essential part of the QFly development, and is therefore mentioned in this section. The general overview of the FDM is covering these points, cf. fig. 2.17:

- FDM Step 1:** Obtain images of the target, cf. section 2.5, while having a proper file management in place, saving the exact measurement time. At least 10 images should be taken for each heliostat group on the target.
- FDM Step 2:** FDM analysis part I: Selecting the outer corners of the target manually for the first image, cf. fig. E.3. The software automatically starts detecting the flux spot centers on every image, which is explained later in detail.
- FDM Step 3:** FDM analysis part II: Outlier flux spots are filtered, because it is possible that a certain heliostat has been moved during the measurement (initial adjustment by operator), or the flux spot has already left the target partially (“*off-target*”). The remaining are used to calculate a mean normal vector for each heliostat, cf. section C.4.

First the outer corners of the target in the first image of the series are selected – it is important that the target position is the same in all following images, in case a series calculation is performed, cf. fig. E.3. This is necessary for the transformation into an orthophoto. The orthophoto is then scaled to a size of 400x400 pixels. The following steps are used to calculate the flux spot center of gravity coordinates:

- Step 1:** Convert the RGB image into a grayscale image to obtain a gray scale image.
- Step 2:** Binarize the image using the gray value average of the present image to obtain a binary image.
- Step 3:** Localize the flux spots via the MATLAB internal *regionprops*-function.
- Step 4:** Overlay the thus generated areas with the original gray scale image .
- Step 5:** Calculate the centers of gravity via the distribution of the gray scale values in the respective area.

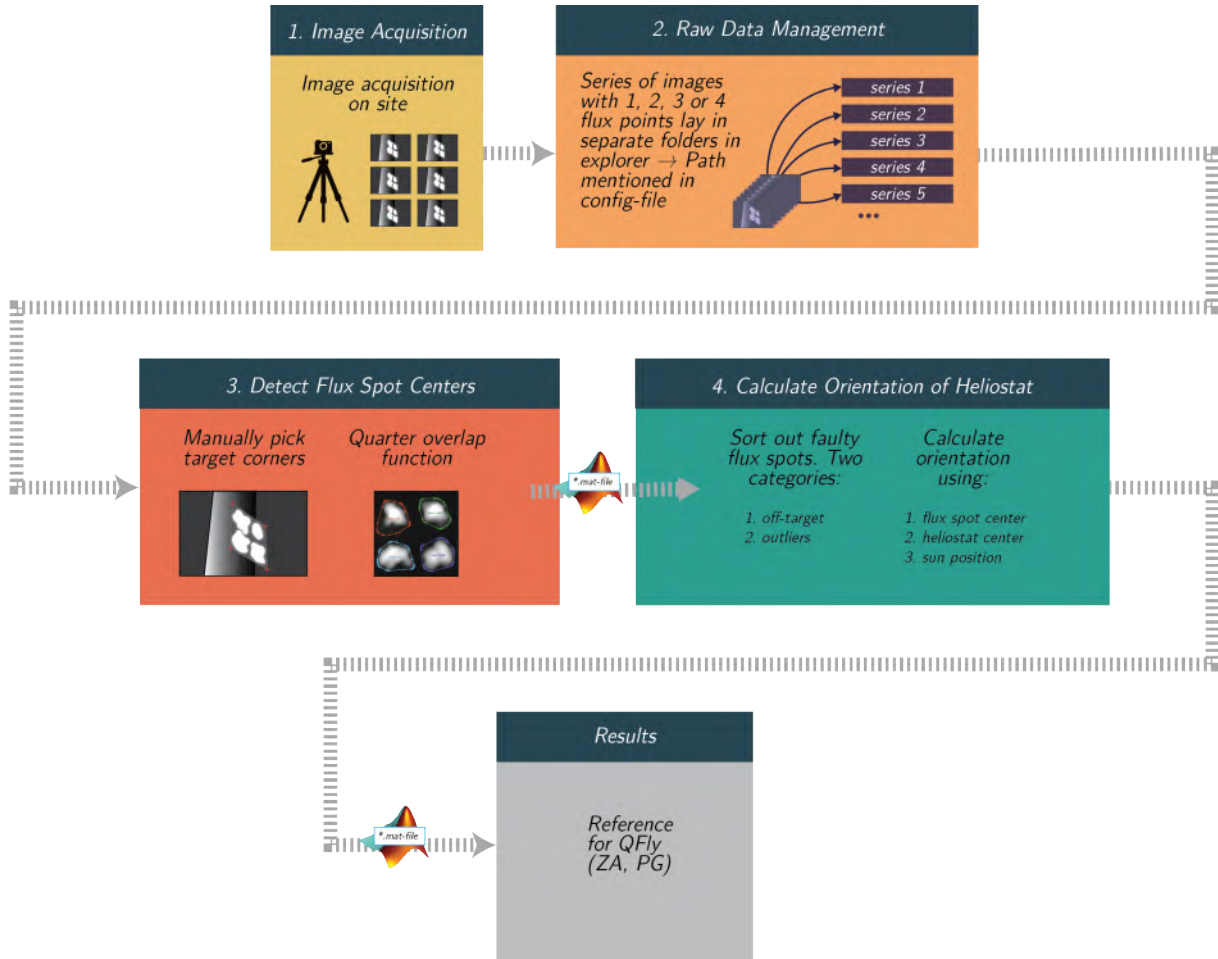


Figure 2.17: FDM process flow

## 2.5 Capture reference data as part of a measurement campaign

An established method for tracking verification is the FDM, cf. subsection 2.3.1. Depending on the speed of adjusting the heliostats, it takes about 3-5 minutes to align the flux spots of a group of four heliostats onto the target<sup>12</sup>. For the FDM measurement a few images are sufficient (10-20), which means a measurement time of <1 minute at a clock frequency of 1/s. During the test campaign, to ensure comparability with QFly, the heliostats have to stay in this position, which leads to a long waiting time depending on the position of the sun. Up to 45 minutes may pass until all four light reflections have left the target entirely. This is the only way to ensure that the QFLY measurement taking place simultaneously is not distorted. In case of a pure FDM measurement for calibration of the heliostats this waiting is not necessary, i.e. the target can be released for the next heliostat group directly after the FDM measurement. With the estimated 4-6 minutes per measurement and 75 groups on the PSA<sup>13</sup>, the measurement procedure would

<sup>12</sup>four heliostats is the maximum quantity to be analyzed simultaneously with FDM at CESA-1

<sup>13</sup>Four heliostats per group and a total of 300 heliostats.

take only 5-8 hours for the complete field, not counting breaks<sup>14</sup>. Between 150 and 350 images are taken per series as part of the CESA-1-2020 measurement.

The measurement campaign consists images from the measurement campaign are shown in fig. E.1.

For the tachymeter measurement, a Trimble S8 is used, cf. section F.1. The heliostat centers of heliostats 34, 35, 36, 104, 108, 159, 161, 163, and 167 are measured. In addition, four more reference points as well as the coordiant origin<sup>15</sup> and the target corners and centers are measured.

Further information can be found in the 25-page protocol.

---

<sup>14</sup>The initial calibration of a newly constructed STPP medium-sized STPP plant with 10,000 heliostats however, would take months to calibrate.

<sup>15</sup>the coordinate origin is in the center of the door of the tower



## 3 Evaluation of tests, data provision and analysis

*To assess the accuracy of the QFLY, it's intermediate and final results have to be analyzed. To develop the optimization models discussed in section 4 and section 5, a clear understanding of the prevalent datasets needs to be obtained. This includes the QFLY measurements itself, as well as the tachymeter, hand-photogrammetry and FDM.*

In section 3.1 the **original datasets** obtained through different measurement campaigns are analyzed. Main focus lays on the CESA-1-2020 dataset, which offers a large quantity of heliostat orientations referenced by FDM. While FDM as a measurement method including the image acquisition during the measurement campaign has already been explained in subsection 2.5, now in section 3.2 it is explained in detail how the orientation of the heliostat is calculated considering those images. Here, some functions newly implemented in MATLAB for this purpose are discussed. The results of the QFLY measurement are compared with reference measurements to obtain a statement about the process safety.

### 3.1 Acquired datasets

The following datasets have been acquired over the past two years on CESA-1:

**CESA-1 2018.** A first validation campaign was performed on the PSA at the end of 2018, cf. fig. 3.1. Three heliostats were referenced using FDM. The left panel fig. 3.1 shows the 3D model of the heliostat field obtained from the photogrammetric measurement. The measured features are plotted as green points. The resulting normal vectors are plotted as red arrows. While all other heliostats were oriented with  $180^\circ$  azimuth and  $60^\circ$  elevation, the orientation of the three heliostats used for the validation measurement (highlighted in yellow) is significantly different from the rest of the field because they had to reflect light beams onto the calibration target. The right side of Fig. 3 shows the corresponding uncertainties of the measured 3D coordinates shown on the left side. The histogram shows that the 1-sigma uncertainties are below 5 mm for two-thirds of all 3D coordinates obtained and below 10 mm for about 90 percent of all 3D coordinates. The mean sigma of all 3D coordinates is 6.35 mm. Table 1 shows the validation result as deviations of the concentrator normal vectors between the UAV-based measurement and the reference. From these values, an RMSD of 5.9 mrad was calculated.

**Table 3.1:** Different characteristics of CESA-1-2018 and CESA-1-2020 datasets. Due to the approx. 1.5 year difference in the measurement runs, there have been changes to the code in many places. A purely quantitative difference, however, is the number of detected features in the respective datasets, which differs significantly.

Criteria	CESA-1-2018	CESA-1-2020
Quantity Detected Features	245319	1489190
Quantity all unique features in heliostat field	3523	10086
Quantity Images	1805	2608
Quantity Images (cleared empty images)	916 (-49%)	2571 (-2%)
Ratio detected Features per images	136	579
Mean height of oblique flights	48,4 m	61,9 m
Turbulences during oblique flights (altitude fluctuation) – standard deviation of height values	0.95 m	1,4 m
Ratio detected Features per images (cleared empty images)	268	583
Image Sizes [px]	6000x4000	6000x4000
Quantity of ZA measurements	7424	58656
Quantity of ZA measurements for FDM heliostats		6583
Quantity Heliostats detected	107	283
Quantity ZA per Heliostat	69, std: 38	207, std: 145
Quantity of ZA-measurements overall in close range to FDM (within +/-1 mrad)		Azim: 543, Elev: 293, NVec: 134
Quantity of ZA-measurements per heliostat in close range to FDM (within +/-1 mrad)		Azim: 17.5, Elev: 9.5, NVec: 4.3
Quantity ZA per FDM-Heliostat	21, std: 19	212, std: 84
Max Quantity ZA per Heliostat	198	553
On how many different images?	852	2411
Average ZA results / quantity detected Heliostats per image	9, std. 7	24, std. 19
Max. detected heliostats per image	30	88 (min: 1)
Uncertainty EOR from Agisoft		X: 2.8 cm, Y: 1.5 cm, Z: 7.3 cm
PG – Quantity objCoo	1063	3059
PG – Quantity eor	241	1041
PG – Quantity observations	27065	583071
NormalVecData.HeliostatData_fit (length)	238	158
NormalVecData.HeliostatData_fit (length) – cleared empty results)	142	146
Quantity of FDM Heliostats in NormalVecData	1 of 4	28 of 31

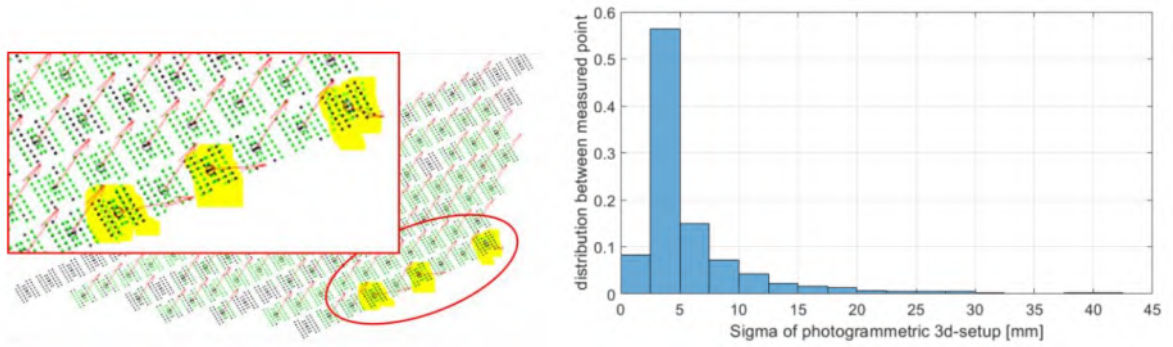


**Figure 3.1:** Left: Measured 3D model and concentrator normal vectors in the first experimental setup for the photogrammetric stage. Measured normal vectors *red*, presumed location of the features for the first preset model of heliostat orientation *black*, features whose 3D coordinates were successfully measured *green*, three reference heliostats in the first row *yellow*. Right: Estimated uncertainties of the photogrammetrically determined 3D coordinates (*green dots on the left side*). [5]

**CESA-1 2020.** A second validation campaign was performed on the PSA in July 2020. 31 heliostats were referenced using FDM.

## 3.2 Reference measurement: FDM

Independently of the time-consuming QFLY calculation, the FDM calculation is performed. The whole process is illustrated in fig. 2.17. By specifying the explorer paths where the images taken on the field are stored, centroids and finally heliostat alignments are calculated based on the image acquisition time (alignment with atomic clock necessary). This process takes less than one hour for the 2020 measurement, where over 1900 images in 9 FDM series (7x 4 heliostats, 1x each 1 and 2 heliostats) have been generated.

The FDM results can then be compared to the ZA or PG results. In the main program (*QflySurveyHeliostatEdgeBased*), the comparison takes place by default after the PG calculation. For this purpose, the QFLY results created independently of FDM are read in as a .mat file. The differences in azimuth, elevation and normal vector are shown in tab. 3.2. Thereby, for 28 FDM-heliostats PG results could be calculated within the prescribed tolerance frame.

A new filter algorithm has been implemented. Off-target flux spots, cf. fig. 3.2 are already indicated during the flux spot center calculation. The filtering for outliers is done using a tripartite filter algorithm that filters outliers in:

- x-direction over timestamp,
- y-direction over timestamp, and
- y-direction over x-direction (actual flux spot movement on target).

Therefore, all outliers can be eliminated securely, as shown in fig. 3.3.

The mean standard deviation of the azimuth across all remaining measurements is 0.12902 [mrad], and for elevation 0.060265 [mrad].

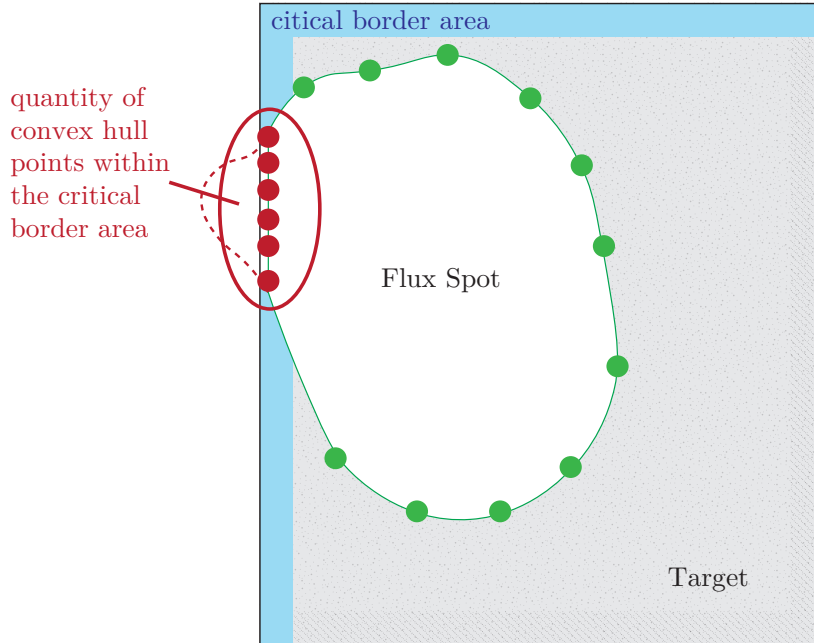


**Figure 3.2:** Schematic: Flux spot leaves the target. The *regionprops*-function detects several points in close range to the border (*red*).

The orientation is calculated using the heliostat center and the position of the sun. The sun position is calculated from the creation date and time of the respective image using the Michalsky algorithm with an accuracy of 0.011 deg. [71, 72] The heliostat center, on the other hand, can be used from four different sources: a) Tachymeter measurement, b) Matlab 3D-model of field, c) ZA results, and d) PG results.

### 3.3 Agisoft

To align the 3D point cloud with the original 3D coordinate system, reference points have to be chosen within the 3D point cloud, cf. fig. 3.4. These reference points are set manually as accurately as possible, by clicking precisely e.g. on the predicted heliostat center in the 3D point cloud. the real x-, y- and z-coordinates are provided for those reference points (heliostat foot point positions measured with tachymeter as part of the construction of the plant. To get the final 3D-coordinates of the heliostat center (which is assumed to lay perfectly on the overall parabolic surface of the heliostat mirrors), the height of the base as a constant and the orientation of the heliostat has to be taken into account). Agisoft automatically allocates the reference points to all the images where they actually show up. Manually, the reference points have to be realigned on several images until they are on the correct position on every image.

As the reference points are located in several of the 2603 images, the final 3D-Point has to be a mean of all these values, which is combined with an uncertainty, cf. fig. 3.4. The error in Z-direction is significantly larger than those in X- and Y-direction. The XYZ-errors in the reference points are propagating in the error of the EOR. This might explain, why the elevation

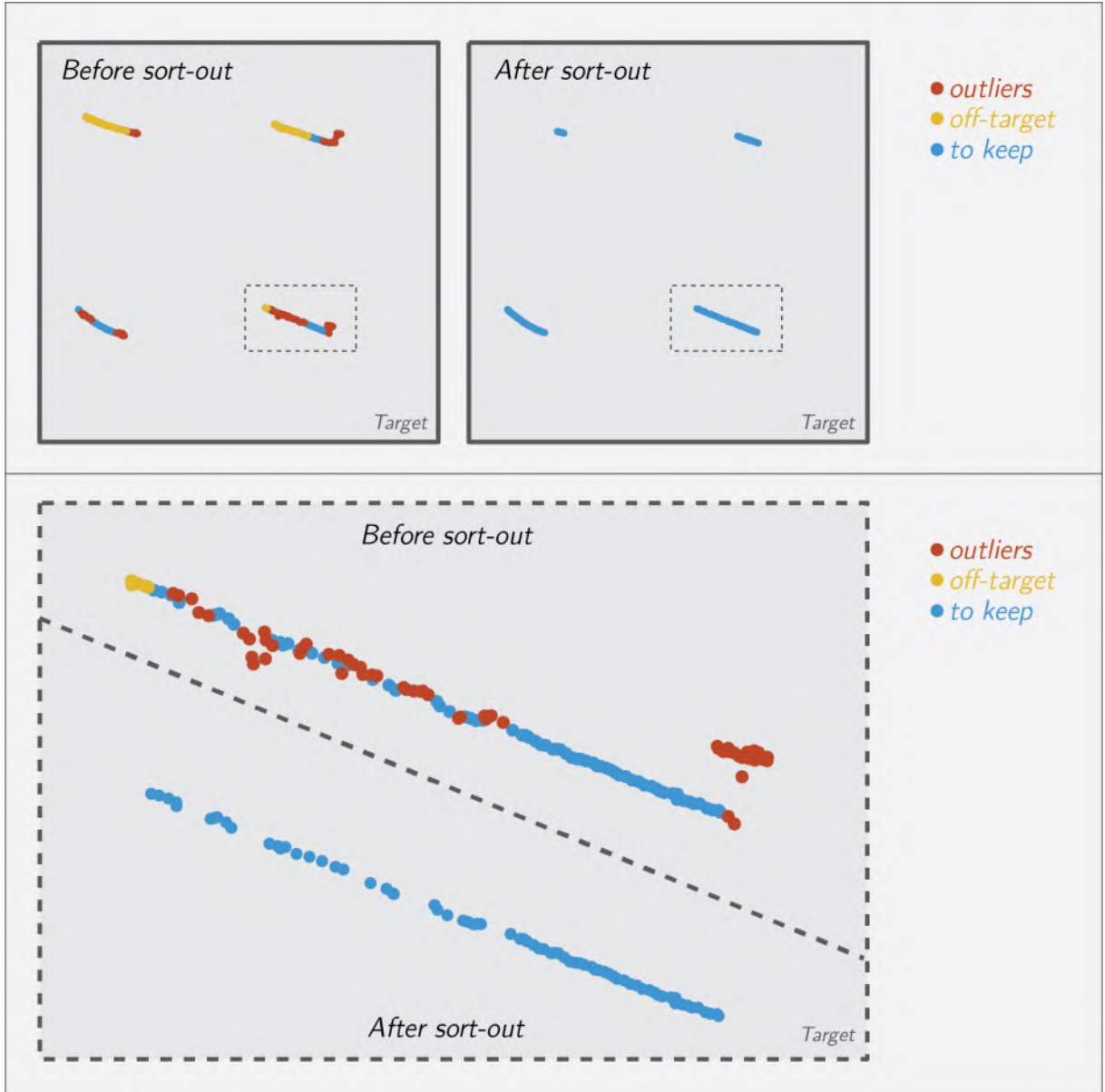


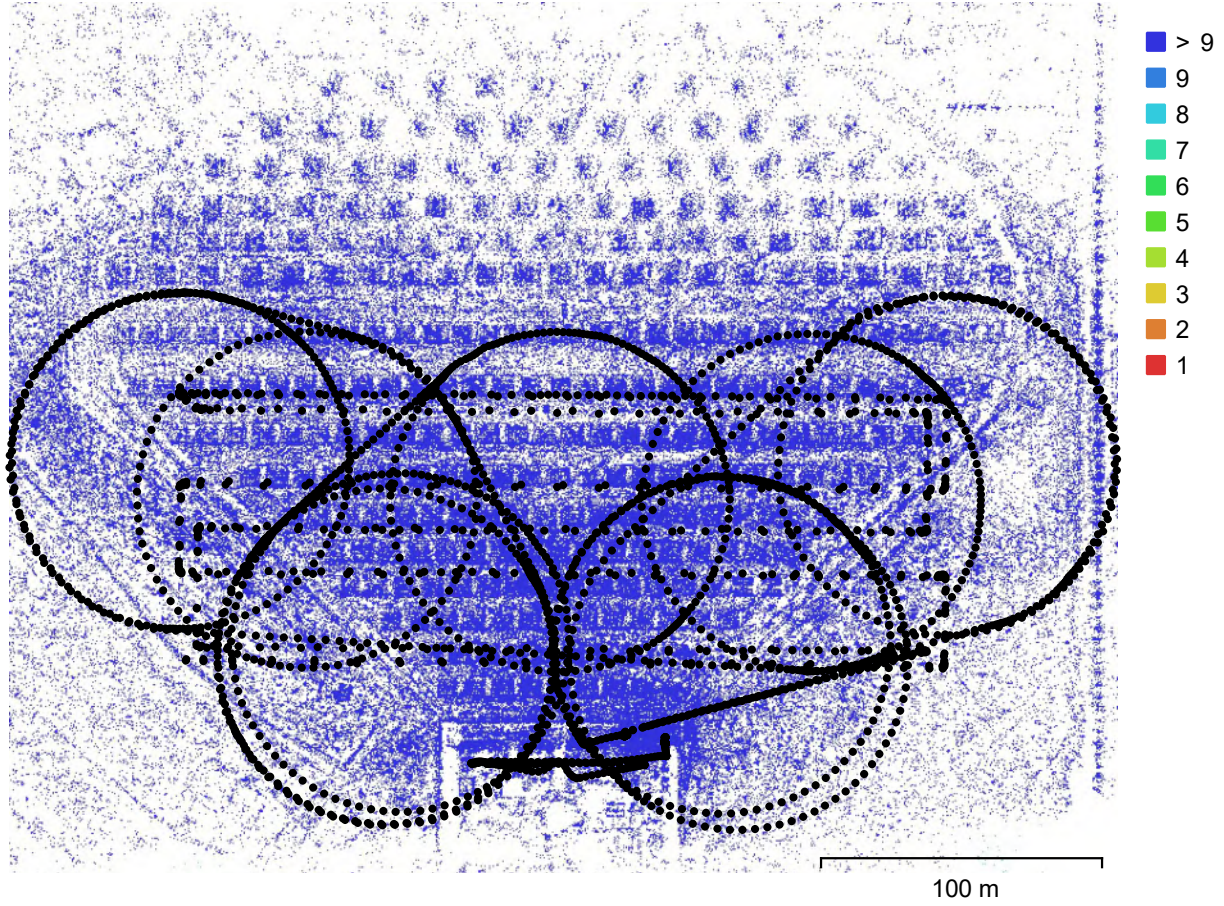
**Figure 3.3:** Filtering for outliers. The small two images on the top show the whole target and the four flux spot movement of this FDM series. Below there's a zoomed view to verify the accuracy of the filtering process for outliers and off-target situations.

values show significantly larger deviations than the azimuth values.

### 3.4 ZA results

To analyze the ZA results, the mean, standard deviation of normal vector, azimuth and elevation are calculated.

The average deviation of the ZA measurements compared to the 31 FDM is 15.6 mrad, which fulfills the requirement to achieve a measurement accuracy of less than 10 mrad, as was already the case for CESA-1-2018. A detailed breakdown of the comparison values can be found in



Label	X error (cm)	Y error (cm)	Z error (cm)	Total (cm)	Image (pix)
H0105	-0.720172	-1.69199	-5.57317	5.8687	0.033 (587)
H0102	-4.76563	1.54307	-0.0192286	5.00926	0.147 (621)
H0308	-1.17668	1.9337	10.2481	10.4951	0.104 (740)
H0929	-1.30193	-1.4577	-0.952662	2.17428	0.171 (540)
H0822	2.19379	-1.4435	-13.4429	13.697	0.164 (572)
H0719	4.62777	-0.538678	3.18417	5.64317	0.073 (730)
H1032	1.14285	1.65509	6.55576	6.85737	0.125 (363)
Total	2.77346	1.52227	7.27835	7.93623	0.123

**Figure 3.4:** EOR-calculation results taken from the AGISOFT report for CESA-1-2020, showing camera positions (*black points*), point cloud (*blue points*), and the reference points and their 7 heliostat centers, as labeled in the image. Below: Reference points and their calculation errors in X, Y and Z-direction.

tab. 3.2

Considering the calculation rule for the angle between two vectors

$$\cos\theta = \frac{\vec{u} \cdot \vec{v}}{\|\vec{u}\| \|\vec{v}\|} \quad (3.1)$$

and the mathematical equation for the mean value

$$\mu = \frac{1}{n} \sum_{i=1}^n a_i = \frac{a_1 + a_2 + \dots + a_n}{n} \quad (3.2)$$

is leaving a mean deviation, based on the FDM normal vector and the ZA normal vectors, where  $\vec{v}_i$  is the respective ZA normal vector,  $\vec{u}$  the FDM normal vector, and  $n$  the quantity of outlier-filtered ZA measurements, in case of heliostat 108 of dataset CESA-1-2020, of

$$\mu_{\theta, \text{NVec}} = \frac{\sum_{i=1}^n \arccos\left(\frac{\vec{u} \cdot \vec{v}_i}{\|\vec{u}\| \|\vec{v}_i\|}\right)}{n} = 38,1 \text{ mrad.} \quad (3.3)$$

Likewise the mean values for both azimuth and elevation deviation, relative to FDM, where  $A_{\text{FDM}}$  and  $E_{\text{FDM}}$  are the FDM orientation angles,  $A_i$  and  $E_i$  the ZA orientations, and  $n$  the quantity of outlier-filtered ZA measurements – in case of heliostat 108 of dataset CESA-1-2020 – are calculated as

$$\begin{aligned} \mu_{\sigma, \text{A, abs}} &= \frac{\sum_{i=1}^n |A_{\text{FDM}} - A_i|}{n} = 6,2 \text{ mrad} \\ \mu_{\sigma, \text{A, rel}} &= \frac{\sum_{i=1}^n A_{\text{FDM}} - A_i}{n} = -2,9 \text{ mrad} \\ \mu_{\sigma, \text{E, abs}} &= \frac{\sum_{i=1}^n |E_{\text{FDM}} - E_i|}{n} = 37,6 \text{ mrad} \\ \mu_{\sigma, \text{E, rel}} &= \frac{\sum_{i=1}^n E_{\text{FDM}} - E_i}{n} = -6,5 \text{ mrad.} \end{aligned} \quad (3.4)$$

Of the 2608 originally in the CESA-1-2020 dataset, only 1560 are oblique images (60.0%) – the rest is climb/sinking flight (372, 14.2%), nadir (478, 18.3%) or images that were not pointing onto the field or just the first row of heliostats (215, 8.2%). Oblique images promise the best heliostat orientations, as heliostats are most likely seen under an angle of 45°. Therefore it was tested, whether the ZA results from the oblique images alone would already bring mean values for azimuth, elevation and normal vector with lesser deviation to FDM. The results of the testing show, that none of the filtered image ZA mean results is more accurate than the whole dataset together:

- only oblique images: 19.6 mrad (+20,4% against 15.6 mrad original)
- only nadir-120 images: 35.5 mrad (+127,6% against 15.6 mrad original)
- only nadir-120 images: 32.1 mrad (+105.8% against 15.6 mrad original)
- only climb/sink images: 23.4 mrad (+50.0% against 15.6 mrad original)
- only front images: 18.6 mrad (+19.2% against 15.6 mrad original)

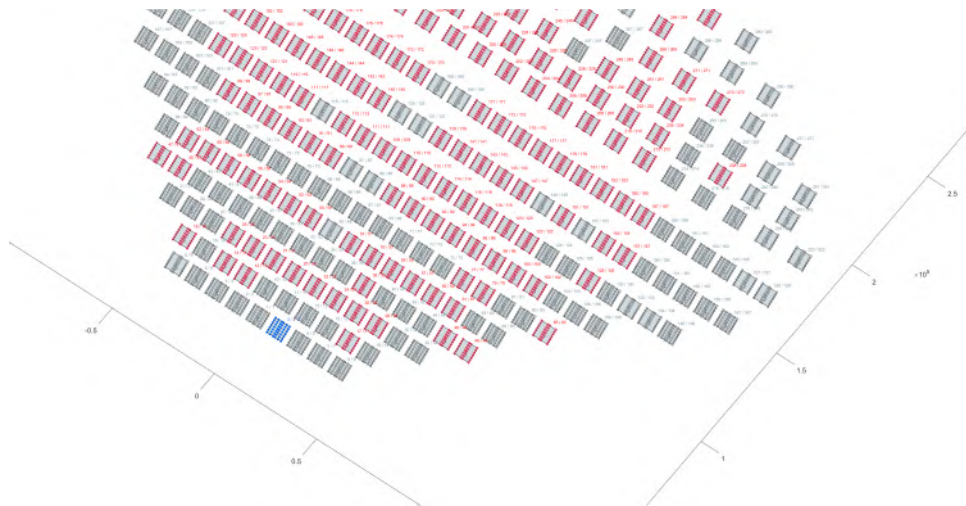
Nadir images are important to get a better EOR determination, but worsen the ZA.

### 3.5 PG results

The average deviation of the 28 calculated PG alignments from the FDM is 8.5 mrad, which fulfills the requirement to achieve a measurement accuracy of less than 10 mrad, as was already the case for CESA-1-2018. The deviation is significantly better than the one obtained from ZA (-46%). A detailed breakdown of the comparison values can be found in tab. 3.2.



a) PG result, CESA-1-2020: 146 heliostat orientations were calculated (*red*), of which 28 have are FDM heliostats (*blue*)



b) PG result, CESA-1-2018: 142 heliostat orientations were calculated (*red*), of which 1 was an FDM heliostats (*blue*)

**Figure 3.5:** Photogrammetry results for CESA-1 measurements

### 3.6 Tachymeter results: Z-differences between tachymeter measurement 2018 and 2020

The tachymeter measurement served for several heliostat centers measured with high accuracy. These heliostat centers could be used to compare with ZA and PG. However, there is a discrepancy in the z-coordinate, as shown hereafter.

During CESA-1-2018, three heliostats in the first row (heliostats 2, 3, and 9) and the target center were measured in the with a tachymeter. From this, a distance in z-direction between heliostat center and target center can be calculated. This distance amounts to 30165 mm on average for the 2018 measurement based on the three measured heliostats. A match of the 2018 and 2020 tachymeter measurements would be present if also in the 2020 measurement for a heliostat in the first row a z-difference of about 30165mm to the target center would result.

However, no heliostat in the first row was measured during the CESA-1-2018 tachymeter measurement, so only an indirect comparison via the MATLAB-3D model is possible, cf. fig. E.4. The heliostats in the 4th, 7th, and 9th rows measured with the tachymeter are used as reference. Because of a slight slope in South-North direction, these heliostats are slightly higher than the heliostats in the first row, and therefore the real z-difference to the target is smaller. This height offset is taken into account accordingly. The feedback is done using the ideal MATLAB-3D field, even though these data were measured years ago and changes have inevitably occurred. First, the vertical heliostat center offset between the averaged value of the 2018 tachymeter heliostats and the respective 2020 tachymeter heliostat center is calculated, cf. results in tab. ??.

Compared to the 2018 measurement, there is a discrepancy in the Z direction of 400-700 mm. This suggests a measurement error (although currently data handling errors cannot be 100% excluded either). The question still remains why the height difference between rows 4,7 and 9, which is now normalized to row 1, varies by 180mm among each other. This could be due to the pivoting of the heliostat (lever arm), because this differs from the ideal position. However, this does not explain why the z-difference in row 9 increases again compared to row 7 – in a row on CESA-1, the heliostat centers scatter only by 5-20 mm in the tachymeter measurement as well as in the ideal model.

### 3.7 Interpretation and correlation of final and intermediate results and reference measurements

The results of the cross comparison between FDM, ZA and PG for CESA-1-2020 are shown in tab. 3.2.

**Table 3.2:** Cross comparison PG, FDM and ZA. ZA data is outlier-filtered and contains of 53637 measurements. HelioStat 108, 195 and 161 show n/a for the PG comparisons, as they haven't been correctly aligned in AICON. For ZA and FDM comparison, showing explicitly totally wrong ZA-measurements (*dark red*) and mostly wrong ZA-measurements (*red*).

HelioStat-Nr	quantity images	Azi PG2FDM [mrad]	Azi PG2ZA [mrad]	Azim FDM2ZA [mrad]	Elev PG2FDM [mrad]	Elev PG2ZA [mrad]	Elev FDM2ZA [mrad]	NVec PG2FDM [mrad]	NVec PG2ZA [mrad]	NVec FDM2ZA [mrad]
108	192	n/a	n/a	2.9	n/a	n/a	6.5	n/a	n/a	6.7
83	134	1.0	0.0	-1.1	0.5	3.7	3.2	0.8	14.9	3.3
104	158	1.8	-1.6	-3.4	-7.2	24.3	31.5	7.3	32.6	31.5
44	89	0.7	2.4	1.7	7.9	8.9	1.0	7.9	10.5	1.4
65	187	-1.3	8.8	10.1	11.7	-13.0	-24.6	11.7	29.5	25.5
81	106	4.7	-2.7	-7.4	10.0	12.1	2.1	10.5	13.2	5.3
63	194	3.5	4.0	0.5	10.7	-2.7	-13.3	10.9	35.8	13.4
159	236	7.0	4.0	-3.0	5.6	27.4	21.8	7.4	50.5	21.9
163	231	3.5	4.8	1.3	9.5	18.6	9.1	9.8	55.4	9.1
167	154	n/a	n/a	-3.5	n/a	n/a	5.0	n/a	n/a	5.5
161	249	5.6	9.6	4.1	4.5	18.3	13.7	5.9	50.0	14.0
189	228	-0.4	13.8	14.2	6.1	13.8	7.8	6.1	18.0	12.7
193	200	-0.2	8.3	8.5	2.6	11.3	8.7	2.6	14.7	10.6
195	177	n/a	n/a	9.3	n/a	n/a	8.2	n/a	n/a	10.5
191	222	0.4	13.8	13.4	4.9	9.6	4.7	4.9	16.6	10.5
33	150	-1.6	9.7	11.2	11.1	36.6	25.5	11.2	37.4	26.6
35	26	7.6	7.1	-0.5	9.8	-4.0	-13.8	11.1	41.0	13.8
36	238	4.3	-0.3	-4.6	5.9	23.9	18.0	6.6	24.4	18.3
34	242	4.5	6.1	1.6	9.0	14.9	5.9	9.4	17.2	6.0
69	305	2.4	9.2	6.9	9.7	19.0	9.3	9.9	22.5	10.4
73	321	-2.1	1.9	4.0	8.2	23.1	15.0	8.3	24.4	15.2
75	262	-1.2	12.5	13.7	6.3	17.0	10.8	6.3	20.3	14.5
71	331	3.5	-1.0	-4.5	5.8	16.0	10.2	6.3	19.0	10.7
5	132	1.9	4.6	2.7	19.6	-19.3	-38.8	19.6	45.1	38.9
9	123	4.0	4.0	0.0	5.7	-73.1	-78.8	6.2	73.5	78.8
19	154	-2.7	5.7	8.5	4.5	13.9	9.5	4.8	17.2	11.0
7	81	8.6	0.2	-8.4	4.9	-16.8	-21.7	6.9	36.9	22.2
10	198	8.0	5.0	-3.0	14.7	7.4	-7.3	15.4	8.6	7.5
13	229	0.3	9.7	9.5	6.4	1.7	-4.7	6.4	10.8	7.7
15	190	5.6	8.1	2.5	9.7	0.3	-9.4	10.4	9.8	9.6
11	233	2.1	1.5	-0.6	12.4	2.7	-9.7	12.5	5.2	9.7





## 4 Assessment and optimization of the accuracy of ZA orientation

*In the past, once a heliostat was found in an image and an orientation was calculated, it was not searched for in the next images in order to save processing time. One pre-orientation per heliostat is already enough to roughly estimate where the features must be located. However, it is very unlikely that the first detection of a heliostat would already give the best results. Since some heliostats are detected hundreds of times, the probability is less than 1%. Maybe the alignment would be completely wrong and would irritate the feature detection. In theory, the pre-orientation can be so bad that far fewer features are detected than actually possible. Therefore, QFly currently works in a way that every theoretically detectable heliostat is analyzed on each image and the average of the resulting orientations is used to assume the feature locations necessary for the FD.*

*Some of the ZA results are highly accurate – the deviation to the reference measurement is less than 1 mrad. Therefore, the ZA could, with applying the right filters, estimate the real orientation of the heliostat under highest quality requirements.*

On average, 207 ZA results are calculated per heliostats for CESA-1-2020 on 2411 images (on average 24 ZA results per image). In principle, there are more heliostats on the images, but overlapping heliostat areas or unfavorable contrasts with the environment cause the image recognition to fall below an uncertainty parameter and return no detected outer corners for these heliostats. By accurately determining the EOR and viewing direction in AGISOFT, it's possible to assume the heliostats that have to be on this image, and through image recognition algorithms, the outer corners can be detected.

The ZA-method is error-prone, because already one falsely detected outer corner influences the overall orientation significantly. If an outer corner is wrong, this is of major importance – in contrast to FD, where up to 39 features are detected and promise a more homogeneous result<sup>1</sup>. Nevertheless, analyzing the pre-orientation is important, because the following steps (FD and PG) add up for about 70% of the total calculation time. The pixel-exact results promise, at least in parts, orientations that deviate less than 5 mrad to the FDM reference. These values have to be found systematically.

---

<sup>1</sup>running the ZA with the FD results was proved to have no impact: Both for CESA-1-2020 and CESA-1-2018 the deviations to the reference have been higher than the original ZA orientation with outer corners.

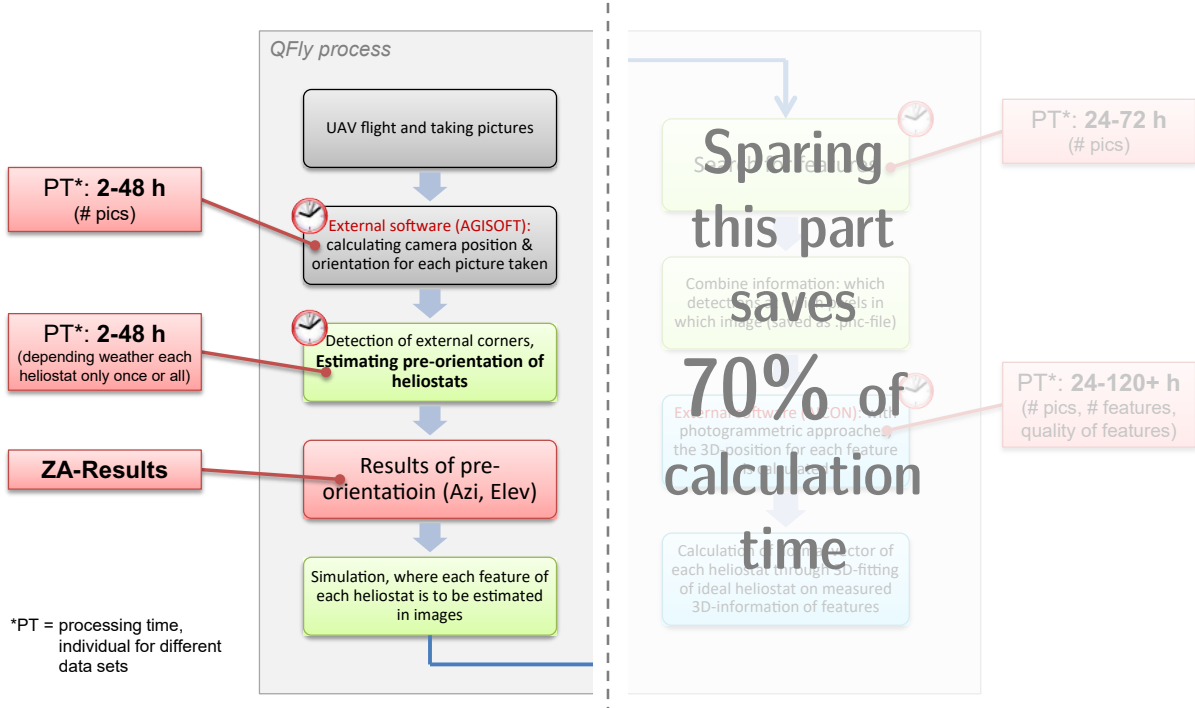


**Figure 4.1:** QFly process: FD and PG take up 70% of the processing time. Therefore it has to be checked, whether ZA is accurate enough to continue directly with deflectometry and sparing FD and PG.

## 4.1 Analyzing the datasets

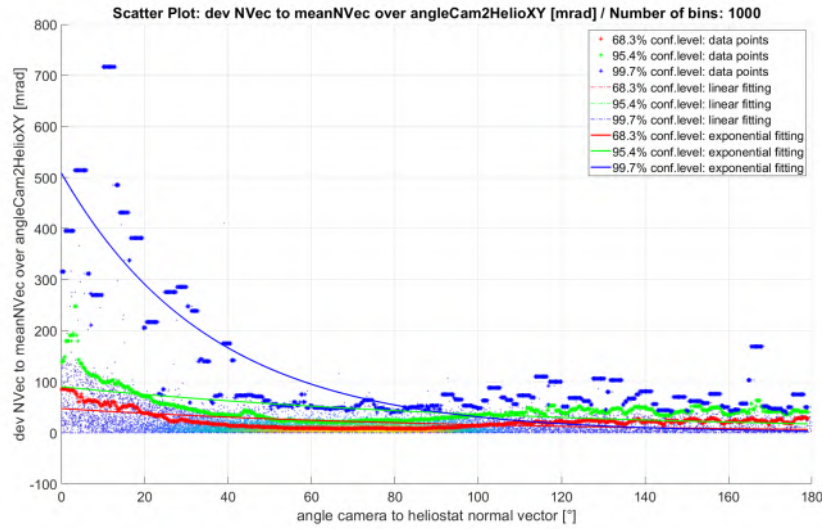
To understand the methodology, different plots are consulted, such as the ones shown on fig. 4.2.

The parameter “angle between camera to heliostat center connecting vector and the individual ZA result’s normal vector” ( $\alpha_{\text{cam2Helio3D}}$ ) seems to be well suited for filtering the ZA results, there is a clear correspondence for small angles to high deviations of the normal vector, cf. fig. 4.2 a). ZA results that lie in an angular range from  $0^\circ$  to  $45^\circ$  with respect to  $\alpha_{\text{cam2Helio3D}}$  could thus be sorted out. Likewise, from  $80^\circ$  onwards, there are more outliers in the data set. Since a sufficiently large database remains in the range  $45^\circ$  to  $80^\circ$  – here the highest concentrations are present – a filtering of the mentioned intervals may be performed. Thus, only the ZA results remain for which an interval of

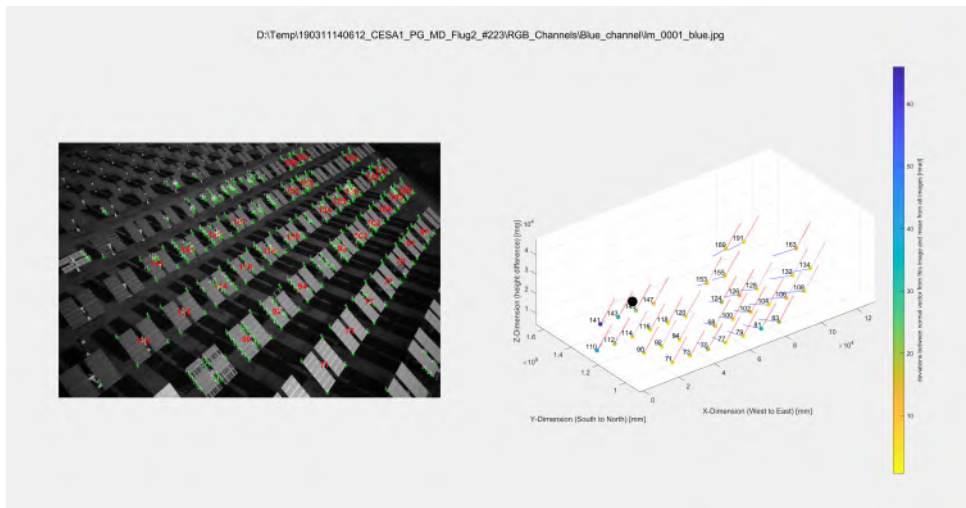
$$\alpha_{\text{cam2Helio3D}} = [40^\circ, 85^\circ] \quad (4.1)$$

applies. It is also useful to project the 3D angle onto the respective coordinate planes. This results in separate angles for the XY, XZ and YZ planes. The XY angle completely reflects the azimuth angle. Analyzing the raw image individually helps to understand synergies between  $\alpha_{\text{cam2Helio3D}}$  and the normal vector deviation, cf. fig. 4.2 b).

The  $\alpha_{\text{cam2Helio3D}}$ -phenomena can be approved by viewing heliostats individually, cf. fig. 4.3. It



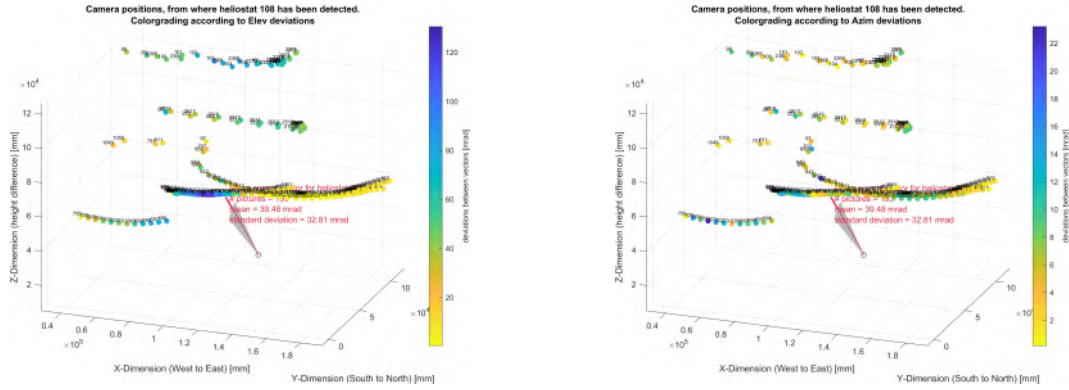
- a) CESA-1-2018: All ZA results shown. Deviation of the individual orientation to the mean normal vector of this heliostat ( $y$ -axis), over the angle between camera to heliostat center connecting vector and the individual ZA result's normal vector ( $x$ -axis).



- b) On the right side, the heliostat centers are plotted as points with an applied color grading according to their deviation to the mean normal vector ( $red$ ) of this heliostat. The individual ZA orientation ( $gray$ ) as well as the connecting vector to the camera position ( $blue$ ) are plotted as well.

**Figure 4.2:** Plots to analyze ZA results and define suitable parameters for optimization.

is evident from the individual normal vectors that the dispersion in the elevation direction is significantly greater than that in the azimuth direction. Thus, the deviations to the mean normal vector in elevation direction also differ significantly higher. ZA results with high deviation tend to be close to the heliostat normal vector, which is obvious especially in elevation direction, cf. fig. 4.3 a).



a) Elevation: Deviations range up to 120 mrad from the mean elevation.      b) Azimuth: Deviations range only up to 20 mrad from the mean azimuth.

**Figure 4.3:** CESA-1-2020, heliostat 108, unfiltered ZA results. For one heliostat all camera positions are shown, on which this heliostat has been detected on. Additionally, all normal vectors are plotted (*gray*) as well as the mean normal vector (*red*).

## 4.2 Methodology for the ZA optimization

First, important characteristic values are calculated per heliostat for the respective ZA results (azimuth, elevation and normal vector), these are, cf. fig. 4.5:

- Mean, standard deviation and median for azimuth, elevation, normal vector
- number of images
- deviation of azimuth, elevation and normal vector from the respective mean value of the heliostat
- Angle between camera-heliostat connection line and normal vector of the heliostat in 3D as well as in XY-, YZ- and YZ-plane
- The distance of the heliostat center to the camera position
- In addition, further information is stored per ZA result: camera elevation, residual of the ZA result in pixels, image number

The 58656 ZA results are then filtered for rough outliers with respect to the respective azimuth/elevation/normal vector average per heliostat. On average 18 ZA results are deleted per heliostat in 4 iterations (13 times because of the deviation of the normal vectors, 7 times because of the deviation in elevation, and 6 times because of the deviation in azimuth. Often several cases apply at the same time). In total 5019 ZA results are deleted (-9%).

Subsequently, the ZA results are filtered based on one or more parameters. A list of possible parameters is given below – besides the  $\alpha_{\text{cam2Helio3D}}$ -parameter, which was already mentioned beforehand:

- $\alpha_{\text{cam2HelioXY}}$
- $\alpha_{\text{cam2HelioXZ}}$
- $\alpha_{\text{cam2HelioYZ}}$
- Distance of the camera to the heliostat center  $d_{\text{cam2Helio}}$

- Residuals of the ZA result  $r$
- Camera elevation  $E_{\text{camera}}$ , as shown in fig. 4.4

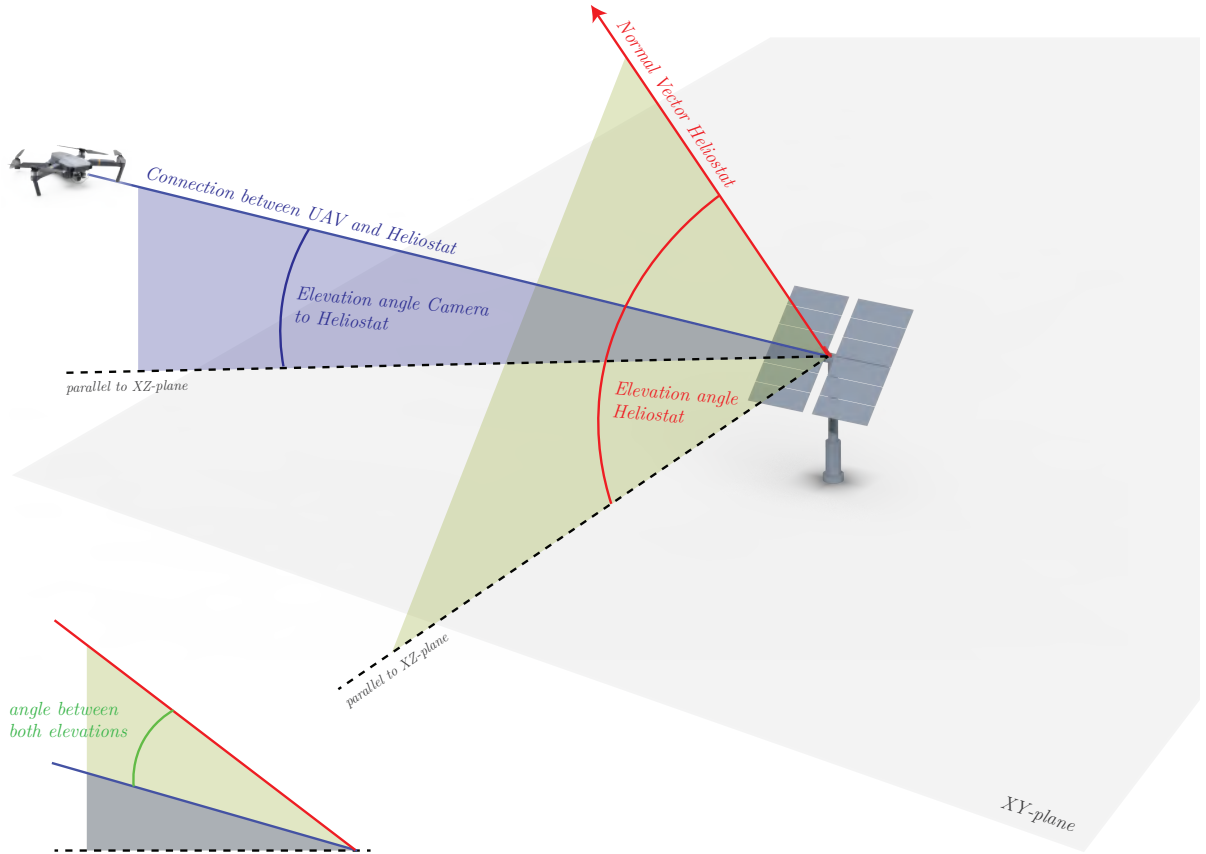


**Figure 4.4:** Parameters for quality analysis of ZA-results: Schematic representation of elevation of camera angle (*blue*), elevation of heliostat (*red*), connecting line between camera and heliostat (*blue*), and normal vector of heliostat (*red*).

It must be ensured that not all measured values are eliminated for a heliostat, otherwise no investigation would be performed at this point in the FD, no salient points would be provided for AICON, and ultimately no alignment would be calculated for this heliostat. E.g. a heliostat had been detected in 50 images, but all these 50 readings are sorted out in the optimization. Therefore, a backup is built in here [yet to be programmed] that keeps at least the five best readings. In the final result it is noted that the alignment of this heliostat may have less significance compared to other heliostats.

The optimization combines different parameters until the improvement of the deviation compared to the initial case has reached a certain level, or until a certain deviation to the FDM has been undercut.

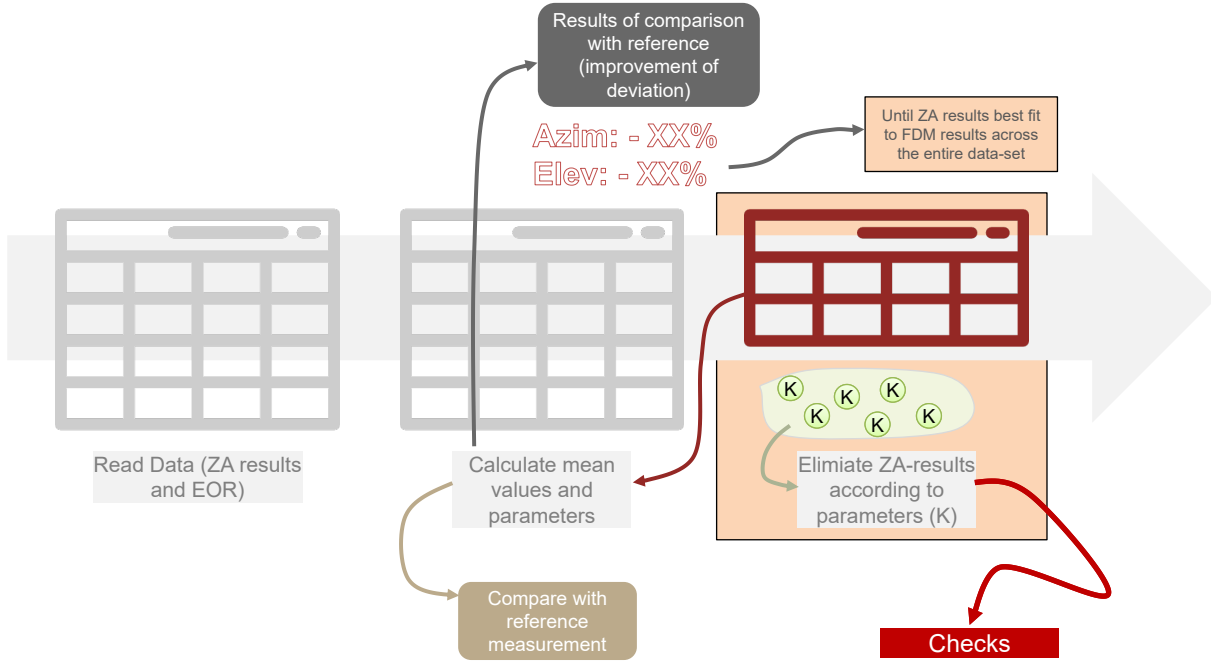


Figure 4.5: Methodology of ZA optimization principles.

### 4.3 Testing and Results

The CESA-1-2020 dataset is more suitable for investigation since 31 FDM heliostats can be used as a reference. First, a quality parameter, in this case  $\alpha_{\text{cam2Helio3D}}$  again, must be specifically selected considering fig. 4.6. The deviations are higher at low  $\alpha_{\text{cam2Helio3D}}$  as already seen in the CESA-1-2018 measurement in comparison. Relatively high outliers are also observed in the range of  $[40^\circ, 55^\circ]$ . Therefore, the angular interval for

$$\alpha_{\text{cam2Helio3D}} = [58^\circ, 70^\circ] \quad (4.2)$$

is chosen. This allows to sort out the unfiltered ZA results not matching the mentioned  $\alpha_{\text{cam2Helio3D}}$  interval. This leaves 7279 ZA results in the dataset (reduction of 87.6%). Likewise, the number of ZA results per FDM heliostat is reduced to an average of 6. For 10 heliostats even all ZA results were deleted, which is why another interval or another characteristic value must be found for these heliostats.

For the remaining ZA results the average deviation from the FDM is 8.9 mrad. Compared to the original ZA results corresponding to the same 21 FDM heliostats, which have a mean deviation to FDM of 14.4 mrad, there is an improvement of the ZA results by 38.2%.

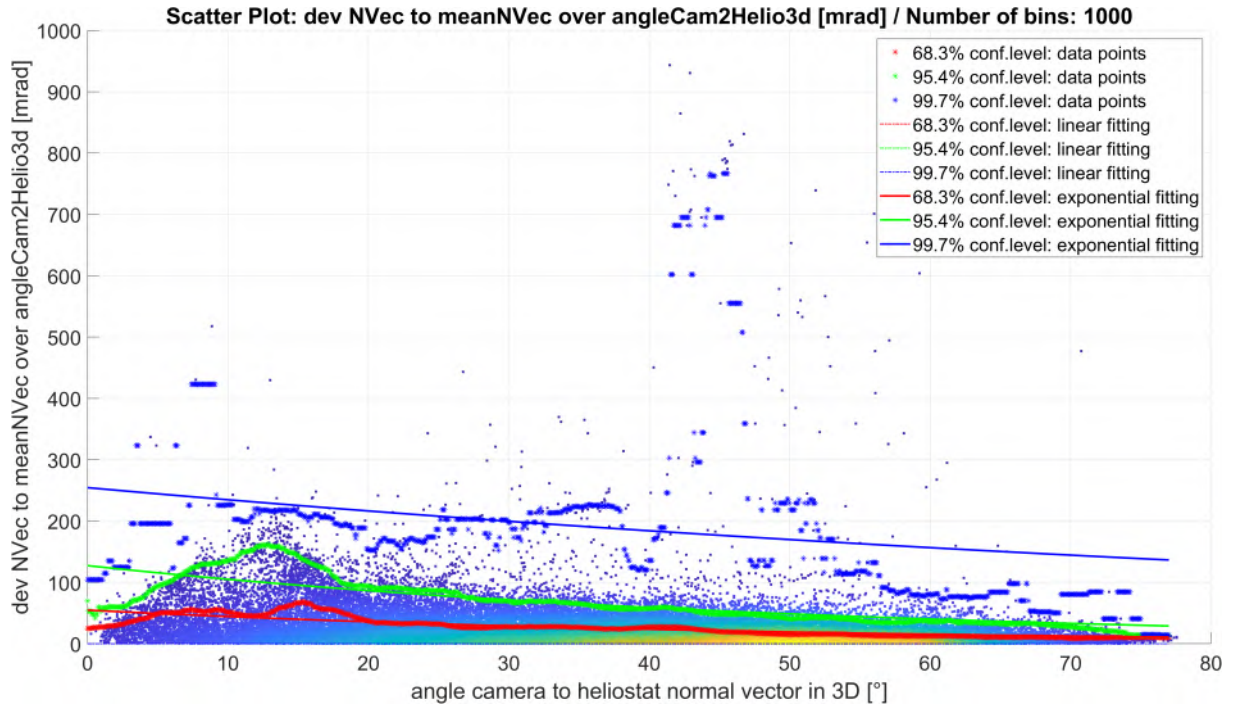


**Figure 4.6:** CESA-1-2020: All ZA results shown. Deviation of the individual orientation to the mean normal vector of this heliostat (*y-axis*), over the angle between camera to heliostat center connecting vector and the individual ZA result's normal vector (*x-axis*).



## 5 Improving Performance of PG in AICON

*For the application of QFLY, a significant reduction of the image and distinct point quantity is mandatory due to otherwise forbidding processing duration in the photogrammetric step of QFly. As demonstrated with the CESA-1-2020 data-set (2571 images, 579 detections per image on average, 1.4 million detections in total<sup>a</sup>), the current approach of utilizing the entire data-set in AICON, results in a computation duration of over three weeks on computer 3, cf. overview of computers in tab. B.1.*

*Connecting images in a photogrammetric software works better, if images show multiple unique points evenly distributed over a large portion of the image [8]. A certain quality of the images is therefore important. This chapter examines three different approaches to reducing the number of utilized images/detections.*

---

<sup>a</sup>further information in section 3.1

Under **methodology**, cf. section 5.1, filter mechanisms and quality parameters for image and detection reduction are classified. One approach to reduce the photogrammetric processing time in AICON is through reducing the number of images given as an input. Another key factor is the quantity of feature detections within an image. Especially given the large quantity of nadir images from CESA-1-2020 (478 nadir images equal to 19% of the entire data-set), detection quantities of over 1000 are making for 14% of all images, as shown in fig. 5.9.

Within the **experimental** (section 5.2) it gets shown, how suitable parameter constellations are determined and how the input data for AICON is created. The **results** obtained in AICON are shown in section 5.3. Finally, the results concerning the calculation duration, deviations to a reference model, and quantity of calculated points are **discussed** for each test series (section 5.4).

### 5.1 Methodology

By means of different selection modes, different phc-files are created, which are then calculated in AICON one after the other. This section is to formulate hypotheses for storing high-quality image and feature information as phc-files. In the phc-file only XY pixel information of the respective features in the image is given as AICON input data. All other orientation specific information like EOR and IOR are reproduced by AICON on basis of the given XY pixel information of features in all images.

The improvement of features can be divided into three levels:

**Level 1: Interconnectedness between images** such as distance of EOR and viewing directions.

**Level 2: Quality of image** such as quantity and distribution of detections.

**Level 3: Quality of detections** such as the quantity of detections of a feature.

The following sections introduce several methods of image and detection reduction to accommodate the mentioned three levels.

### 5.1.1 Image reduction

As a first approach, a filter is applied that analyzes the **value of an image** within the whole set of images. Compared to random selection methods (e.g. choosing every x-th image of the data-set), the similarity of EORs from different images plays an essential role, see fig. 5.1.

The sort-out process for the exclusion of images can be **randomly** or **distinctive**, e.g. a relatively simple indistinctive approach could eliminate every x-th image of the data-set, while a more complex approach could be based on specific interrelations between images. The latter could focus on the elimination of redundant information within the data-set. The degree of redundancy of images increases the more the following three **distinctive** criteria are fulfilled at the same time:

**Criteria 1:** The closer the camera position is between individual images, see fig. 5.1 b)

**Criteria 2:** The more camera normal vectors for individual images match up, see fig. 5.1 b)

**Criteria 3:** The more similar features were detected in individual images, see fig. 5.1 c)

This filter gets especially necessary when having a slow and steady part within the flight route, e.g. during the climb of the UAV. For CESA-1-2020, for more than 60 images the UAV is in climb without changing the viewing direction. As a result, practically all images are the same.

A **random** deletion of images is done through applying one of the following filters:

- reduction of the analyzed field area<sup>1</sup>, s. fig. 5.1 a)
- only focus on such images, where certain heliostats (and their respective feature detections) have been detected on (e.g. FDM heliostats)
- selection of every x-th image of data-set

---

<sup>1</sup>A reduction of 50% means, that length and width of the heliostat field each are being halved. The new rectangular heliostat field area is centered at the midpoint of the heliostat field, and the top and bottom edges are parallel to the east-west placement direction of the heliostats. A factor of 50% reduces the number of heliostats by 78% to 97. These 97 heliostats are now only seen in 900 images (-56%).

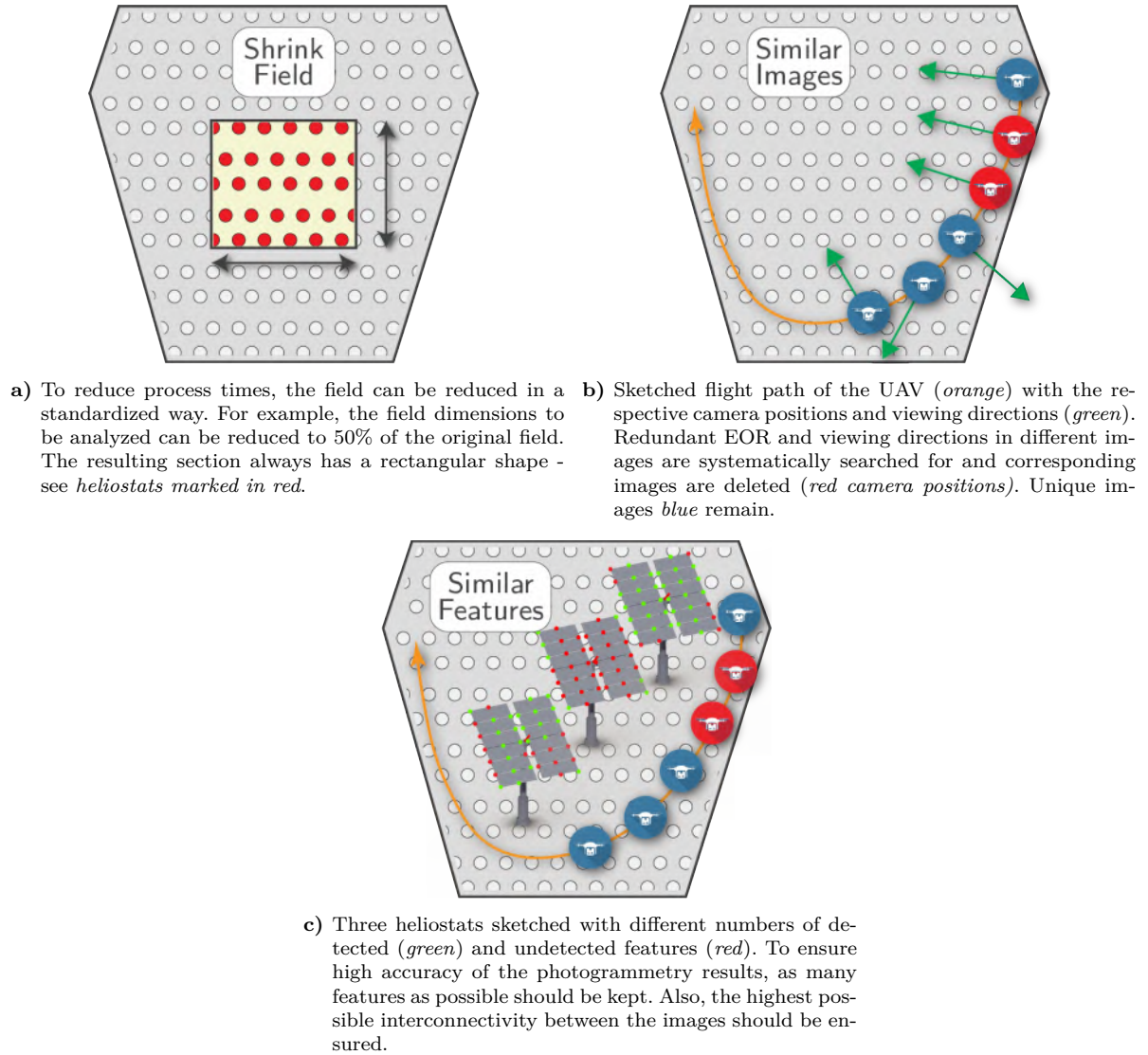


Figure 5.1: CESA-1 schematically shown. Selection mechanisms for image reduction in AICON.

### 5.1.2 Image quality

Quality parameters such as the number of detected features per image can be included in the image selection. While the in section 5.1.1 mentioned sort-out process of images checks the interrelations between images (or is random), the quality parameters are dealing with the individual image concerning the following aspects:

**Parameter 1: Area covered on image by detections.** — A polygon is set around all detected features on the image. The ratio of the polygon area compared to the whole image equals the final quality parameter (concept shown in fig. 5.2 a)). Therefore, images that would show just a fraction of the heliostat field, but a large portion of plant site, meadow, ground or other surroundings, are

spared. The parameter gets calculated as

$$Q_1 = \frac{area_{polygon}}{area_{image}} \quad (5.1)$$

- Parameter 2: Quantity of detections on image.** — The quantity of detections.
- Parameter 3: Distance of each detection to camera.** — Each detection has a unique distance to the camera position. The farther away, the more inaccurate the detection gets as an error in pixel results in a larger XYZ error compare to detections closer to the EOR (concept shown in fig. 5.2 c)).
- Parameter 4: Quantity of heliostats on image.** — This parameter is mixed up by criteria 1 and criteria 3 (concept shown in fig. 5.2 d)).
- Parameter 5: Covered area of heliostats on image.** — This focuses on the area of heliostats on the actual XY-plane that have detections, judged by their center positions (concept shown in fig. 5.2 e)).
- Parameter 6: Homogeneous distribution of features on image.** — a large covered area of detections doesn't ensure a large quantity of detections within the image. The image is divided into a 6x6 raster, which makes for a distribution map as shown in fig. 5.11. The number of features doesn't have to be high, as long as the area on the image is large. This is beneficial to minimize the uncertainty of pixel-resolution, the smaller the actual covered XY-area is (concept shown in fig. 5.2 f)).
- Parameter 7: Quality of individual detections and detection sets per heliostat.** — With a ZA calculation using all detected features from FD as input instead of running the regular image recognition for outer corners, that about 40% of the features have not been used for calculating the ZA orientation. This indicates, that sparing all these detections might not only give significant relief to performance, but also improve accuracy of PG. Another way to classify this parameter is through the distance of every feature to the heliostat center and distance of feature to each other.

Through testing an optimal parameter-set can be found. However, due to timely constraints this has not been part of this thesis.

### 5.1.3 Keeping most distinct detections for each feature

The more often a characteristic point is found in different images, the better this point makes for an interrelation of all images, and therefore the photogrammetric result. One feature is detected more often than another feature, as fig. 5.9 shows. In the CESA-1-2020 measurement, a distinct feature was detected 175 times on average. In 2% of the cases, features get detected more than 500 times. On the other hand, over 900 features (11%) are detected less than 10 times.

The goal is to exclude barely seen features entirely, and reduce the amount of detections per

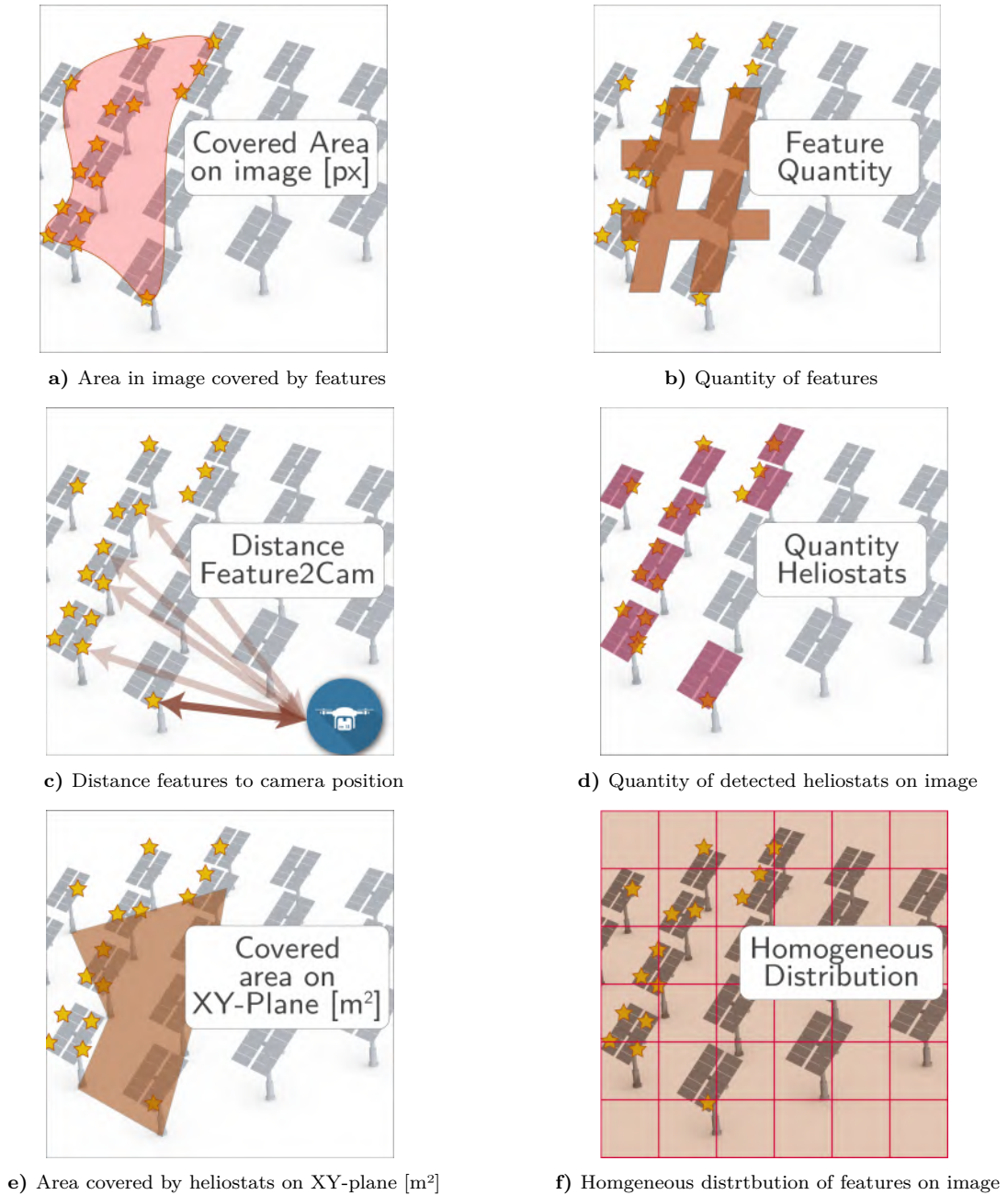


**Figure 5.2:** Overview over the different quality parameters used to determine which images are to be discarded, and which are used for phc-file generation. Every quality parameter is related to the features being detected in the image.

feature to a fixed value by keeping the best detections.

**Reduce quantity of detections per feature to a certain value by choosing max. different EORs.** With more than 500 detections per feature, it is appropriate to reduce the detection quantities rigorously. The goal with large data-sets is to get a fast, yet accurate computation of orientations. Computation times of less than an hour are realistic, whereas the original data-set would take several weeks to compute.

The goal of this reduction process is to find the optimal combination of a given number of camera EOR and viewing directions per feature. A number of about 15 detections are sufficient from a photogrammetric point of view. In the input dataset, 1172 of the 8509 features were detected less than 15 times. For the remaining features, this should result in a total number of points of about 110,000.

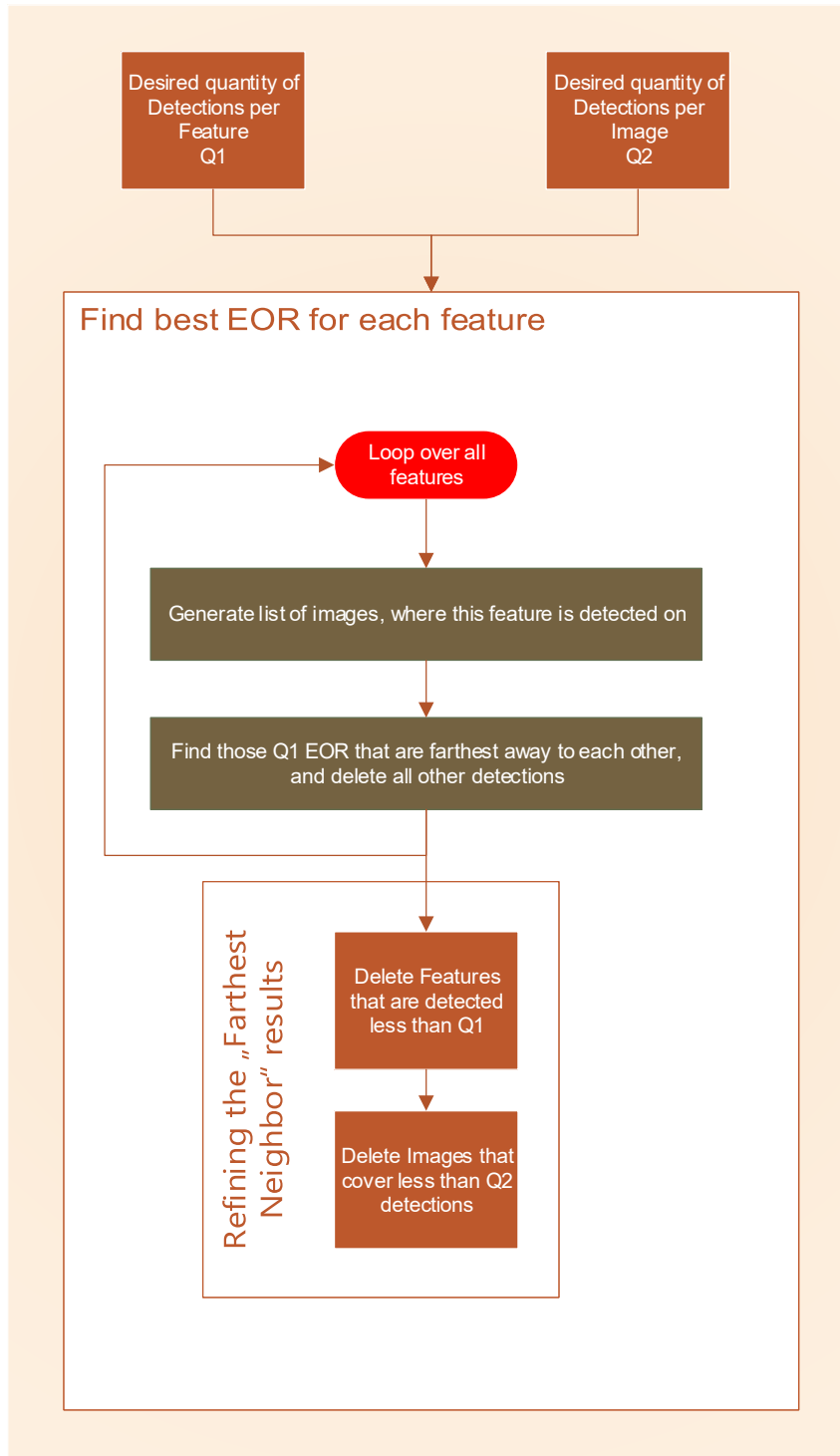


**Figure 5.3:** Flowchart for “*Farthest Neighbors*”-algorithm

A flowchart for this can be seen in fig. 5.3. Each feature is considered individually. Connecting the camera positions of the individual positions to the feature results in a cone-shaped construct of several hundred vectors, cf. fig. 5.4. The first approach is to find an optimization process that computes the desired number of vectors with the maximum different viewing directions – i.e. maximum different angles to each other. For those chosen vectors, the smallest angle to its neighbor is noted for each vector, and then these angles are summed up. With an ideal distributed set of vectors, a maximum angle sum of  $360^\circ$  can result. This is also the optimization goal. Under real conditions, however, this cannot be achieved for several reasons: Since the UAV is constantly several tens of meters above the heliostats (with the exception of takeoff and landing, where the heliostats in the first row can be captured), the vectors are always forming that previously mentioned cone shape. Therefore, after 5000 iterations the optimization process is automatically aborted.

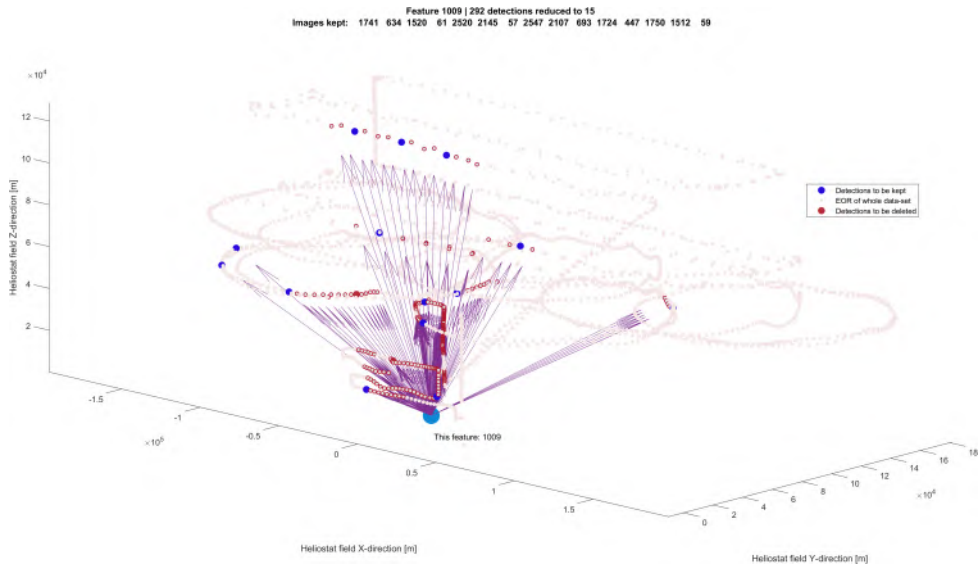


**Figure 5.4:** Feature 1009, CESA-1-2020: The 15 most distinct detections (*blue*) are kept, all the other detections (*red*) are deleted

**The “*Farthest Neighbors*”-algorithm.** Due to the complexity of this algorithm, a different approach is followed. Instead of finding the most distinct viewing directions, the farthest camera positions are detected. This “*Farthest Neighbors*”-algorithm detects the EORs that are maximally far away from each other [73]. To do this, the EOR farthest from the feature<sup>2</sup>, is chosen as the starting point. Then, the EOR with the farthest distance to the starting point is selected and added to the solution set. The distance between two EOR points  $EOR_1$  ( $X = 29658$  mm,  $Y = 12941$  mm,  $Z = 36629$  mm) and  $EOR_2$  ( $X = -580$  mm,  $Y = 9635$  mm,  $Z = 12224$  mm) in

<sup>2</sup>or the EOR whose image has the most detections – this is currently a two-way option

space is calculated to be

$$\|v\| = \sqrt{\sum_{k=1}^N |v_k|^2} \quad (5.2)$$

$$\|v\| = \sqrt{|EOR_1 - EOR_2|^2} = 124460 \text{ mm} = 124,4 \text{ m.}$$

Points are added to the solution set until the desired number of remaining detections per feature is reached. All the other detections are then deleted from the respective images. As an example, the optimization result for feature 1009 is shown in fig. 5.4.

The “*Farthest Neighbors*”-algorithm reduces the 1489190 detections of 8509 features to 116716 detections, while maintaining the number of features. This is 13.7 detections per feature on average, which is due to the fact that some features were detected significantly less often than 15 times, cf. histogram fig. 5.5. Also, several hundred images are currently in the data-set with just a few detections found in them, cf. fig. 5.5 b).

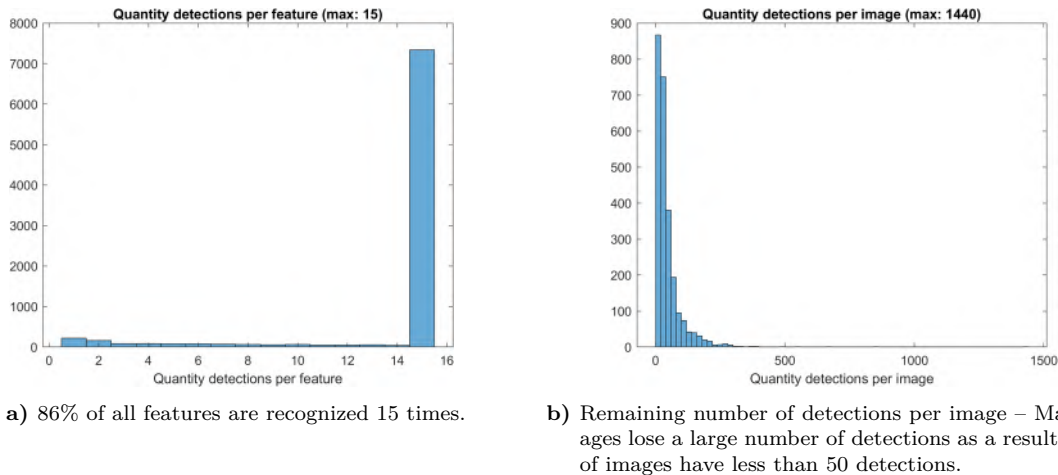


**Figure 5.5:** Results after applying the “*Farthest Neighbors*”-algorithm.

To refine the results derived from the “*Farthest Neighbors*”-algorithm, a two-stage filtering is performed. First, features that have less than a certain number of detections are eliminated, cf. fig. 5.6. It can be seen that these are mainly detections in the back of the field, and those are eliminated completely through this filter. 110055 detections remain in the data set. Subsequently, those images that have less than 10 detections are deleted. In the course of this, 458 images are deleted and 2095 images remain in the data set. This leaves 7337 unique features in the dataset. Finally, features with very few detections created by deleting several hundred images before, are deleted additionally. The original threshold value of allowed detections per feature is multiplied by 2/3, to not lose a large number of features. Again 17 features with all their detections are deleted, whereupon now 107698 detections of 7320 features remain in the data set. The minimum

number of remaining detections per image is 8. The final result is shown in fig. 5.7.

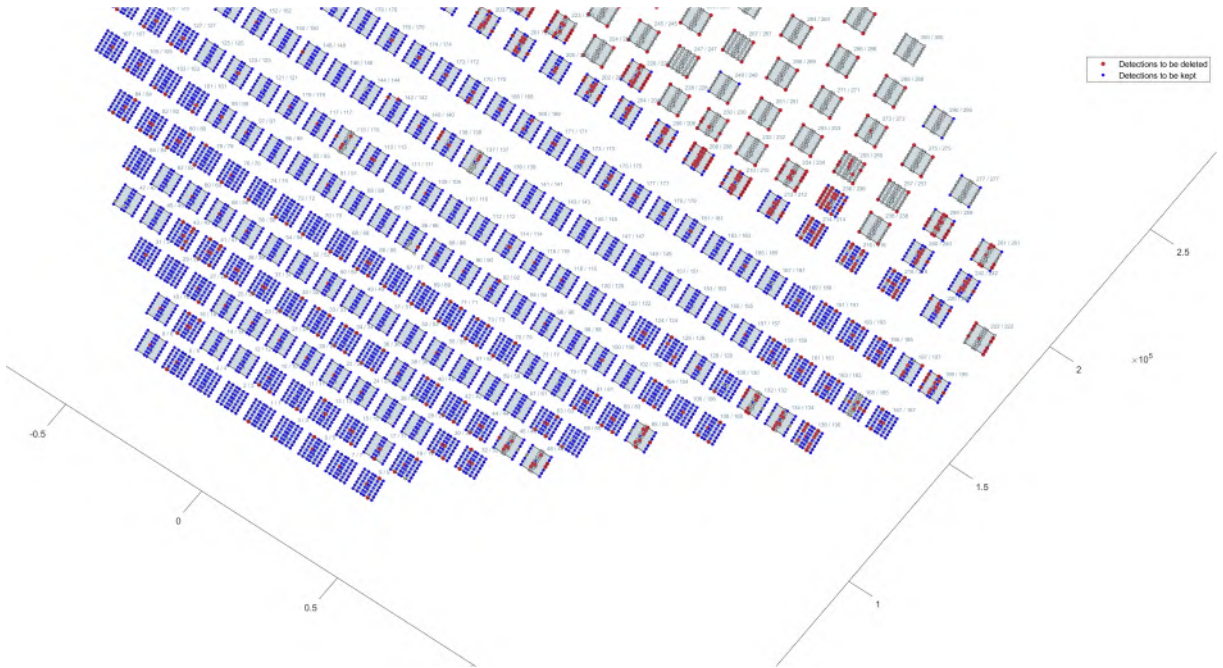


**Figure 5.6:** Delete features and all their detections: *red* features are deleted, the *blue* ones are kept

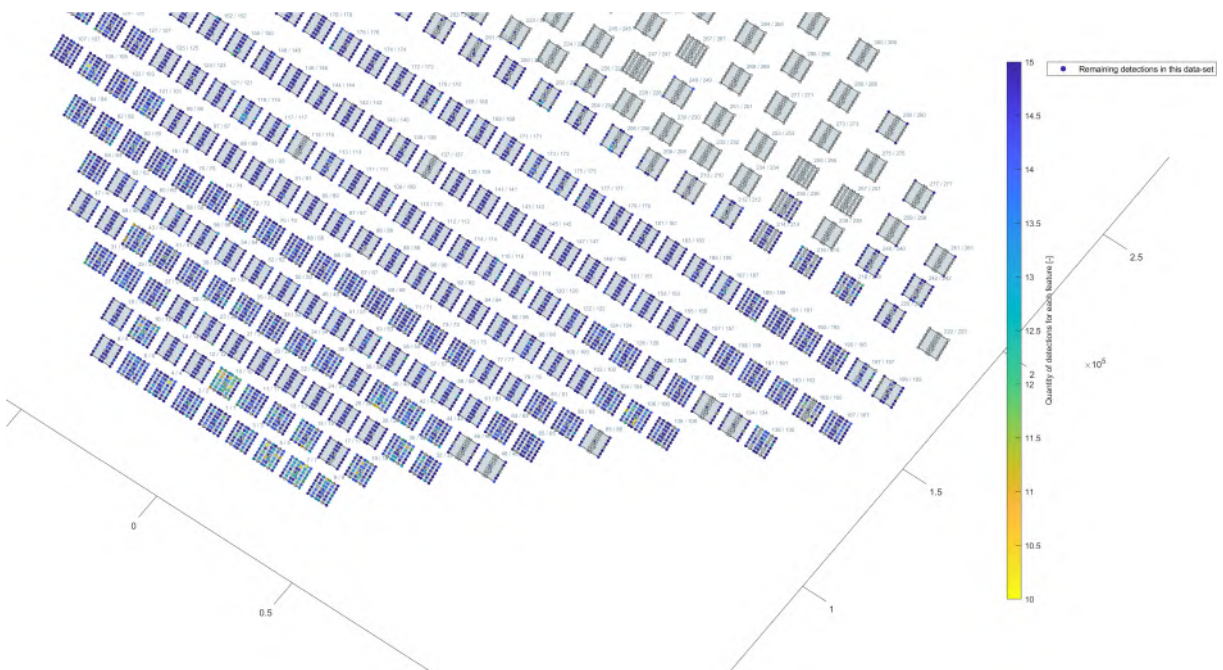


**Figure 5.7:** Features eventually staying in dataset, with colormapping. The majority of features is detected 15 times (*blue features*), and the minimum quantity is 10 (*yellow features*).

The interconnectedness and processing time need to be validated, whether this approach succeeds in computing more orientations than currently achieved in the photogrammetric step, where

about 10% of FDM heliostats weren't successfully aligned in order to achieve an orientation.

## 5.2 Experimental setup and testing

The previous calculations lead to the fact that a basic case with only the outer corners is provided for the test. In the [June AICON calculations], average computational durations of 12 hours could be obtained, with an average of 100,000 features in about 1000 frames. In contrast, the original PG calculations for the 2020 measurements showed that due to the high feature count per image (because of the high flight altitude and the nadir images) a significantly longer phc-file is generated (800,000 lines) than e.g. still in the 2018 measurement (400,000) lines, which is why calculation durations of 1-2 weeks were incurred.

### 5.2.1 Defining a base model

Considering the test scope of over 40 trials, the detected features are therefore reduced to the outer corners, cf. fig. 5.8. For image 680, the feature count was significantly reduced by eliminating all features except the outer corners from the dataset. This results in 72% fewer features in this image. Across all images, this filter can reduce the feature count by -79% (from 1,489,190 to 308,256 features).

Statistics on the base case, cf. fig. 5.18 b):

- calculated 02:11 h in AICON
- 802 images, 164013 detections in .phc-file
- filter: corners and centers
- 1227 unique features
- 134 detections on average
- maximum 561 detections per feature
- > 500 detections: 11 features
- > 300 detections: 144 features
- < 20 detections: 245 features

The number of images is also to be initially reduced on the data set generated in this way. For this reason, four heliostats are selected (heliostat numbers (CESA-1): 69, 71, 73, 75), for which FDM references are available and which have always been recognized in previous PG calculations. This allows a good comparability of the individual test series to be ensured. For this purpose, all images are discarded on which no features (in this case outer corners) of the considered heliostats have been detected.

This results in an initial (base) data set with 809 images and 164,012 features. The histogram in fig. 5.9 shows the distribution of the number of features across the images. For comparison,

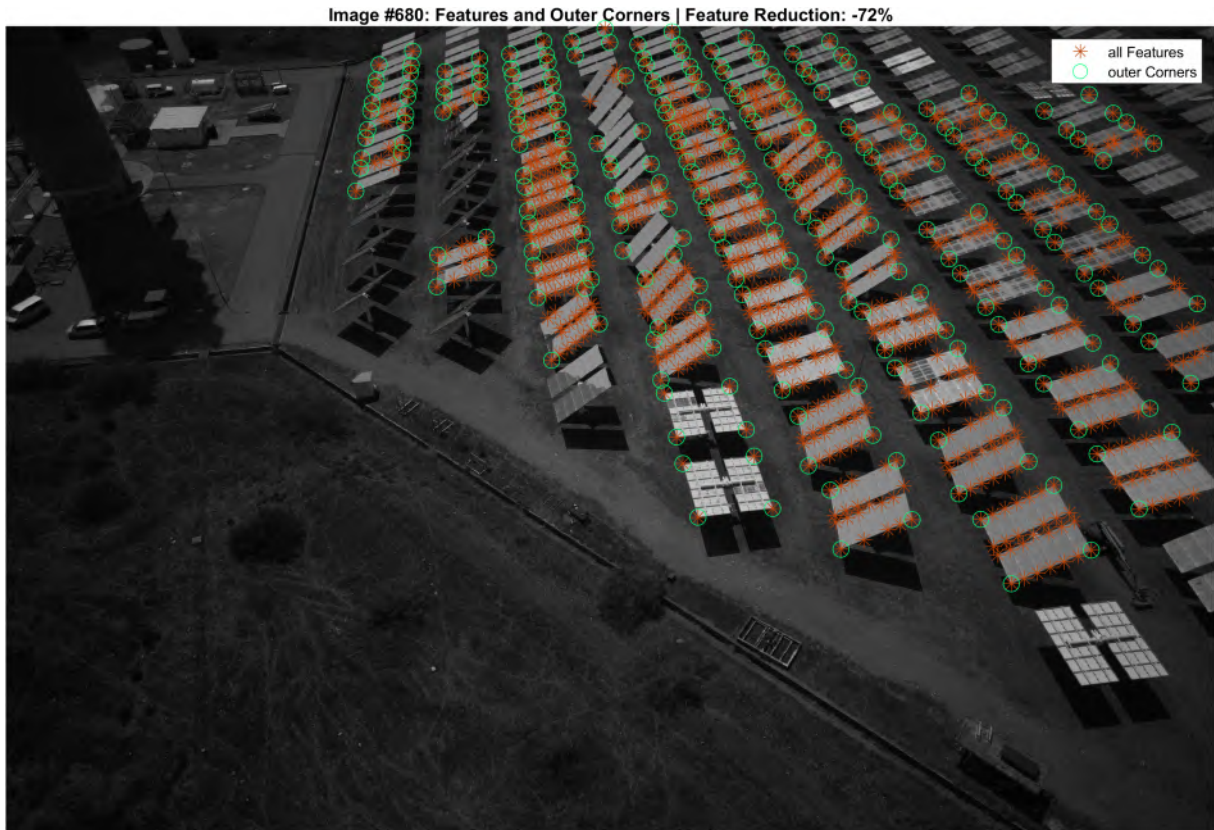


**Figure 5.8:** Reduktion der Features grafisch überlagert mit RGB-Bild, Bild-Nr 680, Datensatz *CESA-1-2020*

a histogram is also shown for the dataset that was only reduced by the images, but not by features, as well as a histogram over the raw dataset.

From the 114 heliostats which have been transferred to AICON, the orientations can be calculated only for 34 heliostats. No result is delivered for any of the reference FDM heliostats. Therefore it is not possible to compare subsequent AICON image reduction tests with their actual orientations. For an orientation to be calculated, at least 4 points are necessary. If you now compare the heliostat alignment instead, the different error sources mix and possibly offset each other and thus give a wrong result. In any case, a comparison with the FDM would not have been useful at this point. The present result from AICON is a point cloud, which would first have to be transferred to the Matlab 3D model. This process in itself again has sources of error. In order to completely evaluate the image and detection reduction, one has to observe how the point cloud changes when images are omitted. For this reason it makes more sense to compare only the original feature XYZ coordinates and estimated uncertainties from AICON.

### 5.2.2 Running .phc-files in AICON

To run all the .phc-files automatically in AICON, a script is written. Even in case of errors, which can occur in AICON when the input data is low quality, the script continues with the next .phc-file. Intermediate steps, required computing times and final results are stored in a

**Table 5.1:** Test specifications of individual data-sets (phc-files) to analyze computing performance and deviations to base model in AICON

Label	Short description	Specifications	Quantity images	Quantity detections
AR_stepped	Every xth image is taken as phc-input	Take every 0.45, 0.3, 0.24, 0.1, 0.01, 2, 3, 4, 5, 6, 7, 8, 9, 10, 15, 20, 30 [th] image. Overall quantity of test runs: 14	405, 270, 203, 162, 135, 116, 102, 90, 81, 445, 566, 615, 728, 800	82318, 54490, 41157, 32656, 27199, 23525, 20908, 18319, 15997, 10940, 8233, 5351, 90729, 114789, 124407, 148017, 161988
AR_percent	If consecutive images have similar detections (not to number, but to the actual unique features detected in this image) compared to the one currently observed, these images are sort out	Congruence of detected features in consecutive image(s): 99, 98, 97, 96, 95, 92, 89, 86.5, 80, 72 [%]. Overall quantity of test runs: 8	802, 779, 725, 681, 618, 467, 358, 276	162707, 157218, 145489, 135125, 120190, 88144, 65636, 49768
AR_area	Quality parameter Q1: if less than a certain area covered by features on image, then image is sort out	Ratio of image covered by features: 0.2, 0.3, 0.35, 0.4, 0.45, 0.5, 0.55, 0.6, 0.65, 0.7, 0.75. Overall quantity of test runs: 11	800, 736, 649, 597, 567, 499, 415, 329, 243, 155, 74	162435, 152158, 135490, 123812, 117244, 103999, 88313, 70496, 52715, 35081, 19605
AR_fullfilter	1) Full filter: If several images adhere to the following three criteria, the image with most detections is kept, the others are discarded: EOR closer than certain value Viewing direction more similar than certain angle Similarity of detections (same as AICONRED_percent) larger than certain threshold	Combinations of close EOR [m], similar viewing direction [°] and similar detected features in other image throughout the field [30, 15, 0.7; ... 10, 2, 0.5; ... 2, 10, 0.5; ... 5, 10, 0.5; ... 2, 2, 0.7; ... 2, 5, 0.7; ... 5, 5, 0.7; ... 10, 10, 0.7; ... 0.1, 0.1, 0.9; ... 1, 1, 0.9; ... 0.5, 0.5, 0.9]. Overall quantity of test runs: 11	108, 524, 402, 219, 570, 441, 281, 157, 807, 666, 727	25017, 116199, 95001, 52817, 123840, 102677, 65242, 36132, 163673, 139601, 150393

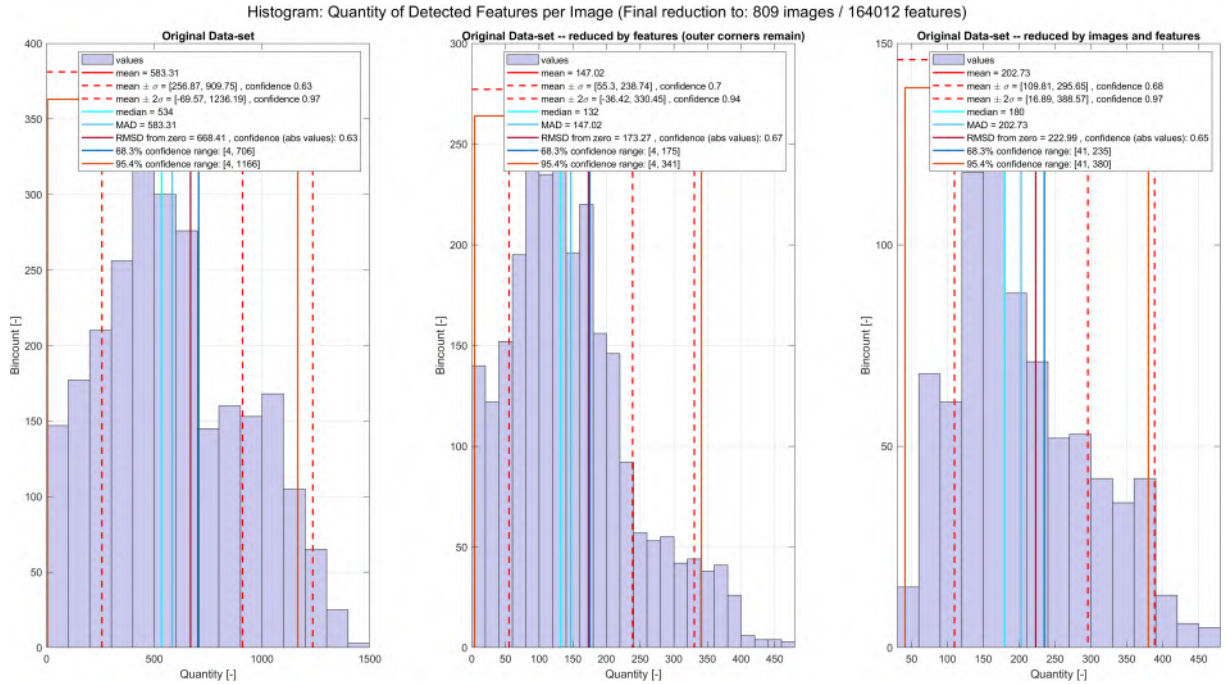


**Figure 5.9:** dataset reduced based on four selected FDM heliostats (69, 71, 73, 75) in two-step process: 1) eliminate features, 2) discard unusable images

process-safe and traceable way.

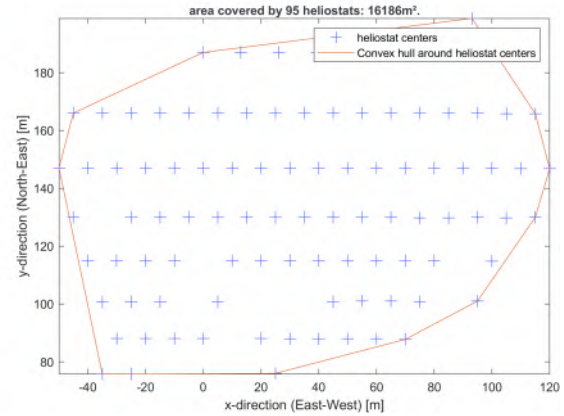
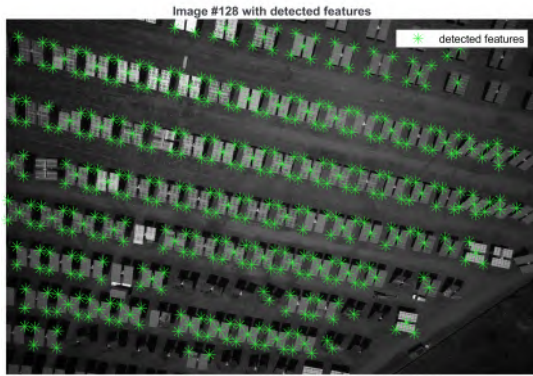
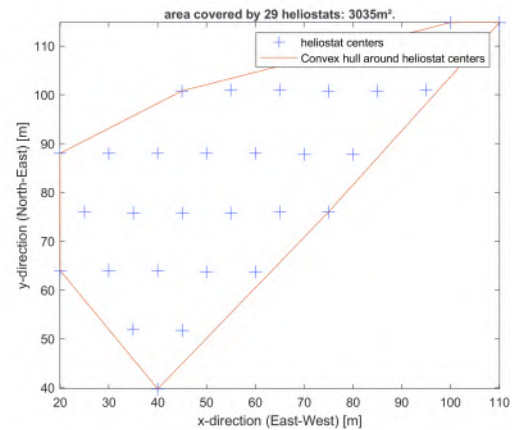
In the second part of the script *scriptPHCFileCalculationInAICON* the results are now evaluated. First the Aicon results are read as *.htm*-files. Afterwards a transformation of the currently still random values to the reference coordinate of the base data set is performed, cf. fig. 5.19.

### 5.3 Results

Already when looking at the minimum calculated number of images, it can be seen that logical filtering also works with a lower number of images. Aicon terminates earlier with the two random test series (stepped images: 81 images, percent: 145 images), while the case with 74 images is still calculated without errors with the logical filtering according to area in the image.

**Consecutive C1: feature detection equivalence.** Out of 10 *.phc*-files, 8 have been successfully calculated in Aicon. For the cases with 145 and 86 images, *htm-bundle*-files were created, but the data was still faulty (EOR block not found).

**Quality Q1: area of features.** Out of 11 *.phc*-files, 11 have been successfully calculated in Aicon. For the case with 33 images, the *htm-bundle*-file was created, but the data was still faulty (EOR block not found).

Image #128: 16186m<sup>2</sup>a) Image #128 (dataset *CESA-1-2020*): Area is big enough (good image) –  $k_1 = 16,186m^2$ Image #49: 3035m<sup>2</sup>b) Image #49 (dataset *CESA-1-2020*): Area is too small (bad image) –  $k_1 = 3035m^2$ 

**Figure 5.10:** Distribution of feature detections on image in a *good* (fig. 5.10 a)) and a *bad* (fig. 5.10 b)) case. Left side showing original image overlaid with detected features. On the right, showing XY-PLANE with heliostat centers, surrounded by an envelope curve. The covered area is displayed on each image. Threshold  $k_{1,TS} = 3000m^2$ .

**Consecutive C1: every xth image.** Out of 17 *.phc*-files, 14 have been successfully calculated in Aicon.

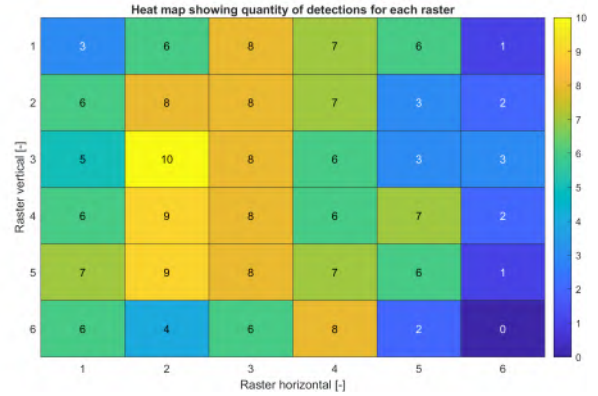
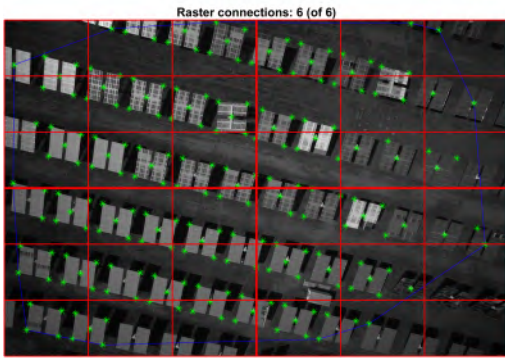
**Combined filter: EOR, viewing direction and feature detection equivalence.** Out of 11 *.phc*-files, 11 have been successfully calculated in Aicon.

**out images based on consecutive and intra-image features.** Via a loop, all images of the base dataset are examined in sequence. First a plot is made, cf. fig. 5.13, on which the original image is overlaid with all detected features. In the image shown, it is already apparent that the heliostats actually under consideration are only marginally detected; in fact, only heliostat 75 has two feature detections. However, this is not analyzed in the context of the characteristic



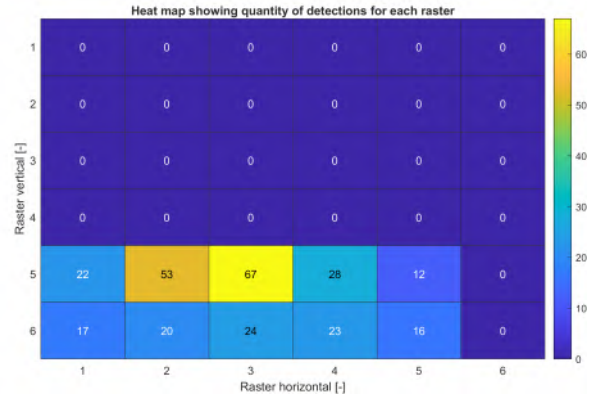
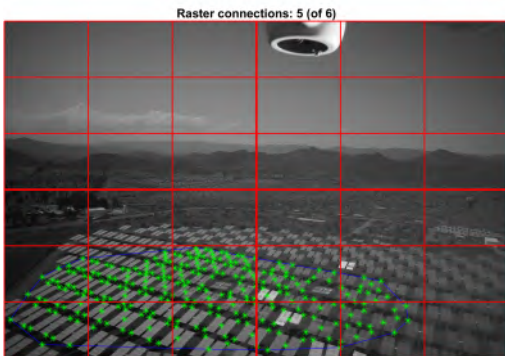
a) Beneficial feature distribution on image

Image #2524: spacial distribution (0.67)



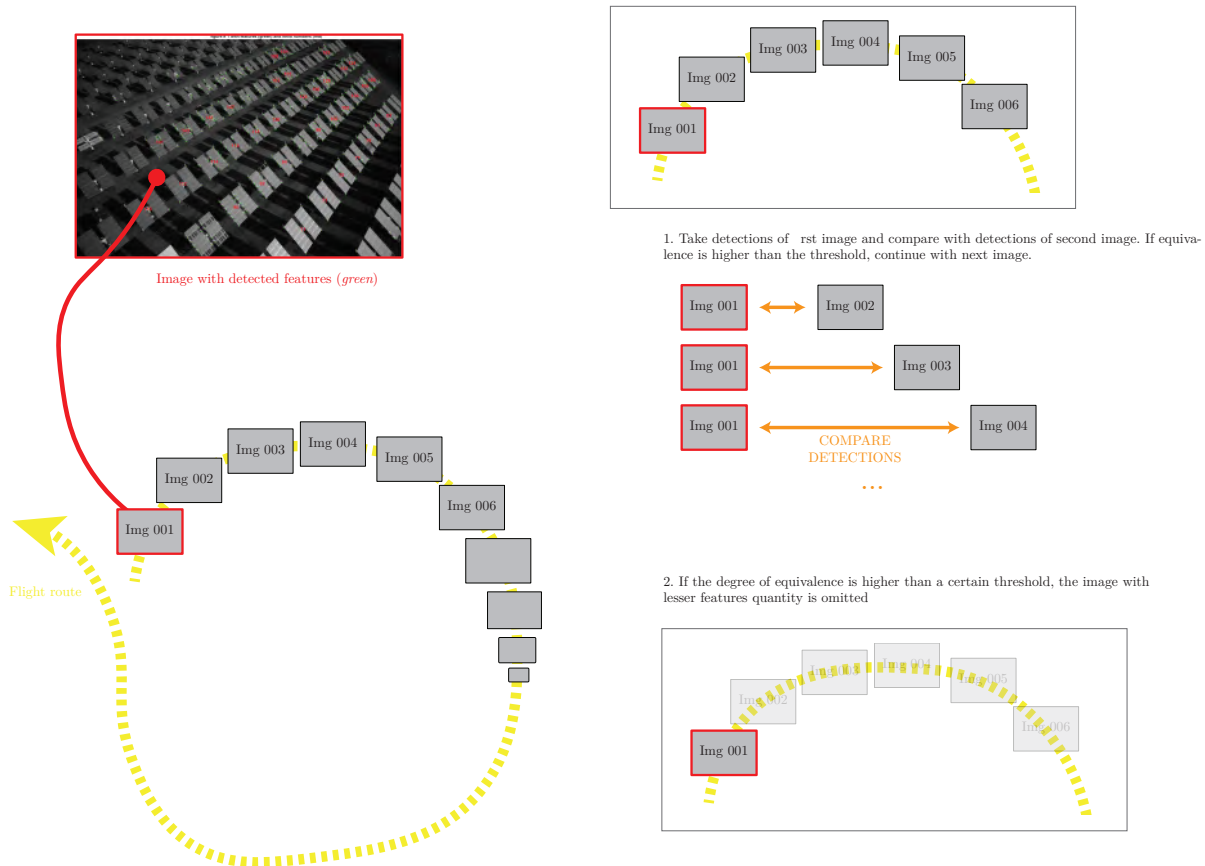
b) Image 2524 (dataset *CESA-1-2020*), high distribution-parameter of 0.67. Showing equal distribution of feature detections except right image border.

Image #2036: spacial distribution (0.06)



c) Image 2036 (dataset *CESA-1-2020*), low distribution-parameter of 0.06. Showing high distribution in the lower-center of the image. On the other hand, this image covers a large area and includes a large number of detected heliostats, which is beneficial, and is therefore not generally discarded – more about this below section 5.4

**Figure 5.11:** Distribution of feature detections on image in a *good* fig. 5.11 b) and a *bad* fig. 5.11 c) case. Left side showing original image overlaid with raster and envelope curve. Right showing feature distribution heat map, color grading shows the intensity of features. Images rastered 6x6. The distribution value is displayed on each image. Threshold  $k_{2,TS} = 0.25[-]$ .



**Figure 5.12:** Similar detections in consecutive images

values shown in the following. Because from a photogrammetric point of view this would not have a negative effect in principle, as long as in many other images all of the features contained here were recognized.

First, images are compared with each other in general. For this, the EOR information, viewing direction as well as the detected features are compared. In fig. 5.14 such a comparison is shown. Due to the quality parameters (see below), image #49 does not carry any significant new information for the photogrammetry calculation. Instead, as an additional image, it would only slow down the computation process. For image #49 there is altogether only one additional image to which all three quality parameters apply (image #50). It becomes more interesting e.g. with image #456: Here there are 28 further images which are similar to image #456. From all similar images, the image on which the most features are detected is selected in each loop cycle; The remaining images are deleted. Considering the parameter set Q1 mentioned in tab. 2.12 b), only 145 images remain in the dataset.

A comparison overview is shown in fig. 5.15. It can be seen here that a very homogeneous distribution of the images can be realized, which is why the parameter set Q1 is found to be good for the time being. It is different with the parameter set Q2.

For instance, a set of the three parameter could look like this:



**Figure 5.13:** State before reduction process sets in – in this case: Image 49, Data-Set *CESA-1-2020*, 110 corner and center features still left in this image

**Quality Parameter 1:** Distance between camera positions of two images larger than 20m

**Quality Parameter 2:** Angle between camera viewing directions larger than 3 deg

**Quality Parameter 3:** Feature equivalence less than 80%

All parameter sets are listed in tab. 5.1.

Discussion always addresses these points for the performance in AICON.

**Discussion Criteria 1:** calculation time

**Discussion Criteria 2:** deviation to base model

**Discussion Criteria 3:** quantity remaining EOR

**Discussion Criteria 4:** quantity remaining features

The whole testing took 62 hours of calculation time in AICON alone, see tab. 5.1.

The following question are to be addressed during the testing:

- Which reduction method improves the calculation performance?
- Which reduction method has more influence than others?
- Which combination of reduction method makes sense?
- Does it always provide the best results, when you apply a mix of reduction methods derived from all levels?

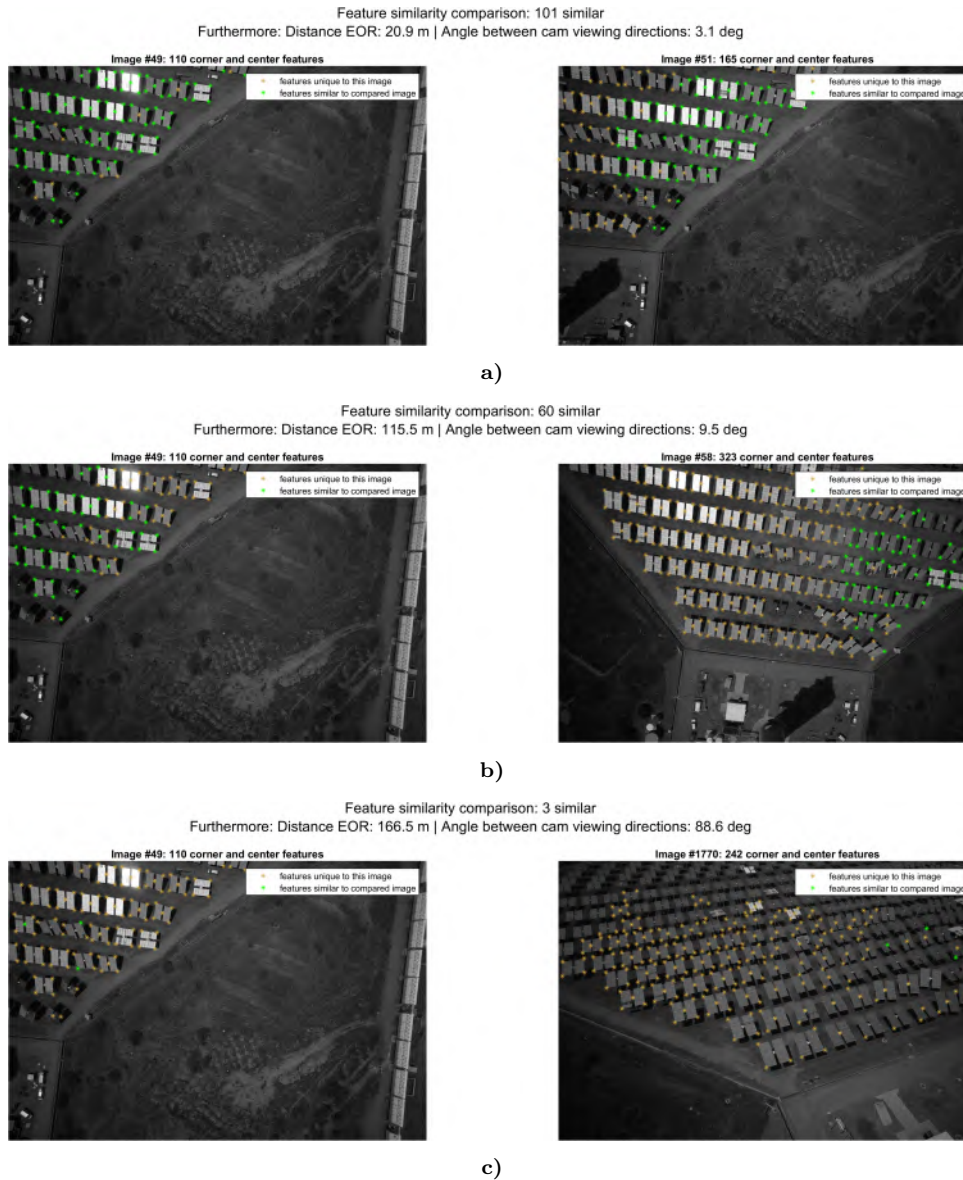


**Figure 5.14:** Comparing two images with each other (in this case: Image 49 (left) and image 51 (right)). 101 Features are similar in both images, which equivalents to 91%. The EOR of both images differs to 20.9 m in distance and 3.1 deg in angle.

- Which parameter / threshold for every reduction method works best?

In Matlab, an EOR structure, i.e. a collection of images and detected features, is used to create a phc-file for photogrammetry calculation. Here it is interesting to follow how many unique features are given as input data to AICON, and how many can finally be assigned in the photogrammetry. In fact, many features remain unconsidered. This has the following reason: To photogrammetrize an object well, it has to be photographed from as many different directions as possible. This is not true for the heliostats in the back of the field – all photographs are either from south or nadir. On the other hand, the features in the front part of the field are observed from various directions. This situation is illustrated in fig. 5.17. Heliostat centers also often remain without

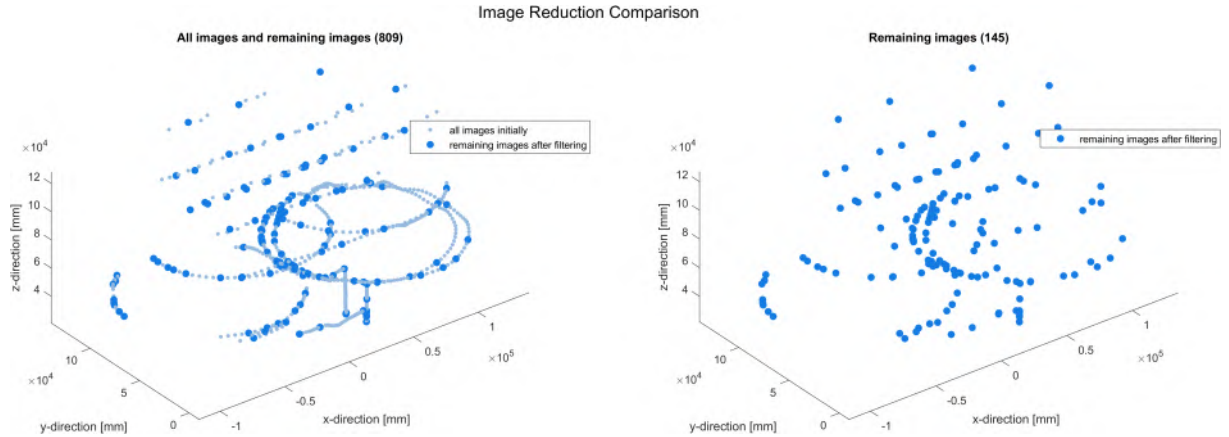


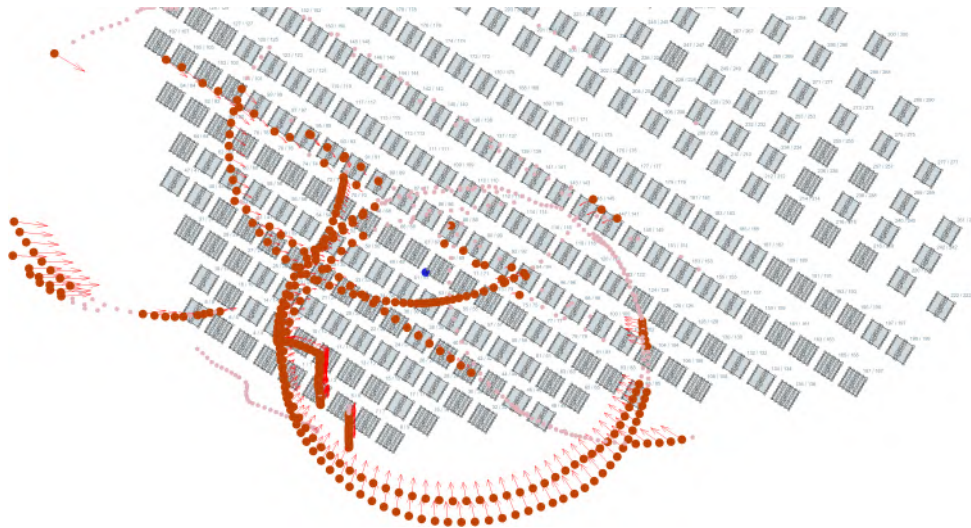
**Figure 5.15:** Reduction of images: The base case is shown on the left, with those EOR positions that remain after sorting out highlighted in color. On the left, the remaining camera positions

photogrammetric fitting because they are not regularly detected in the FD, but projected given a sufficiently large number of other feature detections of that heliostat. However, this then leads to increased uncertainties / inconsistencies, which is why the probability of matching in photogrammetry is lower. This issue is illustrated in fig. ??, where a feature located in the front part of the field (fig. 5.16 a)) is shown, as well as one in the back part of the field (fig. 5.16 b)).

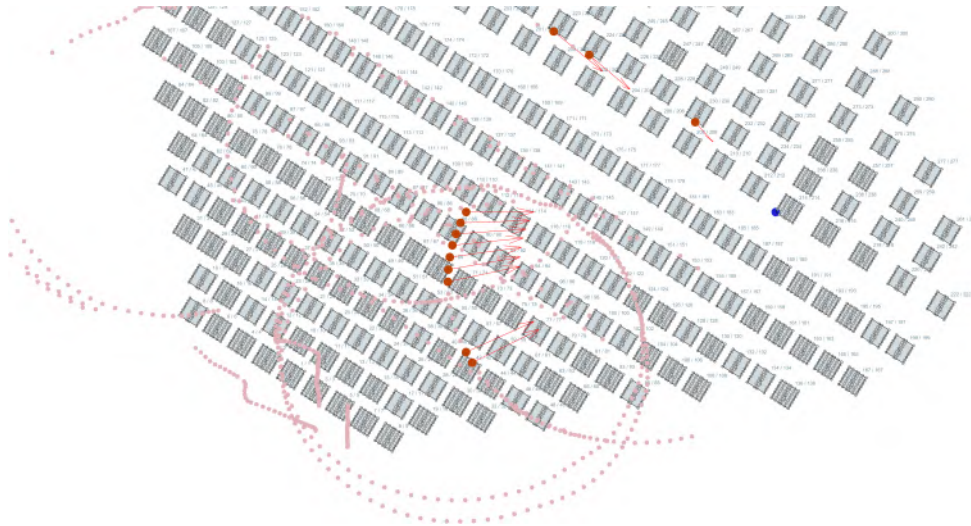
The phc-file for the “AICONRED\_fullfilter”-727 images photogrammetry calculation contains 1227 unique features and 150392 detections, cf. fig. 5.17 b), *left page*. A high concentration is seen in the front center region of the field, where detections per outer corner/heliostat center of over 400 occur. This is also reflected in the available EOR. Features in the back of the field, on the other hand, were detected less frequently. AICON can match almost any EOR (726 out of 727), which is the default considering the other test series – in 70% of the cases all camera positions can be taken, cf. fig. 5.17 b), *right side*. However, number of detected features has decreased significantly. Only 36% of features (443 out of 1227) are uniquely assigned. Except for two more distant detections in rows 9 and 10, all features are located in the main catchment area of the field.

Despite heavily filtering the images to only 73, there are still 1141 unique features in the data set – only a 7% decrease. Nevertheless, the number of detections drops drastically to 16372 (-89%), cf. fig. 5.17 c), *left page*. Due to the nature of the filter, a very homogeneous camera position distribution can be seen. Partially overlapping EOR are due to nadir and oblique images having nearly the same XY components. However, AICON cannot generate a reasonable photogrammetry result with such a small number of images/detections, cf. fig. 5.17 c), *right side*. Only 5 features are calculated (-99%), with 13 remaining EOR (-18%). So, with such an inferior input dataset, AICON discards a great many images in addition to most features. Furthermore, on closer inspection, one notices that the EOR no longer match the original one.

In fig. 5.19 the base case is shown, and exemplified by the fitting of the 405-image and 116-image test runs of the “AICONRED\_stepped” series, respectively. The plots are shown in detail in



a) Feature 69001 – located in the front center of the field, is seen in 456 images from any direction.



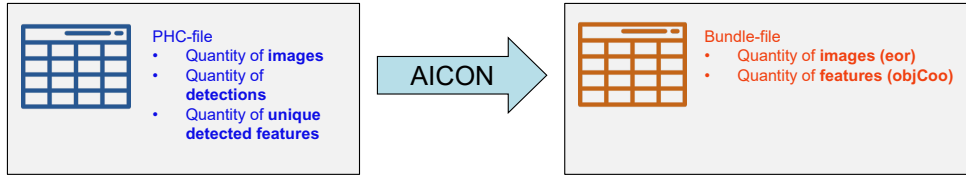
b) Feature 214001 – located in the back of the field, is seen in 12 images from, either coming from southern direction or nadir.

**Figure 5.16:** CESA-1-2020, base model (reduced data-set to 809 images): Viewing directions depending on feature location in field

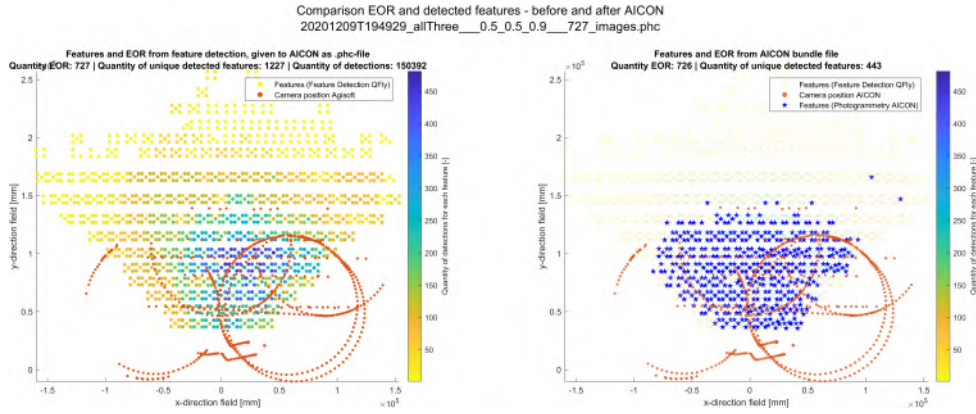
the Appendix, cf. fig. C.14. The plots show the respective residuals, the computation durations in AICON, the number of images passed to AICON via the phc-file, the number of computed features in the base case, and the number of computed features in the test result compared here with the base case, cf. fig. 5.19 a). In the case shown in fig. 5.19 c), 405 images are passed, resulting in only 263 features being detected. The detected pixels deviate by 3.0mm from the reference case. The computation time decreases significantly to only 5 min.

In the case shown in fig. 5.19 b), only 116 images are passed, resulting in only 19 features being detected. The detected image pixels deviate strongly from the reference case (9.6mm RMS). However, the computation time is significantly reduced to only 5 min.

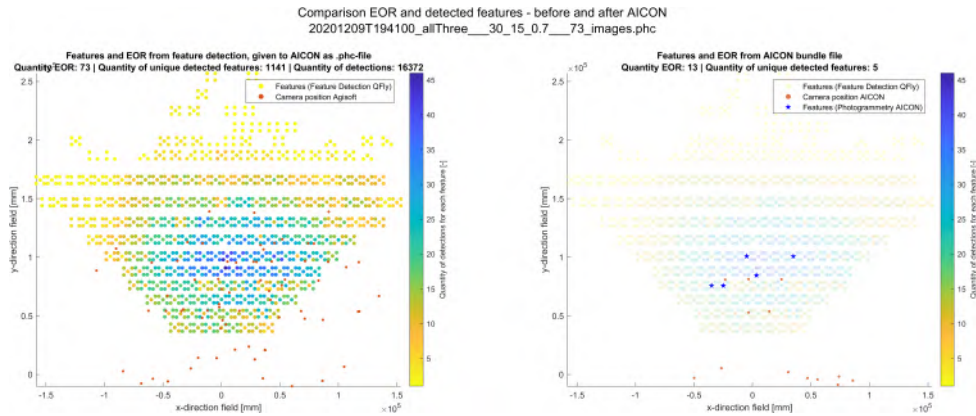
Such comparison (base case with calculated test result) is performed with each photogrammetry



a) Methodology behind this plot



b) 727 images, Filter applied: cartesian appliance 0.5m, angular appliance 0.5°, detection similarity 90%.



c) [73 images, Filter applied: cartesian appliance 30m, angular appliance 15°, detection similarity 70%.

**Figure 5.17:** CESA-1-2020, “AICONRED\_fullfilter”: Comparing input data with AICON results.

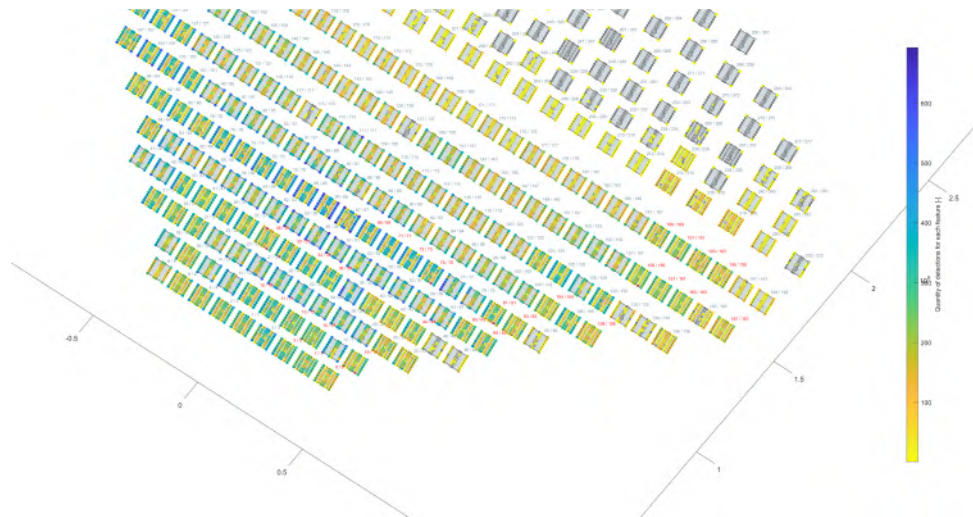
result of the four series, and comparatively discussed in section 5.3.

Specifications on the test runs such as quantity of images or detections are shown in tab. 5.1.

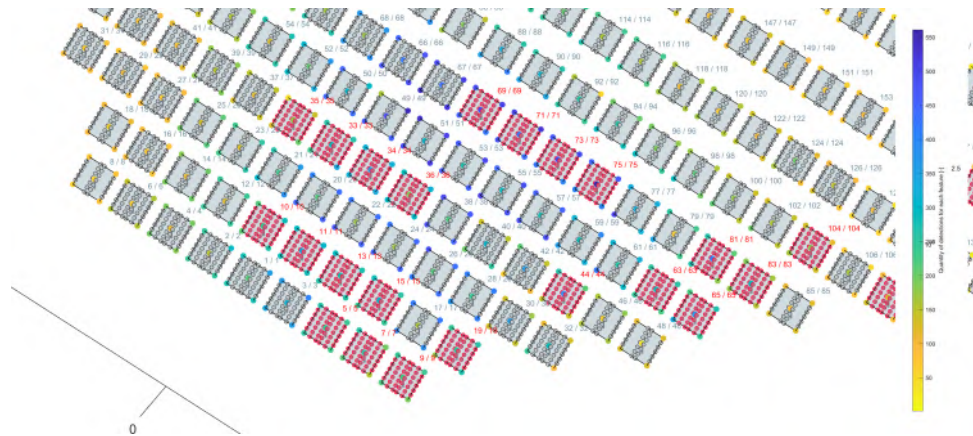
A clear dependency of detections in the input data set and the resulting calculation time in AICON is shown in fig. 5.20. For tests being conducted for this thesis, a maximum number of detections of 400,000 was kept as a preliminary in order to maintain acceptable calculation durations of below 4 hours. AICON calculated about two days<sup>3</sup> for the CESA-1-2018 phc-file. The CESA-1-2020 data-set had first been calculating for over three weeks, before being terminated accidentally through a mandatory restart of the operating system.

To reduce the detections while minimizing the impact on the original data set, those images not

<sup>3</sup>personal conversation with Wilko Jessen



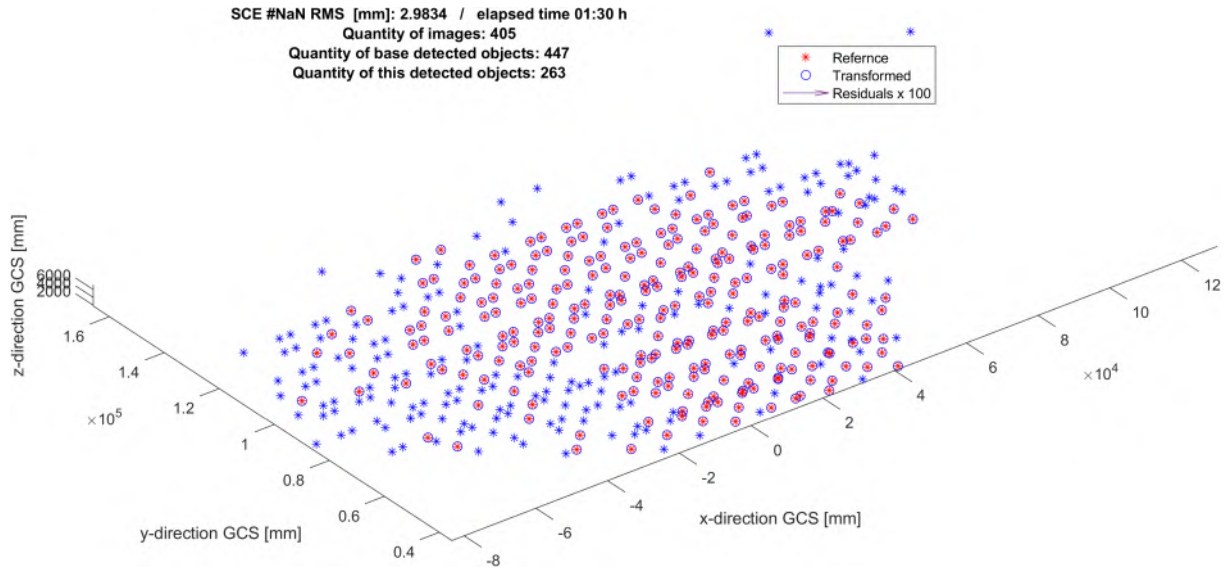
a) Over 1 million points is too much for AICON to calculate photogrammetric result.



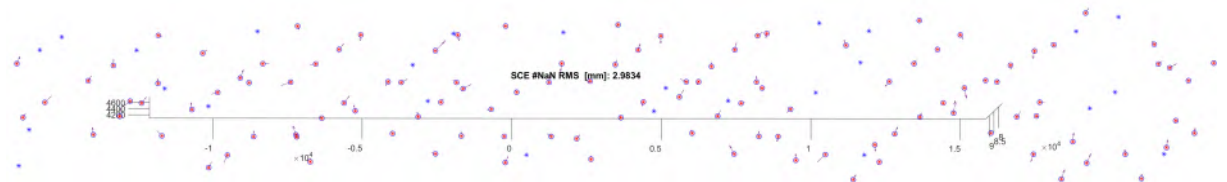
b) Original data-set is reduced to only outer corners and center features, as well as images are discarded where

**Figure 5.18:** CESA-1-2020, color mapping for quantity of detections per feature. FDM heliostats are marked *red*.

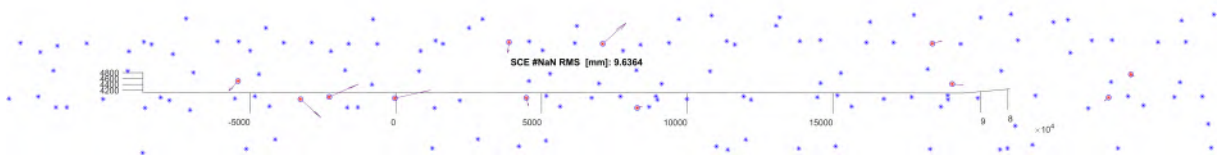
covering any detections of the features of the 31 FDM heliostats as well as neighboring heliostats are discarded, cf. fig. 5.21. This reduces the detection count by 26% to 1,095,475 (if only the 31 FDM heliostats had been taken as the criterion, this would have made only a small difference: 1044315 remaining detections, -30%). The fact that AICON now calculates within ten days is, besides the reduced number of detections, mainly due to the fact that these omitted detections are those in the rear area of the field, which are basically only scatter detections, which are created QFly program-based, but have a much lower quality value and make it more difficult from a photogrammetric point of view to fit the points.



a) 405 images as input in .phc-file. Of originally 447 features, only 263 are aligned correctly in this calculation. The calculation took 1,5 h. In this case the fitting achieves a match of all features below an RMS value of 3.0mm



b) 405 images case – residuals arrows are smaller compared to 116 images



c) 116 images case – residuals arrows are larger. In this case the fitting achieves a match of all features below an RMS value of 9.6mm

**Figure 5.19:** CESA-1-2020, AICON performance testing, “AICONRED\_steped”. Results from AICON. Calculated feature coordinates are fitted onto the coordinates of the reference features. Each plot shows model features are (*blue*), and fitted features (*red*)

## 5.4 Discussion

The plot shows for the four test data sets AICONRED\_steped, AICONRED\_percent, AICONRED\_area and AICONRED\_fullfilter, the respective computation durations in AICON (left y-axis, green), as well as deviations of the 3D fit with respect to the base case (right y-axis, red), over the number of images given as input to AICON. It would be much more useful to complete an AICON run with an FDM comparison, as well as to use a non-prefiltered data set. Comparing the deviation with the base case does not give any indication of the actual deviation to the real orientation. It is assumed that the best orientations would not be calculated with the base case at all. There are too many unwanted detections in the data set for this, which distort the overall fit due to their low interconnectivity potential. However, due to an additional

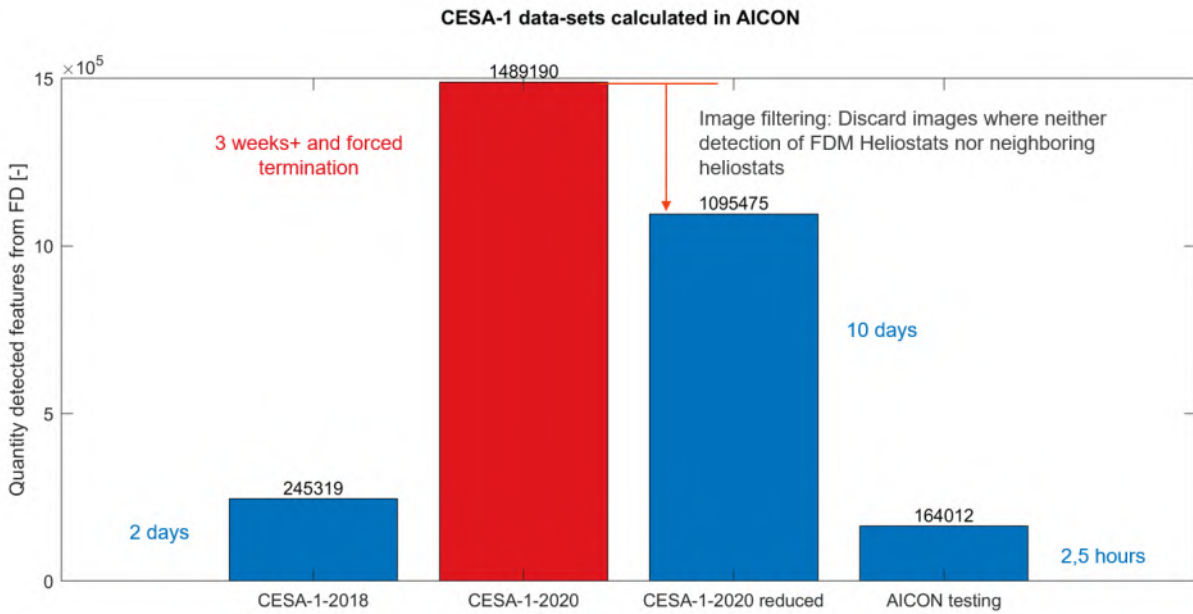


**Figure 5.20:** Barplot showing different data-sets given as .phc-file to AICON. The CESA-1-2020 data-set is marked *red*, as due to too many detections the calculation didn't converge to a sufficient uncertainty.

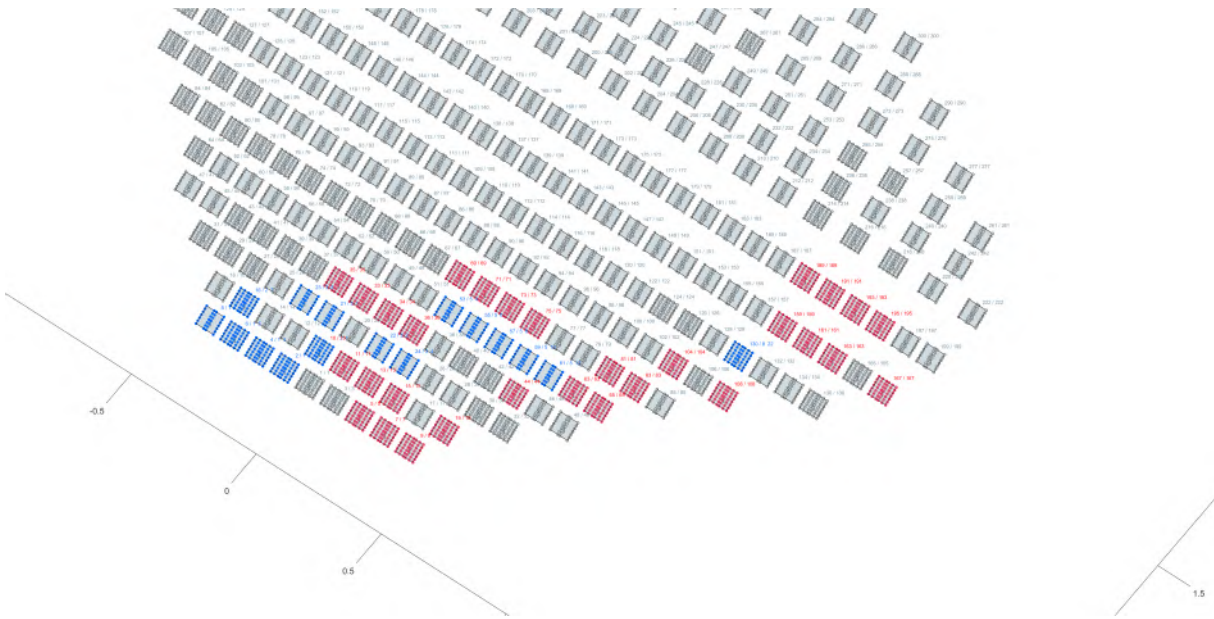


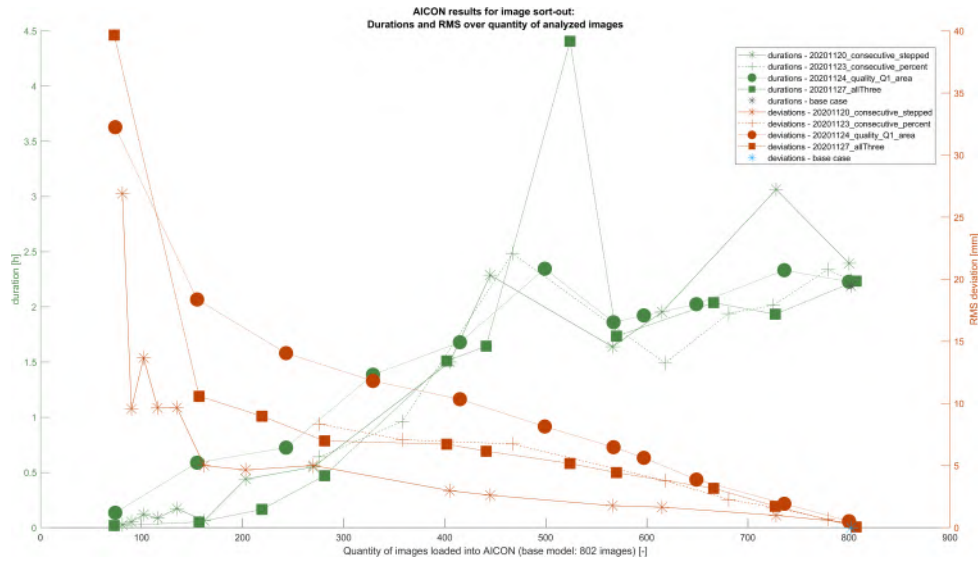
**Figure 5.21:** CESA-2020-1, successful AICON with .phc-file based on FDM Heliostats (*red*) and neighboring heliostats (*blue*)

error budget coming up, the fact that basically orientations would not be computed for always the same heliostats, and due to time constraints, the final orientation of the heliostats was not computed. Basically, in the base case, a certain number of detections were used to generate a photogrammetry result. As far as these input detections are reduced in any way, the photogrammetry result will also change. The computational duration, on the other hand, can very well be compared to each other and represent the quality of the pixel input.

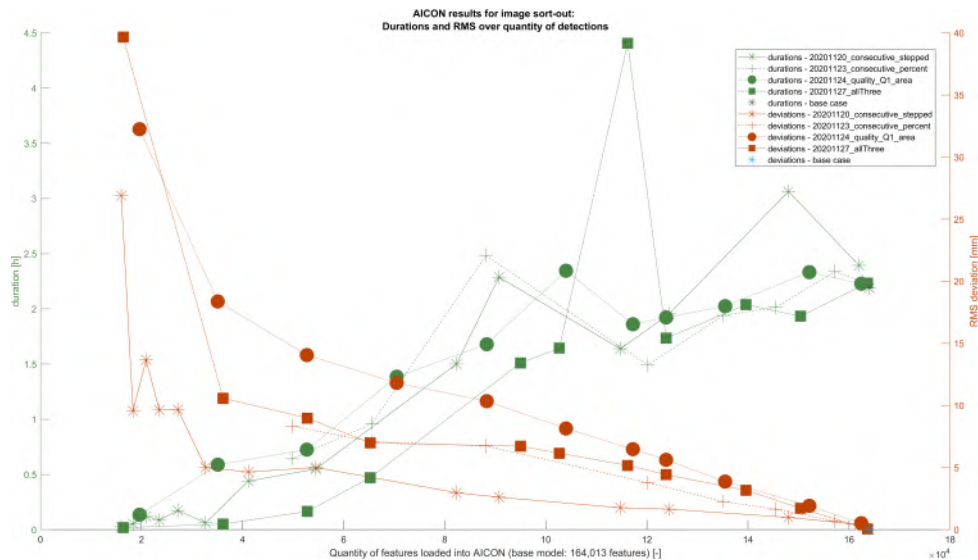
**Deviation.** At first glance, a steadily increasing course of the deviations, or an increasing falling course of the calculation durations (with the exception of a few outliers) with a reduced number of images / features can be observed. The highest deviations are with Quality-Q1, because here specifically those images are sorted out, which have few features - here those images are kept, which ensure a certain area coverage of the image. This tends to leave more detections in the dataset than the other test series. The area coverage filter is very specific, which is why the largest deviations occur compared to the base case. The smallest deviations are found for AICONRED\_stepped - the curve runs entirely below the others. This is due to the randomness of the sorting mechanism which always corresponds most closely to the base case. This is due to the defectiveness of the base case, as mentioned at the beginning. AICONRED\_percent and AICONRED\_fullfilter run between the other two curves, and relatively close to each other, because they both follow a similar filter property. A further experiment would have to clarify to what extent these two filter mechanisms also allowed identical final alignments to be computed. The strong deviations for example at “AICONRED\_fullfilter 73 images” can be traced back to the fact that only very few points can be logically connected to each other due to minor interconnectivity. In this case, only 5 detections are recognized, and the camera positions are also wrongly determined by several meters, as shown by fig. ?? shows.

**Duration.** Regarding the computation duration, it can be said that the AICONRED\_area filter takes the longest. This is because the nature of the filter means that it tends to have the most detections remaining. There are several outliers, including AICONRED\_fullfilter at 524 images with 4.4 hours of computation time. The reason for this cannot be determined, at least no significant differences were noticed when looking at the result plots for the surrounding readings at 570 and 441 images (cf. fig. C.9, fig. C.8, fig. C.10). On average, the shortest computation times are achieved with AICONRED\_fullfilter. With the same number of images (equivalent to number of detections) compared to other filters, a better image quality can be generated, results are calculated faster. The AICONRED\_area filter has disadvantages in performance, because the entered images are trimmed to the maximum number of detections. This inevitably leads to a more difficult mapping of the unique points. AICONRED\_percent also show longer computation times, even though they show quite good results with high amounts of images. AICONRED\_stepped shows the longest computation times, because random filtering is used here and thus the image quality is not improved specifically.

**EOR.** A very homogeneous linear progression can be observed. As already seen in fig. 5.17, the assignment of the camera positions runs without problems, especially with many input images, and coverage rates of often 100% result. Only with very few input images there is often so much information missing for the photogrammetry that only a small number of EORs can be linked. AICONRED\_percent tends to retain the most detections per image, which is why this course is farthest up. AICONRED\_area is below it because this filter generates a high number of pixels



a) Plot shown over quantity of images.



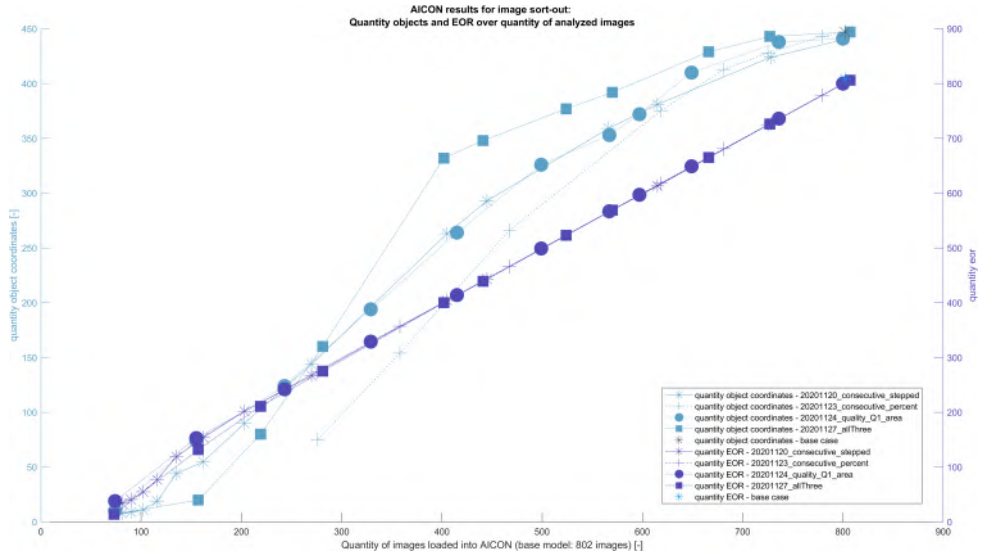
b) Plot shown over quantity of detections.

Figure 5.22: Deviation and duration of AICON testing results.

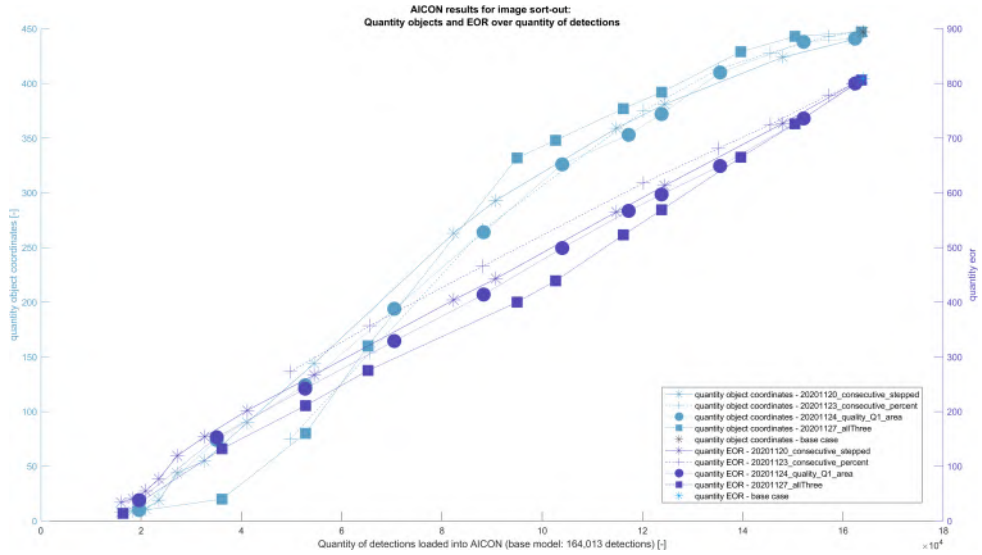
but does not ensure that the images are photogrammetrically linkable. AICONRED\_stepped is in second place. Therefore, in fig. ??, curves for the EOR are different

**Features (object coordinates).** The photogrammetry result consistently provides the most pixels, especially with a sufficiently large number of detections/images received. With AICONRED\_area and AICONRED\_stepped also relatively many image points are detected. AICONRED\_percent produces the weakest matching, because here only the surrounding EOR are considered and not the entire field, and thus possibly important information is lost. The curves of all curves are relatively identical.

A sufficiently high number of images is important for a good photogrammetric result. On top of



a) Plot shown over quantity of images.



b) Plot shown over quantity of detections.

**Figure 5.23:** Object coordinates and EOR

that, also the quantity of features on each image – and their quality (where do they lay, etc.) – is influencing the outcome. Therefore not only the question should be asked, of how many images have been eliminated, but also, to which degree the number of features have decreased.



## 6 Conclusion and Outlook

*The orientation monitoring of solar mirrors has a significant influence on the yield of a solar thermal power plant. Incorrectly oriented heliostats reduce the reflectance of the solar mirrors so that the incident radiation cannot be used efficiently. Therefore a regular check of the orientation is necessary. Currently, this is still done globally using time-consuming methods such as the flux density measurement. “QFLY”, a measuring system for quality control of utility scale solar fields<sup>a</sup> (QFLY) developed by German Aerospace Center (Deutsches Zentrum für Luft- und Raumfahrt e.V.) (DLR), on the other hand, is able to detect an entire heliostat field by means of an unmanned aerial vehicle (UAV) in overflight. This makes it possible to calibrate the field control even before the tower is completed, thus significantly accelerating the commissioning of the power plant. In addition, the heliostat field can be recalibrated if necessary with little time expenditure. However, the measurement accuracy and scalability of QFLY has not yet been researched in detail. Therefore, in this thesis different models are developed, which aim at checking the intermediate results of QFLY for their usability, improving the performance of the whole workflow, and verifying the measurement accuracy of the final calculated alignments. This offers the advantage that, due to the ever decreasing prices for UAVs and concentrated solar power (CSP) power plants, QFLY will be able to monitor and operate efficiently in the future on a global scale.*

---

<sup>a</sup>QFLY is a trademark name of a process developed by DLR for the supply of airborne imaging and related software to obtain information on the geometric, optical and thermal properties of a measured CSP or PV plant.

First, in chapter 2 basics for orientation monitoring of heliostat mirrors are given. QFLY is a multi-stage process that starts with a UAV-supported acquisition of images of the heliostat field. With “AGISOFT METASHAPE”<sup>1</sup> (AGISOFT) the camera positions are calculated. With this information, the heliostats can be clearly localized in each image and the four outer corners detected with an image detection algorithm. This intermediate result can be used for a rough estimate of the heliostat alignment (“QFLY ZERO ASSUMPTION”<sup>2</sup> (ZA)). Due to manufacturing and assembly, larger heliostat mirrors are divided into individual partial mirrors (facets). Since the facets are mounted with a certain gap or, in the case of the present dataset, are separated from each other by a steel frame, this offers the possibility to detect, in addition to the heliostat

---

<sup>1</sup>AGISOFT METASHAPE is a stand-alone software product that performs photogrammetric processing of digital images and generates 3D spatial data to be used in GIS applications, cultural heritage documentation, and visual effects production as well as for indirect measurements of objects of various scales, developed by AGISOFT LLC.

<sup>2</sup>The so-called ZERO ASSUMPTION is a preliminary assumption of orientation of heliostats as part of the QFLY code structure.

corners, the crossing points of the frame or gap between the facets by image recognition. Depending on the image quality, this results in a multitude of additional features, which is useful for the final photogrammetry in a second commercial photogrammetry software (“AICON 3D STUDIO”<sup>3</sup> (AICON)). Here, instead of the original images, only the point coordinates of the features detected on each image are transferred. The orientations calculated with the help of the photogrammetry result have a measurement error of <10 mrad compared to the flux density measurement. Furthermore, the program structure of QFLY is explained.

In chapter 3, the data sets available for this work, their evaluation, and new features of the program code are described. The acquisition of orientation by flux density measurement is described in detail. This is done by flux spot tracking on a white 12x12m target of a limited number of heliostats. The orientation of a heliostat then corresponds to the bisector between the connection vector of the light cone center on the target to the heliostat center and the parallel radiation of the sun hitting the heliostat center. The heliostat orientations calculated by photogrammetry are on average closer to the reference than the ZA results, both outlier-filtered and non-outlier-filtered.

In chapter 4 different methodically motivated optimization algorithms are determined, which examine the ZA results for their accuracy. In the context of the data basis, parameters like the distance of the heliostat to the camera or the angle, which is calculated from the heliostat mirror normal vector and the connecting line between camera and heliostat center points, and which can also be viewed in a differentiated way when projected onto the XY plane, play a decisive role for the optimization.

In chapter 5 several models are set up and investigated which aim to improve the performance of the second photogrammetry in AICON. The algorithms developed for this purpose are to reasonably reduce the number of detections in order to achieve high quality photogrammetric results. The elimination of redundant images and detections plays a central role. Redundancy in images is present, the more similar the camera position, camera viewing direction and the detected features are. In addition, image-specific parameters are developed, such as the fill level and coverage of features per image. Another important aspect is the filtering of features based on expected weak results - this can be defined by a ZA calculation with all detected features instead of the outer corners.

It was shown in the case of CESA-1<sup>4</sup> (CESA-1)-2020, that for  $\alpha_{\text{cam2Helio3D}} = [58^\circ, 70^\circ]$  an improvement of 38.2% of the deviation from the reference measurement is achieved based on an unfiltered data set. The mean deviation between FDM and ZA for all available FDM heliostats is 8.9 mrad (standard deviance of 7.0 mrad), and therefore lies within the required error spectrum of 10 mrad compared to the reference measurement. The ZA results are thus as accurate as the PG result, which has a mean deviation in normal vector of 8.9 mrad for the same FDM

<sup>3</sup>AICON 3D STUDIO is a photogrammetry software developed by AICON 3D SYSTEMS GMBH in 2002. The company got meanwhile acquired by HEXAGON MANUFACTURING INTELLIGENCE.

<sup>4</sup>CESA-1 is a STPP featured on the PSA. Technical specifications: 300 heliostats with 40 m<sup>2</sup> each, 7 MWth, tower height 83 m. [1]

---

heliostats.

It could be approved, that filtering images having similar EOR ( $<0.5\text{m}$ ), similar viewing direction ( $<0.5^\circ$ ) and similar detections ( $>90\%$ ) calculate 8% faster than filtering out the same quantity of images randomly. The accuracy of the measurement regarding the heliostat orientation was not scope of the investigations.

Further analysis as a means of industrializing QFLY needs to be done, as shown in the following list:

- The actual mirror shape deviates from the ideal mirror shape, especially the older the heliostat field is (except e.g. measured with hand photogrammetry). So it is possible that each side of the mirror has a different elevation angle, or that each half of the mirror has different deformations due to gravity. When fitting the ideal heliostat to the randomly shaped, real heliostat, errors occur due to the unknown mirror shape. To explain the partially completely different azimuth orientations compared to flux density measurement (FDM), a recalibration of the facets is essential.
- The influence of soiling on image recognition is not analyzed in detail. Contamination of the mirror surfaces leads to the fact that contrasts no longer stand out significantly from the steel frame or background. Filters in image recognition therefore produce less homogeneous results. With CESA-1-2020 the mirrors were not cleaned before measurement, with CESA-1-2018 they were. There is a clear difference in the scattering of the ZA results which could be caused by this.
- A question that needs further empirical investigation is ... whether an initial photogrammetry using AGISOFT is necessary at all. The camera positions have to be calculated only during the currently used circling and nadir flights, because here a prediction of the camera position is impossible due to turbulences and high tolerance in the flight path compliance. Would a few (15-25) images taken by a stationary camera (high-precision EOR recording) – mainly from a southern direction towards the heliostat field – be sufficient to ensure a comparable accuracy to QFLY-ZA? The corresponding function in Matlab is available; however, such images were not taken as part of the CESA-1-2020 measurements.
- The “*Farthest Neighbors*”-algorithm to reduce the quantity of detections per feature, cf. section 5.1.3, currently relates to the distance between EOR. In this case, it can be that two similar viewing directions stay in the data-set, e.g. one nadir image and one oblique-45 image. This problem can be solved by applying the “*Farthest Neighbors*” algorithm on the angles between EOR viewing directions.
- So far it has not been proven that the combination of all mentioned filters would significantly improve the orientation accuracy. Information about this would be provided by a transformation of the AICON results into the Matlab 3D model, calculation of the normal vectors and comparison with the FDM results.
- The parameters that were set to optimize the ZA results have to be tested with other data sets. For a full test, a new measurement at CESA-1 had to be set including QFly and

FDM. The CESA-1-2018 only served for one FDM-heliostat with sufficiently enough ZA measurements.





# Glossary

**“off-target”** Bei der Auswertung der Schwerpunkte als Zwischenergebnis der Flussdichtemessung, ist es wichtig, Außreiser, sowie Lichtschwerpunkte, nur noch in Teilen auf dem Target zu sehen sind, zu eliminieren. Letzte werden als “off-target” Messwerte bezeichnet..

**binary image** A binary image is one that consists of pixels that can have one of exactly two colors, usually black and white. Binary images are also called bi-level or two-level. This means that each pixel is stored as a single bit—i.e., a 0 or 1..

**CSP** (also called solar thermal electricity, STE). Technology that uses mirrors to focus sunlight into an intense solar beam that heats a working fluid in a solar receiver, which then drives a turbine or heat engine/generator to produce electricity. The mirrors can be arranged in a variety of ways, but they all deliver the solar beam to the receiver. There are four types of commercial CSP systems: parabolic troughs, linear Fresnel, power towers and dish/engines. The first two technologies are line-focus systems, capable of concentrating the sun’s energy to produce temperatures of 400°C, while the latter two are point-focus systems that can produce temperatures of 800°C or higher.

**feature** The mirror surface of the CESA-1 heliostats covers 21 m<sup>2</sup>. For production and maintenance reasons the mirror surfaces are divided into smaller sub-elements. One speaks then of mirror facets. A CESA-1 heliostat has 20 facets.

The image recognition algorithm works to the whiteness that it detects the high contrast between facet and the only a few mm wide gap to the next facet – i.e. edge detection. Wherever these edges intersect, a point of intersection of edges is created. And these crossing points are called features.

The CESA-1 heliostats have either 39 or 25 features (center point included) depending on the design. Features are stored in the system with ideal 3D coordinates and are uniquely named across all heliostat fields. CESA-1 with its 300 heliostats includes about 8600 features. By localizing the heliostats in the images, all features of a heliostat can theoretically be recognized in the QFly step *feature recognition*, which then determines the alignment in photogrammetry with AICON..

**gray scale image** An 8-bit integer grayscale image provides 255 available tonal steps from 0 (black) to 255 (white)..

**orthophoto** transformation of the measurement imagery into image-based products using arbitrary projections.

**ZA** Zero Assumption orientation, or pre-orientation. The calculation of the normal vector orientation in the QFly process is based on several intermediate steps. The basis is the Zero Assumption method, where a pre-orientation is output for each heliostat detected on an image. This is an unfounded calculation of the orientation over the four outer corners..

# Index

## Symbols

National Renewable Energy Laboratory  
(NREL) ..... 24

## A

Agisoft ..... 27

AICON

    “*Farthest Neighbors*”-algorithm ..... 61

    coordinate transformation ..... 65

    feature reduction ..... 58

    final results ..... 77

    image filters ..... 73

    image quality ..... 56

    image reduction ..... 56

    performance improvement ..... 55

    phc-file ..... 65

angle between vectors ..... 61

azimuth ..... 13

## C

camera calibration ..... 18

canting ..... 14

CESA-1 ..... 16

CSP ..... 9, 11

    electricity costs ..... 9

    tower ..... 10–12

    types ..... 11

    working principle ..... 11

## E

elevation ..... 13

EOR

    viewing direction ..... 61

## F

FDM ..... 19, 31

    filtering of flux spots ..... 37

    flux spot center calculation ..... 20, 31

    with four cameras placed around

        receiver ..... 21

    with photodiodes around receiver ... 22

    working principle ..... 20

fringe projection ..... 23

## H

heliosotat

    quality parameters ..... 13

heliostat ..... 12

    corners ..... 27

    facets and shape ..... 14

    features and nomenclature ..... 15

    parabolic shape ..... 12

    size ..... 14

Hydrosol pilot plant ..... 14

**J**

Julich ..... 18

**L**

linear Fresnel ..... 11

**P**

parabolic trough ..... 11

photogrammetry ..... 18

    high quality of images ..... 55

photogrammetry:best practice ..... 18

photogrammetry:point cloud ..... 18

Plataforma Solar de Almería ..... 16

PPK ..... 25

PTK ..... 25

**Q**

QDec ..... 14, 23

QFly ..... 26

    CESA-1-2018 ..... 30

    CESA-1-2020 ..... 30

    AGISOFT ..... 38

        reference points, 38

    AICON ..... 30

deflectometry ..... 26

Feature Detection ..... 30

Matlab 3D model ..... 28

measurement campaign ..... 32

photogrammetry ..... 26, 30

program structure ..... 26

Zero Assumption ..... 28, 39

**S**

SAPHIR ..... 23

Solar Dish ..... 12

STPP ..... 12

    receiver ..... 12

**T**

target ..... 20

**V**

VRS ..... 25

**Z**

Zero Assumption ..... 47

    -deviations ..... 47

    -optimization ..... 47

    -results ..... 47





## Bibliography

- [1] CENTER (DLR), Institute for Solar Research of the German Aerospace: *DLR - Institute of Solar Research - CIEMAT Plataforma Solar de Almería - Europe's biggest Test Center for Concentrating Solar Power (CSP)*,  
URL [https://www.dlr.de/sf/en/desktopdefault.aspx/tabid-7176/11942\\_read-28189/](https://www.dlr.de/sf/en/desktopdefault.aspx/tabid-7176/11942_read-28189/) (Access date 2020-12-03).
- [2] HENNECKE, K.; SCHWARZBÖZL, P.; KOLL, G.; BEUTER, M.; HOFFSCHMIDT, B.; GÖTTSCHE, J.; HARTZ, T.: *The Solar Power Tower Jülich — A Solar Thermal Power Plant for Test and Demonstration of Air Receiver Technology*, in GOSWAMI, D. Yogi; ZHAO, Yuwen (Hrsg.), *Proceedings of ISES World Congress 2007 (Vol. I – Vol. V)*, S. 1749–1753, Springer, Berlin, Heidelberg.
- [3] *DLR - Das DLR im Überblick*,  
URL <https://www.dlr.de/content/de/artikel/das-dlr.html> (Access date 2020-11-30).
- [4] *Solar forecast using cloud parameters WDC-RSAT*,  
URL [https://wdc.dlr.de/data\\_products/SERVICES/SOLARENERGY/solar\\_forecast.php](https://wdc.dlr.de/data_products/SERVICES/SOLARENERGY/solar_forecast.php) (Access date 2020-04-28).
- [5] JESSEN, Wilko; RÖGER, Marc; PRAHL, Christoph; PITZ-PAHL, Robert: *A Two-Stage Method for Measuring the Heliostat Offset*, in SolarPACES 2020. Online Event. The proceedings of SolarPACES 2020 will be published online with AIP, the American Institute of Physics ([www.aip.org](http://www.aip.org)), 2020, (5).
- [6] *Espacenet – search results*,  
URL [https://worldwide.espacenet.com/patent/search/family/058054912/publication/DE102015217086A1?called\\_by=epo.org&q=102015217086](https://worldwide.espacenet.com/patent/search/family/058054912/publication/DE102015217086A1?called_by=epo.org&q=102015217086) (Access date 2020-12-02).
- [7] HAJER, Lewin L.: *Auslegung und Erprobung eines reflexbasierten Verfahrens zur Charakterisierung von Heliostaten | Institut für Photogrammetrie | Universität Stuttgart*, in .
- [8] LUHMANN, Thomas: *Nahbereichsphotogrammetrie. 2., überarbeitete Auflage*, in Verlag Wichmann, 2003.
- [9] *Nadir*, 2020, page Version ID: 989491671,  
URL <https://en.wikipedia.org/w/index.php?title=Nadir&oldid=989491671> (Access date 2020-12-03).

- 
- [10] MARTIN: *Energy*,  
URL <https://www.un.org/sustainabledevelopment/energy/> (Access date 2020-04-28).
- [11] DINCER, IBRAHIM: *Energy and Environmental Impacts: Present and Future Perspectives*, in *Energy Sources*, 1998, Vol. 20 (4-5), S. 427–453.
- [12] ANDRE, Thomas: *Renewables 2020 Global Status Report*, 2020, ISBN 978-3-948393-00-7.
- [13] RÖGER, Marc; PRAHL, Christoph; ALGNER, Niels; REINALTER, Wolfgang: *Regelmäßige Vermessung thermischer und optischer Komponenten in Parabolrinnenfeldern*.
- [14] SÄCK, Jan-Peter: *Entwicklung und Simulation einer Wasserstoffherstellungsanlage auf einem Solarturm*, in , 2012.
- [15] RÖGER, Marc; PITZ-PAAL, Robert: *Solarthermische Kraftwerke: Sensoren im FuE Prozess, Herstellungsprozess und Einsatzmonitoring*, in *Sensorik für Erneuerbare Energien und Energieeffizienz*.
- [16] JIN, Zhang; WEI, Wang: *Analysis on Flux Density of Light Spot in Heliostat Field and Its Error Correction*, in *Journal of Shanghai Electric Technology*, 2017, (1), S. 14.
- [17] OFFERGELD, Matthias; RÖGER, Marc; STADLER, Hannes; GORZALKA, Philip; HOFFSCHMIDT, Bernhard: *Flux density measurement for industrial-scale solar power towers using the reflection off the absorber*, in *AIP Conference Proceedings*, 2019, Vol. 2126 (1), S. 110002.
- [18] SANTAMARTA, Jose: *World's largest Concentrated Solar Power plant ties tariffs to big storage to hit record price*,  
URL <http://helioscsp.com/worlds-largest-concentrated-solar-power-plant-ties-tariffs-to-big-storage-to-hit-record-price/> (Access date 2020-12-01).
- [19] DEIGN, Jason: *Solar-Plus-Storage Beats Combined-Cycle Gas in Jordan and Morocco*, 2019,  
URL <https://www.greentechmedia.com/articles/read/solar-storage-beats-combined-cycle-gas-in-jordan-and-morocco> (Access date 2020-04-21).
- [20] *World's largest CSP plant ties tariffs to big storage to hit record price | New Energy Update*,  
URL <http://newenergyupdate.com/csp-today/worlds-largest-csp-plant-ties-tariffs-big-storage-hit-record-price> (Access date 2020-04-21).
- [21] *German heliostat tracker raises bar for CSP tower accuracy | Reuters Events | Renewables*,  
URL <https://www.reutersevents.com/renewables/solar/german-heliostat-tracker-raises-bar-csp-tower-accuracy> (Access date 2020-12-01).
- [22] *HelioControl Project Completed: Determination and control of aim points for heliostat fields in operation - Fraunhofer ISE*,
-

- URL <https://www.ise.fraunhofer.de/en/press-media/press-releases/2020/heliocontrol-project-completed-determination-and-control-of-aim-points-for-heliostat-fields-in-operation.html> (Access date 2020-12-01).
- [23] ALEXOPOULOS, Spiros; HOFFSCHMIDT, Bernhard: *Concentrating Receiver Systemsconcentrating receiver system (CRS)(Solar Power Tower)solar powertower*, in MEYERS, Robert A. (Hrsg.), *Encyclopedia of Sustainability Science and Technology*, S. 2349–2391, Springer, New York, NY, 2012, ISBN 9781441908513, doi:10.1007/978-1-4419-0851-3\_677. URL [https://doi.org/10.1007/978-1-4419-0851-3\\_677](https://doi.org/10.1007/978-1-4419-0851-3_677)
- [24] JU, Xing; XU, Chao; HU, Yangqing; HAN, Xue; WEI, Gaosheng; DU, Xiaoze: *A review on the development of photovoltaic/concentrated solar power (PV-CSP) hybrid systems*, in *Solar Energy Materials and Solar Cells*, 2017, Vol. 161, S. 305–327.
- [25] ISLAM, Md Tasbirul; HUDA, Nazmul; ABDULLAH, A.B.; SAIDUR, R.: *A comprehensive review of state-of-the-art concentrating solar power (CSP) technologies: Current status and research trends*, in *Renewable and Sustainable Energy Reviews*, 2018, Vol. 91, S. 987 – 1018.
- [26] NEHER, Ina; BUCHMANN, Tina; CREWELL, Susanne; MEILINGER, Stefanie: *Impact of atmospheric aerosols on solar energy production - Dust outbreak in West Africa*, in , 2018.
- [27] WANG, Zhifeng: *Chapter 2 - The Solar Resource and Meteorological Parameters*, in WANG, Zhifeng (Hrsg.), *Design of Solar Thermal Power Plants*, S. 47 – 115, Academic Press, 2019, ISBN 978-0-12-815613-1, doi:<https://doi.org/10.1016/B978-0-12-815613-1.00002-X>. URL <http://www.sciencedirect.com/science/article/pii/B978012815613100002X>
- [28] *Solar Resource Glossary / Grid Modernization / NREL*,  
URL <https://www.nrel.gov/grid/solar-resource/solar-glossary.html#directnormalirradiance> (Access date 2020-11-30).
- [29] *Solar irradiance*, 2020, page Version ID: 990017971,  
URL [https://en.wikipedia.org/w/index.php?title=Solar\\_irradiance&oldid=990017971](https://en.wikipedia.org/w/index.php?title=Solar_irradiance&oldid=990017971) (Access date 2020-11-30).
- [30] *Renewable Power Generation Costs in 2018*,  
URL </publications/2019/May/Renewable-power-generation-costs-in-2018> (Access date 2020-04-21).
- [31] *Concentrating solar power – Tracking Power – Analysis*,  
URL <https://www.iea.org/reports/tracking-power-2019/concentrating-solar-power> (Access date 2020-04-20).
- [32] *Saudi Arabia to tender 2,225MW solar in 2019 and targets 2.7GW CSP in 2030*,  
URL [http://www.cspfocus.cn/en/market/detail\\_1244.htm](http://www.cspfocus.cn/en/market/detail_1244.htm) (Access date 2020-04-20).

- 
- [33] 6 Concentrated Solar Power projects with 350 MW capacity will be newly built in China this year / REVE News of the wind sector in Spain and in the world,  
URL <https://www.evwind.es/2019/09/11/6-concentrated-solar-power-solar-projects-with-350-mw-capacity-will-be-newly-built-in-china-this-year/70772> (Access date 2020-04-27).
- [34] SATTLER, Johannes Christoph; RÖGER, Marc; SCHWARZBÖZL, Peter; BUCK, Reiner; MACKE, Ansgar; RAEDER, Christian; GÖTTSCHE, Joachim: *Review of heliostat calibration and tracking control methods*, in Solar Energy, 2020, Vol. 207, S. 110 – 132.
- [35] CHAANAOU, Meriem; VAUDREUIL, Sébastien; BOUNAHMIDI, Tijani: *Benchmark of Concentrating Solar Power Plants: Historical, Current and Future Technical and Economic Development*, in Procedia Computer Science, 2016, Vol. 83, S. 782 – 789.
- [36] HELLER, P.: *1 - Introduction to CSP systems and performance*, in HELLER, Peter (Hrsg.), *The Performance of Concentrated Solar Power (CSP) Systems*, S. 1 – 29, Woodhead Publishing, 2017, ISBN 978-0-08-100447-0, doi:<https://doi.org/10.1016/B978-0-08-100447-0.00001-8>.  
URL <http://www.sciencedirect.com/science/article/pii/B9780081004470000018>
- [37] XU, Xinhai; VIGNAROUBAN, K.; XU, Ben; HSU, K.; KANNAN, A.M.: *Prospects and problems of concentrating solar power technologies for power generation in the desert regions*, in Renewable and Sustainable Energy Reviews, 2016, Vol. 53, S. 1106 – 1131.
- [38] *Technology Roadmap - Concentrating Solar Power – Analysis*,  
URL <https://www.iea.org/reports/technology-roadmap-concentrating-solar-power> (Access date 2020-12-03).
- [39] BREEZE, Paul: *Chapter 13 - Solar Power*, in BREEZE, Paul (Hrsg.), *Power Generation Technologies (Third Edition)*, third edition Auflage, S. 293 – 321, Newnes, 2019, ISBN 978-0-08-102631-1, doi:<https://doi.org/10.1016/B978-0-08-102631-1.00013-4>.  
URL <http://www.sciencedirect.com/science/article/pii/B9780081026311000134>
- [40] DLR, Institut für Solarforschung im: *DLR - Institut für Solarforschung - Solarturm-Kraftwerk Jülich*,  
URL [https://www.dlr.de/sf/desktopdefault.aspx/tabid-8560/15527\\_read-44867/](https://www.dlr.de/sf/desktopdefault.aspx/tabid-8560/15527_read-44867/) (Access date 2020-11-30).
- [41] HÄBERLE, A.: *Concentrating solar technologies for industrial process heat and cooling*, in *Concentrating Solar Power Technology*, S. 602–619, Elsevier, 2012, ISBN 9781845697693, doi:10.1533/9780857096173.3.602.  
URL <https://linkinghub.elsevier.com/retrieve/pii/B9781845697693500194>
-

- [42] SHEPPARD, Drew A.; BUCKLEY, Craig E.: *The potential of metal hydrides paired with compressed hydrogen as thermal energy storage for concentrating solar power plants*, in *International Journal of Hydrogen Energy*, 2019, Vol. 44 (18), S. 9143 – 9163.
- [43] *Concentrated Solar Power (CSP) – from niche to winning technology (2) | Ingenuity | Siemens*,  
URL <https://ingenuity.siemens.com/2019/01/concentrated-solar-power-csp-from-niche-to-winning-technology-2/> (Access date 2020-12-01).
- [44] *Heliostat*, 2020, page Version ID: 987518141,  
URL <https://en.wikipedia.org/w/index.php?title=Heliostat&oldid=987518141> (Access date 2020-11-30).
- [45] ROSA-CLOT, Marco; TINA, Giuseppe Marco: *Photovoltaic Electricity*, in *Submerged and Floating Photovoltaic Systems*, S. 13–32, Elsevier, 2018, ISBN 9780128121498, doi:10.1016/B978-0-12-812149-8.00002-8.  
URL <https://linkinghub.elsevier.com/retrieve/pii/B9780128121498000028>
- [46] KRECH, Mj: *How to Teach Altitude*, 2008,  
URL <http://scienceteachingideas.blogspot.com/2008/12/how-to-teach-altitude.html> (Access date 2020-12-02).
- [47] GUO, Minghuan; SUN, Feihu; WANG, Zhifeng; ZHANG, Jianhan: *Properties of a general azimuth–elevation tracking angle formula for a heliostat with a mirror-pivot offset and other angular errors*, in *Solar Energy*, 2013, Vol. 96, S. 159–167.
- [48] RÖGER, Marc: *Heliostat Performance Testing Guideline - Status Update Sept. 2017*, in *SolarPACES Task III Workshop*.
- [49] PFAHL, Andreas; COVENTRY, Joe; RÖGER, Marc; WOLFERTSTETTER, Fabian; VÁSQUEZ-ARANGO, Juan Felipe; GROSS, Fabian; ARJOMANDI, Maziar; SCHWARZBÖZL, Peter; GEIGER, Mark; LIEDKE, Phillip: *Progress in heliostat development*, in *Solar Energy*, 2017, Vol. 152, S. 3–37.
- [50] BJOERKMAN, Nils: *Heliostat Design*, in , 2014.
- [51] KOCH, Henning; RÖGER, Marc; BENITEZ, Daniel; PRAHL, Christoph; WEINREBE, Gerhard: *From Research to Industry: Development of a High-Resolution Measurement System for Mirrored Heliostats in Series Production*, Vol. 2126, Vol. 2126.
- [52] ULMER, Steffen; MÄRZ, Tobias; PRAHL, Christoph; REINALTER, Wolfgang; BELHOMME, Boris: *Automated high resolution measurement of heliostat slope errors*, in *Solar Energy*, 2011, Vol. 85 (4), S. 681–687.

- 
- [53] *Plataforma Solar de Almería - Central Receiver Facilities*,  
URL [https://www.psa.es/en/facilities/central\\_receiver/cesa1.php](https://www.psa.es/en/facilities/central_receiver/cesa1.php) (Access date 2020-12-02).
- [54] *Jülich Solar Tower*, 2020, page Version ID: 970743601,  
URL [https://en.wikipedia.org/w/index.php?title=J%C3%BClich\\_Solar\\_Tower&oldid=970743601](https://en.wikipedia.org/w/index.php?title=J%C3%BClich_Solar_Tower&oldid=970743601) (Access date 2020-11-30).
- [55] *r/modernwarfare - This is the Photogrammetry room designed by Bernardo Antoniazzi used for the development of Modern Warfare.*,  
URL [https://www.reddit.com/r/modernwarfare/comments/djnojv/this\\_is\\_the\\_photogrammetry\\_room\\_designed\\_by/](https://www.reddit.com/r/modernwarfare/comments/djnojv/this_is_the_photogrammetry_room_designed_by/) (Access date 2020-08-26).
- [56] CLASS, with MikaelaHolmes in 3D SCANNING: *3D Scanning Class*,  
URL <https://www.instructables.com/class/3D-Scanning-Class/> (Access date 2020-08-26).
- [57] BERENGUEL, M.; RUBIO, Francisco; VALVERDE, A.; LARA, P.J.; ARAHAL, M.R.; CAMACHO, Eduardo; LÓPEZ, M.: *An artificial vision-based control system for automatic heliostat positioning offset correction in a central receiver solar power plant*, in *Solar Energy*, 2004, Vol. 76, S. 563–575.
- [58] STONE, Kenneth W.: *Automatic heliostat track alignment method*, 1984,  
URL <https://patents.google.com/patent/US4564275A/en> (Access date 2020-12-02).
- [59] KRIBUS, Abraham; VISHNEVETSKY, Irina; YOGEV, Amnon; RUBINOV, Tatiana: *Closed loop control of heliostats*, in *Energy*, 2004, Vol. 29, S. 905–913.
- [60] CONVERY, Mark: *Closed-loop control for Power Tower heliostats*, in *Proceedings of SPIE - The International Society for Optical Engineering*, 2011, Vol. 8108, S. 17–.
- [61] PEÑA-CRUZ, Manuel I; ARANCIBIA-BULNES, Camilo A; IRIARTE-CORNEJO, Cuitlahuac; CABANILLAS, Rafael E; ESTRADA, Claudio A: *Heliostat Characterization by Optical Techniques and Image Processing*, in *ASME 2012 6th International Conference on Energy Sustainability collocated with the ASME 2012 10th International Conference on Fuel Cell Science, Engineering and Technology*, S. 353–362, American Society of Mechanical Engineers.
- [62] BURISCH, Michael; OLANO, Xabier; SANCHEZ, Marcelino; OLARRA, Aitor; VILLASANTE, Cristobal; OLASOLO, David; MONTERREAL, Rafael; ENRIQUE, Raul; FERNÁNDEZ, Jesús: *Scalable heliostat calibration system (SHORT) - Calibrate a whole heliostat field in a single night*, in *AIP Conference Proceedings*, 2018, Vol. 2033 (1), S. 040009.
- [63] RÖGER, Marc; PRAHL, Christoph; ULMER, Steffen: *Heliostat Shape and Orientation by Edge Detection*, in *Journal of Solar Energy Engineering*, 2010, Vol. 132 (2), S. 021002.
-

- [64] SCHELL, Steve: *Design and evaluation of esolar's heliostat fields*, in *Solar Energy*, 2011, Vol. 85 (4), S. 614 – 619.
- [65] ZAVODNY, Maximilian; SLACK, M; HUIBREGTSE, R; SONN, A: *Tower-based CSP artificial light calibration system*, in *Energy Procedia*, 2015, Vol. 69, S. 1488–1497.
- [66] MITCHELL, Rebecca A.; ZHU, Guangdong: *A non-intrusive optical (NIO) approach to characterize heliostats in utility-scale power tower plants: Methodology and in-situ validation*, in *Solar Energy*, 2020, Vol. 209, S. 431–445.
- [67] ŠTRONER, Martin; URBAN, Rudolf; REINDL, Tomáš; SEIDL, Jan; BROUČEK, Josef: *Evaluation of the Georeferencing Accuracy of a Photogrammetric Model Using a Quadcopter with Onboard GNSS RTK*, in *Sensors*, 2020, Vol. 20 (8), S. 2318.
- [68] TADDIA, Yuri; STECCHI, Francesco; PELLEGRINELLI, Alberto: *Coastal Mapping Using DJI Phantom 4 RTK in Post-Processing Kinematic Mode*, in *Drones*, 2020, Vol. 4 (2), S. 9.
- [69] *What's the difference between PPK and RTK drones, and which one is better?*, 2020, URL <https://wingtra.com/ppk-drones-vs-rtk-drones/> (Access date 2020-09-02).
- [70] GÖHRING, Felix; HILGERT, Christoph; ULMER, Steffen; PRAHL, Christoph; RÖGER, Marc: *Verfahren zur Vermessung von Heliostaten*, German Patent DE102015217086 (A1), March 2017, URL <https://patents.google.com/patent/DE102015217086A1/it> (Access date 2020-12-03).
- [71] MICHALSKY, Joseph J.: *The Astronomical Almanac's algorithm for approximate solar position (1950–2050)*, in *Solar Energy*, 1988, Vol. 40 (3), S. 227–235.
- [72] GRENA, Roberto: *An algorithm for the computation of the solar position*, in *Solar Energy*, 2008, Vol. 82 (5), S. 462–470.
- [73] *The Farthest Neighbors Algorithm | Frolian's blog*, URL <https://flothsof.github.io/farthest-neighbors.html> (Access date 2020-12-11).
- [74] *Ivanpah Solar Electric Generating System*, 2014, URL <https://www.greencitytimes.com/ivanpah-solar-electric-generating-system/> (Access date 2020-04-27).



# Appendices



# A Original task description (Aufgabenstellung)

Lehrstuhl für Fertigungsautomatisierung  
und Produktionssystematik

Prof. Dr.-Ing. Jörg Franke

Friedrich-Alexander-Universität Erlangen-Nürnberg  
Egerlandstraße 7-9 91058 Erlangen  
Telefon: (09131) 85-27971 Telefax: (09131) 30 25 28



---

## Vergabe einer Masterarbeit an Herrn Michael Fischer, Matr.-Nr. 22067080

### Thema:

### **Verification of the process reliability and scalability of an airborne measuring system for the heliostat orientation in solar power tower plants**

Zur Energiewende trägt u.a. auch konzentrierte Solarthermie bei, die an Standorten mit hoher direkter Sonnenstrahlung z.B. in Solarturmkraftwerken Anwendung findet. Rund um den Turm sind Sonnenspiegel (Heliostate) positioniert, welche das Sonnenlicht auf den am Turm montierten Receiver reflektieren. Um ein solches Kraftwerk effizient zu betreiben, ist eine exakte Ausrichtung jedes Heliostats erforderlich. Das aktuell zur Kalibrierung eingesetzte Messverfahren ist allerdings sehr zeitintensiv, weshalb das Deutsche Zentrum für Luft- und Raumfahrt e. V. (DLR) ein auf Bilderkennung, Photogrammetrie und Deflektometrie basierendes luftgestütztes System (QFly) entwickelt.

Ziel der Arbeit ist es, die Skalierbarkeit und Genauigkeit von Teilschritten des QFly-Verfahrens zu beurteilen. Für die Skalierbarkeit ist die Effizienz, Robustheit und Dauer der Auswertung relevant. Die Skalierbarkeit ist außerdem verbunden mit der Anzahl der verwendeten Bilder, da der Aufwand für einzelne Teilschritte des Verfahrens exponentiell mit der Anzahl der Bilder steigt. Ein möglicher Ansatz dazu ist die Untersuchung der Skalierbarkeit unter Bezugnahme der Auswahl der verwendeten Bilder unter photogrammetrischen Gesichtspunkten. Für die Beurteilung der Genauigkeit des Verfahrens müssen die neuen Ansätze gegen Referenzmethoden geprüft werden. Im Zuge dessen werden geeignete Parameter definiert, um die QFly-Ergebnisse und die Skalierbarkeit systematisch zu optimieren.

Die Arbeit beinhaltet folgende Schwerpunkte:

- Literaturrecherche zur Solarthermie sowie zur Messung der Heliostatausrichtung
- Analyse der Datensätze, welche die Vorausrichtung der Heliostate beschreiben
- Optimierung der Auswertung der QFly-Messungen über geeignete Anpassung der Parameter der Bilddatenverarbeitung
- Verringerung der benötigten Bildanzahl bei gleichbleibend guten Ergebnissen
- Vergleich der Ergebnisse von Teilschritten des QFly-Systems mit Referenzdaten
- Beurteilung der Skalierbarkeit und Genauigkeit der QFly-Messung

**Betreuer:** Lehrstuhl FAPS  
Prof. Dr.-Ing. J. Franke  
M. Sc. C. Hofmann

Deutsches Zentrum für Luft- und Raumfahrt e. V.  
M. Eng. Wilko Jessen

**Beginn:** 01.04.2020

Die Masterarbeit wird nach den Vorgaben der Studienordnung durchgeführt.

---

Prof. Dr.-Ing. J. Franke



## B Data

### B.1 Technical infrastructure

Table B.1: Computers used for calculations

	Computer 1	Computer 2	Computer 3	Computer 4
Computer Type	Laptop	Laptop	Desktop PC	Laptop
Model	Lenovo Thinkpad E560	Dell Latitude E7450	Fujitsu CELSIUS W530	Macbook Pro
Processor	Intel(R) Core(TM) i5-6200U CPU @ 2.30GHz, 2401 Mhz, 2 Core(s), 4 Logical Processor(s)	Intel(R) Core(TM) i7-5600U CPU @ 2.60GHz, 2594 MHz, 2 Kern(e), 4 logische(r) Prozessor(en)	Intel(R) Xeon(R) CPU E3-1276 v3 @ 3.60GHz, 3601 MHz, 4 Kern(e), 8 logische(r) Prozessor(en)	Intel(R) Core(TM) i7-4870HQ CPU @ 2.50GHz
Installed Physical Memory (RAM):	16,00 GB	8,00 GB	32,00 GB	16,00 GB
OS Name	Microsoft Windows 10 Home	Microsoft Windows 10 Enterprise	Microsoft Windows 10 Enterprise	macOS 11: Big Sur
System Type	x64-based PC	x64-based PC	x64-based PC	n/a

### B.2 Agisoft testing data

**Table B.2:** Agisoft Testing: Heliostat centers taken as reference for Photo Alignment

Heliostat-Nr	X-Coordiante [mm]	Y-Coordiante [mm]	Z-Coordiante [mm]
#1	-6	39775.5	4346.77344
#8	-40004	39997	3954
#9	40000	39763.5	4367.77344
#34	4999	75762.5	4487.68262
#64	-80013	87821.5	4937.77344
#65	80013	87781.5	4920.77344
#93	-40019	115036	4850
#96	49996	115033	4870
#166	-150007	146818.5	5643.773438
#167	150005	146779.5	5640.773438
#169	5010	166007	5118
#184	-85004	165987	5125
#187	95025	166026	5114
#221	-156264	187002	5741
#249	44339	211017	5999

## C Plots

### C.1 Measurement results

### C.2 General overview of data sets

### C.3 Plots for AICON Testing

#### C.3.1 Reduction of image and detections quantity through “*Farthest Neighbors*” algorithm

#### C.3.2 Residuals of each test AICON result compared to the base model

#### C.3.3 Reducing images for AICONRED\_stepped

### C.4 Plots for FDM

#### C.4.1 Plots showing final results for each series

#### C.4.2 Flux Spot movement of different series

#### C.4.3 Photos of FDM measurement



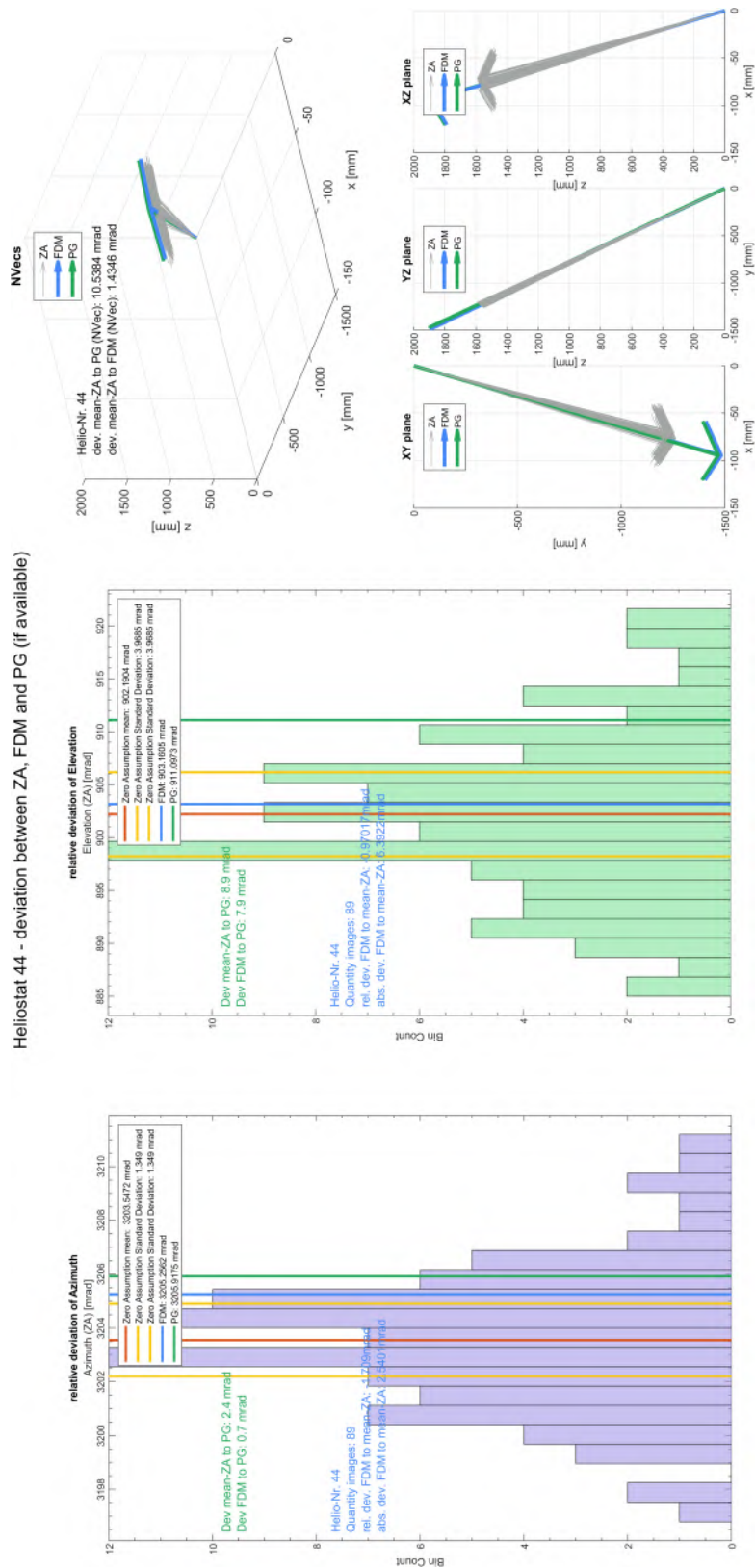


**Figure C.1:** CESA-1-2020: Comparison ZA, FDM and PG – HelioStat 44. ZA results are drawn as histograms in the left – Azimuth (*light blue*) – and centered – Elevation (*light blue*) – subplot. The actual normal vectors are drawn in the right-side plots. Deviations between ZA and FDM are quite low (1.7 mrad for Azimuth, 1.0 mrad for Elevation, 1.4 mrad between normal vectors)

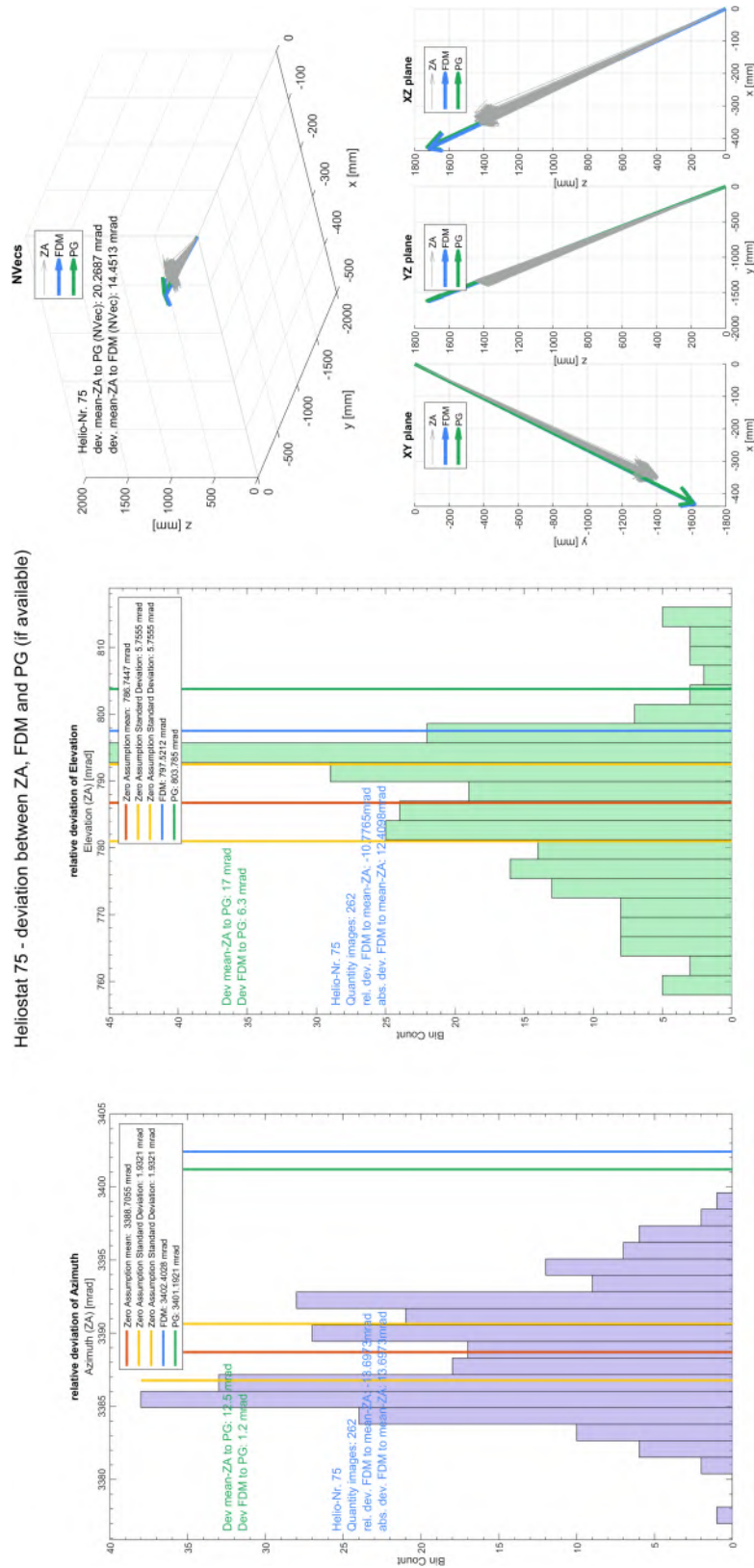


**Figure C.2:** CESA-1-2020: Comparison ZA, FDM and PG – Heliostat 75. All azimuth angles are smaller than the FDM or PG azimuth angle. ZA results are drawn as histograms in the left – Azimuth (*light blue*) – and centered – Elevation (*light blue*) – subplot. The actual normal vectors are drawn in the right-side plots. Deviations between ZA and FDM are quite high (13.7 mrad for Azimuth, 10.8 mrad for Elevation, 14.5 mrad between normal vectors)

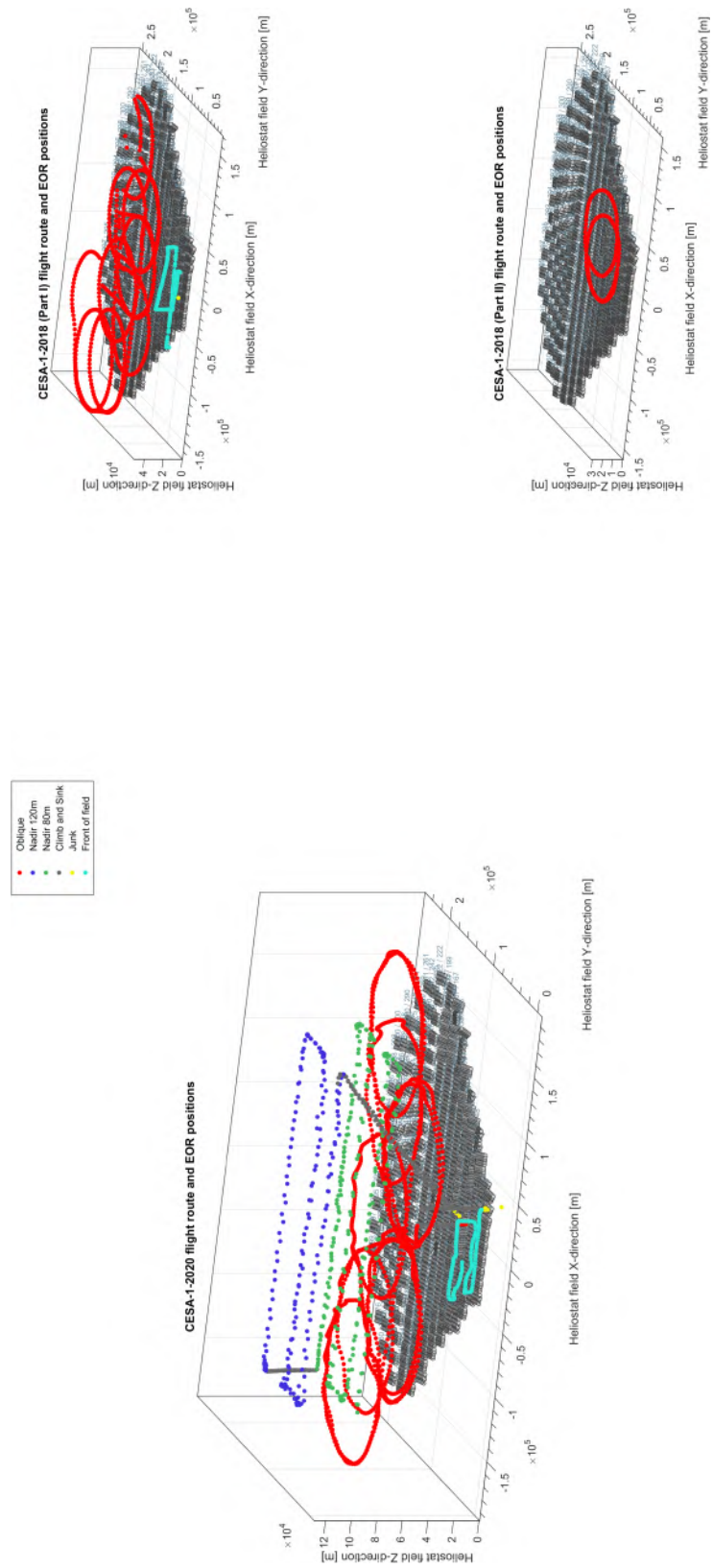


Figure C.3: CESA-1-2020, CESA-1-2020 Part I, CESA-1-2020 Part II: Overview of different images types.

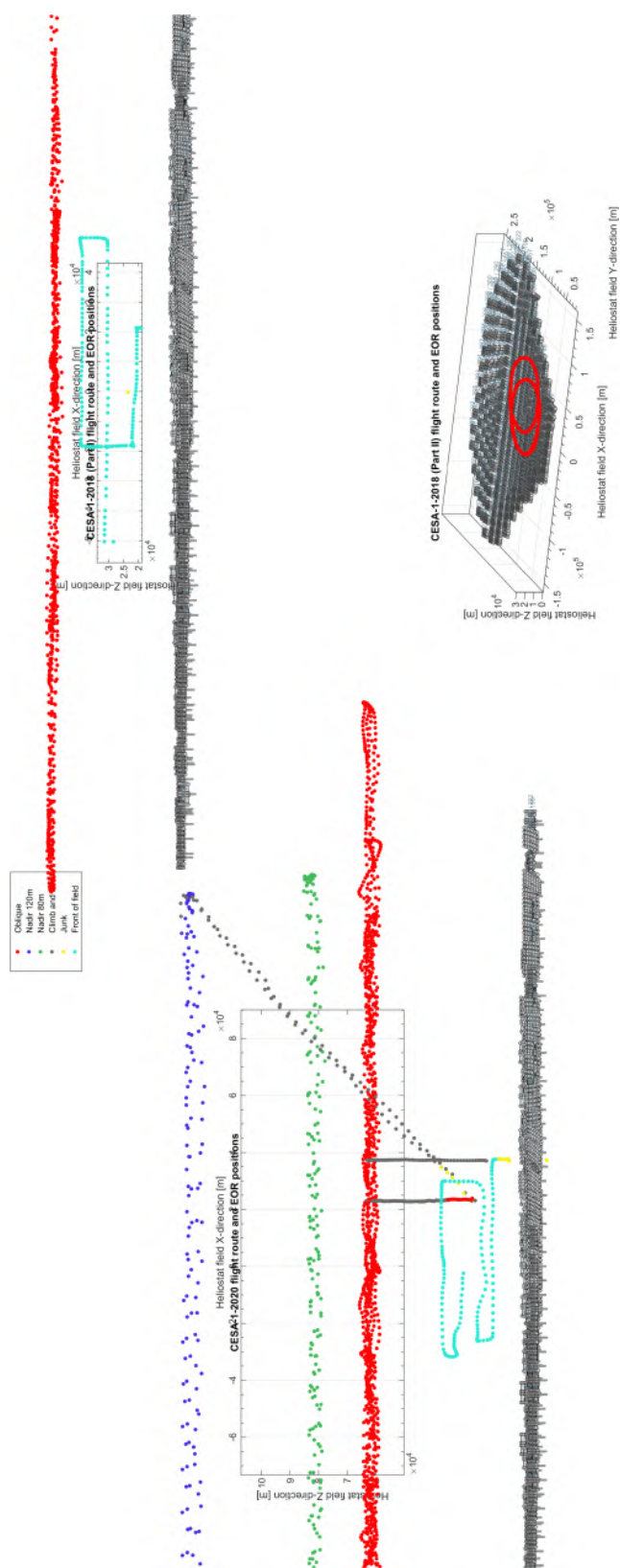
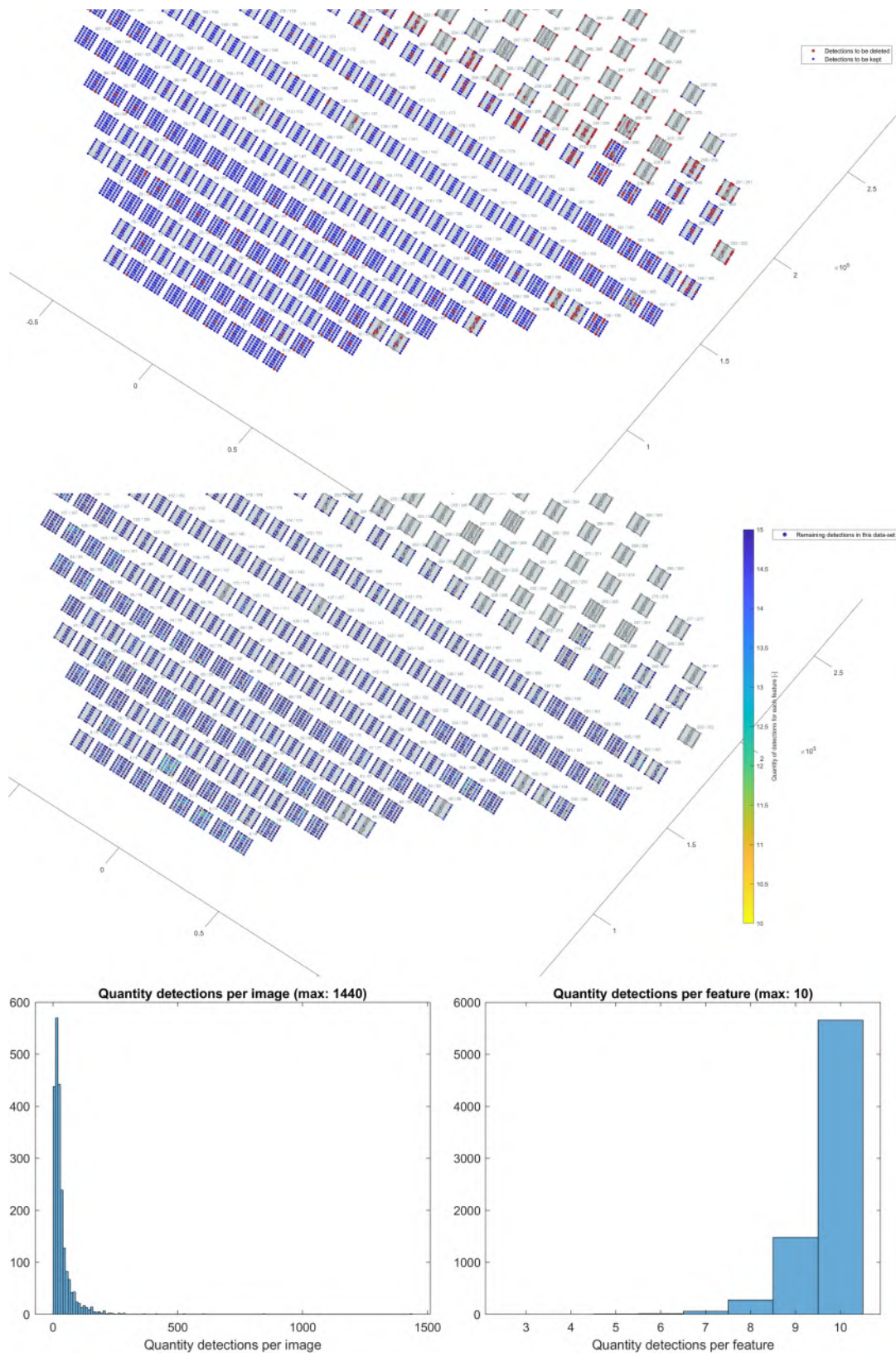
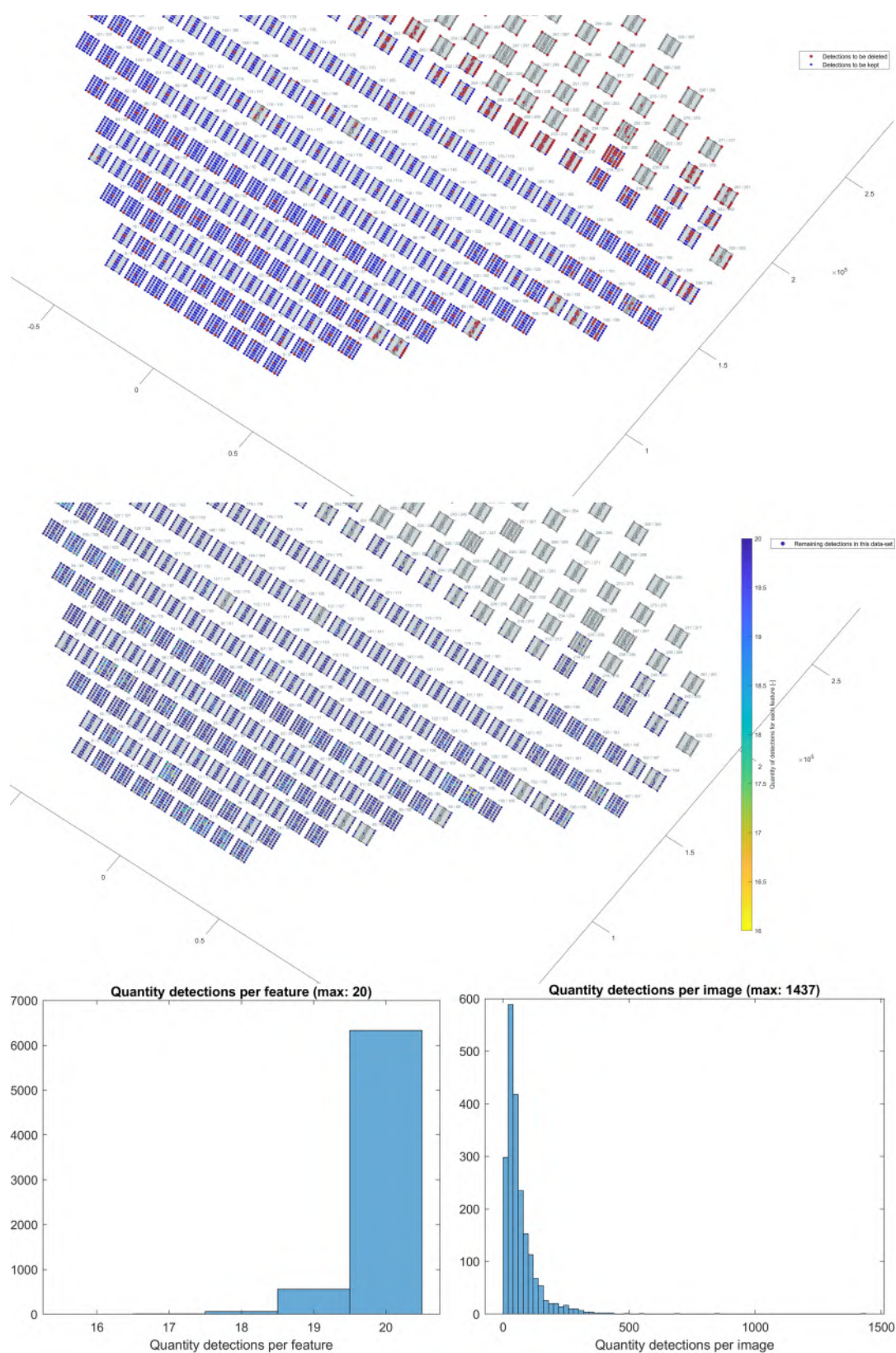


Figure C.4: CESA-1-2020, CESA-1-2020 Part I, CESA-1-2020 Part II: Focusing on the altitude fluctuation of oblique flights. The standard deviations of the z-coordinate is 0.95 m for 2018, and 1,4 m for 2020.



**Figure C.5:** PHC-file generation for AICON, image and detections reduction. CESA-1-2020, original data-set. Filter applied: 1) angular appliance  $10^\circ$ , Cartesian appliance 5m, detection similarity 90%. 2) **Maximum 15 detections per feature**)



**Figure C.6:** PHC-file generation for AICON, image and detections reduction. CESA-1-2020, original data-set. Filter applied: 1) angular appliance  $10^\circ$ , Cartesian appliance 5m, detection similarity 90%. 2) **Maximum 20 detections per feature**)

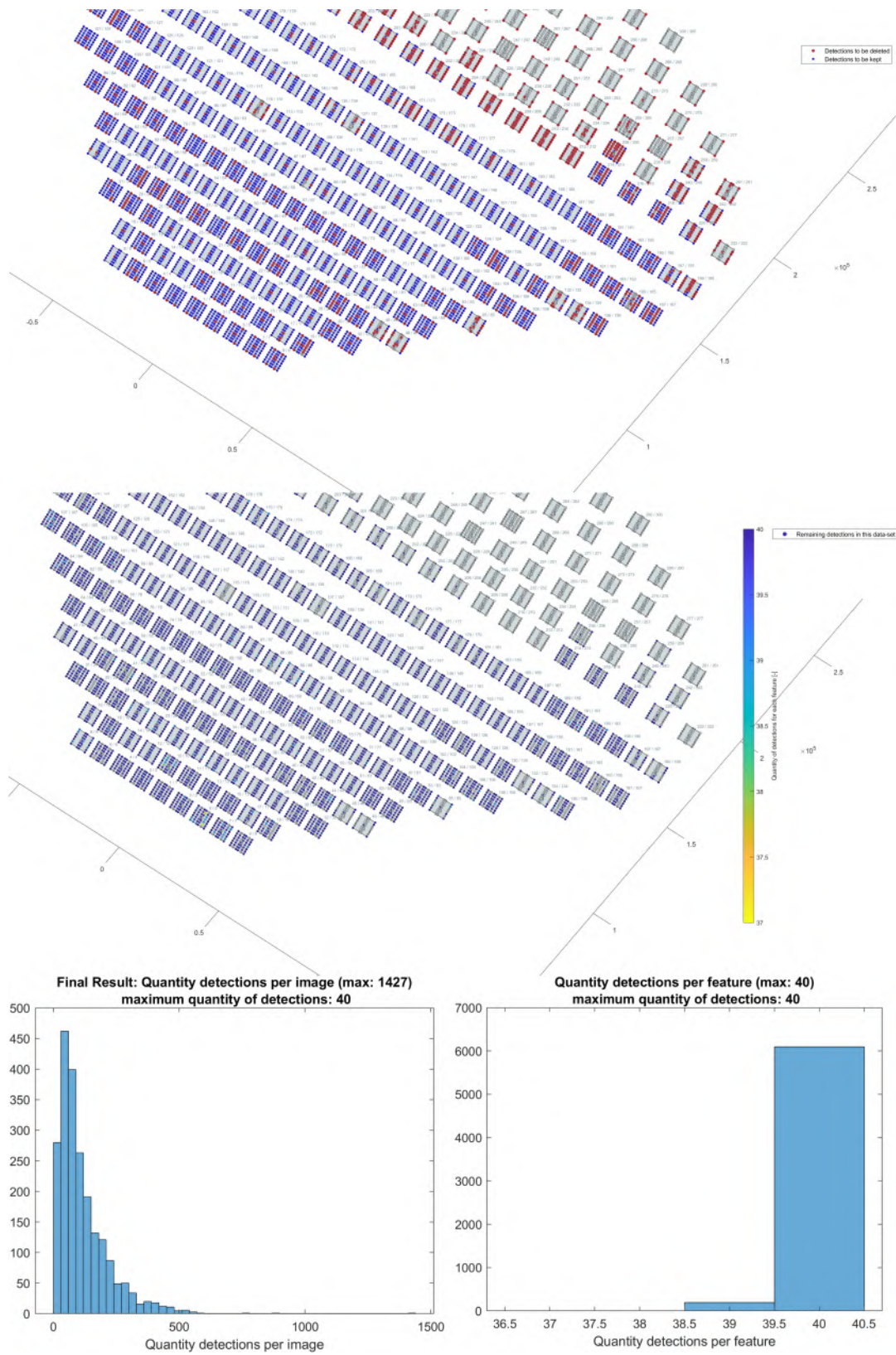


**Figure C.7:** PHC-file generation for AICON, image and detections reduction. CESA-1-2020, original data-set. Filter applied: 1) angular appliance  $10^\circ$ , Cartesian appliance 5m, detection similarity 90%. 2) **Maximum 40 detections per feature**)

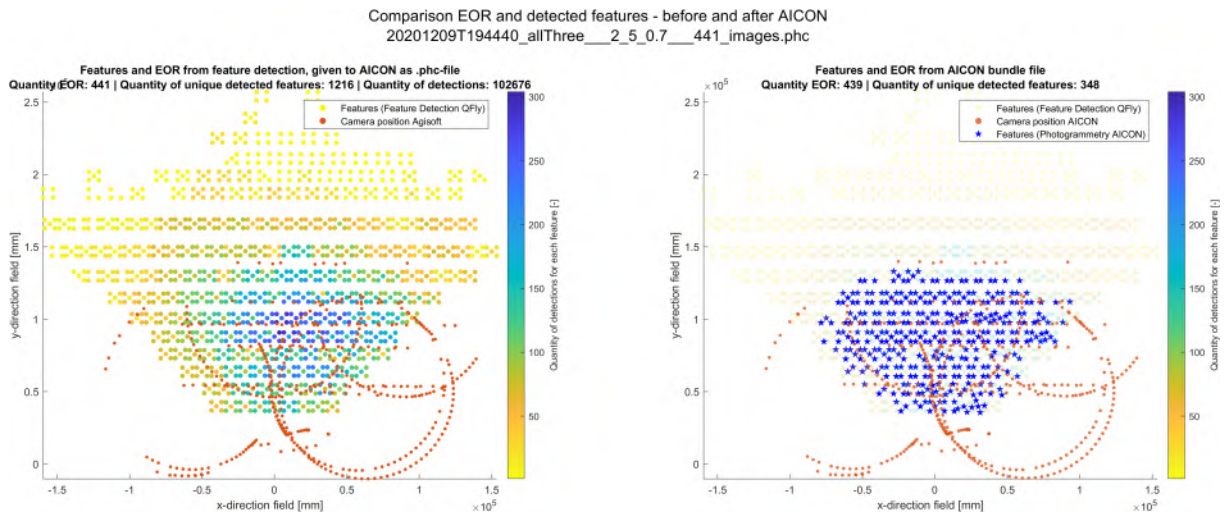


**Figure C.8:** comparison of EOR and detections in .phc file creation (Matlab) by applying “AICONRED\_fullfilter” filter and after calculation in AICON. Input image count 441, filter parameters 2m EOR, 5° viewing direction, 70% match of detections.

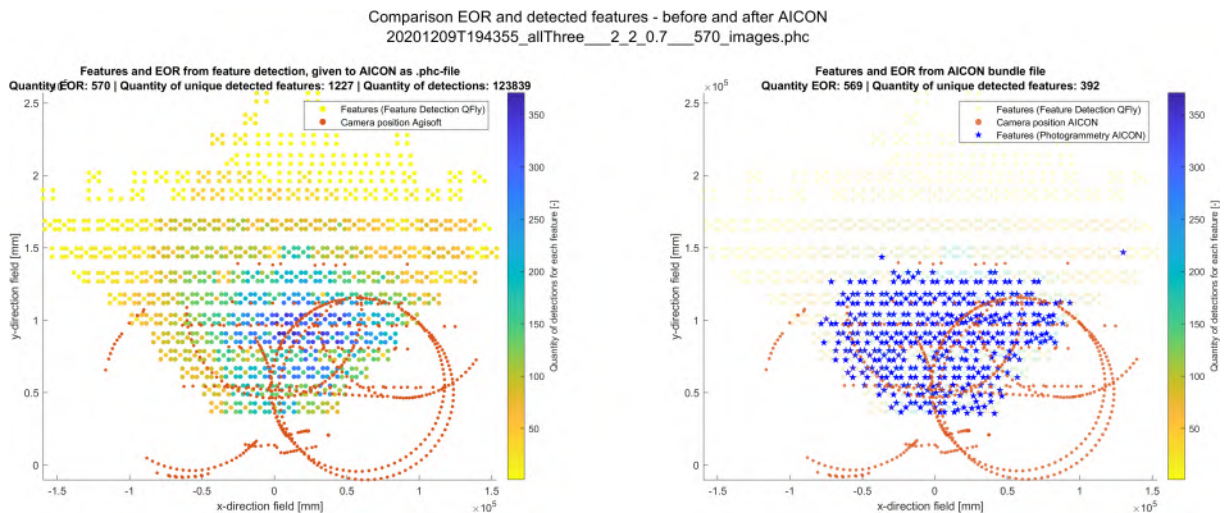


**Figure C.9:** comparison of EOR and detections in .phc file creation (Matlab) by applying “AICONRED\_fullfilter” filter as well as after calculation in AICON. Input image count 570, filter parameters 2m EOR, 2° viewing direction, 70% match of detections

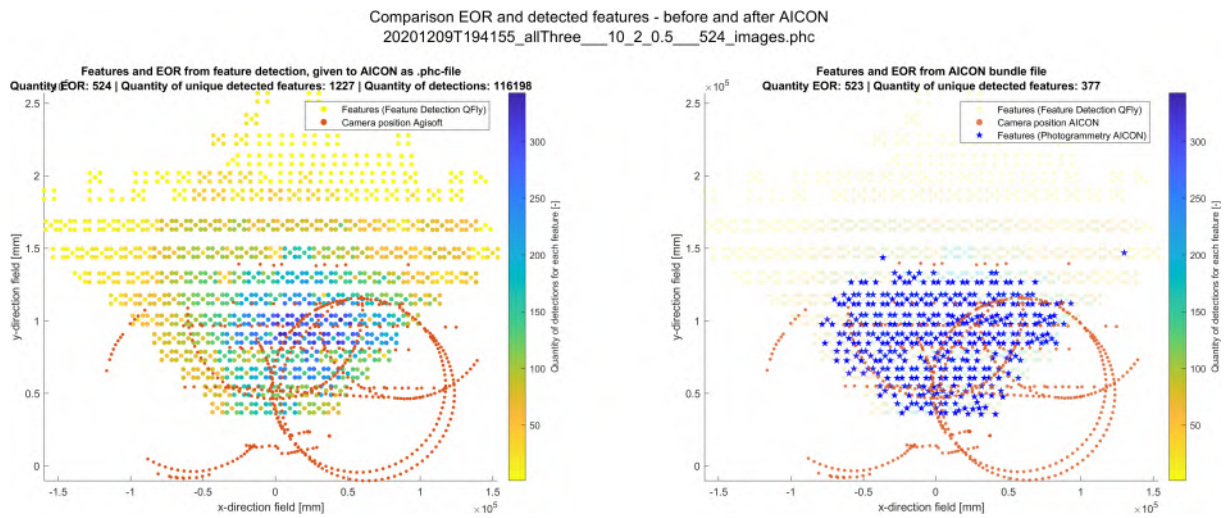


**Figure C.10:** comparison of EOR and detections in .phc file creation (Matlab) by applying “AICONRED\_fullfilter” filter as well as after calculation in AICON. Input image count 524, filter parameters 10m EOR, 2° viewing direction, 50% match of detections

AICON objectCoords RMS compared to base model: 20201120\_consecutive\_stepped

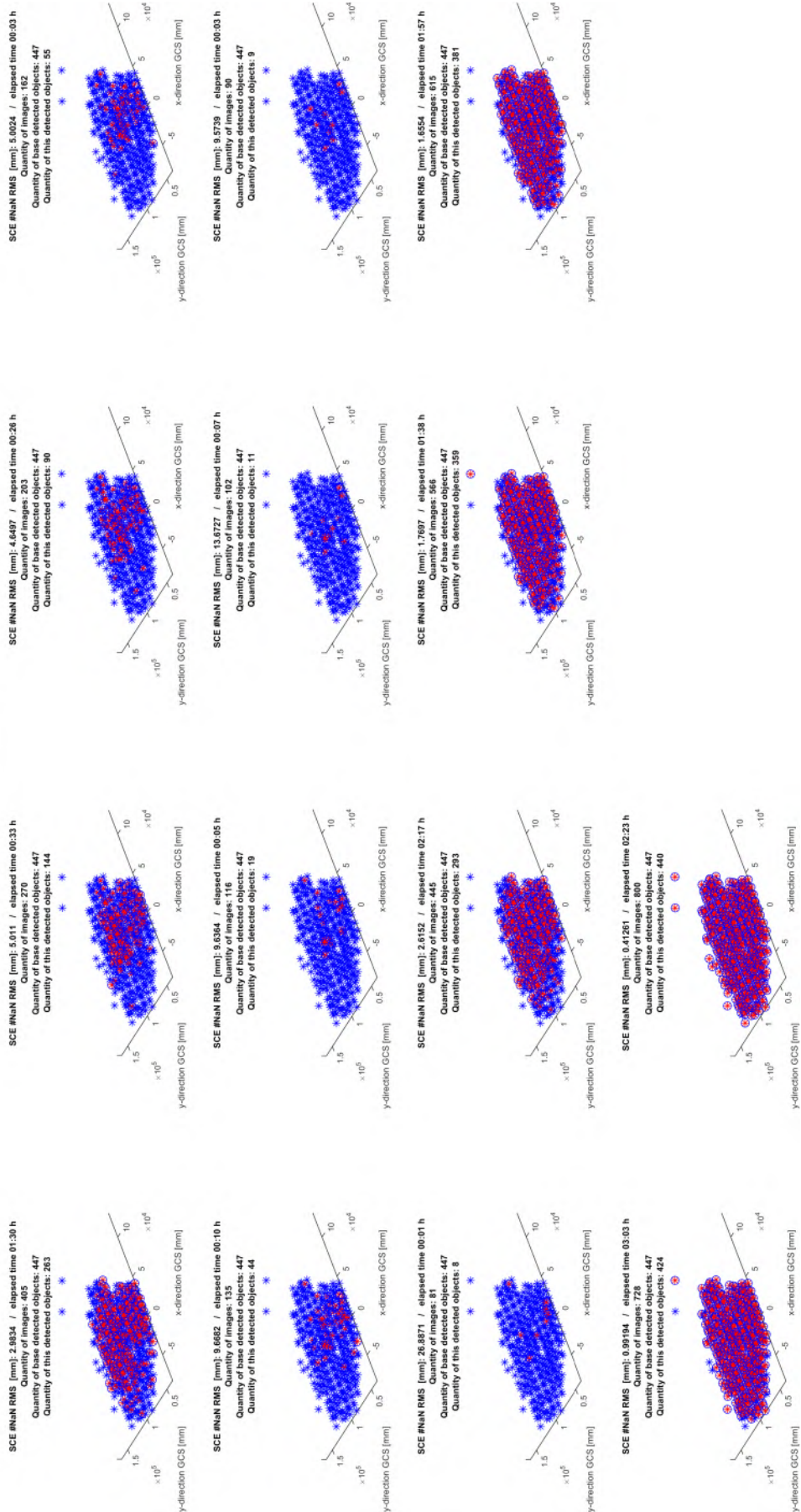


Figure C.11: Remaining residuals for test series “AICONRED\_stepped”

AICON objectCoords RMS compared to base model: 20201123\_consecutive\_percent

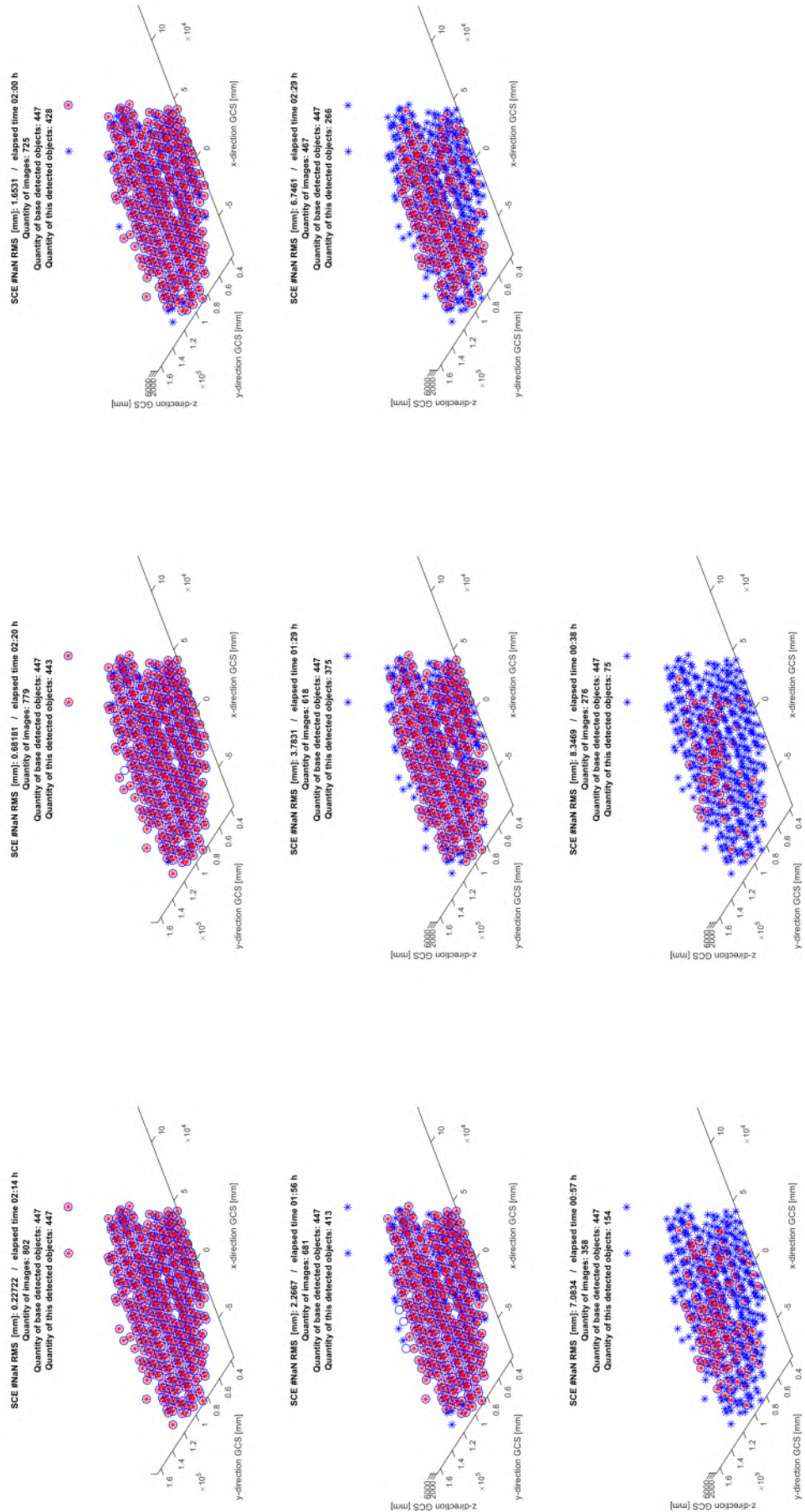


Figure C.12: Remaining residuals for test series “AICONRED\_percent”

AICON objectCoords RMS compared to base model: 20201124\_quality\_Q1\_area

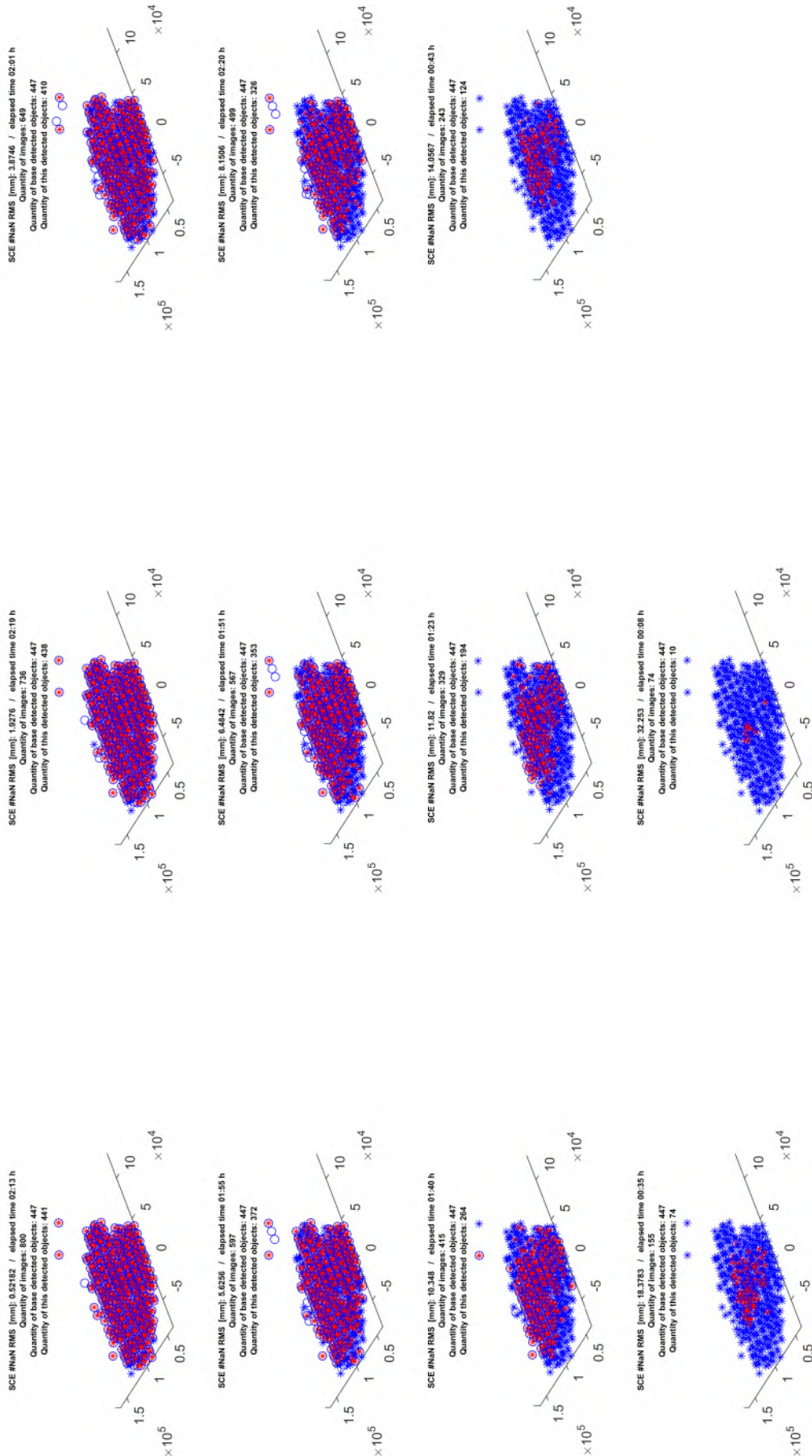


Figure C.13: Remaining residuals for test series “AICONRED\_area”

AICON objectCoords RMS compared to base model: 20201124\_quality\_O1\_area

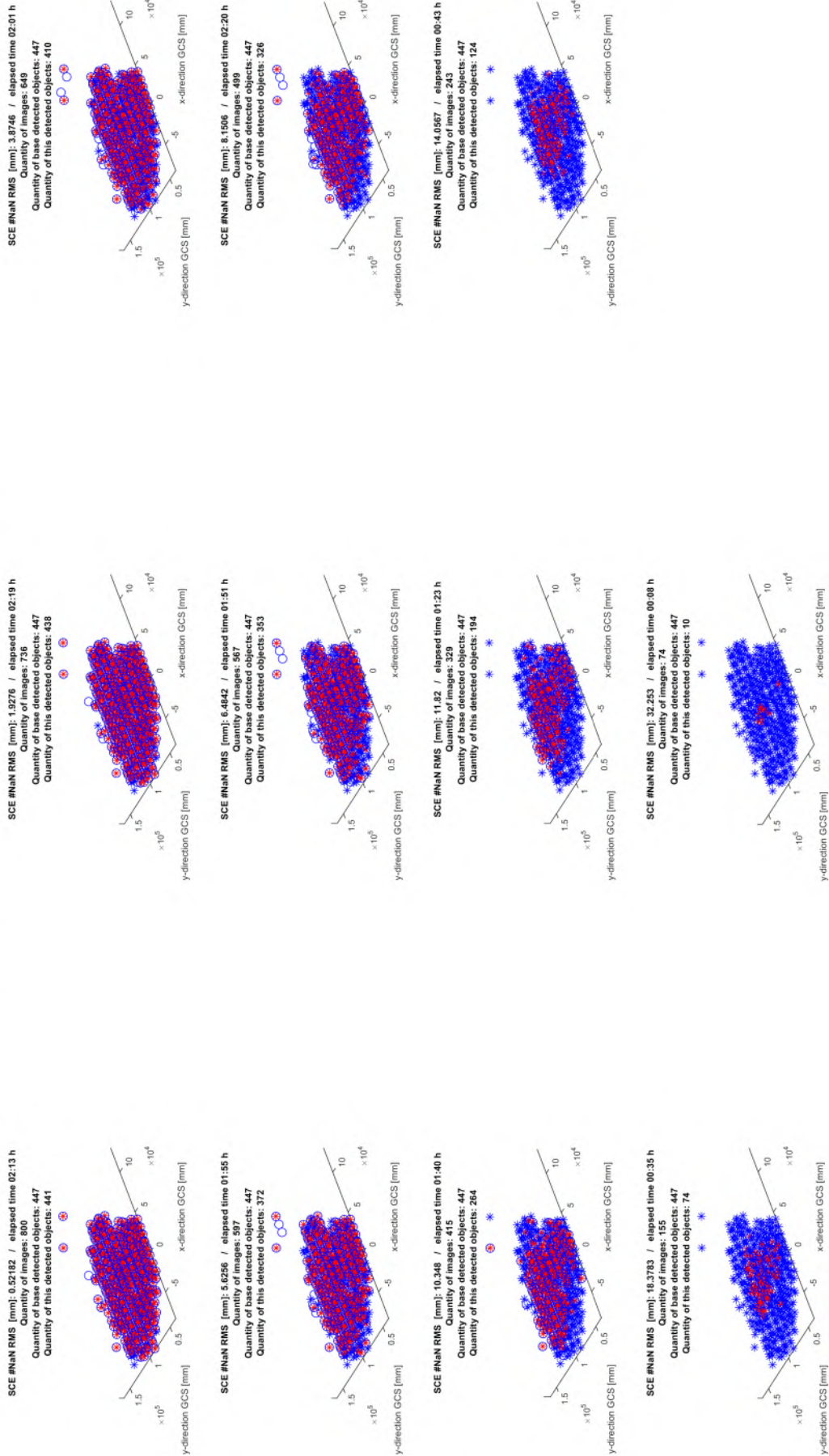


Figure C.14: Remaining residuals for test series “AICONRED\_fullfilter”

Image reduction through fixed steps:  
Every [0.45]th image. --> 445 images remaining.

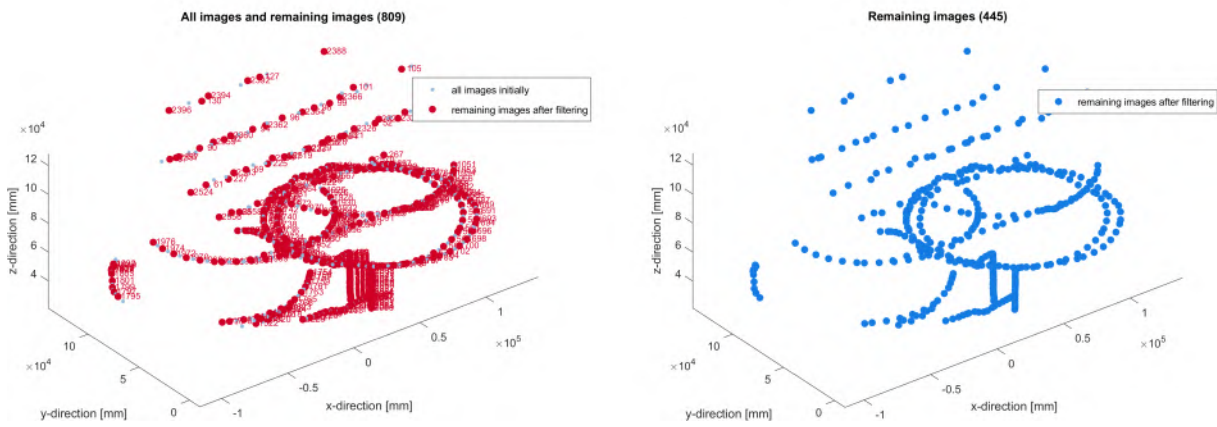


Figure C.15: Creation of AICONRED\_steped dataset by image reduction - every tenth image

Image reduction through fixed steps:  
Every [0.1]th image. --> 728 images remaining.

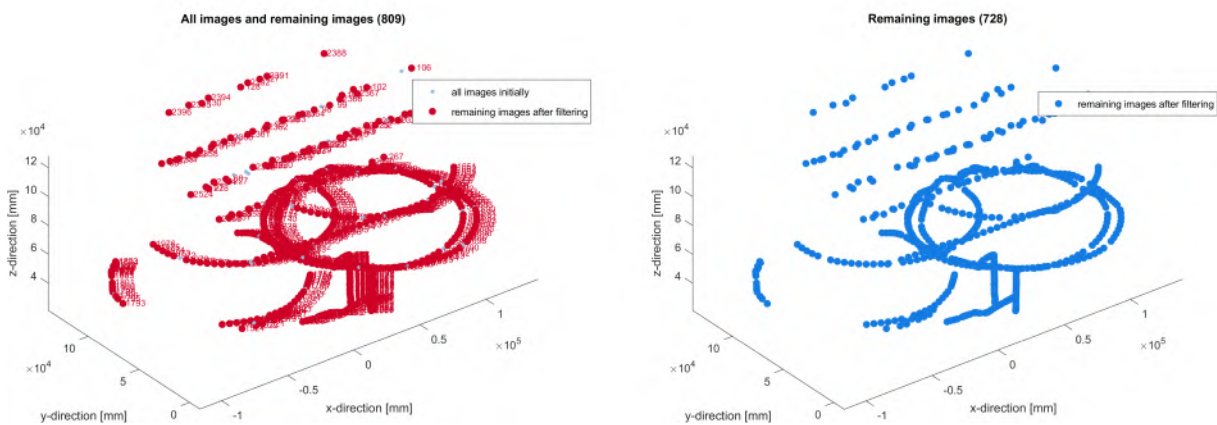


Figure C.16: Creation of AICONRED\_steped dataset by image reduction - every tenth image

Image reduction through fixed steps:  
Every [0.01]th image. --> 800 images remaining.

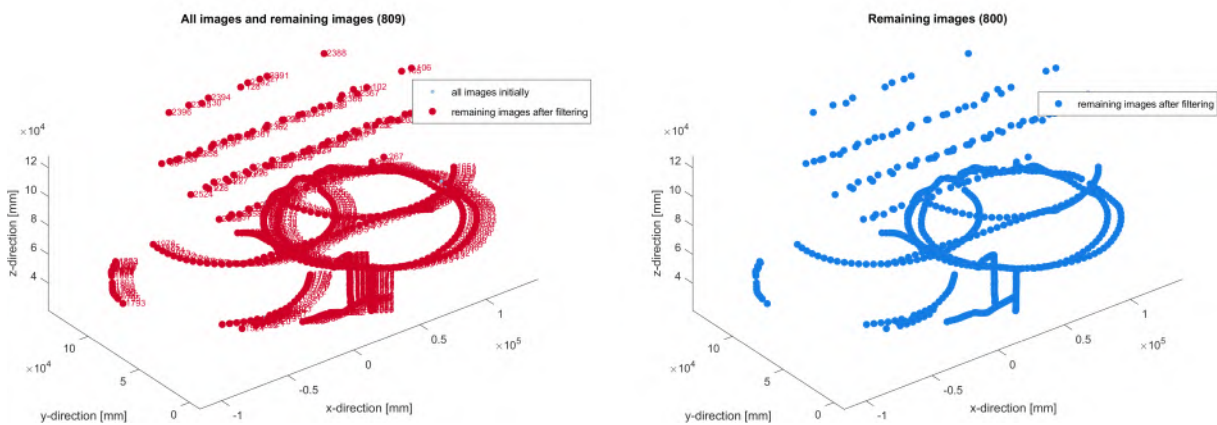


Figure C.17: Creation of AICONRED\_steped dataset by image reduction - every tenth image

Image reduction through fixed steps:  
Every [2]th image. --> 405 images remaining.

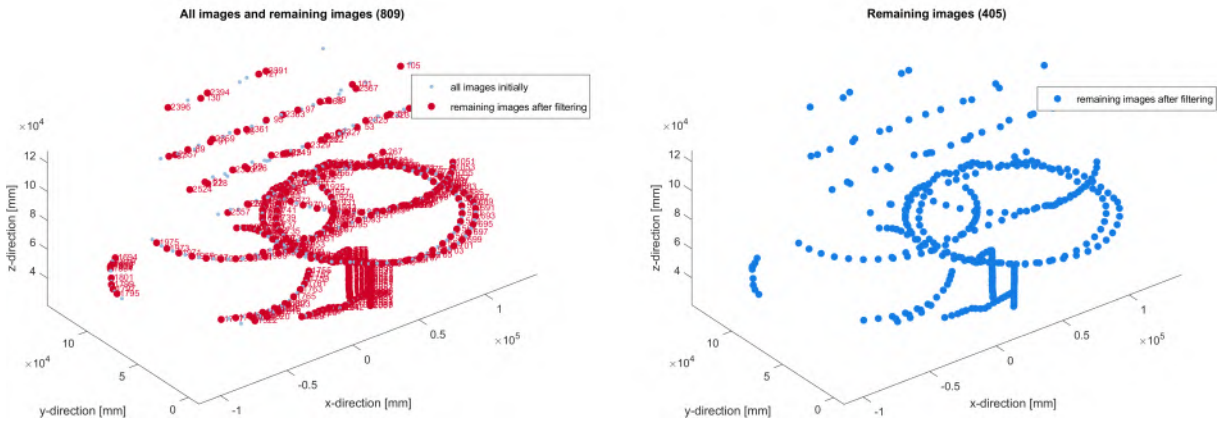


Figure C.18: Creation of AICONRED\_steped dataset by image reduction - every tenth image

Image reduction through fixed steps:  
Every [3]th image. --> 270 images remaining.

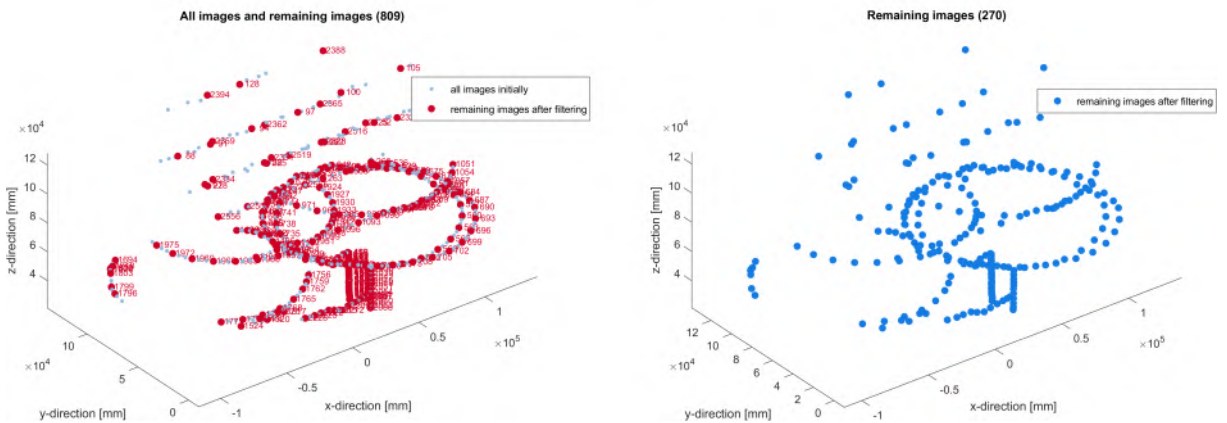


Figure C.19: Creation of AICONRED\_steped dataset by image reduction - every tenth image

Image reduction through fixed steps:  
Every [4]th image. --> 203 images remaining.

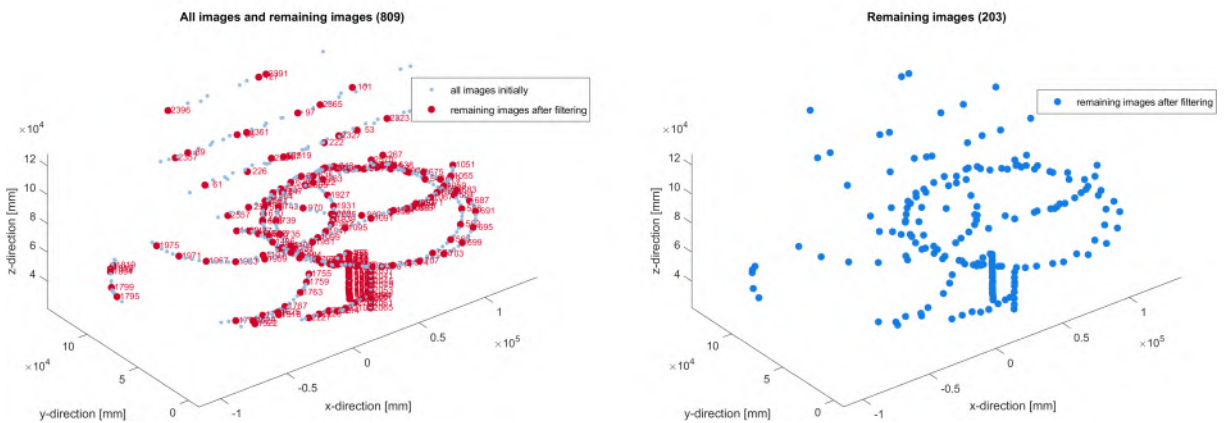


Figure C.20: Creation of AICONRED\_steped dataset by image reduction - every tenth image

Image reduction through fixed steps:  
Every [5]th image. --> 162 images remaining.

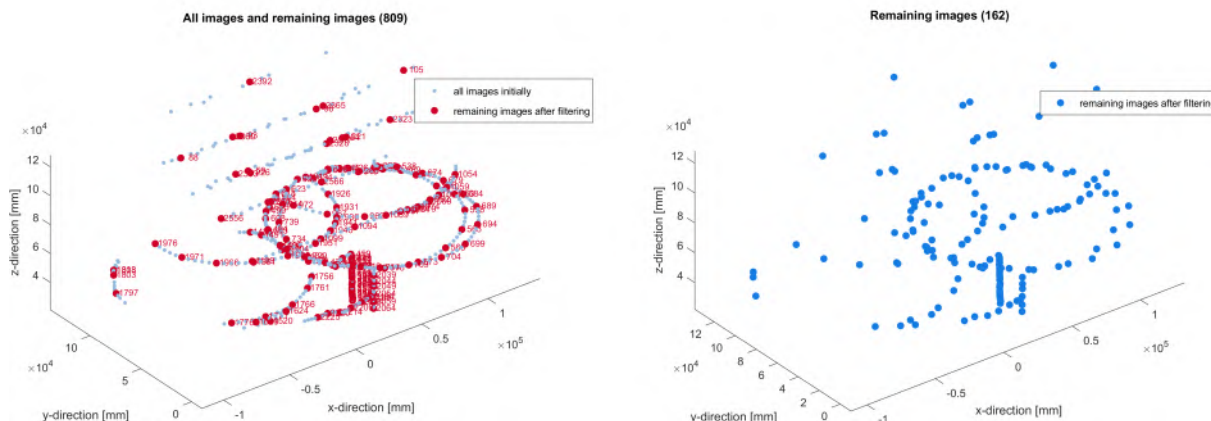


Figure C.21: Creation of AICONRED\_steped dataset by image reduction - every tenth image

Image reduction through fixed steps:  
Every [6]th image. --> 135 images remaining.

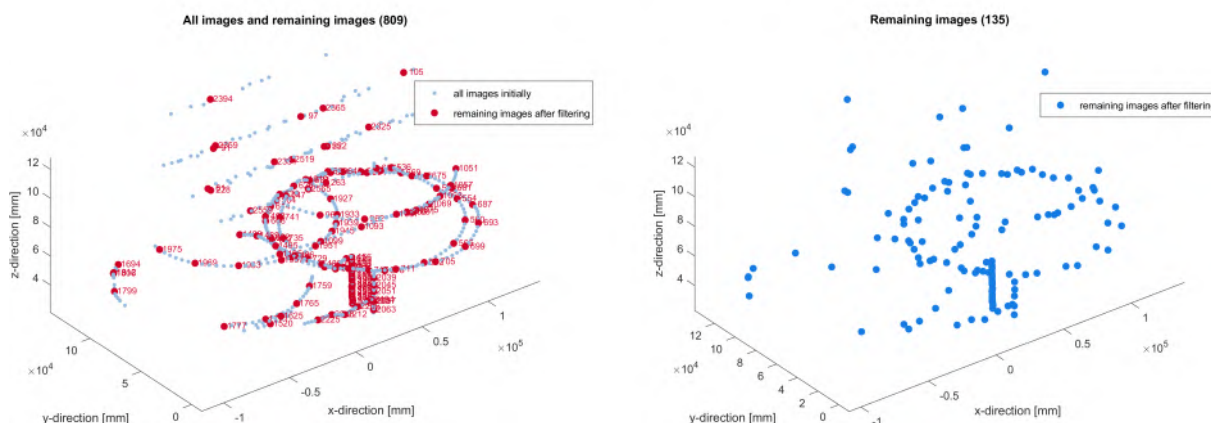


Figure C.22: Creation of AICONRED\_steped dataset by image reduction - every tenth image

Image reduction through fixed steps:  
Every [7]th image. --> 116 images remaining.

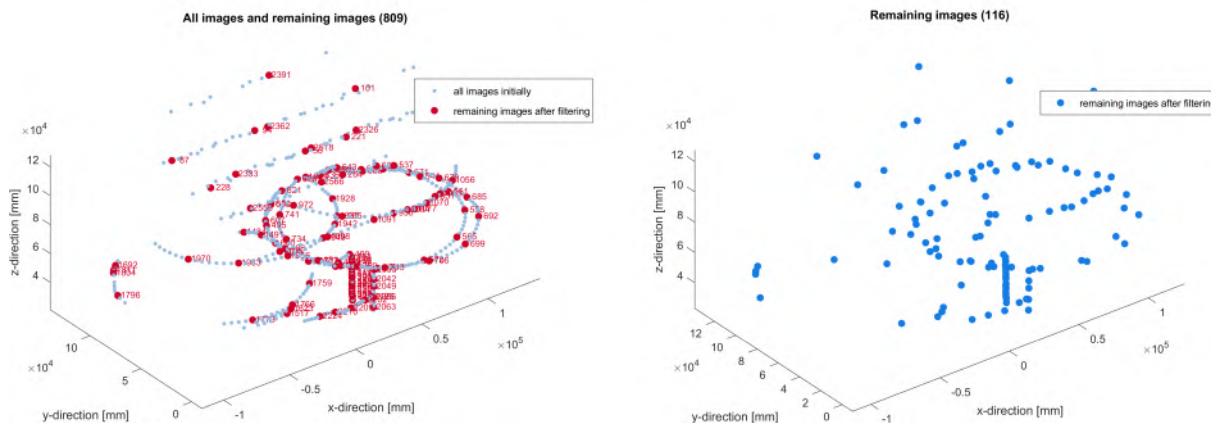


Figure C.23: Creation of AICONRED\_steped dataset by image reduction - every tenth image

FDM orientation vectors for 20201125\_000411\_Serie\_14\_start\_1456\_H0201\_H0202\_H0204\_H0206\_results.mat

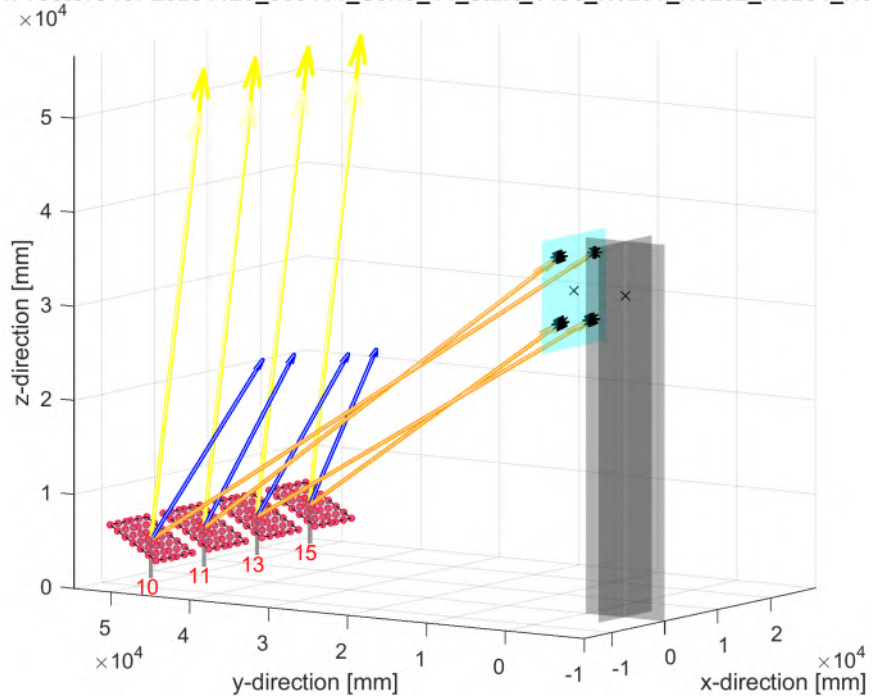


Figure C.24: FDM results for series 14, CESA-1-2020

FDM orientation vectors for 20201124\_235921\_Serie\_13\_start\_1414\_H0104\_H0106\_H0108\_H0210\_results.mat

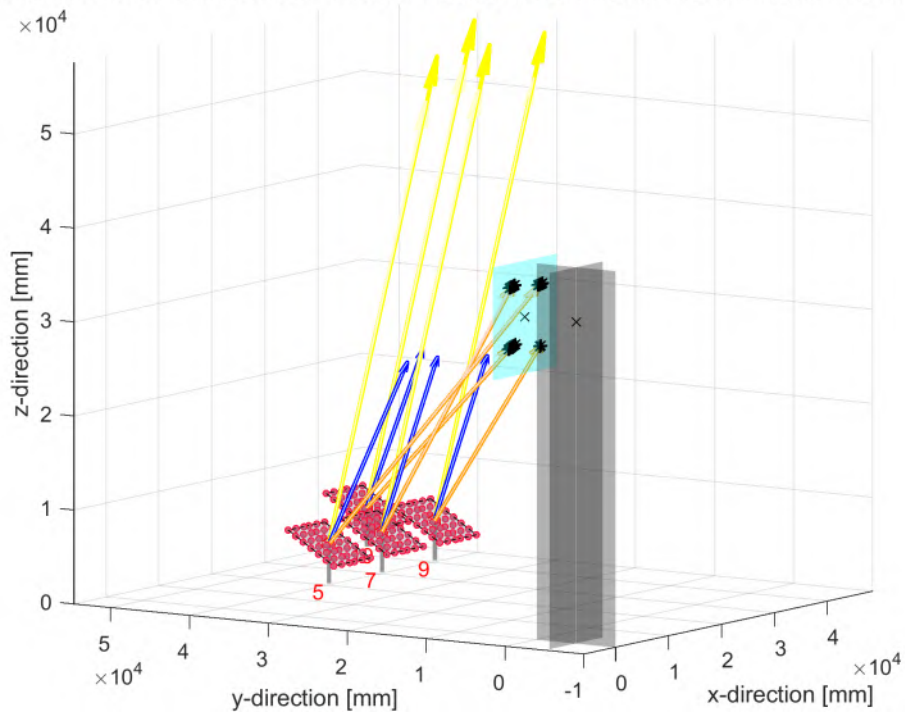


Figure C.25: FDM results for series 13, CESA-1-2020

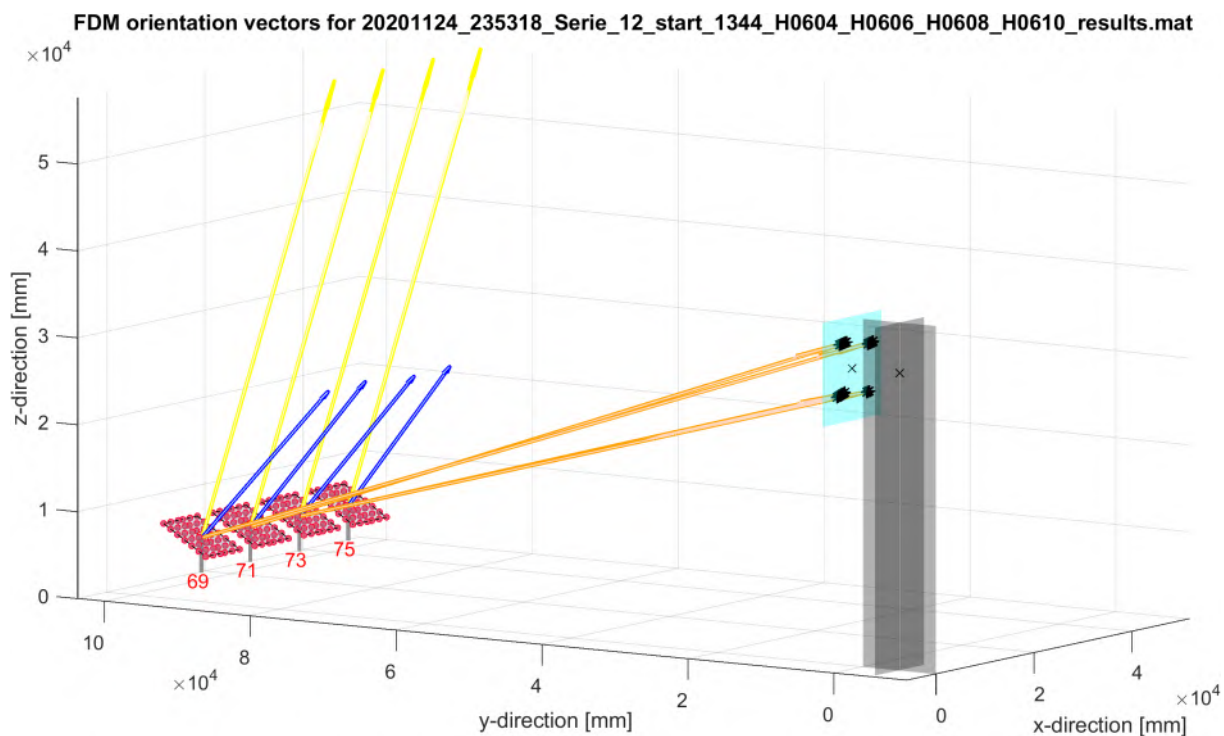


Figure C.26: FDM results for series 12, CESA-1-2020

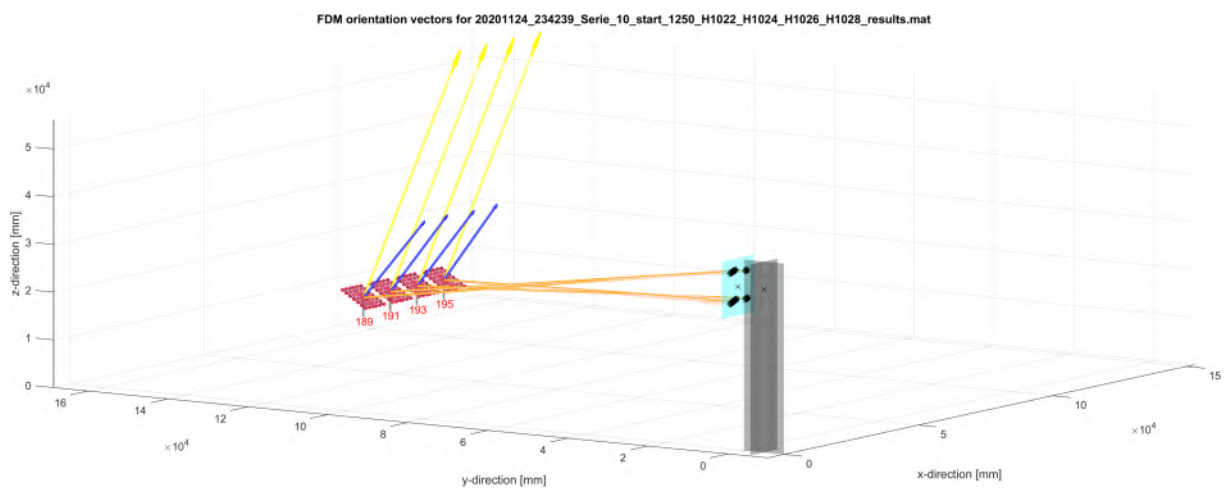
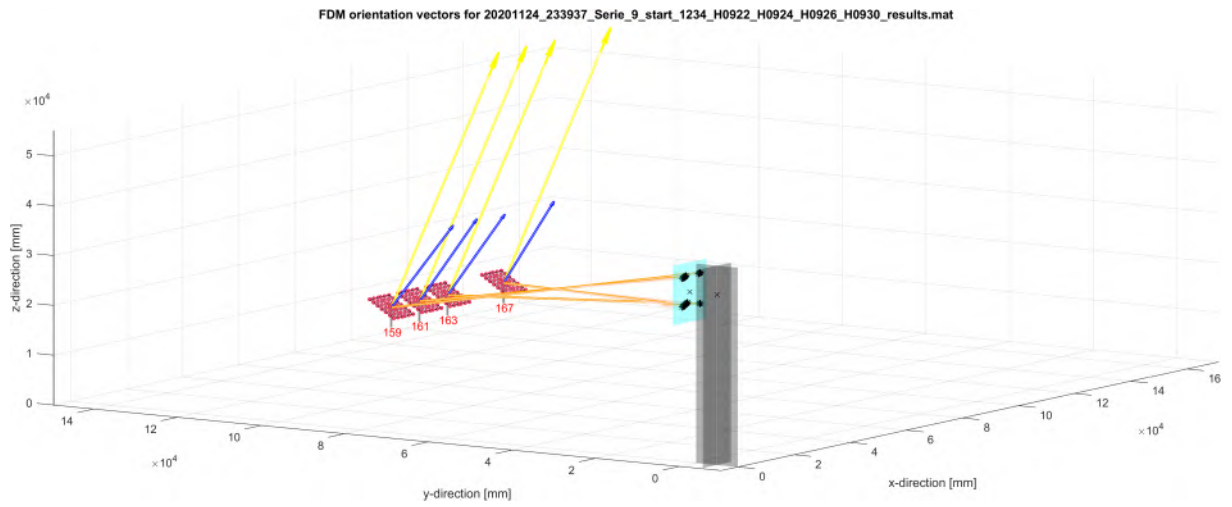
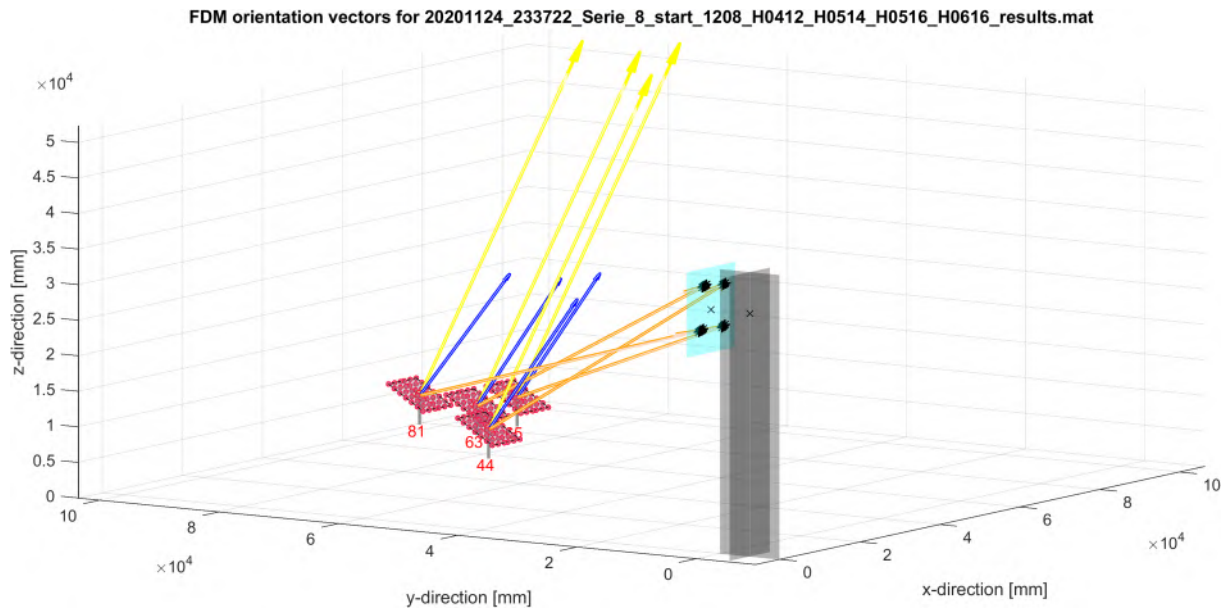


Figure C.27: FDM results for series 10, CESA-1-2020



**Figure C.28:** FDM results for series 9, CESA-1-2020



**Figure C.29:** FDM results for series 8, CESA-1-2020

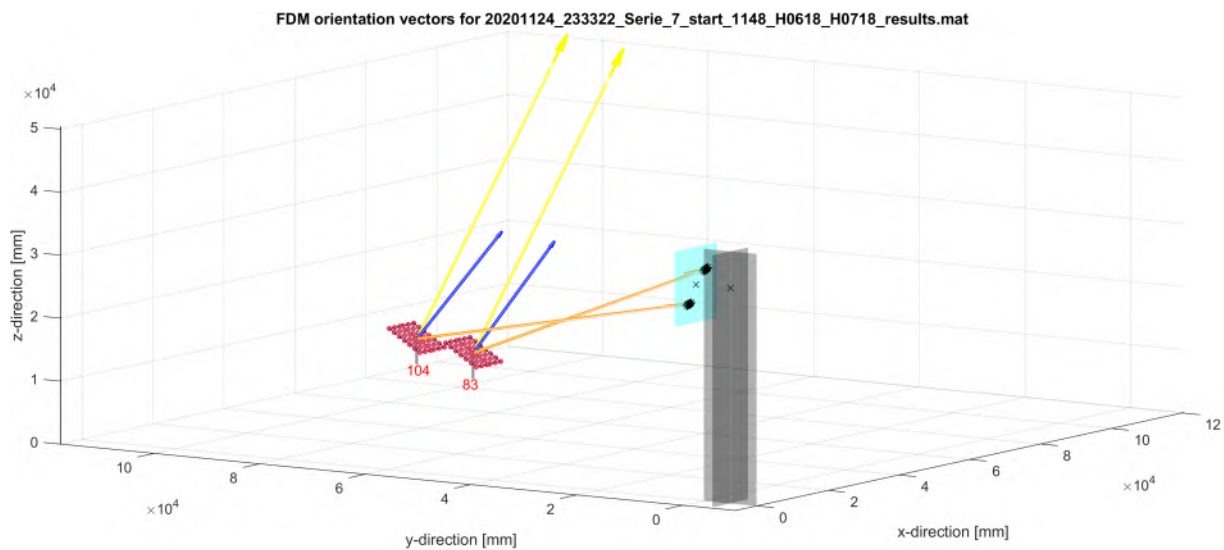


Figure C.30: FDM results for series 7, CESA-1-2020

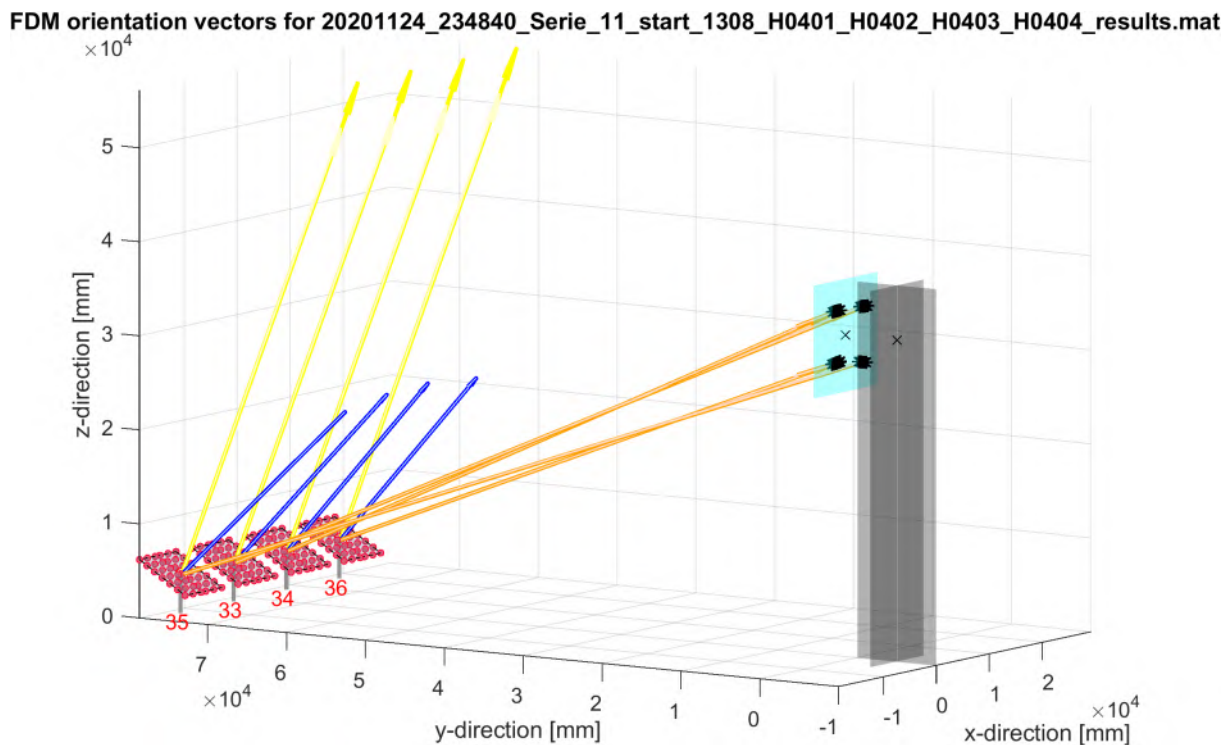
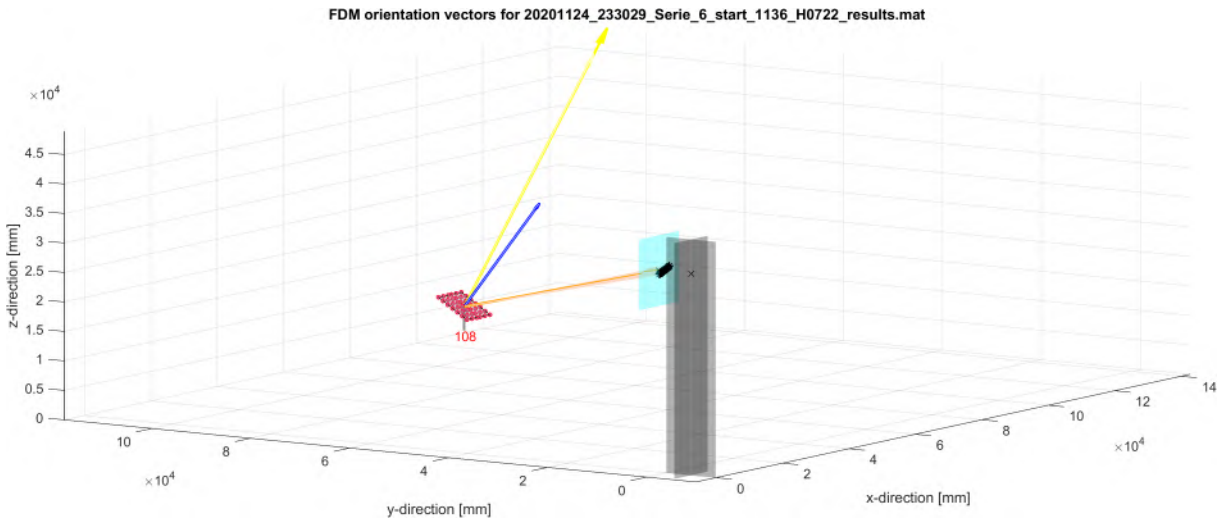
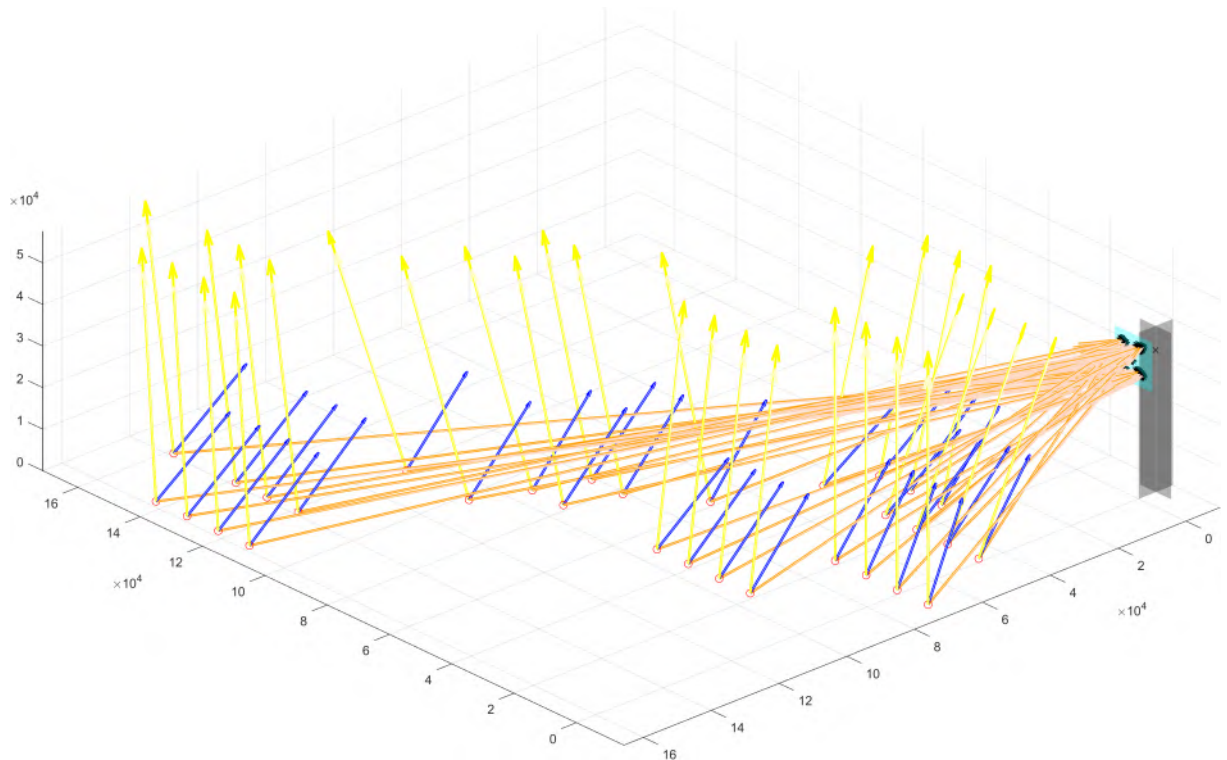


Figure C.31: FDM results for series 11, CESA-1-2020



**Figure C.32:** FDM results for series 6, CESA-1-2020



**Figure C.33:** All FDM results, CESA-1-2020

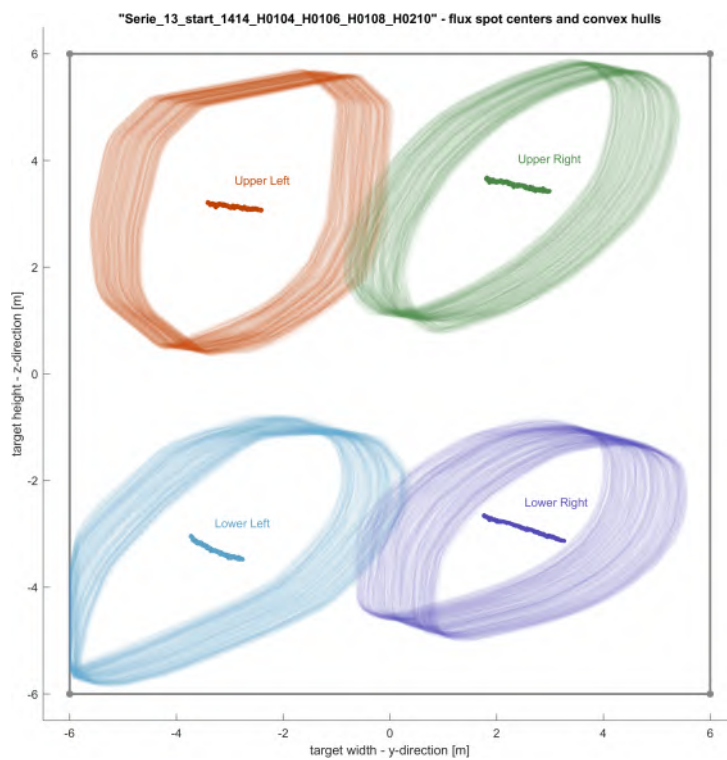


Figure C.34: CESA-1-2020, Flux spot movement of Series 13

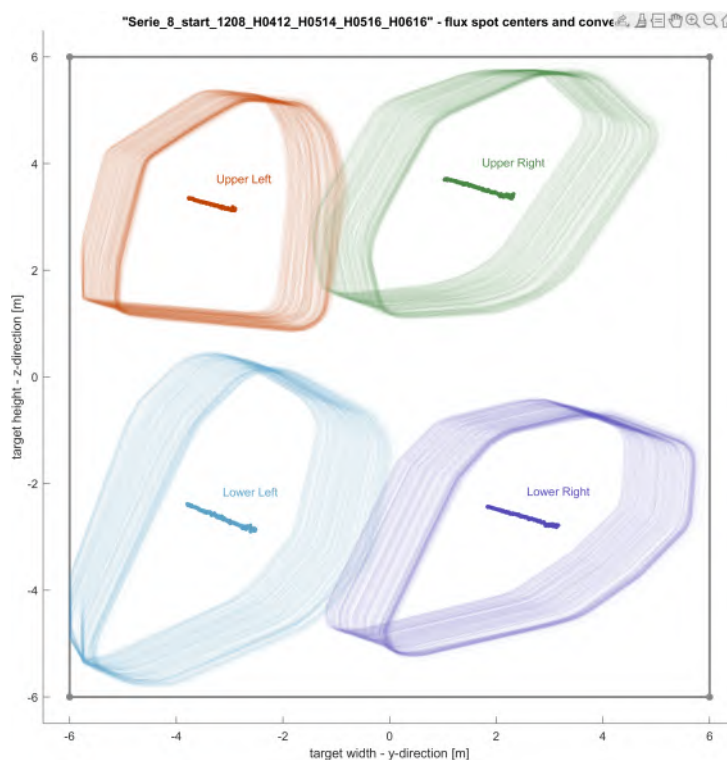


Figure C.35: CESA-1-2020, Flux spot movement of Series 8

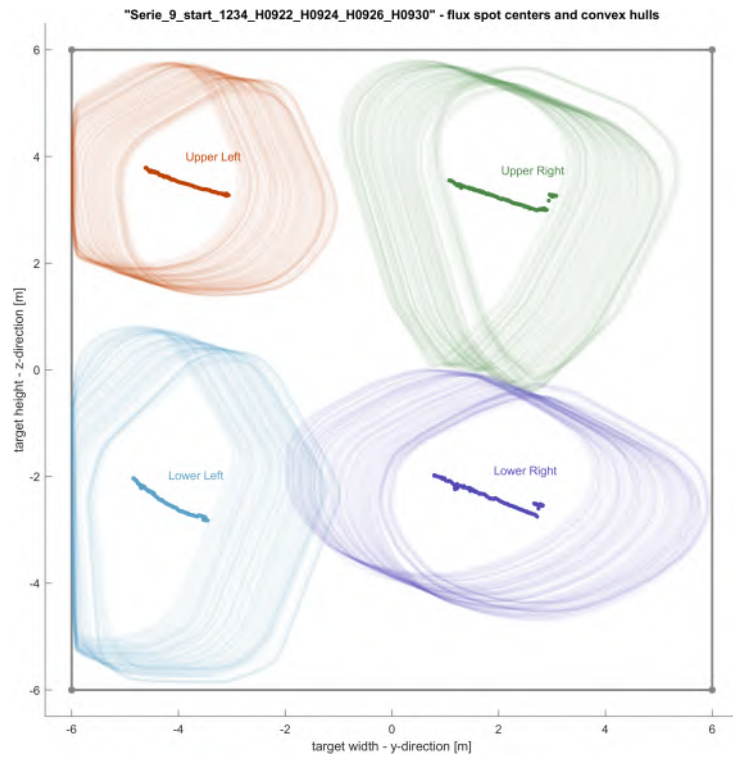


Figure C.36: CESA-1-2020, Flux spot movement of Series 9

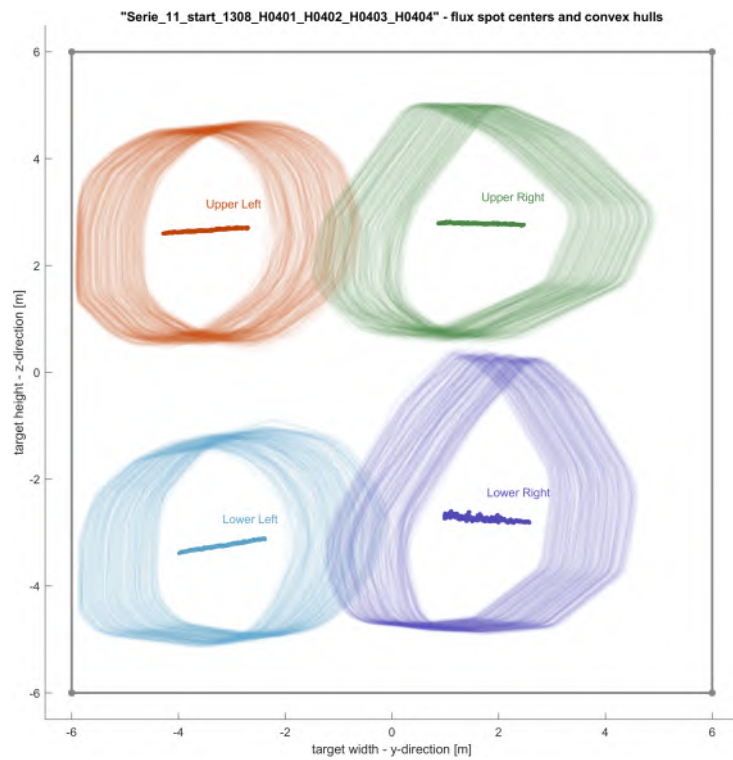


Figure C.37: CESA-1-2020, Flux spot movement of Series 11

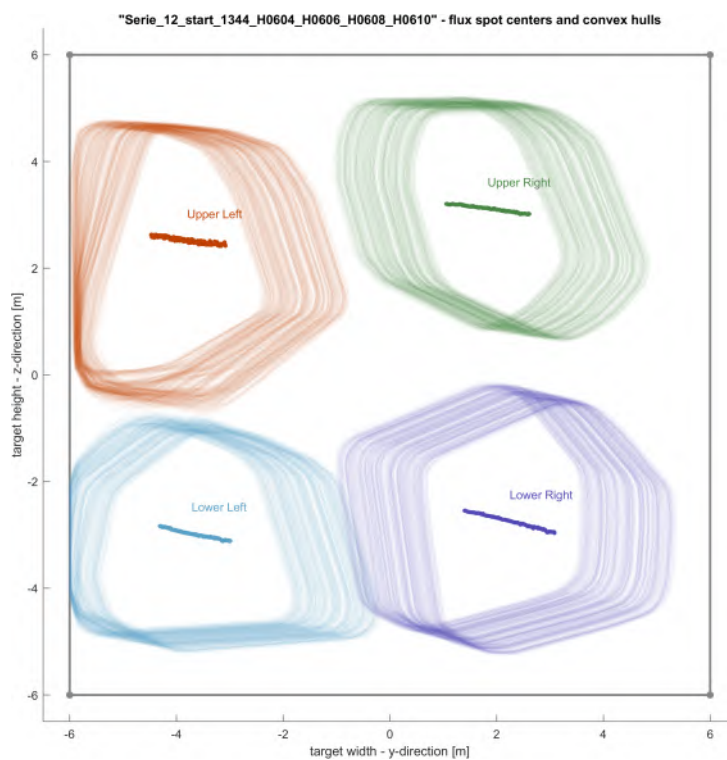


Figure C.38: CESA-1-2020, Flux spot movement of Series 12

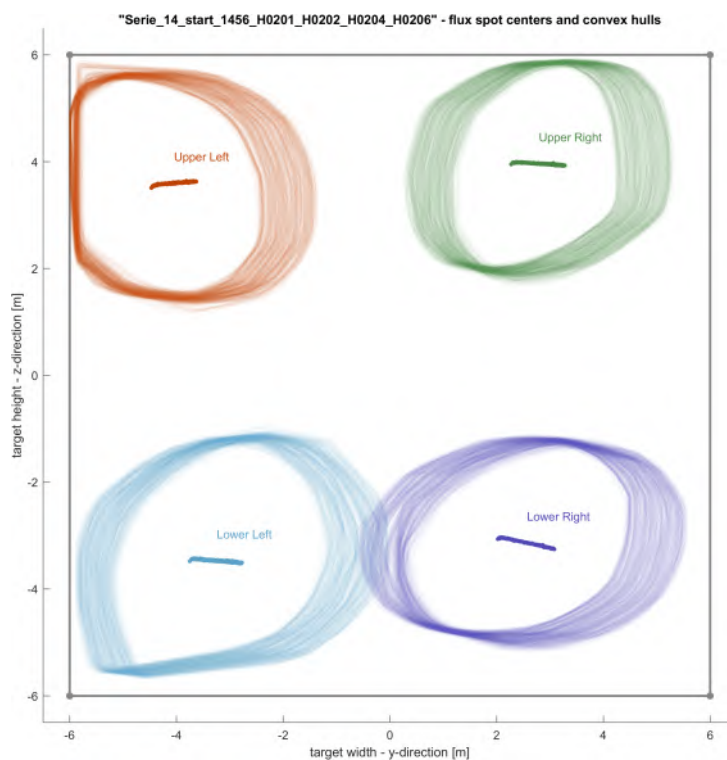


Figure C.39: CESA-1-2020, Flux spot movement of Series 14



**Figure C.40:** CESA-1-2020, Flux density measurement, series 9. Especially the lower left heliostat indicates that its mirror facets are misaligned.



## D Flowcharts

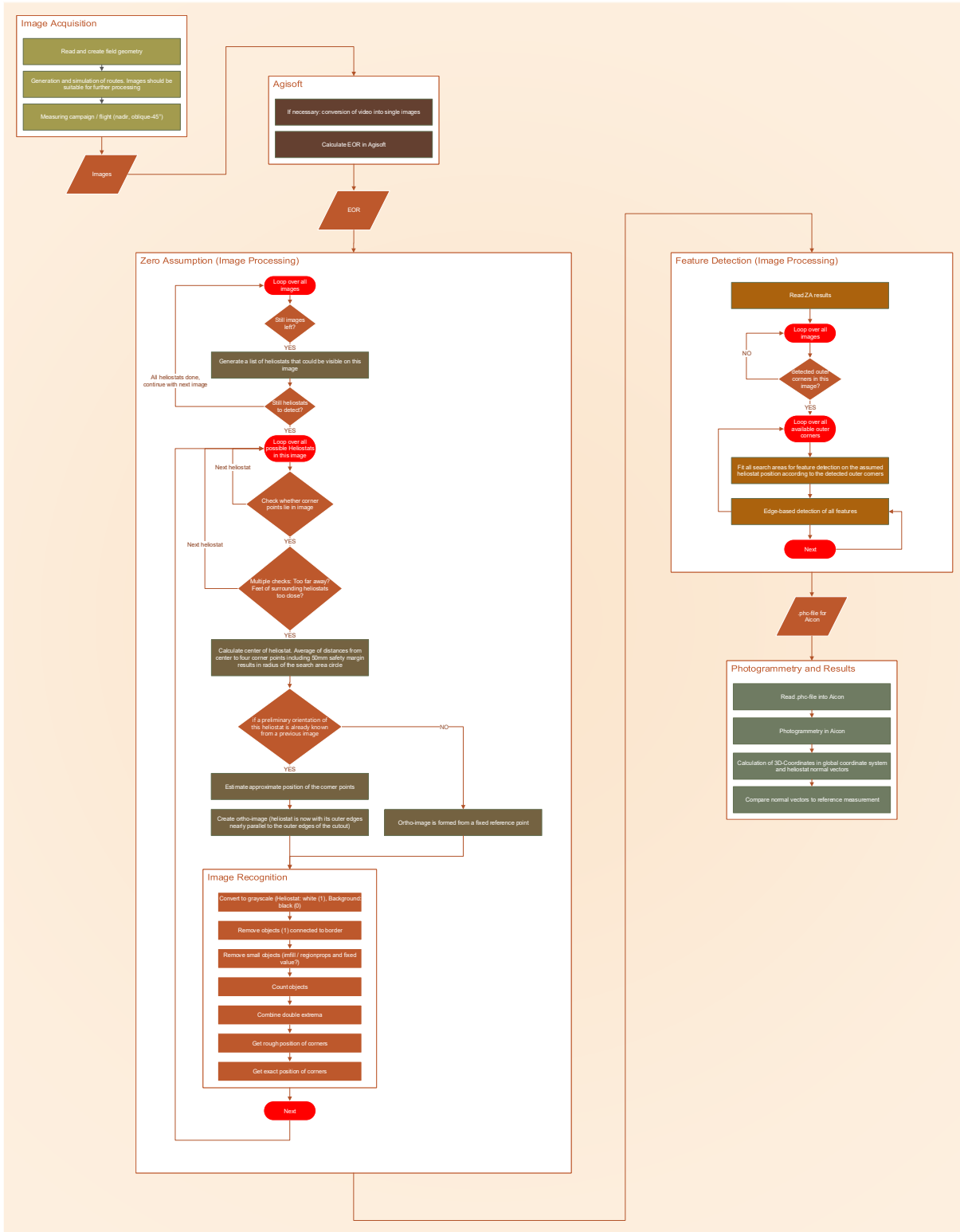


Figure D.1: Program structure of 1st part of QFLY for solar tower power plant (STPP) “photogrammetry”

## E Further Images



a) Quadcopter shortly after takeoff, use for circling flight.



b) Base Camp: recording of flight routes, preparation of UAV, battery change.



c) Added Targets for Hand Photogrammetry on Heliostat 159.



d) Performance of hand photogrammetry: Taking different angles of view with camera, plus lifting platform.

**Figure E.1:** Plataforma Solar de Almería<sup>1</sup> (PSA), CESA-1: Measurement campaign, performed on 09.07.2020, 9:00 AM - 8:00 PM. Preparation time: 1 day (06.07.2020). Performed measurements: QFLY nadir and circling flights, hand photogrammetry, deflectometry, total station measurement. Five team members: Wilko Jessen, Christoph Prahl, Benjamin Brix, David Muruve Tejada and Michael Fischer.



**Figure E.2:** The Ivanpah Solar Electric Generating System is a concentrated solar thermal plant in the Mojave Desert. It is located at the base of Clark Mountain in California. [74]

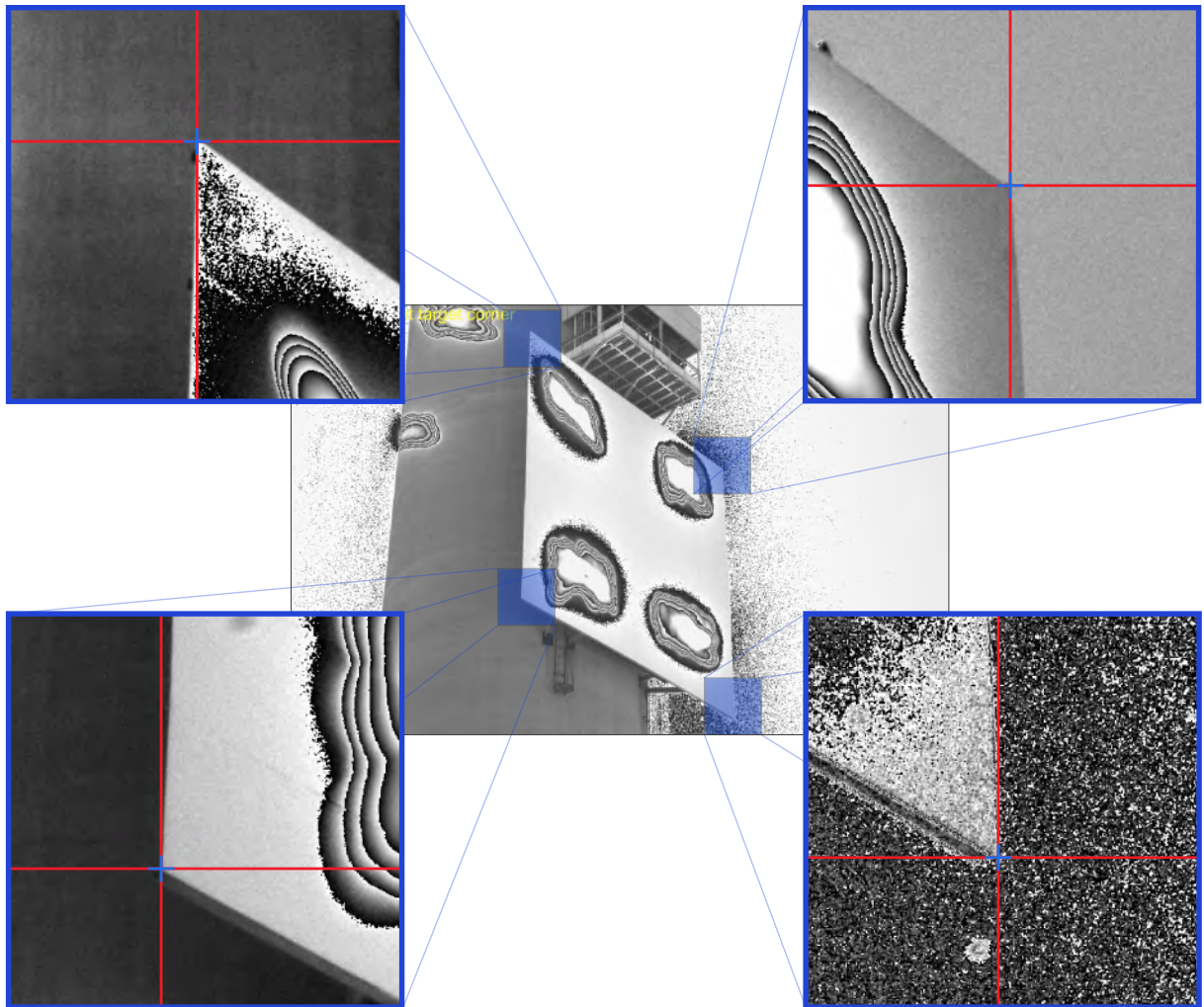
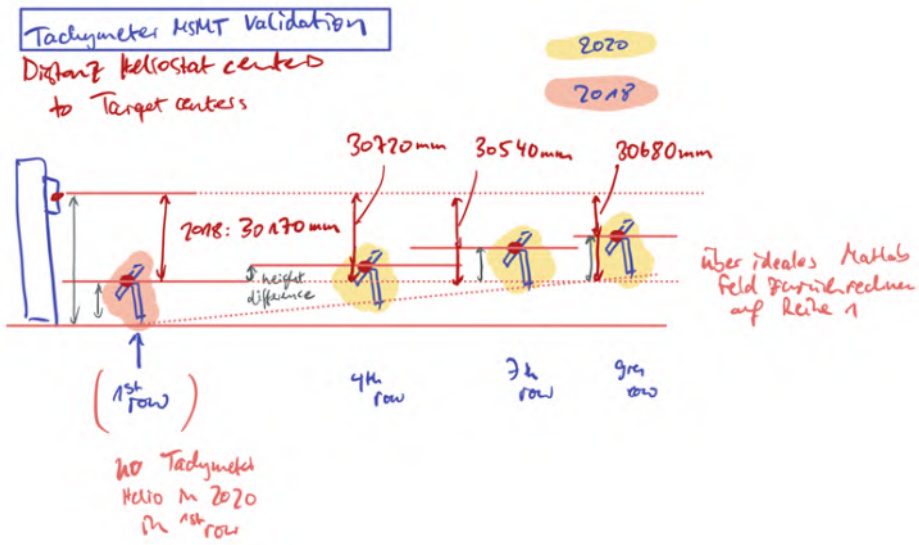
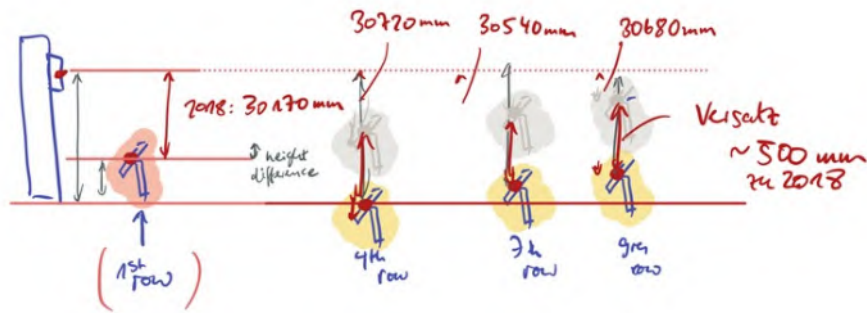


**Figure E.3:** Selecting the outer corners of the target – the revised script brings some improvements: If several image series are to be evaluated at once, the user has the possibility to read in all corners at the beginning of the program, whereupon the program automatically calculates the flux spot centers of gravity for all series afterwards. In addition, all target positions are stored in a .mat file, which are automatically read in during a later calculation run.



a) Methodology.



b) Apparent offset of heliostats in z-direction compared to 2020 measurement.

Figure E.4: Difference in Tachy measurements heights.

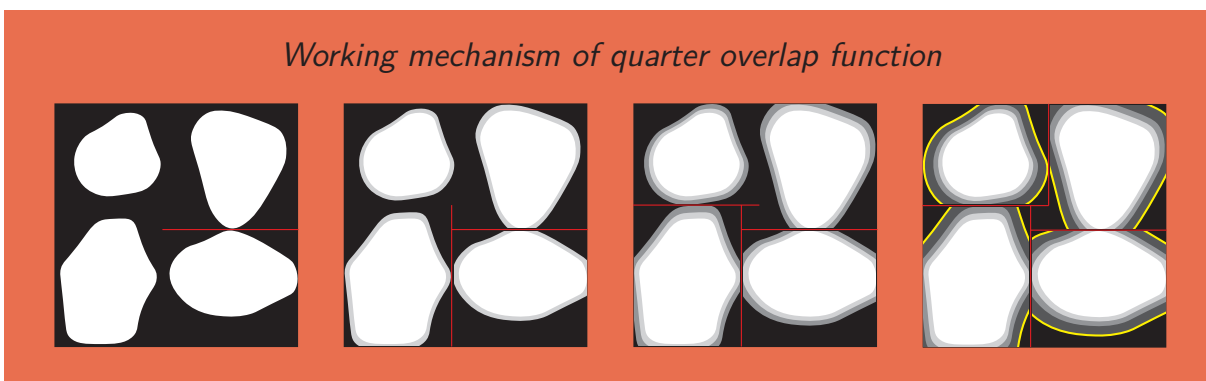


Figure E.5: Working mechanism of the image recognition: The images are related in time and are interpreted from left to right. As soon as one area intersects with another, a fictitious barrier is created. This happens successively until all four areas have reached their maximum extent.

## **F Data sheets**

### **F.1 Tachymeter: Trimble S8**

## EIGENSCHAFTEN

Neue, flexiblere Trimble-Totalstationsplattform bietet zusätzliche Anwendungsmöglichkeiten

Vielfältigere Geschäftsmöglichkeiten mit kompletter Unterstützung für die Ingenieurgeodäsie, z. B. Überwachungsmessungen

MagDrive-Servomotoren für maximale Geschwindigkeit und Effizienz

MultiTrack™-Technik zur Verfolgung aktiver und passiver Prismen



Die Trimble® S8-Totalstation ist unser fortschrittlichstes Tachymeter. Die Trimble S8 ist auf unerreichte Leistung bei Vermessungs- und Ingenieur Anwendungen ausgelegt. Sie hat eine Richtungsmessgenauigkeit von 1", das EDM misst auf 1 mm + 1 ppm genau. Umfangreiche Funktionen erhöhen die Effizienz und die Produktivität im Außendienst.

### DIE FORTSCHRITTLICHSTE TOTALSTATIONSPLATTFORM

Der Trimble S8-Totalstation liegt die neueste Trimble-Totalstationsplattform zugrunde. Ganz egal, ob Sie sich auf Vermessungen oder Ingenieur Anwendungen spezialisiert haben: Sie können mit der neuen Totalstationsoptik im Außendienst produktiver arbeiten.

Die Trimble® MagDrive™-Servomotoren garantieren eine schnelle, flüsterleise Bewegung, so dass Sie eine größere Anzahl von Zielen bis zu 40% schneller messen und geräuschloser überwachen können, als mit herkömmlichen Totalstationen. Das bedeutet, bei Überwachungsanwendungen werden Bewegungen schneller erkannt und Sie können früher geeignete Maßnahmen in die Wege leiten. Die verschleißarmen MagDrive-Servofeintriebe ermöglichen einen wartungsfreien Betrieb rund um die Uhr.

### EIN KOMPLETTES SYSTEM FÜR INGENIEURAPPLIKATIONEN

Die Trimble S8-Totalstation arbeitet nahtlos mit der Trimble Survey Controller™ Feldsoftware und der neuen Trimble® 4D Control Software. Sie ist eine komplette Lösung für Spezialanwendungen im Außendienst.

### Trimble S8-Totalstation

Die Trimble S8 verfügt über einzigartige neue Funktionen, z. B.:

- Trimble® FineLock: ein intelligenter Trackersensor, mit schmalen Sehfeld, mit dem die Trimble S8 das Prisma ohne Interferenzen durch andere Reflektoren in unmittelbarer Nähe erkennt. Diese Funktionen erlauben eine flexiblere Prismennutzung und bieten eine außergewöhnlich zuverlässige Genauigkeit.
- Die synchronisierte Ausgabe mit 10 Hz beschleunigt die Datenerfassung bei dynamischen Anwendungen, beispielsweise bei der Überwachung von Schienennetzen. Prismen können ohne Genauigkeitseinbußen mit höherer Geschwindigkeit bewegt werden.

### Trimble Survey Controller Feldsoftware – Ingenieurmodul

Die Trimble Survey Controller Software verfügt jetzt über ein separates Ingenieurmodul. Da dieses Modul über die Trimble Survey Controller Benutzeroberfläche ausgeführt wird, können Vermessungsbüros Ingenieur Anwendungen in ihr Dienstleistungsangebot integrieren, ohne dass die Messtruppen die neue Software zuerst erlernen müssen.

### Trimble 4D Control Software

Die Trimble 4D Control Software ist eine Postprocessing-Software, die für Ingenieur Anwendungen, inkl. Überwachungsanwendungen, entwickelt wurde. Sie liest Richtungssätze aus der Trimble Survey Controller Software als Einzelmessungen im JobXML-Format ein und verfolgt Prismenbewegungen innerhalb eines vorgegebenen Zeitraums. Die Ergebnisse sind auf der visuellen Benutzeroberfläche extrem einfach zu analysieren. Sie können außerdem Alarmmeldungen vordefinieren, die Sie umgehend über alle Prismenbewegungen informieren.

### INTEGRATED SURVEYING

Die Trimble S8-Totalstation ist eine vollständige Integrated Surveying™ -Lösung, ganz gleich, für welche Anwendungen Sie sie einsetzen.

Das System bietet bei Ingenieur Applikationen einen nahtlosen Datenfluss zwischen Messungen vor Ort und der Trimble 4D Control Software. Die Ergebnisse werden schnell angezeigt. Selbstverständlich integriert sich die Trimble S8 auch bei typischen Vermessungsanwendungen nahtlos in jede Trimble-Lösung. Sie haben beispielsweise die Möglichkeit, Totalstationsdaten mit GPS- und 3D-Scanningdaten übergangslos zusammenzuführen oder das Instrument zusammen mit einem Trimble I. S. Rover zu nutzen.

Die Flexibilität der Trimble S8-Totalstation garantiert darüber hinaus eine schnelle Amortisation.

# TRIMBLE S8-TOTALSTATION

## LEISTUNGSSPEZIFIKATIONEN

Richtungsmessung	
Genauigkeit (Standardabweichung gemäß DIN 18732)	1" (0,3 mgon)
Richtungsablesung (Auflösung)	
Standardmessung	1" (0,1 mgon)
Tracking	2" (0,5 mgon)
Präzisionsmessung	0,1" (0,01 mgon)
Automatischer Stehachskompensator	
Typ	Zweiachskompensator (zentriert)
Genauigkeit	0,5" (0,15 mgon)
Kompensatorbereich	±6' (±100 mgon)
Distanzmessung	
Genauigkeit (Standardabweichung)	
Prismenmodus	
Standardmessung	1 mm + 1 ppm <sup>1</sup>
Tracking	5 mm + 2 ppm
DR-Modus	
Standardmessung	3 mm + 2 ppm
Tracking	10 mm + 2 ppm
Messzeit	
Prismenmodus	
Standardmessung	2 Sek.
Tracking	0,4 Sek.
Präzisionsmessung <sup>1</sup>	2 Sek. pro Messung
DR-Modus	
Standardmessung	3–15 Sek.
Tracking	0,4 Sek.
Präzisionsmessung <sup>2</sup>	3–15 Sek. pro Messung
Reichweite (bei normaler Sicht <sup>3,4</sup> )	
Prismenmodus	
1 Prisma	3000 m
1 Prisma, Long Range (LR)	5000 m
3 Prismen	5000 m
3 Prismen (LR)	7000 m
Kürzeste Zielweite	1,5 m
DR-Modus (typisch)	
Kodak-Grau Karte (18% Reflexion) <sup>5</sup>	>120 m
Kodak-Grau Karte (90% Reflexion) <sup>5</sup>	>150 m
Kürzeste Zielweite	1,5 m

## EDM-SPEZIFIKATIONEN

Lichtquelle	Laserdiode 660 nm; Laserklasse 1 im Prismenmodus, Laserklasse 2 im DR-Modus
Koaxial angeordneter Laserpointer (Standard)	Laserklasse 2
Strahldivergenz Prismenmodus	
Horizontal	4 cm/100 m
Vertikal	4 cm/100 m
Strahldivergenz DR-Modus	
Horizontal	2 cm/50 m
Vertikal	2 cm/50 m
Atmosphärische Korrektur	-130 ppm bis 160 ppm kontinuierlich

## ALLGEMEINE SPEZIFIKATIONEN

Horizontierung	
Dosenlibelle im Dreifuß	8/2 mm
Elektronische zweiachsige Libelle im LC-Display mit einer Auflösung von	0,3" (0,1 mgon)
Servosystem	MagDrive-Servomotoren, integrierter Servo-/ Winkelsensor; elektromagnetischer Direktantrieb
Drehgeschwindigkeit	115 Grad/Sek. (128 gon/Sek.)
Wechsel der Fernrohrlage	3,2 Sek.
Positioniergeschwindigkeit 180 Grad (200 gon)	3,2 Sek.
Klemmen und Feintriebe	Servogesteuerte Endlosfeintriebe

© 2007, Trimble Navigation Limited. Alle Rechte vorbehalten. Trimble, das Globus- & Dreieck-Logo und Autolock sind in den USA und in anderen Ländern eingetragene Warenzeichen von Trimble Navigation Limited. Integrated Surveying, MagDrive, MultiTrack und Trimble Survey Controller sind Warenzeichen von Trimble Navigation Limited. Alle anderen Warenzeichen sind Eigentum der entsprechenden Inhaber. Bestellnr 022543-410-D (09/07)

Zentrierung	
Zentriersystem	3-Zapfen
Optisches Lot	integriertes optisches Lot
Vergrößerung/Fokussierung	2,3x/0,5 m – ∞
Fernrohr	
Vergrößerung	30x
Öffnung	40 mm
Sehfeld auf 100 m	2,6 m
Fokussierung	1,5 m – ∞
Beleuchtetes Fadenkreuz	ja, variabel (10 Schritte)
Tracklight	Standard
Betriebstemperaturbereich	-20°C bis +50°C
Staub- und wasserdicht	gemäß IP55
Stromversorgung	
Interne Batterie	aufladbare Lithium-Ionen Batterie 11,1V, 4,4 Ah
Batteriebetriebszeit <sup>6</sup>	
Eine interne Batterie	ca. 6 Stunden
Drei Batterien (über Multibatteriehalterung)	ca. 18 Stunden
Robotic-Halterung mit einer internen Batterie	12 Stunden
Gewicht	
Instrument (Servo/Autolock <sup>®</sup> )	5,15 kg
Instrument (Robotic)	5,25 kg
Trimble CU-Controller	0,4 kg
Dreifuß	0,7 kg
Interne Batterie	0,35 kg
Kippachshöhe	196 mm
Datenübertragung	USB, serielle Schnittstelle, Bluetooth <sup>®7</sup>

## ROBOTIC-MESSUNGEN

Reichweite bei Autolock und Robotic-Messungen <sup>4</sup>	
Passive Prismen	500–700 m
Trimble MultiTrack-Prisma	800 m
Autolock-Zielgenauigkeit auf 200 m (Standardabweichung) <sup>4</sup>	
Passive Prismen	2 mm
Trimble MultiTrack-Prisma	<2 mm
Kürzeste Suchdistanz	0,2 m
Richtungsablesung (Auflösung)	
Standardmessung	1" (0,1 mgon)
Tracking	2" (0,5 mgon)
Präzisionsmessung	0,1" (0,01 mgon)
Datenfunkgerät intern/extern	2,4 GHz Frequenzsprung-/ Spread Spectrum-Datenfunk
Suchdauer (typisch) <sup>8</sup>	2-10 Sek.

## FINELOCK

Reichweite mit passiven Prismen (Min.–Max.) <sup>4</sup>	20 m–700 m
Mindestabstand zwischen Prismen auf 200 m	0,5 m

## GPS-SUCHE/GEOLOCK MIT TRIMBLE MULTITRACK-PRISMA

GPS-Zielsuche/GeoLock	360 Grad (400 gon) oder definierter horizontaler oder vertikaler Suchsektor
Positionsberechnungszeit	15–30 Sek <sup>9</sup>
Erneute Zielerfassung bei Verlust der Zielverbindung	<3 Sek
Reichweite	beschränkt auf Autolock- + Robotic-Reichweite

1 Begrenzter Betriebstemperatur für Präzisionsmessungen (1 mm + 1 ppm): +5°C bis +45°C.

2 Wiederholungsmessung einstellbar (bis zu 99 Messungen).

3 Normale Sicht: Keine Nebel-/Dunstbildung, Bewölkung oder mittlere Sonneneinstrahlung mit leichtem Hitzeflimmern.

4 Reichweite und Genauigkeit sind abhängig von den atmosphärischen Bedingungen, der Größe des Prismas und der Hintergrundstrahlung.

5 Kodak-Grau Karte, Katalognr. E1527795.

6 Die Batteriekapazität bei -20°C beträgt 75% der Batteriekapazität bei +20°C.

7 Bluetooth-Zulassungen sind länderspezifisch. Weitere Informationen erhalten Sie bei Ihrem zuständigen Trimble-Vertriebspartner.

8 Abhängig vom gewählten Suchsektor.

9 Die Positionsberechnungszeit ist abhängig von der Lösungsgeometrie und der Qualität der GPS-Positionen.

Spezifikationen können ohne vorherige Ankündigung geändert werden.

## NORDAMERIKA

Trimble Engineering & Construction Group  
5475 Kellenburger Road  
Dayton, Ohio 45424-1099 • USA  
(Gebührenfrei in den USA)  
800-538-7800  
Tel.: +1-937-245-5154  
Fax: +1-937-233-9441

## EUROPA

Trimble GmbH  
Am Prime Parc 11  
65479 Raunheim  
DEUTSCHLAND  
Tel.: +49-6142-2100-0  
Fax: +49-6142-2100-550

## ASIEN & SÜDPAZIFIK

Trimble Navigation  
Singapore PTE Limited  
80 Marine Parade Road  
#22-06, Parkway Parade  
Singapore 449269 • SINGAPUR  
Tel.: +65-6348-2212  
Fax: +65-6348-2232

AUTORISIERTER TRIMBLE-VERTRIEBSPARTNER



www.trimble.com

## F.2 UAV: Microdrones mdMapper1000+



Unsere microdrones sind miniaturisierte VTOL-Fluggeräte (Vertical Take Off and Landing). Sie können ferngesteuert werden oder mit Hilfe einer GPS Wegpunkt Navigation autonom fliegen.



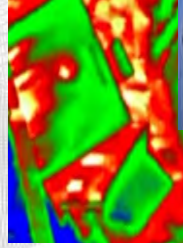
Dank des einzigartigen AAHRS (Attitude, Altitude and Heading Reference System) können auch unerfahrene Piloten die Maschine nach einer Lernphase von unter einer Stunde problemlos bedienen.

Abhängig von Nutzlast und Akku, sowie Windgeschwindigkeit und Temperatur erreicht das System Flugzeiten von bis zu 70 Minuten. Mit der optionalen Videobrille sind darüber hinaus Flüge außerhalb der Sichtweite möglich.

Die vier bürstenlosen Motoren arbeiten geräuschlos und sind dadurch bei sehr hoher Effizienz extrem leise (< 68 dBA, Schwebeflug in 3m Entfernung).

### Anwender

- Fotografen
- Journalisten
- Medienagenturen
- Archäologen
- Landvermesser
- Architekten / Immobilienmakler
- Umweltschutz (z.B. Energiepass)
- Wetterdienste / Umweltbeobachtung
- Feuerwehr / Polizei / Sicherheit
- Film & Fernsehen
- Sportveranstaltungen



- ### Einsatzgebiete
- Dokumentation
  - Koordination
  - Kommunikation
  - Inspektion
  - Observation

... und alles, was Sie sich sonst noch vorstellen können!

### Mobilität



### Kameras

Es stehen Foto- und Videokameras mit hoher Auflösung, sowie leichtgewichtige Tageslicht-, Dämmerungs- und Wärmebild- bzw. Thermalkameras zur Verfügung. Alle Nutzlasten der md4-200 können auch an der md4-1000 eingesetzt werden.



### Base Station

Das Base Station Set ist in einem stabilen Koffer eingebaut, der das Equipment wirkungsvoll schützt. Die Base Station beinhaltet neben einem Diversity-Videoempfänger einen Downlinkempfänger, Frametrabber sowie optional eine Videobrille.

Die Energieversorgung erfolgt über den 230V Anschluss oder einen 12V KFZ-Anschluss. Ein Akku ermöglicht den Betrieb im Feld für mehr als 10 Stunden.

Mit einem Notebook kann der Pilot das Video und den Telemetriedatenstrom der Drohne empfangen, aufzeichnen und beliebig kopieren und verteilen.



### Software

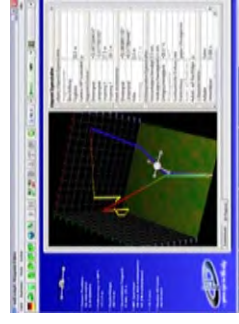
mdCockpit ist eine Anwendung für Microsoft™ Windows™, das alle zur Flugplanung, -überwachung und -auswertung nötigen Aufgaben übernimmt:



Temperatur, Motordrehzahl, Fernbedienungsangaben, Betriebszustand und viele weitere Details an. Alle Daten werden ebenfalls vom Flugschreiber zur späteren Analyse gespeichert.



Der Waypoint Editor bietet die Möglichkeit detaillierte Routenbeschreibungen zu erstellen, welche die Drohne autonom abfliegen kann.



Über die Route hinaus gibt es zahlreiche Fotofunktionen, wie die Erstellung von Panoramen oder die Umkreisung eines Punktes von Interesse.

Die geplante Route wird dreidimensional dargestellt und kann bei Bedarf auch nach GoogleEarth™ exportiert werden.

Falls durch die Arbeit mit dem Waypoint Editor ein Kartenbild für die gegenwärtige Flugregion zur Verfügung steht, kann der Downlink Decoder auch bei nicht-Waypoint-Flügen die aktuelle Drohnenposition auf dieser Karte anzeigen.





## G Data stored on flash disk

On data medium, which is attached to the print version of this thesis, several files are saved. In fig. G.1, you can see the files that are saved on the flash disk. Summarized, it covers:

- **Code**, that has been developed as part of this master's thesis (overall lines of code without empty lines and comments: 10454 in 132 functions, average lines per function: 79)
- **Video tutorials and screen recordings** describing novel code structure and functions
- The **master's thesis** itself including full appendix in high-resolution
- **All images and plots** included in this master's thesis in high-resolution
- (not (too large): original data sets (images of flight 2020 measure 7 GB.))
- downsized QFly images and videos
- references (papers, website screenshots)
- bibliography (jabref-file / latex-file)
- large tables (if any)
- relevant data (such as *.mat*-files)
- Measured values, models
- additional files

The files are stored on the FAPS-server and can be accessed by contacting Christian Hofmann (FAPS, christian.hofmann@faps.fau.de / +49 9131 8520196), who then provides the link to download the *.zip*-file.

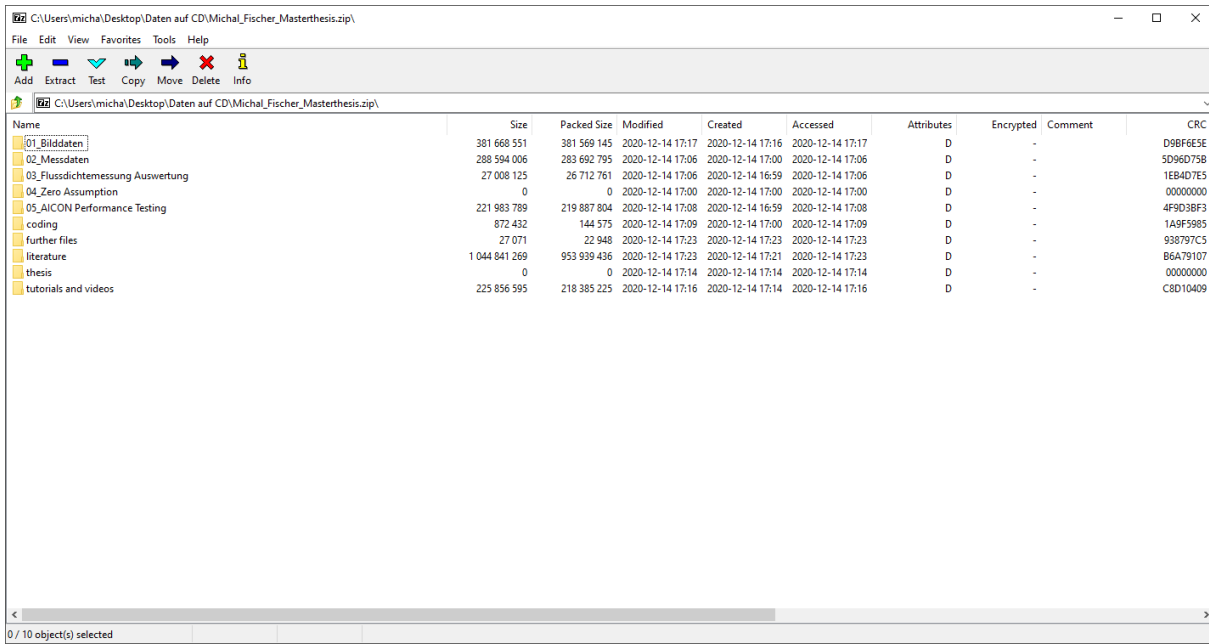


**Figure G.1:** Screenshot of explorer window, showing what the un-zipped folder looks like at the time when the master's thesis was handed in.

## H Curriculum Vitae



# MICHAEL FISCHER

Bachelor of Engineering (TH) Mechanical Engineering



## Address

Otto-Goetze-Strasse 11, 91054 Erlangen, Germany



## Date of birth

13. November 1992



## Phone

+49 (0) 163 2569157



## E-mail

michaelfischer1992@web.de

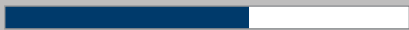


## SKILLS


Catia V5/V6 (incl. VBA for Catia, ENOVIA)



PTC Creo Parametric 3.0



MS Office (incl. Project and Visio)



Technical Product Development Process



Adobe Creative Suite CS6 (Id, Ps, Ai, Pr)



Visual Basic for Applications (VBA)



Automotive Engineering



MATLAB



### Further software skills:

Siemens NX, Minitab, CAD/CAM, ANSYS Workbench, Solidworks, Autodesk Alias, ...

### Programming:

C++, Java, Matlab, VBA, HTML, LaTeX, ...



## OBJECTIVE

I'm an ambitious Masters student with **passion for sustainable processes and products**. In addition to extensive experience (internships, thesis, university projects) in the sectors **engineering, design, simulation and production**, I have an excellent ability to work in a team and a creative way of thinking.

I'm thrilled to solve **global and industrial challenges** in an innovative environment. Image processing for UAVs in the surveying of solar TTPs would best suit these expectations.



## EDUCATION

since 04/2018

**Master's degree (M.Sc.) in Mechatronics Eng.**  
**Univ. of Erlangen-Nuremberg, Germany.**

FACULTY OF ENGINEERING. CURRENT GRADE: **1.3**

02/2018 - 06/2018

**Semester abroad**  
**RMIT University, Melbourne, Australia.**

M.ENG., AUTOMOTIVE ENGINEERING.

09/2017 - 01/2018

**Semester abroad**  
**Budapest Univ. of Techn. and Economics, Hungary.**

FACULTY OF TRANSPORTATION AND VEHICLE ENGINEERING.

10/2015 - 03/2018

**Master's degree (M.Sc.) in Mech. Eng. (NF)**  
**Univ. of Erlangen-Nuremberg, Germany.**

FACULTY OF ENGINEERING., Focus on Product Development

Final Grade: **1.3**

10/2011 - 09/2015

**Bachelor's degree (B.Eng.) in Mech. Eng.**  
**Technische Hochschule Ingolstadt, Germany.**

FACULTY OF MECH. ENG., Focus on Automotive Eng.

Final Grade: **2.1**

09/2003 - 07/2011

**Gymnasium Schrobenhausen, Germany.**

SCIENCE- AND TECHNOLOGY-ORIENTED HIGH SCHOOL

Final Grade (Abitur): **1.8**



## LANGUAGES



## INTERESTS

- New Mobility
- Design
- Soccer
- Language
- Education
- Entrepreneurship
- Guitar and Singing
- Permaculture
- Dancing
- Indonesia



## SEMINARS

- „MedTech, 5G & AI“ Fall School  
Shenzhen, China - Sep 2019, 1 week
- „Oceans & Waters“ Summer School  
Shanghai, China - Aug 2019, 1 week
- „Global Challenges“ Summer School  
Trento, Italy - Jul 2019, 2 weeks
- Silicon Valley Spring School  
San José, USA - March 2019, 2 weeks
- Start-Up seminar  
FAU Erlangen - June 2019, 6 days
- Storytelling seminar  
FAU Erlangen - May 2019, 1 day
- Conversational skills seminar  
FAU Erlangen - May 2019, 2 days
- Presentation rhetoric seminar  
FAU Erlangen - April 2019, 2 days

Erlangen, 25 November 2019

Michael Fischer



## WORK EXPERIENCE & PROJECTS

- 04/2019 - 07/2019 **Valeo Siemens eAutomotive Germany GmbH**  
**Trainee in production planning**  
Production planning for inverters for BEVs.
- 10/2016 - 06/2017 **High-Octane Motorsports e.V.**  
**Formula Student team of the FAU**  
Development and manufacturing of the CFK-monocoque, head restraint, dash panel, fire wall and driver's seat.
- 03/2016 - 09/2016 **BMW Manufacturing Co., Spartanburg, USA.**  
**Internship in the car factory**  
Interface management between development department and assembly line. Coordinating process chain partners and solution finding for issues affecting chassis
- 05/2015 - 09/2015 **BMW AG, Munich.**  
**Internship in the development department**  
Predevelopment, series development and quality management for axle components.
- 10/2014 - 04/2015 **Bertrandt Ingenieurbüro GmbH, Ingolstadt.**  
**Bachelor thesis (grade: 1.0)**  
Development of a mounting concept for bent exhaust gas temperature sensors.
- 09/2013 - 02/2014 **MAN Truck & Bus AG, Munich. Internship**  
Solving manufacturing issues regarding new parts and developing a special holding rod.



## MEMBERSHIPS & HOBBIES

- since 08/2019 **Start-Up ClimateConnect**  
Acceleration platform for projects that mitigate GHG.
- since 07/2019 **Owner and Founder of „Aresing Youth Academy“**  
Seminars for teenagers (12-18 years) to enhance personal development and start-up affinity.
- since 06/2019 **Start-Up CONNECT**  
Application for flexible ridesharing.
- 07/2017 - 12/2018 **English Teacher, voluntary work. Indonesia**  
English teacher at Universities and high schools, paradigm changer in education and environmental mgmt.
- since 05/2013 **Village community in Aresing**  
Periodical performances in dancing Schuhplattler and Bavarian folk dance.
- since 2009 **Voluntary work as lecturer**  
Parish „St. Martin“ in Aresing.
- 1998 - 2017 **Soccer**  
In Aresing's soccer team (BC Aresing).

*I have no doubt  
that we will be successful  
in harnessing the sun's energy.  
If sunbeams were weapons of  
war,  
we would have had  
solar energy centuries ago.*

GEORGE PORTER